ÉCOLE POLYTECHNIQUE DE BRUXELLES
UNIVERSITÉ LIBRE DE BRUXELLES

KU LEUVEN
ARENBERG DOCTORAL SCHOOL
Faculty of Science

Study of one-neutron halo through (d, p) transfer reactions

Thesis submitted by Jiecheng YANG

in fulfillment of the requirements of the PhD Degree in Engineering Sciences and Technology (ULB - "Docteur en Sciences de l'ingénieur et technologie") and in Science (KUL)

Academic year 2015-2019

Supervisors: Prof. Pierre CAPEL (Université libre de Bruxelles)

and Prof. Riccardo RAABE (Katholieke Universiteit Leuven)

Co-Supervisor: Prof. Jean-Marc SPARENBERG (Université libre de Bruxelles)

September 2019

Study of one-neutron halo through (d, p) transfer reactions

Jiecheng YANG

Examination committee:
Prof. Dr. Nicolas Pauly, chair
Prof. Dr. Pierre Capel, supervisor
Prof. Dr. Riccardo Raabe, supervisor
Prof. Dr. Jean-Marc Sparenberg, co-supervisor
Prof. Dr. Nathal Severijns
Prof. Dr. Thomas Elias Cocolios
Prof. Dr. Antonio M. Moro
(Universidad de Sevilla)
Prof. Dr. Manuela Cavallaro
(INFN - Laboratori Nazionali del Sud)

Dissertation presented in fulfillment of the requirements of the PhD Degree in Engineering Sciences and Technology (ULB - "Docteur en Sciences de l'ingénieur et technologie") and in Science (KUL)

September 2019

This work was partly created with the support of the China Scholarship Council (CSC), the European Union Horizon 2020 research and innovation programme under grant agreement No 654002 (ENSAR2), the Belgian Research Initiative on eXotic nuclei (BriX), Programme No. P7/12 on interuniversity attraction poles of the Belgian Federal Science Policy Office, and Research Foundation Flanders (FWO, Belgium) by GOA/2015/010 (BOF KU Leuven).

Acknowledgement

This is probably the most unscientific part of the thesis. No formula or data will be presented here. But that does not mean it is not important. In contrast, it is a great chance to express my sincere gratitudes to many persons who have helped me. Living and studying abroad for four years is not an easy task. During this period, I was once depressed, felt struggled but also had a lot of fun. I could not make it till this stage if without support from you. Now it is my duty and pleasant to thank those nice and great people.

First of all, I would really like to thank my promoters, Pierre and Riccardo, for offering me the opportunity to continue an exciting research life on both theoretical and experimental aspects. Their sharp minds and profound understanding of nuclear physics have guided me all the way through. Personally, I am very impressed that whenever I sent a report or presentation to Pierre, he is always able to point out the mistakes which are important but easy to ignore. I have also been correcting some reports from time to time so that I know how much time one needs to do that. Pierre, your efforts are really appreciated and also thank you for your tolerance in my writing skills. In these four years, I have been to many dreaming laboratories like CERN, GANIL, LNL, etc. had the chance to get into touch with the most advanced techniques and collaborated with many excellent experimentalists, for which my big thanks go to Riccardo, thank you for your trusts on me during the process. Not only on the aspect of research, both of my supervisors also provide a lot of help regarding my administration issues and living problem. Thank you again!

I am also grateful to the rest of my jury members, Prof. Dr. Jean-Marc Sparenberg, Prof. Dr. Nicolas Pauly, Prof. Dr. Nathal Severijns, Prof. Dr. Thomas Elias Cocolios, Prof. Dr. Antonio M. Moro, Prof. Dr. Manuela Cavallaro for their comments, remarks and enlightening discussion. I feel very proud to have you in my final examination committee.

A huge thank should also be sent to all my friends and colleagues at IKS

and PNTPM, old and new ones. Thank you for your scientific, language and emotional helps when they were really needed. Because of you, Alice, Oleksii, Simone, Jonas, Maxime, Alex, Stefano, Marek, Tommaso, Nam, Frederic, Cobus ..., these four year are made rather smooth and delightful. My cordial thanks are extended to Jesper and Karsten, who have been so kind to share with me their extensive knowledge and experience on the data analysis.

The special thanks are to all my Chinese friends who have also been studying in Belgium. They helped me through the initial transition period and made me feel at home whenever staying with them. There are still many other people who have directly or indirectly offered help to me, some of them I even do not know the name. Here I would also like to say a thank you to all of them.

Last but not the least, the most heartfelt thanks go to my parents, and especially my dear wife Yusi, without whom I would be completely lost. Their encouragement and trust in me give me courage and strength to move on each single day in the past, present and future. I am very thankful to you for everything.

A sweet thank to my new arrived child Muzhi, who is so cute that relieves a lot of pressure during my final writing period. When you grow up, one day you will be able to read this part.

Jiecheng

in summer of 2019

Abstract

In modern nuclear physics, a special group of nuclei located close to the drip line named halo nuclei has received tremendous attention due to their unique cluster structure. These nuclei exhibit large matter radii and are qualitatively described as a compact core surrounded by a diffuse halo which is formed by the loosely-bound valence nucleon(s). Their existence breaks down the consistent predictions by the classical shell model and challenges nuclear-structure calculations. To understand this exotic feature from first principles, lots of efforts have been undertaken by nuclear physicists during the past decades. One of the most successful probes to look into these questions is the (d,p) transfer which has been proved to be a very powerful tool to extract single-particle properties of nuclei and hence is ideal to study one-neutron halo nuclei.

The major objective of the present work is to extract more reliable structural information about a halo nucleus using the (d,p) reaction. For that purpose, the experiment done by Schmitt *et al.* on the ^{10}Be(d,p)^{11}Be transfer reaction at four beam energies [Phys. Rev. Lett. 108, 192701 (2012)] is reanalyzed to determine the beam-energy and angular ranges at which such reaction is strictly peripheral. These peripheral conditions are systematically identified by coupling a Halo EFT description of the ^{11}Be nucleus at leading order (LO) with the adiabatic distorted wave approximation (ADWA) to model the reaction. The results suggest that focussing on the transfer data collected with low beam energies and at forward scattering angles ensures us to probe only the halo of the nucleus and hence reliably extract the asymptotic normalization coefficient (ANC). The resulting values of ANC are $C_{1s1/2} = (0.785 \pm 0.030)$ fm$^{-1/2}$ for the ground state and $C_{0p1/2} = (0.135 \pm 0.005)$ fm$^{-1/2}$ for the excited state of ^{11}Be. These values are in excellent agreement with the *ab initio* calculations of Calci *et al.*, who have obtained the ANC values of 0.786 fm$^{-1/2}$ for the ground state and 0.129 fm$^{-1/2}$ for the first excited state [Phys. Rev. Lett. 117, 242501 (2016)].

An alternative way to explore the sensitivity of transfer calculations to the

short-range physics of the ^{10}Be-n wave function using Halo EFT is offered by the supersymmetry (SuSy) method, which also serves as a cross-check to test the peripheral conditions. The idea here is to use the phase-equivalent transformations to generate bound-state wave functions that have an identical ANC but exhibit very different behavior in the internal part.

As an application of the aforementioned method, the ANC of another halo nucleus ^{15}C is extracted from the cross sections of the ^{14}C(d,p) transfer measured by Mukhamedzhanov *et al.* [Phys. Rev. C, 84, 024616 (2011)]. The ANC value obtained for the ground state and first excited state of ^{15}C are (1.26 ± 0.02) fm$^{-1/2}$ and (0.056 ± 0.001) fm$^{-1/2}$, respectively. Especially for the ground state case, again, a perfect agreement is reached between our result and the one predicted by Navrátil *et al.* ($C_{1/2^+} = 1.282$ fm$^{-1/2}$) in an *ab initio* calculation.

We have also looked at the extension of this idea to resonant states. After an analogous analysis using a bin description, it is figured out that the resonant width plays a key role in determining the magnitude of the cross sections for such transfers. Its effect on resonance can be comparable to that of the ANC on bound states. But the associated uncertainty is larger than that in the case of bound state.

In collaboration with Prof. Obertelli, we have studied the use of sub-Coulomb (d,p) transfer to investigate the possible presence of a halo structure in the excited nuclear states of some nuclei in medium to heavy mass region. Based on the promising test case ^{95}Sr, the dependencies of the transfer calculation on several crucial parameters including Q-value, nuclear spin and beam energy have been tested to understand better how the halo feature could be revealed by measuring transfer cross sections. The feasibility of this idea requires an accurate theoretical prediction and sensitive detection systems.

On the experimental side, efforts have been made to progress in the data analysis of the IS561A experiment on ^{9}Li(d,p) transfer performed at HIE-ISOLDE, CERN. Thanks to the preprocessing of the acquired data done by Jesper Halkjær Jensen (Aarhus), the necessary information on the elastic-scattering channel has been successfully collected and matches well with our theoretical calculation. Due to some practical problems happening during the measurement which would propagate to the analysis and result in a low statistics, the extraction of the (d,p) channel will require further detailed analyses. To make up for this, the available data measured by Jeppesen *et al.* [Phys. Lett. B, 642(5): 449 – 454, 2006] and Cavallaro *et al.* [Phys. Rev. Lett. 118, 012701 (2017)] are taken into account to check in those cases the validity of the chosen model which has been used to study the resonance of ^{11}Be. The outcome is rather promising when confronting the theory to the data points.

Abbreviations

ADWA	Adiabatic Distorted Wave Approximation
AGS	Alt-Grassberger-Sandhas
ANC	Asymptotic Normalization Coefficient
BE	Binding Energy
CDCC	Continuum-Discretized Coupled-Channel
CRC	Coupled Reaction Channels
DSSD	Double-sided Silicon Strip Detector
DWBA	Distorted Wave Born Approximation
EFT	Effective Field Theory
ex.s.	excited state
FR	Finite Range
FWHM	Full Width at Half Maximum
g.s.	ground state
KD	Koning and Delaroche potential
LO	Leading Order
NCSMC	No-Core Shell Model with Continuum
NLO	Next-to-Leading Order
NNDC	National Nuclear Data Center
OMP	Optical Model Potential
SEC	Scattering Experiments Chamber
SPANC	Single-Particle Asymptotic Normalization Coefficient
SuSy	SuperSymmetry
TPC	Time Projection Chamber
ZR	Zero Range

Contents

List of Figures

List of Tables

Chapter 1

Physics Motivation

When people refer to the word "halo", it will always bring a feeling of elusiveness or bizarreness. Being observed in several disciplines [WH68, Tho02, BGC+08], the halo phenomenon in nuclear physics is understood to be a larger spatial extension arising from a threshold effect. Since its discovery by Tanihata and his collaborators in 1985 [THH+85], this exotic structure has triggered many studies with lots of exciting achievements reached during the past decades. As the motivation for the study presented here, this chapter aims to give an introduction of this topic and outline some of the theoretical and experimental techniques developed to understand the properties of halo nuclei. The first section introduces some of the key features of halo nuclei followed by the motivation and methods to study it. As one of the main experimental methods to study halo nuclei, transfer reaction is another focus of this study and will be reviewed in the second section.

1.1 Halo nuclei

Halo nuclei usually lie, as shown in Fig. 1.1, near the drip lines which are far away from the "valley of stability". This exotic structure is the result of a threshold effect. In these exotic systems, the last nucleon(s) can be so weakly bound that, due to its quantum wave nature, it can easily tunnel out and spend most of its time outside the classically allowed region [HJ87, Rii13]. Such tunnelling effect implies a dilute probability of presence of the valence nucleon(s) which thus can be seen visually as wandering in a misty cloud. That is why the

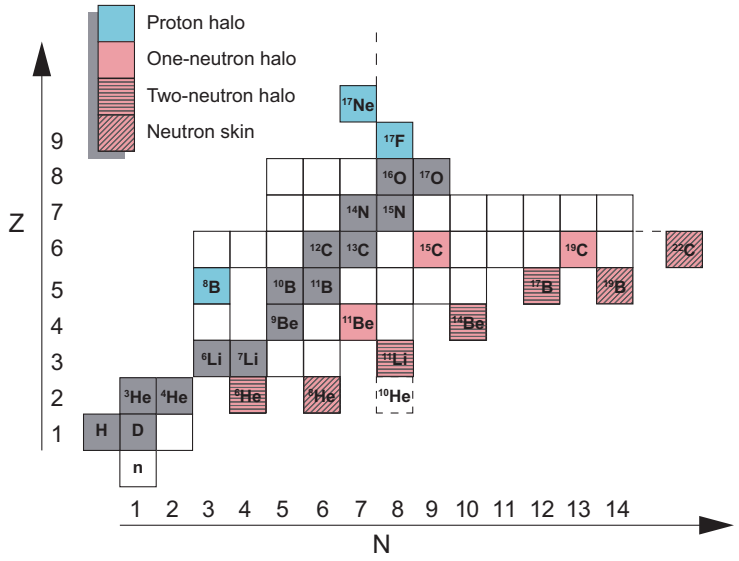

Figure 1.1: The lowest part of the Segrè chart showing the known halo nuclei based on Ref. [AK04]. Stable nuclei are represented by grey blocks.

term "halo" was assigned to this kind of nuclei by Hansen and Jonson in their seminal work [HJ87].

Even though the understanding of halo has continuously evolved and deepened, it is still hard nowadays to draw a clear boundary to define a halo nucleus. The well accepted definition of a halo nucleus is that in some states (typically the ground state) of a nucleus, one or two nucleons (mostly neutrons) decouple from the core and exhibit a large probability of presence away from the other nucleons, i.e., have more than 50% probability of its density being outside the range of the core potential [Rii94, HJJ95, AK04] (note the value chosen here is arbitrary and not met within most of the known halo nuclei). Besides this crude definition, there are several key features of the halo structure that have to be taken into account in order to use the concept consistently according to Ref. [Rii13]. A halo system should be well-clustered for distinguishing between an inert core and valence part. It can be approximately described by few-body models to reproduce its characteristics [HJP17]. Halo nuclei are weakly bound. Compared with the common binding energy per nucleon of 6 to 8 MeV in stable nuclei, a typical one or two-nucleon separation energy in a halo nucleus is around or less than 1 MeV. It is much easier to separate the halo nucleons

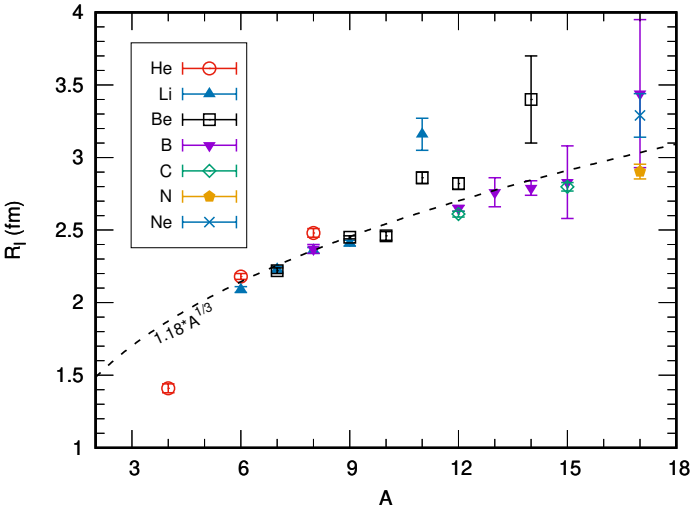

Figure 1.2: Interaction radii R_I of several light isotopes extracted from the interaction cross sections [TKY+88, OKS+94, Tan96] as a function of the mass number A. Compared to the usual $A^{1/3}$ dependence of the nuclear size shown as the dashed line, sudden increase of the radius is observed for some of the nuclei close to the neutron dripline.

than to excite the core. Therefore, they are rather fragile and easy to break up. The interaction between the core and valence part is of nuclear origin and hence should be described by a short-range potential which drops with the distance r much faster than r^{-2}. In other words, the potential multiplied by the square of the distance is approaching 0 when the distance goes to infinity [JRFG04]. As a counterexample, a long-range attractive potential deriving from the Coulomb force in Rydberg atoms [Gal88] will not give halos in general. Relative to the core, the halo nucleon prefers to be located in a state with a relatively low orbital angular momentum (expressed as l) such as an s wave. This is due to the fact that larger values of l lead to a confining centrifugal barrier. The combination of weak binding and short-range potential suggests that the quantum tunneling effect must be a remarkable property in the halo system. All the above points result in a larger matter radius of the halo nucleus, viewed as a dilute and large peripheral distribution surrounding the central core, which breaks the normal relationship of $r_0 A^{(1/3)}$ learned from the stable nuclei as shown in Fig. 1.2. Inspired by Ref. [Tan96], in the figure the interaction radii R_I are defined with a relationship to the interaction cross section σ_I as

$\sigma_I = \pi[R_I(P) + R_I(T)]^2$ using a simple geometrical model where P is set for projectile and T for target. Although not strictly equivalent, the interaction radius is a good measure of the size of the nucleus.

After introducing a basic and general picture of halo nuclei in the last paragraph, a few more technical derivations in terms of the potential model would be useful to help understand the formation of halos. Since this study is mainly focussed on one-neutron halo nuclei, let us consider for instance an ideal two-body model with a pointlike neutron loosely bound to a structureless core in a simple spherical finite square well potential, the size R of which is that of the core itself. Quantum mechanically, the wave function $\psi(r, \theta, \phi)$ describing the relative motion between the neutron and the core in the spherical coordinates can be obtained by solving the following Schrödinger equation [GS18]

$$-\frac{\hbar^2}{2\mu r^2}[\frac{\partial}{\partial r}(r^2\frac{\partial}{\partial r}) - \hat{l}^2]\psi(r,\theta,\phi) + V(r)\psi(r,\theta,\phi) = -S_n\psi(r,\theta,\phi) \qquad (1.1)$$

where μ is the reduced mass of the core-neutron system, $V(r)$ stands for the spherically symmetric potential such that $V(r) = V_0$ (some certain depth of the potential well, smaller than 0) for $|r| < R$ and $V(r) = 0$ elsewhere, $\hat{l}$ represents the angular momentum operator, and S_n is the one-neutron separation energy (here $S_n > 0$ for bound states). By introducing a further simplification that the excess neutron is bound in an s wave, i.e., $l = 0$, the only degree of freedom for the wave function in Eq. (1.1) comes from the relative core-valence distance r. The wave function outside the potential well can be expressed by the formula [HJ87]

$$\psi(r,\theta,\phi) = (\frac{\kappa}{2\pi})^{1/2}\frac{e^{\kappa R}}{(1+\kappa R)^{1/2}}[\frac{e^{-\kappa r}}{r}] \qquad (1.2)$$

which gives a clear asymptotic behavior (note in fact the angular dependence of this wave function is nil). The parameter κ that determines the slope of the decaying exponential tail is related only to the separation energy S_n and the reduced mass μ via $\kappa = \sqrt{2\mu S_n/\hbar^2}$. As can be seen clearly here, the smaller S_n becomes, the slower the tail of the wave function decays. This means that the state with an eigen-energy just below the separation threshold could have a well extended surface in contrary to the deeply-bound states which are mostly restricted within the potential radius R. The mean-square radius to quantify the extension of the valence neutron in an s wave can be written as

$$\langle r^2\rangle = 4\pi\int_0^\infty r^4|\psi(r)|^2dr \xrightarrow{R\to 0} \frac{1}{2\kappa^2} \qquad (1.3)$$

This indicates that, with a δ potential, the root-mean-square (rms) radius $\langle r^2\rangle^{1/2}$ diverges when the separation energy S_n of the s-wave state goes to 0. Though this is a rather simple approach, it reveals that for halo nuclei (especially

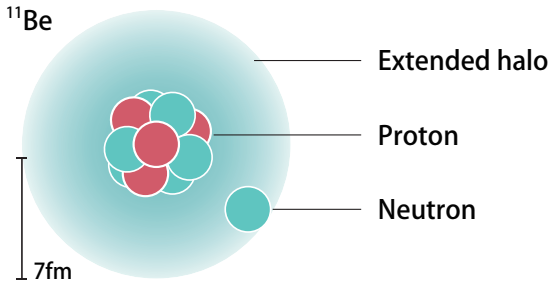

Figure 1.3: Neutron-rich beryllium nucleus ^{11}Be can be modeled as a neutron halo that extends beyond a compact core of ^{10}Be.

for neutron halo) the dominant characteristic comes from the tail of the wave function, which is closely related to the associated separation energy. This is the key and starting point of the theoretical study in the present work. Furthermore, one obtains a less diverging radius with a higher orbital angular momentum or a confining Coulomb barrier. The existence of the Coulomb force which acts as the centrifugal barrier is the reason why proton halos are less frequent than the neutron halos. In addition to that, with a simple semi-classical model [Ser47], the wave function expressed in Eq. (1.2) can be turned by the Fourier transform into a longitudinal momentum distribution $f(p_i)$ of the neutron in the Breit-Wigner form [Tan96, AK04]

$$f(p_i) \propto \frac{1}{p_i^2 + \kappa^2} \tag{1.4}$$

in which p_i is the Cartesian component of the momentum. Obviously, the width of the momentum distribution gets smaller when S_n decreases. This implies that such system follows exactly the Heisenberg's uncertainty principle [Hei27], i.e., when a quantum system is widely distributed in the coordinate space, it exhibits a narrow distribution in momentum space.

A few halo nuclei have been confirmed so far as shown in Fig. 1.1. Among them, the most carefully studied nuclei are ^{11}Be with a one-neutron halo and, ^{6}He and ^{11}Li as two-neutron halo nuclei. Some of their properties are listed in Table 1.1 along with the other well established halo states. Being close to the limits of particle stability, few halo nuclei have more than one bound state. Therefore, most halos tend to be manifest in the ground state of the nuclei. However, it is notable that both the ground state (g.s.) and the first excited state (ex.s.) of ^{11}Be exhibit halos. Another peculiar feature brought with ^{11}Be is the g.s. parity inversion noticed by Talmi and Unna [TU60] in the early 1960s. Regarding the n+^{10}Be configuration, the measured g.s. parity of ^{11}Be

Table 1.1: Properties of some typical halo nuclei. E_x represents the excitation energy of the halo state. S_h is the separation energy for the halo part. J^π gives the spin and parity of the state. l is given as either the orbital angular momentum of the valence nucleon or the admixture of the states for the last two neutrons in the 2-n halo case.

Type	Nucleus	Config	E_x (keV)	S_h (keV)	J^π	l	r_h^{rms} (fm)	Half-life
1-n halo	^{11}Be	n+^{10}Be	g.s.	501.6(3)	$1/2^+$	0	5.77(16)[a]	13.76(7)s
	^{11}Be	n+^{10}Be	320.04(10)	181.6*	$1/2^-$	1	4.65(20)[b]	115(10)fs
	^{15}C	n+^{14}C	g.s.	1218.1(8)	$1/2^+$	0	†[c]	2.449(5)s
2-n halo	^{6}He	n+n+^{4}He	g.s.	975.45(5)	0^+	1	2.97(26)[d]	806.7(15)ms
	^{11}Li	n+n+^{9}Li	g.s.	378(5)[e]	$3/2^-$	0,1[f]	5.98(32)[g]	8.75(14)ms
1-p halo	^{8}B	p+^{7}Be	g.s.	137(1)[h]	2^+	1	4.24(25)	770(3)ms
	^{17}F	p+^{16}O	495.33(10)	104.9*	$1/2^+$	0		64.49(16)s

Data is mostly collected from the NNDC compilations [ENS18] besides some updates as follows
[a] Extracted from Coulomb dissociation data [FNA+04].
[b] Derived from the (d,p) transfer reaction [BPTO+14].
[c] Disagreement found between the studies of Refs. [KHH+16] (r_h^{rms} = 4.2(5) fm) and [OST01] (2.50(8) fm).
[d] Obtained from the analysis of proton elastic scattering at an intermediate energy [ADE+02].
[e] Measured using the radio-frequency spectrometer MISTRAL at ISOLDE [BAG+08].
[f] Strong mixing of s and p neutrons claimed in [TAB+08].
[g] From the analysis of [DAA+06].
[h] From the Atomic Mass Evaluation in [AW95].
* Calculated using the E_x and g.s. separation energy.

is positive, whereas the valence neutron should lie in the 0p1/2 shell in the standard shell model [MJ55]. The $1/2^+$ g.s. is separated by 320 keV from its parity-inverted $1/2^-$ partner [KKP+12]. This also serves as a great example of the disappearance of the $N = 8$ magic number with an increasing neutron to proton ratio. An artist's view of the ^{11}Be nucleus is displayed in Fig. 1.3 which shows the orbits of the loosely-bound neutron at a mean distance of 7 fm from the center-of-mass [NTicv+09]. With the binding energy just above 1 MeV, ^{15}C is another good testing ground for understanding the halo phenomenon due to its clear single-particle feature [OST01, KHH+16].

The two-neutron halo nuclei also known as Borromean nuclei [ZDF+93], ^{6}He and ^{11}Li, present a three-body dynamics that involves two loosely-bound neutrons and a core. The internal mechanism of this system is thus more complex compared to that of one-neutron halos. Similar to the concept of the Borromean rings, there are no bound states in any binary subsystems. This point causes

special interests to understand the nature of the interaction and correlation between the two halo neutrons. Several theoretical predictions, such as di-neutron assumption [ZDF+93, OZV99] and Efimov effect [Rii13], have been developed for this purpose. The structure of ^{6}He is well understood as the two neutrons in p-orbits outside the alpha core [ZDF+93]. For ^{11}Li, the analysis from Refs. [ZHN+97, TAB+08] suggests the necessity of considerable mixing of s and p waves in its ground state.

On the proton-rich side, as quickly discussed before, the formation of proton halos is much less probable than that of neutron halos due to the existence of a repulsive Coulomb barrier. Nevertheless, examples include ^{8}B, ^{17}Ne and the first excited state of ^{17}F. The spatial extension of the p-wave proton in the g.s. of ^{8}B was recognized early in the studies of proton radiative capture [CD61]. Considering ^{17}F, the first excited state is modeled as the valence neutron occupying an s wave. A proton halo can therefore form since no centrifugal term is added to the potential in this case compared to the g.s. viewed as a d wave [MKM+97].

1.1.1 Why is it interesting?

In the past 35 years, the halo field has generated a lot of exciting findings together with even more questions. A growing interest deals with the challenges posed by studying and describing this system. This section aims to quickly go over some of the hot topics regarding halo nuclei.

Halo nuclei are challenging research objects to provide a fresh viewpoint on the mysteries of the nuclear binding and pairing. For a long time, the nucleus has been pictured as a liquid drop composed of protons and neutrons that has a sharp surface, which works well for the stable cases. However, the halo concept emerges with a entirely novel structure in which some loosely-bound nucleons venture far beyond such surface, resulting in a diffuse and extended distribution in space. Under the stress of extreme neutron-proton ratio, they also experience smaller obstacles than the stable nuclei to get excited or broken apart. Studying halo nuclei could help reveal the subtle balance inside the many-body nuclear system, and hence gives hints to the puzzles physicists have on the possible combinations of neutrons and protons to stay together as a nucleus.

A better understanding of the halo phenomenon is needed to improve the present theoretical models of nuclear structure. Facing this open structure, the conventional shell-model and mean-field (Hartree-Fock) approaches have to be questioned and reconsidered [AB95]. The main requirements here are to describe the relative behavior between the core and the valence nucleon(s) at large distance accurately. To account for these effects, the no-core shell

model with continuum (NCSMC) [NQH+16], which solves exactly a many-body problem from first principles using chiral interactions, has been adopted in studying the cases of ^{11}Be [CNR+16] and ^{15}C [Nav18] by Navrátil *et al.* In addition, the effective field theory (EFT) has been developed to exploit the separation of scales in halo nuclei [BHvK02, HJP17]. Generally speaking, an EFT offers a framework to include the appropriate degrees of freedom to treat physical phenomena occurring at long distances explicitly without resolving the short-distance physics (which might be reflected by some constants in the calculation) of the substructure. As a branch of this theory, the EFT for halo nuclei, called *Halo EFT*, permits the theoretical fitting of several observables, such as the halo binding energy, the radius, etc, with respect to different types of halos (mostly at s wave and p wave). In the present study, the *Halo EFT* is used within reaction models to help devise a way to extract the structural information of halo nuclei from transfer reactions. A comparison between our results and the predictions of other advanced structure model like *ab initio* calculations which model explicitly the dynamics of the nuclear system could reveal the degrees of freedom that actually matter in the reaction modelling.

Another related open question is where nuclear halo states exist. There have been considerable efforts made on the theoretical sides to predict the occurence of halos [Ham17, CLG19]. One of the widely-used models is the convariant density functional theory, for instance, the Hartree-Fock-Bogoliubov (HFB) theory. The interested reader is referred to the review paper [MZ15] for more information. Due to the fact that most confirmed halo nuclei nowadays are found in the light mass range, the existing tools and definitions might be incomplete and too qualitative for heavier ones. As already pointed out in Ref. [RBD09], it is necessary to have different criteria for defining halos in heavier nuclei. Instead of applying the previous concept in Sec. 1.1, the halo part is identified for heavy nuclei as the region beyond a certain radius r_0 where the core density is one order of magnitude smaller than the halo one [RBD09]. Under this new standard, halos, at least for even-even heavy nuclei which are tremendously influenced by the pairing effect, are estimated to be less abundant than those in the light-mass region. In addition, it is also reasonable to expect that halos could exist in the excited states since many highly excited nuclei will be rather weakly bound. However, when considering this, one has to be really careful since a small breakup threshold is not the only criterion to judge a halo as listed before. Different from the g.s., an additional restriction here is the inevitable mixing with other nuclear states if the corresponding local density is high. According to the estimation proposed by Ref. [JR00], for an excitation energy E^* with the level distance following the relationship of $7e^{-2\sqrt{aE^*}}$ MeV (with $a = A/7.5$ MeV^{-1}), the s-wave neutron halo would appear with the condition of the binding energy being smaller than $0.27(A/Z)^2e^{-4\sqrt{aE^*}}$ MeV. But this has

not yet been explored experimentally. A more general and realistic formulation awaits to be figured out to suggest necessary and sufficient conditions for predicting halos. In the present thesis, some efforts are made to contribute to this topic, taking into account the very basic single-particle characteristics of halo nuclei. In particular, transfer reaction is suggested as a tool to search for the halos in excited states of nuclei.

Studying halos would also yield unique insights into some other fields. With two-neutron halo nuclei, it offers a new type of systems where the Efimov effect [Efi70] could possibly occur besides the molecular and atomic ones. The large size of halo nuclei leads to threshold phenomena having important general consequences for low-energy reaction rates in nuclear astrophysics. Such extreme systems are supposed to be found in extreme environments, for example, the crust of neutron stars. Hypernuclear halos have also been speculated to exist in several cases [CJF97] by theoretical calculations and wait for more experimental data to support this claim. In line with Ref. [PR18], a careful investigation of the neutron behavior in halo nuclei helps distinguish if neutrons can undergo a dark-matter decay mode or not. Of course, it is not possible to cover all the aspects within this short section. But at least from this glimpse of the field, the reader can see how many challenges and opportunities remain.

1.1.2 How to study halo nuclei?

To verify the assumption and enrich the knowledge physicists have about halo nuclei, experimental observables are definitely required to describe their behavior quantitatively. Rather than making a general coverage of the whole field, the goal in this section is to present some of the typical methods and probes to learn and characterize the nuclear halo states. Combining the information extracted from different experiments can ensure the accuracy of the hypothesis and help reach a more convincing conclusion about the halo states. For more information, the reader is referred to Refs. [TB05, Bla06, KAKR09, CF10, PKGR12] for reviews from different aspects regarding this topic.

As the consequence of the mass–energy equivalence, measurements of nuclear masses can determine the binding energy of the nucleus which is one of the most crucial driving forces to produce a halo phenomenon. The mass of a nucleus can be derived indirectly from the energy balance in nuclear reactions and decay processes [YBF$^+$93]. Furthermore, thanks to the development of the experimental techniques, ion traps at low energy (such as Penning trap) and time-of-flight (TOF) methods enable the direct measurement of the masses far from stability and provide an alternative solution with sufficient accuracy as well as precision [MLSO97]. The main challenge associated with the direct

methods lies in the difficulty of producing the exotic nuclei along the dripline in large amount.

Laser spectroscopy on radioactive beams offers a model-independent way of collecting the nuclear properties, including the nuclear spin, mean-square charge radius, magnetic dipole moment and spectroscopic electric quadrupole moment [CF10, CMP16]. Historically, a series of optical measurements has been prompted by the halo phenomenon. It began with laser-induced nuclear orientation to study the moments of ^{11}Li [NBB$^+$08] and ^{11}Be [GKK$^+$99], which is helpful to understand the behavior of their wavefunctions. The recent isotope shift (i.e., the frequency intervals between isotopes) measurements of He [WMB$^+$04, MSV$^+$07], Li [SNE$^+$06] and Be isotopes [NTicv$^+$09] take a step forward to learn the core polarization caused by the diffuse neutron structure. This suggests that the charge radii are very valuable not only for a direct determination of the proton halos' sizes, such as ^{17}Ne [Jon04], but also for giving information on the core modification with respect to the neutron halo case.

Beta decay can carry signals of a halo structure in some specific cases [Rii13]. On the one hand, the decay probability heavily relies on the overlap of the wavefunctions between the initial and final states, which could be slightly reduced by the spatial extension of the halo. On the other hand, due to the decoupling form embedded in the halo nuclei, they might experience a decoupled decay. This is to say that the core and valence clusters might decay independently from each other. Such process is of special interest to the two-neutron halo systems, which is known as beta-delayed deuteron emission [RAB$^+$08].

Electromagnetic processes such as electromagnetic dissociation and radiative capture have also been used as a probe to study the halo formation. The electromagnetic matrix elements of type $E(\lambda)$ or $M(\lambda + 1)$ depend on the dimension of the nucleus by a factor of r^λ and therefore are very sensitive to the halo formation. In particular, the *E1*-strength will be affected by the extra degree of freedom of neutron halos. Higher multipoles such as *E2* will contain the contribution from proton halos while the *E1*-strength is reduced in these cases.

The most classical and widely-used method to study halo nuclei is nuclear reaction including elastic and inelastic scattering, transfer reaction, electromagnetic dissociation and so on. It is often the only means to get nuclear information because the lifetime of these nuclei are usually short. To assert the type of the reactions, it is accustomed to refer to the beam energy. The high to intermediate energy reactions usually take place around and above the Fermi energy while the low energy reactions happen well below that (around the Coulomb barrier). A rough demarcation energy point for these two kinds of reactions is some tens

of MeV per nucleon. Reactions at different energies have their own advantages on investigating the halo nuclei since the reaction mechanisms do develop differently as the energy changes. For the high to intermediate energy nuclear reactions, the short interaction time and the small nucleon-nucleon cross sections reduce the complexity to describe the reaction mechanism. When bombarding the target with different isotopes as in the pioneering experiment of this field [THH+85], the extended size of a halo system gives an increased total reaction cross section (see Fig. 1.2). The corresponding theoretical explanation can rest on a coupled-channel calculation of breakup at an intermediate energy or the sudden (Glauber-type) geometrical approximation [Kar75] at a high beam energy. It shows that for the halo case the major contribution for the dissociation reactions comes from the region at large internuclear distances. As discussed before with Eq. (1.4), another valuable probe to learn the halo property is the measurement of the momentum distribution of either the core or the valence part from breakup reactions. Simultaneous detection of all the fragments at distinct states emerging from the reactions is possible with the current experimental set-ups at most nuclear facilities, allowing the reconstruction of the complete kinematics and hence a better understanding of the process.

Considering low energy reactions, they include elastic scattering, breakup reaction, transfer reaction and other channels. They are useful in studying halo nuclei as:

- Elastic scattering: a process where the total kinetic energy of the system is conserved. The diffuse halo modifies the elastic scattering cross section due to the strong coupling to the transfer and/or breakup channel [DPRS+10];
- Breakup reaction: dissociation of the projectile through the interaction with a target. The process reveals the underlying cluster structure of the nuclei [FNA+04];
- Transfer reaction: one or more nucleons are transferred between the projectile and target. This method provides a probe to study the single-particle structure of the interesting nuclei, and hence are particularly well suited to study halo nuclei [SJB+12].

During the past decade, this field has evolved and achieved milestones from identification of halo nuclei to extraction of the halo property. Among those methods, transfer reaction is employed as a powerful tool to study the nuclear structure. It is also one of the main topics in this work. More details will be shown and discussed in the next section.

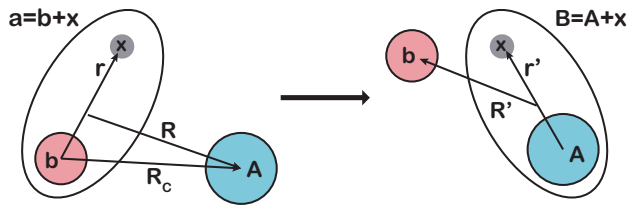

Figure 1.4: Stripping reaction with associated coordinates for the reaction $A+a \rightarrow b+B$ with x being the transferred cluster. Experimentally, A and a are usually in their ground states while B and b can be excited to higher states.

1.2 Transfer reaction

The history of transfer reaction can be traced back to the 1950s for extracting the spins and parities of nuclear energy levels [But50] when most of the information in nuclear structure (like collective modes including rotational, vibrational and so on) has come from beta and gamma spectroscopy [ES08]. Later developments involving accelerator technology, spectrographs and theoretical models boosted the research with transfer reactions in the 60s and 70s. In the 1990s, (d,p) transfer reaction was applied using a short-lived beam in inverse kinematics for the first time [KEF$^+$94]. As a kind of direct nuclear reactions, transfer reaction is a general designation of transferring up to several nucleons between the projectile and target nuclei that can be denoted as $A+a \rightarrow b+B$ where $a=b+x$ and $B=A+x$. Fig. 1.4 gives an intuitive description of this reaction. Its interaction time is rather short (10^{-22} s) compared to the lifetime of most exotic nuclei, making a clean cut between the formation and the decay of the produced nuclei. Historically, it is also named stripping reaction when the target gains nucleon(s) from the projectile. And pickup reaction represents the opposite way. Depending on how many nucleons get exchanged during the process, transfer reaction can be subdivided into multi-nucleon transfer and single-nucleon one. Multi-nucleon transfer is widely used with heavy ions [CPS09, ZZK$^+$14], providing a method to learn the component responsible for particle correlations such as the pairing interaction. The corresponding process can be single-step (such as α-transfer where the α cluster is preformed and

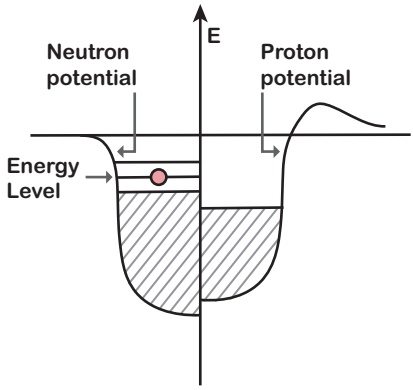

Figure 1.5: Schematic single-nucleon model description with one neutron added to a core filling the lower energy levels. The shape difference of the potential well between the proton and neutron side is caused by the Coulomb repulsion and the symmetry correction which takes into account the fact that the most stable arrangement has equal numbers of protons and neutrons.

transferred) or multiple-step which conceivably would lead to a complex analysis and interpretation of these reactions. In the present work, the emphasis is on single-nucleon transfer, primarily (d,p) reactions, aiming at the understanding of single-particle structure in the halo nuclei.

The selectivity of a single-nucleon transfer makes it an excellent tool for mapping out the single-particle structure of nuclei and hence studying the migration of shell gaps and magic numbers [Ots13, SP13] while venturing away from the stability. The so-called single-particle structure can be treated in a simplified picture shown in Fig. 1.5 as a core (namely the original nucleus) filling the lower energy levels with the transferred nucleon added to it, which shares many similarities with the halo phenomenon. However, this simple picture can be complicated in the real case by several detailed issues, for example the coexistence of the single-particle structure and other configurations giving the same spin and parity. To solve the problem of mixing, one main branch of the transfer study is to extract the intensity of the single-particle component as the quantity called spectroscopic factor [End77]. Experimentally, it is the ratio between the theoretical calculation under the assumption of a pure single-particle

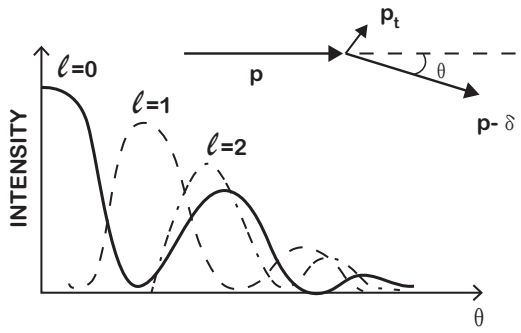

Figure 1.6: Different transfer momenta can lead to different angular distribution of the transfer probability due to the momentum matching effect [Cat14].

state and the corresponding measured cross section. A different approach focuses on the concept of the asymptotic normalization coefficient (ANC) [BDB77, TN09] which corresponds to the normalization of the tail of the overlap wave functions of the nuclei (see Sec. 2.4 for more details). Determined by measuring peripheral reactions, the ANCs have often been used to indirectly obtain the reaction rate for the synthesis of nuclei in astrophysical sites and to characterize the halo structure of loosely-bound nuclei [KAB$^+$03, BSM$^+$16]. In this work, one of our main contributions is to propose a new, systematic and reliable way to extract the ANC of loosely-bound nuclei from transfer measurements. More details regarding this will be explained in Chapter 2 and 3.

In addition to being a powerful probe of the single-particle state which is learned from the magnitude of the transfer cross sections, another striking initial feature of the transfer reaction is the direct determination of the transferred orbit angular momentum when the beam energy is above its Coulomb barrier. This comes from the shape of the angular distribution of the reaction products and could help indicate into which orbit the single nucleon has been added [Coh71]. Considering the transfer in a semi-classical picture, the main maximum of the transfer probability occurs around the angle where the momentum matches. As shown in the inset of Fig. 1.6, the projectile with a momentum magnitude p impinges on the target. The momentum transferred to the target nucleus has magnitude p_t while the remaining momentum magnitude is expressed as $(p - \delta)$. Applying the conservation of linear momentum there implies a relationship of the transferred momentum to the laboratory scattering angle θ, which can be

written as

$$2(1-\cos\theta) = \frac{(p_t/p)^2 - (\delta/p)^2}{1-\delta/p} \tag{1.5}$$

For a small scattering angle θ, the reduction δ in the incoming momentum magnitude p can be regarded as perturbation and thus dropped. And taking use of the Taylor expansion to the second order for cosine, Eq. (1.5) has a simplified form as $\theta^2 \approx (p_t/p)^2$. If the transfer takes place peripherally at the surface of the target nucleus which has a radius R, the transferred orbital angular momentum l can be estimated by

$$\sqrt{l(l+1)}\hbar \approx \theta p R, \tag{1.6}$$

where θ is in radians. Based on this, one can immediately learn about the l value from the location of the primary maximum in the angular distribution, which is also drawn schematically in Fig. 1.6.

1.2.1 Theoretical reaction model

More accurate theoretical interpretations of transfer reactions originate from the scattering theory treated in an optical model. Twenty years after probably the first (d,p) transfer measurement by Lawrence and his colleagues in 1933 [LLL33], Horowitz and Messiah tried to explain the transfer phenomenon in terms of plane wave approximation [HM53]. In 1961, a more complex model using the distorted wave solutions due to the presence of the scattering potential was developed for experimental data explanation [BH61], which became later the well known distorted wave Born approximation (DWBA). Then Satchler got this method improved by taking into account the spin-orbit effects in the distortion [Sat64]. This theory is still popular nowadays in interpreting reaction data [JA14, TBC+14, BT18] whilst challenges remain in its fundamental framework, such as a proper consideration of the spatial localisation of the transferred nucleon in the initial and final nucleus. Regarding in particular the (d,p) transfer, another important factor is the coupling to the continuum states. Such coupling is not necessarily one-way from bound state to continuum and could take place in more than one step. Furthermore, the continuum of both the deuteron and the final nucleus can contribute significantly in the coupling. In order to include this effect, one solution is to perform the coupled reaction channels (CRC) calculations [Sat83, KKT86, Gle04] which incorporates explicitly contributions from the several mass partitions during the reaction. A specific way is via the continuum-discretized coupled channels (CDCC) technique [AIK+87, YMM+12]. It allows the treatment of couplings to unbound states by dividing the continuum into a finite number of bin states and inserting those states in the coupled-channel calculation as several contributing reaction

pathways. As an approximate version of CDCC in some ways, the zero-range adiabatic distorted wave approximation (ZR-ADWA) initially introduced by Johnson and Soper [JS70] offers an ingenious shortcut to effectively include the deuteron breakup effect. The formalism for a finite-range version of the adiabatic wave method (FR-ADWA) was given by Johnson and Tandy [JT74] afterwards. In practice, the ADWA method maintains the relative simplicity of DWBA by having a large overlap with the DWBA framework and is thus not as computationally expensive as the CDCC method. The applicable situation and accuracy of ADWA have been studied by direct comparison with other methods in Refs. [ND11, UDN12]. It is concluded that when the transfer angular momentum is small and the neutron-nucleus system is loosely bound, ADWA presents an adequate way to predict the transfer cross sections at 5 to 10 MeV/A of the incident energy. Therefore, the ADWA has significant advantages in investigating halo structure using the (d,p) reactions and is preferred in the present work. Computer codes available for performing the ADWA calculations are TWOFNR [TTIK12] and FRESCO [Tho06, TN09]. Technical derivations and comparisons with respect to these models will be given in the next chapter.

1.2.2 Experimental techniques

With the advent of the radioactive beams, transfer reactions in inverse kinematics have been employed in many experiments to study the property of exotic nuclei. Descriptions of the inverse kinematics can be found in most introductory nuclear reaction textbooks [Sat90, Cat02]. Due to the experimental features brought with the radioactive beams, special care has to been taken on two aspects of the experimental setups: i) eventual dumping of the beam is necessary; ii) beam intensity is usually weak in contrast with that of stable beams which requires a careful design of the target. Connected with the case of single-nucleon transfer, the minimum demand for the beam intensity should go beyond the order of 10^4 pps. A measurable magnitude of the reaction cross section is typically higher than 1 mb. Facilities available to carry out the single-nucleon transfer in different energy regimes include, but are not limited to HIE-ISOLDE at CERN for up to 10 MeV/A and SPIRAL at GANIL for 10 to 50 MeV/A. Depending on the techniques used experimentally, four basic categories arise following the idea in Ref. [Cat14].

- Magnetic spectrometer. The basic principle is to separate the reaction products from the projectile via a magnetic field and analyze the beam-like ejectile with high accuracy. The forward focussing of the reaction is always favoured in the measurements, resulting in a limited resolution in the angle for heavier beams. Existing equipments include SPEG [BFG$^+$89] and VAMOS [PRN$^+$08] at GANIL.

- Silicon array. In order to cover a large part of the angular range and obtain useful information in both energy and position of the target-like ejectile, an array of silicon detectors is by far the most versatile choice, such as the TIARA array [LCL+10], T-REX [BGK+12] and SHARC [DFS+11]. A normal resolution of silicon detectors is around 100 to 200 keV [Cat14]. And a high degree of segmentation in the detectors is also required to achieve a better determination of the position where the particle hits. At present, the double-sided silicon strip detector (DSSD) with an arrangement of strip-like shaped implants on the front and rear of the silicon wafer [DSM+90] is commonly used to conduct a two-dimensional position measurement. Besides, silicon detectors can be coupled in a telescope configuration called ΔE-E detector for particle identification. Although the silicon arrays offer a rather flexible and economical solution for detection, the constraints caused by the choice of the target still exist. If a solid target is adopted, its thickness will bring a certain ambiguity when reconstructing the kinematics.
- Gamma-ray detection. Gamma detection is popular because of its high energy resolution for excited states in heavy nuclei. In addition, the measurement of the gamma-ray decay branches could point out the coupling between the spin and l-value, and hence help identify the state more precisely. The challenges of this technique in practice are to achieve a high efficiency of the detection (an array of gamma detectors always preferred) and make a sufficiently good correction for the substantial Doppler shift effect.
- Active target. By filling the time projection chambers (TPCs) with a gas that serves as both the target and tracking medium (active target), this approach largely removes the uncertainty by the energy loss effects in thick targets [ABBN+18]. In this condition, it is possible to rebuild the trajectories of the charged particles in three dimensions and extrapolate the reaction energy precisely. By construction, an active target has a solid angle coverage of 4π and thus can reach a high detection efficiency. This novel method has been realized in many setups, e.g., MAYA [DMS+07] and ACTAR TPC [Raa09].

Note that the above classification does not mean that only one choice has to be made for particle detection. The combination between those methods can make up for the shortcomings and provide from different aspects a better recovery of the transfer picture. One very classical way is to combine a compact silicon array together with the gamma-ray detection (like T-REX with MINIBALL [REF+02]). Another intelligent approach utilized by the HELIOS project [WSB+07] is to place the position-sensitive silicon array along the axis of a solenoid so that the emerging particles are going to be focused and brought back to the array in the magnetic field. Successful measurements [SFB+16, KH16] regarding this concept have been performed at the recently commissioned ISOLDE solenoidal spectrometer (ISS) at CERN [FAB+10]. It is also appealing

to couple the active target with a silicon array or the gamma-ray detection. In Leuven, a more complete and ambitious approach named SPECMAT is under construction. The final aim is to mount the active targets coupled with the scintillator array inside the ISOLDE solenoid.

In summary, all the experimental methods and devices mentioned here could deliver rich information from transfer reactions. Continuous efforts are made to improve the current possibilities and exploit the potential of the upgraded and upcoming facilities.

Chapter 2

Few-body Description of Transfer Reactions

This chapter starts by introducing the basic framework of scattering theory used in the description of nuclear reactions. Such a formalism offers a framework within which several physical models can be embedded. In particular, the optical model is briefly discussed in Sec. 2.2 to provide a way to simulate the interaction between two nuclei in terms of a complex potential. Having a significance similar to the concept of optical model, the wave function of the single-particle bound state in a nucleus and its asymptotic behavior are discussed afterwards. Based on the above content, several models (DWBA, ADWA and so on) for the specific case of (d, p) transfer reaction are presented in Sec. 2.4. The elementary knowledge about quantum mechanics and nuclear-reaction theory is assumed, which one can find in most of the available textbooks such as Refs. [Aus70, Sat83, Sat90, Gle04, TN09]. Thus, instead of a profound mathematical derivation, the most important formulas will be given and annotated. The following developments are restricted to the non-relativistic Schrödinger equation since the practical cases, which will be studied in this work, are measured at low beam energies.

2.1 Scattering theory

2.1.1 Scattering wave function and notion of cross section

Let us first consider a two-body system composed of the projectile a with mass m_a and the target nuclei A with mass m_A. The interaction between them can be described by the potential $V(\mathbf{r_a} - \mathbf{r_A})$ in which $\mathbf{r_a}$ and $\mathbf{r_A}$ represent the coordinates of a and A, respectively. Omitting the internal structure of the particles, the Schrödinger equation that describes the a-A relative motion reads

$$i\hbar\frac{\partial}{\partial t}\Psi(\mathbf{r_a},\mathbf{r_A},t) = \left[-\frac{\hbar^2}{2m_a}\nabla^2_{\mathbf{r_a}} - \frac{\hbar^2}{2m_A}\nabla^2_{\mathbf{r_A}} + V(\mathbf{r_a}-\mathbf{r_A})\right]\Psi(\mathbf{r_a},\mathbf{r_A},t). \quad (2.1)$$

Making the coordinate transformations towards the center-of-mass (c.m.) to generate the relative coordinates $\mathbf{S} = (m_a\mathbf{r_a}+m_A\mathbf{r_A})/(m_a+m_A)$ and $\mathbf{r} = \mathbf{r_a}-\mathbf{r_A}$ [TN09], Eq. (2.1) can be rewritten to

$$i\hbar\frac{\partial}{\partial t}\Psi(\mathbf{S},\mathbf{r},t) = \left[-\frac{\hbar^2}{2(m_a+m_A)}\nabla^2_{\mathbf{S}} - \frac{\hbar^2}{2\mu}\nabla^2_{\mathbf{r}} + V(\mathbf{r})\right]\Psi(\mathbf{S},\mathbf{r},t), \quad (2.2)$$

in which $\mu = m_a m_A/(m_a+m_A)$ is the a-A reduced mass. Substituting the separable solution of the form $\Psi(\mathbf{S},\mathbf{r},t) = \chi(t)\Phi(\mathbf{S})\psi(\mathbf{r})$ in Eq. (2.2), one can solve the equation by separating it into

$$\chi(t) = Ce^{-iE_{\rm tot}t/\hbar}, \quad (2.3)$$

$$-\frac{\hbar^2}{2(m_a+m_A)}\nabla^2_{\mathbf{S}}\Phi(\mathbf{S}) = (E_{\rm tot}-E)\Phi(\mathbf{S}), \quad (2.4)$$

$$\left[-\frac{\hbar^2}{2\mu}\nabla^2_{\mathbf{r}} + V(\mathbf{r})\right]\psi(\mathbf{r}) = E\psi(\mathbf{r}), \quad (2.5)$$

where $E_{\rm tot}$ gives the total energy of the system while E represents only the energy for the relative motion between a and A. C is a normalisation constant. From Eq. (2.3), it is learned that $|\Psi(\mathbf{S},\mathbf{r},t)|^2$ experiences a time-independent form as $|\Phi(\mathbf{S})\psi(\mathbf{r})|^2$ which indicates that the probability density in the space for this system does not change with time. Eq. (2.4) treats the center-of-mass of the two-body system as a free particle and has plane wave solutions to describe its motion. The information about the relative motion between the projectile and the target is fully contained in Eq. (2.5). The motion such equation simulates can also be seen as a single particle with mass μ moving in a potential field created by $V(\mathbf{r})$. In the case of scattering (or unbound states), there is always a solution for any positive eigenvalue E in Eq. (2.5), meaning that the scattering-state spectrum is continuous. The scattered particles can travel far

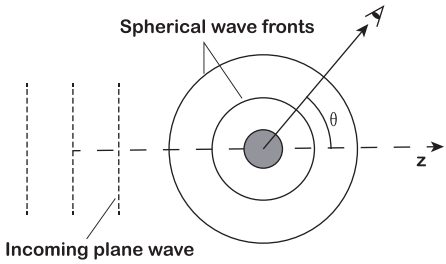

Figure 2.1: Schematic description of the reaction mechanism when a plane wave travels towards a spherical field and gets scattered. The direction of the incoming wave is chosen as z axis. The generated scattering waves are represented by the spherical wave fronts.

away to infinity. Whereas for the bound states, the wave function $\psi(\mathbf{r})$ tends to 0 at infinity with the eigenenergy E being discrete and negative. Indeed, this is the basic difference between the description of nuclear reaction and that of nuclear structure. Additionally, the wave function $\psi(\mathbf{r})$ should always be normalized to 1 to be physically meaningful. This section will be focussed on the scattering problem. Concerning nuclear structure, a typical example is presented in Sec. 2.3 which is of special interests to this work. Henceforth, the theoretical derivations and methods will be built around the formula Eq. (2.5) in the c.m. rest frame unless stated otherwise. Solving this equation is not always trivial since the potential $V(\mathbf{r})$ can exhibit quite complicated forms.

Before diving into finding the solutions for the equation, it is worth to point out which value can be extracted to quantify the reaction rates. The differential cross section is accepted as an excellent meeting point between theory and experiment. On the experimental point of view, it is a measure of the number of the particles dN coming out in a unit time dt after reactions within an element of solid angle $d\Omega$ and divided by the target density n and the beam intensity I, which has the form

$$\frac{d\sigma}{d\Omega} = \frac{1}{I\ n\ dt}\frac{dN}{d\Omega}. \tag{2.6}$$

On the theoretical aspect, this observable can be derived from the wave functions and the notion of probability. Let us assume a schematic picture as shown in Fig. 2.1 that the projectile hits the target along the z axis, giving rise to radiating scattered waves for the outgoing particles. The incoming beam can be described as a plane wave $\psi^{beam} = e^{ik_i z}$ with the wave number $k_i = \sqrt{2\mu_i E_i/\hbar^2}$. The E_i cited here is to replace the E in Eq. (2.5) for the incident channel.

Since the detection usually takes place outside the range of the interaction, at such distances the outgoing spherical wave ψ^{scat} has a radial dependence as $\exp(ik_f r)/r$ with an amplitude $f(\theta,\phi)$ which depends on the scattering angle arising from the a-A interaction. Similarly, k_f is the wave number for the exit channel. The asymptotic form of the complete waves ψ is thus

$$\psi(\mathbf{r}) \xrightarrow{r\to\infty} \psi^{beam} + \psi^{scat} = e^{ik_i z} + f(\theta,\phi)\frac{e^{ik_f r}}{r}. \tag{2.7}$$

According to the formula of the probability current

$$J = \frac{\hbar}{2i\mu}(\psi^*\nabla\psi - \psi\nabla\psi^*), \tag{2.8}$$

the cross sections then can be calculated as the ratio of the scattered angular flux per steradian $r^2 J_{scat}$ to the beam flux J_{beam}, yielding to

$$\frac{d\sigma}{d\Omega} = \frac{r^2 J_{scat}}{J_{beam}} = \frac{\mu_i}{\mu_f}\frac{k_f}{k_i}|f(\theta,\phi)|^2. \tag{2.9}$$

Therefore, it is the goal of reaction theories to determine the scattering amplitude $f(\theta,\phi)$ by solving Eq. (2.5). The following content starts with deriving the formalism of the elastic scattering case ($k = k_i = k_f$ and $\mu = \mu_i = \mu_f$) in spherically symmetric nuclear potentials.

2.1.2 Case with a spherically symmetric nuclear potential

A spherical short-range nuclear potential $V(r)$ is considered here, which only depends on the relative distance between the colliding nuclei. And since the beam comes along the z axis, the scattered waves are always cylindrically symmetrical. It means that the wave function ψ in Eq. (2.5) and the amplitude f in Eq. (2.7) do not depend on ϕ. Applying the method called the partial wave expansion, the wave function can be expanded in angular orbital momentum l [1] as

$$\psi(\mathbf{r}) = \sum_{l=0}^{\infty}\sqrt{\frac{2l+1}{4\pi}}R_l(r)P_l(\cos\theta), \tag{2.10}$$

in which P_l are the Legendre polynomials. Now the key to solve the scattering problem is to find out the expression for the radial wave function $R_l(r)$. Making use of the reduced radial wave function $u_l(r) = rR_l(r)$, the corresponding Schrödinger equation (see Eq. (2.5)) can be simplified to

$$\frac{d^2u_l(r)}{dr^2} + \left[k^2 - \frac{2\mu}{\hbar^2}V(r) - \frac{l(l+1)}{r^2}\right]u_l(r) = 0. \tag{2.11}$$

[1] l = 0, 1, 2, 3 ... corresponds to s, p, d, f ... wave, respectively.

The solution in the external region, i.e., outside the potential range, is expressed as

$$u_l(r) \xrightarrow{r\to\infty} \sqrt{4\pi(2l+1)}\frac{i^l}{2} r \left[h_l^{(2)}(kr) + \mathbf{S}_l h_l^{(1)}(kr)\right]. \tag{2.12}$$

where $h^{(1)}(kr)$ and $h^{(2)}(kr)$ are the spherical Hankel functions of the first and second kind [AS64], representing the outgoing and incoming waves respectively. The introduction of the partial-wave S-matrix element $\mathbf{S}_l$ is due to the existence of the potential V. For each partial wave in the outgoing channel, it brings a phase shift δ_l by $\mathbf{S}_l = e^{2i\delta_l}$. The phase shift δ_l is determined by matching the asymptotic expression of Eq. (2.12) with the exact (usually numerical) solution in the internal part of the potential. The value of δ_l is positive for attractive potentials and negative for repulsive ones. When the potential V is nil, namely $\delta_l = 0$ ($\mathbf{S}_l = 1$), the radial wave function $R_l(r)$ derived from Eq. (2.12) degenerates to a plane wave.

Combining Eqs. (2.12) and (2.10), and comparing the asymptotic solution of the wave function to Eq. (2.7), the scattering amplitude can be obtained as [TN09]

$$f(\theta) = \frac{1}{2ik}\sum_{l=0}^{\infty}(2l+1)(\mathbf{S}_l - 1)P_l(\cos\theta), \tag{2.13}$$

which can also be written in terms of the partial-wave T-matrix element $\mathbf{T}_l$ defined as $\mathbf{T}_l = (\mathbf{S}_l - 1)/2i = e^{i\delta_l}\sin\delta_l$. Thus the outgoing waves are basically represented by $\mathbf{T}_l$.

2.1.3 Case with a Coulomb interaction

What has been discussed in the last section is valid for a short-range potential. When both the projectile and the target are charged, it is necessary to take into account the long-range Coulomb force. Considering first a pure point-Coulomb potential $U_c(r)$ as $Z_a Z_A e^2/r$ between two interacting particles of charge $Z_a e$ and $Z_A e$, Eq. (2.5) gets modified. To characterize the Coulomb interaction, let us define the Sommerfeld parameter η,

$$\eta = \frac{\mu Z_a Z_A e^2}{\hbar^2 k}. \tag{2.14}$$

The corresponding wave function $\psi_c(\mathbf{r})$ can be expanded in partial-wave form as

$$\psi_c(\mathbf{r}) = \sum_{l=0}^{\infty}(2l+1)e^{i\sigma_l(\eta)}i^l P_l(\cos\theta)\frac{F_l(\eta, kr)}{kr}, \tag{2.15}$$

with the regular Coulomb function $F_l(\eta, kr)$ for $\eta \neq 0$ [AS64], and the Coulomb phase shift $\sigma_l(\eta) = \arg\Gamma(l+1+i\eta)$. From the analysis of the asympototic form

of $F_l(\eta, kr)$, the wave function can also be decomposed at large values of $(r-z)$ into the Coulomb-modified incident wave plus the outgoing scattered wave

$$\psi_c(\mathbf{r}) \xrightarrow{(r-z)\to\infty} e^{i[kz+\eta \ln k(r-z)]} + f_c(\theta)\frac{e^{i(kr-\eta \ln 2kr)}}{r}, \tag{2.16}$$

where the Coulomb scattering amplitude $f_c(\theta)$ shares the same form with Eq. (2.13) but replacing the phase shift by $\sigma_l(\eta)$. The asymptotic amplitude of $f_c(\theta)$ is found to be [TN09]

$$f_c(\theta) = -\frac{\eta}{2k\sin^2(\theta/2)} e^{-i\eta \ln(\sin^2(\theta/2))+2i\sigma_0(\eta)}. \tag{2.17}$$

This leads directly to the Rutherford cross section for the scattering of two pointlike particles [Rut11]

$$\left(\frac{d\sigma}{d\Omega}\right)_{\text{Ruth}} = |f_c(\theta)|^2 = \frac{\eta^2}{4k^2\sin^4(\theta/2)}. \tag{2.18}$$

Note here that since f_c diverges at forward angles, it is not possible to compute a total elastic-scattering cross section for the Coulomb interaction.

Then including the nuclear potential in the presence of Coulomb potential brings an additional nuclear phase shift δ_l to the Coulomb phase shift $\sigma_l(\eta)$. Repeating the partial-wave analysis, the wave function is found asymptotically to be [Sat83]

$$\psi(\mathbf{r}) \xrightarrow{r\to\infty} \psi_c(\mathbf{r}) + f_n(\theta)\frac{e^{i(kr-\eta \ln 2kr)}}{r}, \tag{2.19}$$

where $f_n(\theta)$, arising from the extra nuclear potential, is the Coulomb-distorted nuclear scattering amplitude and reads

$$f_n(\theta) = \frac{1}{2ik}\sum_{l=0}^{\infty}(2l+1)P_l(\cos\theta)e^{2i\sigma_l(\eta)}(e^{2i\delta_l}-1). \tag{2.20}$$

This is analogous to Eq. (2.13) when only a short-range nuclear potential is involved. The total scattering amplitude f becomes the combination of this nuclear amplitude f_n and the point-Coulomb scattering amplitude f_c, which is

$$f(\theta) = f_c(\theta) + f_n(\theta). \tag{2.21}$$

Then the differential cross section can be obtained from Eq. (2.9). In practice, to show the influence of the nuclear force and avoid the divergence of the cross section in the forward direction, it is useful to present the ratio of the elastic scattering cross section to the Rutherford one. This ratio is close to unity at small scattering angle.

2.1.4 Case of particles with spins

If the projectile a arrives with a non-zero spin $\mathbf{I}_a$ (the spin of the target $\mathbf{I}_A$ remains zero), the interaction potential may depend on that spin. In particular, usually there is a spin-orbit term which can be expressed in J basis[2] as

$$(\mathbf{I}_a \cdot \mathbf{l})U_{so}(r) = \frac{\hbar^2}{2}\left[J_t(J_t+1) - I_a(I_a+1) - l(l+1)\right]U_{so}(r), \tag{2.22}$$

in addition to the previous central-force potentials. Considering the possible values of $\mathbf{J}_a$ resulting from $\mathbf{l}$ and $\mathbf{I}_a$, the complete phase shifts (or S-matrix elements) and therefore the scattering amplitude in each case can be solved numerically with the partial-wave expansion method [Sat90, TN09].

A more general case is given when I_A does not equal zero. Furthermore, the possible exit channel which is still within the two-body model might differ from the entrance one and contain a variety of mass rearrangements. For the convenience of notation, the set of quantum numbers for the entrance channel $(a+A)$, abbreviated as α, is $\{\alpha\colon\ lI_aI_A\}$. The corresponding magnetic quantum numbers are M_i $(i = a, A)$. The total angular momentum J_t and its projection M_t can then be generated in J basis. Similar strategy can also be exploited to the exit channel β, giving $\{\beta\colon\ l'I_bI_B\}$ with the magnetic quantum numbers M_b and M_B. In terms of S-matrix elements, the full scattering amplitude with Coulomb and nuclear potentials can be found to be [Sat83]

$$\begin{aligned} f_{\beta M_b M_B,\alpha M_a M_A}(\theta,\phi) = f_c(\theta)\delta_{\beta,\alpha}\delta_{M_bM_B,M_aM_A} + \frac{i\sqrt{\pi}}{k}\sum_{lJ_al'J_bJ_t}\sqrt{2l+1} \\ \cdot e^{i(\sigma_l(\eta_\alpha)+\sigma_{l'}(\eta_\beta))}(\delta_{\beta l'J_b,\alpha lJ_a} - \mathbf{S}^{J_t}_{\beta l'J_b,\alpha lJ_a}) \\ \cdot C^{J_aM_a}_{l0I_aM_a}C^{J_tM_t}_{J_aM_aI_AM_A}C^{J_bM_t-M_B}_{l'M_t-M_B-M_bI_bM_b} \\ \cdot C^{J_tM_t}_{J_bM_t-M_BI_BM_B}Y^{M_t-M_B-M_b}_{l'}(\theta,\phi), \end{aligned} \tag{2.23}$$

where the Clebsch-Gordon (CG) coefficient, for instance $C^{J_tM_t}_{J_aM_aI_AM_A}$, is used for coupling two angular momentum states J_aM_a and I_AM_A to a total of J_tM_t. The symbol Y represents the spherical harmonics. The excitation information of the nuclear states for both channels is embedded in the channel notations α and β. Of course, when ignoring all the spins, Eq. (2.23) reduces to Eq. (2.21) for the elastic scattering case.

[2] In J basis [TN09], first $\mathbf{l}+\mathbf{I}_a = \mathbf{J}_a$, then the total angular momentum $\mathbf{J}_t = \mathbf{J}_a + \mathbf{I}_A$.

2.1.5 Born approximation

As one can find out now from the previous derivation, the most important scattering information is included in the S- or T-matrix elements. Given a channel potential V that can be decomposed into two parts: the distorting potential U_1 and the remaining interaction U_2, in an inhomogeneous format the Schrödinger equation (2.5) becomes

$$\left[E - \hat{T} - U_1\right] \psi = U_2 \psi, \tag{2.24}$$

with $\hat{T}$ being the kinetic energy operator. Using the Green's function method [TN09], the exact wave function ψ is the solution of the Lippmann-Schwinger equation

$$\begin{aligned} \psi &= \chi + \hat{G}_1^+ U_2 \psi \\ &= \chi + \hat{G}_1^+ U_2 \left[\chi + \hat{G}_1^+ U_2 \left[\chi + \hat{G}_1^+ U_2 \left[\cdots\right]\right]\right], \end{aligned} \tag{2.25}$$

in which the distorted wave χ is obtained by the equation of $\left[E - \hat{T} - U_1\right] \chi = 0$ and represents the exact solution when $U_2 = 0$. The Green's integral operator $\hat{G}_1^+$ equals to $\left[E - \hat{T} - U_1\right]^{-1}$ with outgoing-wave boundary conditions marked as + sign. The expansion shown in Eq. (2.25) is also called the Born series. The Born approximation is a way to treat the perturbation in such series, namely making a truncation at a certain order. The scattering from the initial channel α to the final channel β by the potential V can be written in the integral expression of vector-form T-matrix[3] as

$$\mathbf{T}_{\beta\alpha}^{\text{post}} = \langle \phi_\beta^{(-)} | U_1 | \chi_\alpha^{(+)} \rangle \delta_{\beta\alpha} + \langle \chi_\beta^{(-)} | U_2 | \psi_\alpha^{(+)} \rangle, \tag{2.26}$$

where the ϕ_β is defined as the solution for the free field in a certain channel β and therefore is the plane wave in this two-body case. The definitions of other symbols used in this equation remain the same as before. For instance, ψ_α means the exact wave function for the channel α. The $(-)$ and $(+)$ superscripts are employed to indicate complex conjugation in the bra-ket notation, satisfying the asymptotic unusual incoming boundary condition and the normal outgoing one respectively. When U_1 becomes a central potential that cannot by itself cause transition between different channels, the division of the potential V is particularly useful since the first term in Eq. (2.26) representing the elastic scattering case equals 0 when $\alpha \neq \beta$. Then the transition between the two channels is basically described by the second term. This point is closely related to the modeling of transfer reactions in Sec. 2.4.

[3]The so-called $\mathbf{T}$ matrix here is distinct from the previous partial-wave form $\mathbf{T}_l$ and depends on the initial and final $\mathbf{k}$ values [TN09]

2.2 Optical model

In real life, multiple channels are open during nuclear reaction. To account for that, a phenomenological way is to describe all other channels as "absorption from the elastic channel", which is analogous to optics where a complex refraction index is used to simulate the propagation of light through a cloudy refractive medium. This concept leads to one of the most successful nuclear models which is known as the optical model. In the optical model, the usually complicated many-body problem brought by the collision of two nuclei is approached by a two-body interaction via a complex potential. In a sense, such potential is presumed to provide an effective version of the actual interaction. The model itself is particularly useful in emphasizing elastic scattering besides few other channels. The occurrence of the non-elastic reaction is considered as a loss of the flux from the elastic channel. This removal is accomplished by making the potentials complex. Applying the concept in Eq. (2.11), an imaginary term $iW(r)$ is introduced in addition to the real component $V(r)$. In this case the scattering theory described above remains valid. Then it can be demonstrated that the corresponding phase shift δ_l will also become complex. Since the optical potential is absorptive, the imaginary part W is expected to be negative. Hence the modulus $|S_l|$ for the outgoing wave (see Eq. (2.12)) is smaller than one. Indeed, the difference given by $1-|S_l|^2$ contributes to the reaction cross section after summing over all the partial waves.

In order to adapt to general circumstances, a realistic and quantitative representation of the potential is necessary. For this purpose, a widely-used procedure is to adequately parameterize a particular functional form of the optical potential. The parameters of the function are fitted to reproduce the scattering data for either one specific projectile-target couple at one energy, or a given type of projectile on a wide range of target nuclei at many bombarding energies. One main criteria here is that the generated potential parameters should vary smoothly and slowly with the incident energy and the target mass number. This phenomenological *global optical potential* has been proven to be successful especially for interpreting the scattering of protons and neutrons on various nuclei. Two of the available and well-known optical potentials for the nucleon-nucleus case are

- CH89 (Chapel Hill 1989) by Varner *et al.* [VTM+91] (Z = 20−83, A = 40−209, E = 10−65 MeV),
- Koning and Delaroche [KD03] (Z = 12−83, A = 27−209, E = 0.001−200 MeV),

which will also be the main ingredients of the calculations in this work. The range of the target type and incident energy within which the potentials have been fitted is provided between parentheses. A common form for the optical

model potentials (OMP) shared by both parameterizations can be written as

$$\begin{aligned} U(r,E) = &-V_v(E) f_{ws}(r,R_v,a_v) - iW_v(E) f_{ws}(r,R_w,a_w) \\ &- iW_s(E)(-4a_s)\frac{d}{dr} f_{ws}(r,R_s,a_s) + V_c(r) \\ &+ \left(\frac{\hbar}{m_\pi c}\right)^2 (V_{so}(E) + iW_{so}(E)) \left[\frac{1}{r}\frac{d}{dr} f_{ws}(r,R_{so},a_{so})\right] l \cdot I \end{aligned} \tag{2.27}$$

in which $V_{v,so}$ and $W_{v,s,so}$ being the energy-dependent well depth of the real and imaginary potentials with respect to the volume (v), surface (s) and spin-orbit (so) terms [KD03]. m_π is the pion rest mass. The form factor $f_{ws}(r,R_i,a_i)$ has a Woods-Saxon shape

$$f_{ws}(r,R_i,a_i) = \frac{1}{1+e^{\left(\frac{r-R_i}{a_i}\right)}}, \tag{2.28}$$

with R_i being the target radius which is approximately proportional to $A^{1/3}$ by a constant r_i, and a_i giving the diffuseness while $i = v, w, s, so$ corresponds to each term of the potential. The Coulomb potential V_c is a bit different from the previous point-Coulomb potential at small radii when the projectile penetrates the nucleus, which is given by

$$V_c(r) = Z_a Z_A e^2 \times \begin{cases} \left(\frac{3}{2} - \frac{r^2}{2R_c^2}\right)\frac{1}{R_c} & (r \le R_c) \\ \frac{1}{r} & (r \ge R_c) \end{cases} \tag{2.29}$$

considering a uniformly charged sphere of radius $R_c = r_c A^{1/3}$. The detailed parameters and way of construction for these two potentials can be found in Refs. [VTM+91, KD03]. Besides, one can also find other older global OMP as alternative choice for incident neutrons and protons, such as Becchetti and Greenlees [BG69], Walter and Guss [WG86], and so on.

As for the scattering of deuterons, there are also global OMPs, e.g., from Daehnick *et al.* [DCV80] or Perey and Perey [PP74], to generate the associated wave function for the relative motion of a deuteron on a target. In practice, these potentials can be used as a rough estimation or an outset for further refitting with one particular set of experimental data from elastic scattering on deuteron. The aim is to reproduce an accurate effective interaction in that case for the colliding pair.

Up to now, the mentioned phenomenological potentials are taken to be local and energy-dependent. But it is worth to point out that those spherically-symmetric potentials might imply a compromise of simplicity over precision [DC19] since

nonlocality would arise significantly due to the influence of nuclear structure (shell closure and deformation) [Hod84] and the coupling to the non-elastic channels [Sat83]. In order to minimize the ambiguities brought by the global fits, an advocated way is to do the fits for a single target nucleus or at least in a designated region of the nuclear chart. Regarding the inclusion of nonlocalities, a pioneering work has been done by Perey and Buck in the early 60s [PB62]. More recent efforts have been carried out in Refs. [TPM15, LBC$^+$17].

Even though there is a belief by a significant fraction of the nuclear-reaction community that the energy dependence could be removed from the optical potentials after a proper introduction of the nonlocality, it is still early to draw the final conclusion since more formalism of the nonlocality must still be figured out and tested. Due to the numerical complexity when solving the integro-differential equations with a non-local potential and the reason of effectiveness, this work will not go in this direction. But this definitely would be an interesting aspect to investigate more in the future.

2.3 Single-particle properties

2.3.1 Single-nucleon states

Since this study focuses mostly on one-neutron halo nuclei which have strong single-particle properties (see Sec. 1.1), the following discussion in this part will be unfolded around this aspect. With a mean-field approximation, the valence particle is assumed to be bound by the average attraction of the other nucleons inside the nucleus. The potential form (without imaginary components) shown in the last section is often used here. To simulate the single-nucleon structure as a two-body problem, typically, a combination of nuclear, Coulomb and spin-orbit potentials is considered in Eq. (2.5) where the motion of the center of mass of this system has already been removed. The corresponding eigenvalue E should be consistent with the measured single-nucleon binding energy of the state. The associated normalized wave function of the individual nucleon for a specific bound state reads [TN09]

$$\psi^m_{lsj}(\mathbf{r}) = \left[Y_l(\hat{\mathbf{r}}) \otimes \chi_s\right]_{jm} \frac{u_{lsj}(r)}{r} \tag{2.30}$$

with angular momentum l, intrinsic nucleon spin s, magnetic quantum number m, total spin j and the spinor χ_s. Actually at small distances, usually deep potentials are considered, which would bring "unphysical" bound states. These states simulate the presence of other nucleons within the core of the nucleus and therefore are forbidden for the valence nucleon due to the Pauli principle.

In the wave function, such forbidden states are reflected as nodes whose number is denoted as n_r. At large distances, it can be proved that the reduced radial wave function u_{lsj} exhibits the following asymptotic behavior [TN09]

$$u_{lsj}(r) \xrightarrow{r\to\infty} b_{lj} W_{-\eta,l+\frac{1}{2}}(2\kappa r), \tag{2.31}$$

where $W_{-\eta,l+\frac{1}{2}}$ is the Whittaker function [AS64], $\kappa = \sqrt{2\mu S_{sp}/\hbar^2}$ gives the actual wave number, and b_{lj} is defined as the single-particle asymptotic normalization coefficient (SPANC), being a quantity characterizing the magnitude of the decay of the wave function at large distances. The value of the SPANC is sensitive to the choice of the nuclear potential.

A specific case comes up when the single nucleon is set to be neutron. There the Sommerfeld parameter η becomes 0 and hence the Whittaker function in Eq. (2.31) gets simplified to $i\kappa r h_l^{(1)}(i\kappa r)$ in terms of the spherical Hankel function $h_l^{(1)}$ [AS64]. Another unique configuration is that of the deuteron which binds a neutron together with a proton and acts as a crucial component in the (d,p) transfer. Its property is believed to be well understood through numerous studies in the past [MF77, GVO01]. To reproduce the interaction between the proton and the neutron inside the deuteron, two ways are commonly used. One is with the Reid soft-core potential [Rei68]. The soft core is an intuitive concept to describe the strong but finite short-range repulsion, indicating that the wave function does not vanish in the repulsive force region. The other is to adopt the Gaussian form with $V_0 = 72.15$ MeV, $r_0 = 1.05$ fm in Eq. (2.32) [AIK$^+$87].

In practice, to solve the Schrödinger equation with these different kinds of potentials, numerical methods with the boundary condition are highly favored since it is not always feasible to find the overall analytical solution. One of the most widely used algorithms for this purpose is the Numerov method [Nou24].

2.3.2 Halo EFT

Being an extension of the Pionless EFT [vK14] for light nuclei, Halo EFT emerges to offer a systematic treatment of the halo phenomenon. For a comprehensive and systematic review of this field, the interested readers are recommended to check Refs. [vK14, HJP17]. Based on the halo concept as introduced in Sec. 1.1, this framework considers the valence nucleon(s) and the core of a halo nucleus as the effective degrees of freedom. Thus, the core is always structureless. The associated quantum mechanical amplitudes can then be expanded on the basis of the hierarchy between the size of the core ($R_{\rm core}$) and the halo ($R_{\rm halo}$) as $R_{\rm core}/R_{\rm halo}$ to the power of $n+1$ ($n = 0$ at leading order, abbreviated as LO). Depending on the separation of scales present in the nuclear system,

this effective theory will become questionable when the reaction resolves the structure of the core or leads to its excitation. Indeed, the influence of the core excitation effect can be further implemented in this theory via adding extra parameters [ZNP14, RFHP14]. However, for the ^{11}Be case, it is not necessary to worry about the breaking down of the structureless assumption of the ^{10}Be core. Giving its first core excitation at 2+ state with the energy $E(2+)$ of 3.4 MeV, a good separation of scales is achieved with the expansion parameters $\sqrt{S_{1n}/E(2+)}$ (equivalent to the parameter $R_{\rm core}/R_{\rm halo}$) being around 0.4 for the ground state and 0.2 for the excited state of ^{11}Be [CPH18].

To formulate the Halo EFT, the Lagrangian (elsewhere in this thesis only Hamiltonians are used) is organized in a controlled expansion with the operators up to a given order. Combined with the focus of this work (one-neutron halo systems), for the loosely-bound case at the limit ($R_{\rm core}/R_{\rm halo} \to 0$), the many-body interactions in the Lagrangian are reduced to the two-body contact interaction at LO described by the zero-range potential. Following the idea developed in Ref. [CPH18], this interaction can be regulated with the Gaussian shape

$$V(r) = -V_0 e^{-\frac{r^2}{2r_0^2}}, \tag{2.32}$$

where r_0 is the Gaussian width that can be varied (the coefficient 2 used here is due to historical reasons). The only free parameter V_0 of this potential is simply tuned to reproduce the one-neutron separation energy S_{1n} of the bound state. This quick but rough assumption runs through the development presented in this work. It is made based on the idea that the essential physics of halo nuclei lies with the long-distance effects without explicit contributions from the core structure. In other words, the low-energy observables of such weakly-bound systems are expected to be independent of the interaction at short distances and can be approached by few-body approximation. Up to this point, the philosophy basically overlaps with the previous single-particle description which aims at calculating the related wave function.

2.3.3 Supersymmetry (SuSy) method

It is of particular interest in the present work to check how different regions of the wave function contribute to the reaction calculation so that we can better understand which part of the nucleus is probed by the reaction process. One strategy considered here is to apply the supersymmetry (SuSy) method [GL71, Ram71, NS71] to build phase-equivalent potentials which can be used to produce single-particle wave functions with the same asymptotics, viz. the same ANC, but very different internal parts after removing deeply bound states. The SuSy method was first introduced to unify bosonic and fermionic sectors in

string theory [CKS95]. Later the ideas and mathematical tools brought with SuSy have stimulated new approaches to other branches of physics [Gie97], such as the field of theoretical nuclear physics [Iac85]. The application of SuSy to Schrödinger quantum mechanics [Wit81] in our case allows removing the nodes in a wave function without changing its phase shift. The principle of the supersymmetry method to produce the phase-equivalent potentials is presented according to Refs. [AB92, SB97]. Let us start with the basic factorization of the 1-D Hamiltonian in quantum mechanics. The eigenvalue of a Hamiltonian H_0 acting on a known ground-state wave function $\psi_0(r)$ for partial wave l is the factorization energy E_0 (The lower index 0 is to help distinguish the supersymmetry partners). The Schrödinger equation can be written as

$$H_0\psi_0(r) = -\frac{\hbar^2}{2\mu}\frac{d^2}{dr^2}\psi_0(r) + V_0(r)\psi_0(r) = E_0\psi_0(r). \tag{2.33}$$

The Hamiltonian H_0 can be factorized into two operators

$$H_0 = A_0^\dagger A_0 + E_0 \tag{2.34}$$

with

$$A_0^\dagger = -\frac{\hbar}{\sqrt{2\mu}}\left(\frac{d}{dr} + \frac{d(\ln\psi_0(r))}{dr}\right), \quad A_0 = \frac{\hbar}{\sqrt{2\mu}}\left(\frac{d}{dr} - \frac{d(\ln\psi_0(r))}{dr}\right). \tag{2.35}$$

If E_0 does not exceed the ground-state energy $E_0^{(0)}$ (The superscript $^{(0)}$ is to indicate the ground state), the solution ψ_0 in Eq. (2.33) is nodeless. By exchanging the order of the two operators $A_0^\dagger$ and A_0, the supersymmetric partner of H_0 is defined as

$$H_1 = -\frac{\hbar^2}{2\mu}\frac{d^2}{dr^2} + V_1(r) = A_0A_0^\dagger + E_0 = H_0 - \frac{2\hbar}{\sqrt{2\mu}}\frac{d^2}{dr^2}\ln\left(\psi_0(r)\right) \tag{2.36}$$

Within this step, the ground state is removed from the original Hamiltonian [BSPMS14] and the phase shift is modified according to the Darboux transformations [BS95]. To compensate the change in the phase shift and generate phase-equivalent potentials with the initial one, further SuSy transformations are needed provided that the factorization energies are chosen to be equal and thus no longer required to be smaller than $E_0^{(0)}$ [LBS97]. The resulting potential as given in Ref. [AB92] is written as

$$V_2(r) = V_0(r) - \frac{2\hbar}{\sqrt{2\mu}}\frac{d^2}{dr^2}\ln\int_0^r \left[\psi_0^{(0)}(x)\right]^2 dx \tag{2.37}$$

The change in the generated wave function using this superpotential is limited to the short range of $\psi_0^{(0)}$. Thus, the long-range part of the wave functions for

the rest of the spectrum, i.e., the ANCs of other bound states and the phase shift in the continuum, is conserved. To compute this superpotential, basically one has to follow Eq. (2.37) by replacing the ground-state wave function ψ_0 with the u_{lsj} in Eq. (2.30).

2.3.4 Resonances

Besides bound cases, we are also interested in studying the resonant states that can be produced with transfer reactions. A resonance usually describes a nuclear state with a short lifetime, reflected by a peak located around some certain energy in the excitation function of a scattering experiment. The energy width of the resonance Γ is connected to the mean lifetime τ of the state by an inverse relationship $\Gamma \sim \hbar/\tau$. The typical sign of a resonance in theory is a rapid change in the scattering phase shift δ_l within a small energy range. The phase shift can be split into one background phase shift δ_{bg} and another resonance phase shift δ_{res}. In the present study, mainly single-particle resonances will be discussed. To be more specific, the sensitivity of the transfer calculation to the energy width in the description of the resonance is of special interest. For this purpose, the following derivation is carried out according to Refs. [TN09, MT99]. In a single-particle configuration, considering a Breit-Wigner resonance [TN09] located at $E_\gamma = E_0 - i\Gamma_{sp}/2$ with an energy width Γ_{sp}, the S-matrix element is found to be [MT99]

$$\mathbf{S}(k) = e^{2i\delta_{bg}} \frac{(k + k_r)(k - k_r^*)}{(k - k_r)(k + k_r^*)} \tag{2.38}$$

in which the δ_{bg} varies smoothly and slowly near the resonance energy, the real k and k_r ($\approx k_0 - i\mu\Gamma_{sp}/(2k_0\hbar^2)$) are the wave numbers of the energy E and the resonance energy E_r, respectively. At the limit of $k \to k_r$, the S-matrix element can be rewritten as a leading term $A_{lj}/(k - k_r)$ plus some regular function. The coefficient A_{lj} gives the residue of the S-matrix in the resonance pole, being

$$A_{lj} \approx -ie^{2i\delta_{bg}} \frac{\mu}{k_0\hbar^2} \Gamma_{sp} \tag{2.39}$$

up to the order of $\Gamma_{sp}/2E_0$. This would indicate that the resonance width could be revealed in a relevant reaction. Indeed, it has already been pointed out in Ref. [MT99] that transfers to resonant states can be used to extract the widths of the resonances. In a sense, the role of the resonance width in transfers to resonant states would be comparable to that of ANC in transfers to bound states since both can be linked to the residue of the corresponding S-matrix. This point has direct implications in our work for the analysis regarding resonances.

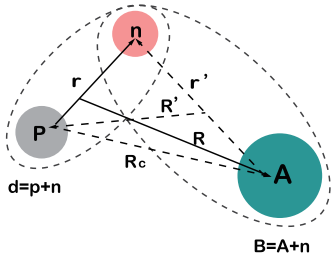

Figure 2.2: Illustration of the three-body system for the $A(d,p)$ transfer reaction with associated coordinates.

2.4 Modeling (d, p) transfer reaction

2.4.1 Theoretical formalism

In this section, the theoretical notions presented above will be applied to model explicitly the (d,p) transfer which is widely used as a powerful tool to probe the single-neutron property of nuclei. In a simple physical picture, a stripping reaction with the form $A(d,p)B$ can be viewed as a process in which the neutron n from the incident deuteron d populates an unoccupied state in the target nucleus A, producing a composite nucleus $B = n + A$. An illustration for this one-neutron transfer process is shown in Fig. 2.2 with the associated coordinates. In this study, the nucleon is considered as the basic constituent of nuclei and hence its internal structure is ignored in the following derivation. The complete Hamiltonian for the three bodies [TN09] can be written as

$$H = T_{\mathbf{r}} + T_{\mathbf{R}} + V_{pn}(\mathbf{r}) + V_{An}(\mathbf{r'}) + U_{pA}(\mathbf{R_c}), \tag{2.40}$$

in which the sum of the first two kinetic energy terms equal to $T_{\mathbf{r}'} + T_{\mathbf{R}'}$, $U_{pA}(\mathbf{R_c})$ is called the core-core optical potential, and V_{pn} and V_{An} represent the two-body interaction inside the deuteron d and the produced nucleus B, respectively. The coupling of the transfer reaction arises from the remaining interaction in the mean field. To expand the Hamiltonian when including the remaining potential, there are two ways: post or prior form, corresponding to the choice of the channel: final or initial. And the results obtained with these two forms should not differ from each other, particularly being identical in the case of first-order DWBA [TN09]. Using either post or prior form, the

Hamiltonian can be expressed as [TN09]

$$\begin{aligned} H = H_{\text{post}} &= T_{\mathbf{r}'} + T_{\mathbf{R}'} + V_{An}(\mathbf{r}') + U_{pB}(R') + \mathcal{V}_f(\mathbf{R}', \mathbf{r}') \\ &= H_{\text{prior}} = T_{\mathbf{r}} + T_{\mathbf{R}} + V_{pn}(\mathbf{r}) + U_{dA}(R) + \mathcal{V}_i(\mathbf{R}, \mathbf{r}) \end{aligned} \tag{2.41}$$

with the $U_{pB}(R')$ and $U_{dA}(R)$ being the exit and entrance diagonal potentials respectively. The interaction terms $\mathcal{V}_f(\mathbf{R}', \mathbf{r}')$ and $\mathcal{V}_i(\mathbf{R}, \mathbf{r})$ are

$$\begin{aligned} \mathcal{V}_f(\mathbf{R}', \mathbf{r}') &= V_{pn}(\mathbf{r}) + U_{pA}(\mathbf{R_c}) - U_{pB}(R') \\ \mathcal{V}_i(\mathbf{R}, \mathbf{r}) &= V_{An}(\mathbf{r}') + U_{pA}(\mathbf{R_c}) - U_{dA}(R) \end{aligned} \tag{2.42}$$

to cause the transition. The first part in $\mathcal{V}_{f,i}$ is the binding potential for the corresponding nucleus while the combination of the other two is called the remnant term.

Let us first focus on the post form. Besides the interacting potential, to build the T-matrix shown in Eq. (2.26), effective descriptions for the final and initial channels are also required. The final channel of $p + B$ after the transfer can be expressed by $\psi_{pB} = \chi_{pB}\Phi_B$ in which χ_{pB} describes the relative motion between the proton and the product B while Φ_B represents the quantum mechanical state of the nucleus B. Regarding the state Φ_B, it can be further decomposed by

$$\Phi_B = \phi_A I^B_{An} + \Phi^B_C, \tag{2.43}$$

into a single-particle component $\phi_A I^B_{An}$ and the rest part Φ^B_C with more complex configurations. In this notation, ϕ_A is taken as the internal wave function of the core A, and I^B_{An} as the overlap wave function between states of nuclei $B = A + n$ and A. Assuming that during the transfer the contribution from the term Φ^B_C becomes negligible and no internal state of the core A is altered (refer to the Halo EFT in Sec. 2.3.2), the description of the final state can be simplified to $\chi_{pB} I^B_{An}$ in a three-body model. Therefore, the overlap function is always the central element of the analysis of the transfer reaction, reflecting the single-particle strength of $A + n$ in the produced nucleus B. In the nuclear exterior, the radial overlap function $I^B_{An(lj)}(r')$ extracted from the partial wave expansion of the overlap function [MMT+14] is connected to the radial wave function from Eq. (2.30) by a constant $K_{An(lj)}$, yielding

$$I^B_{An(lj)}(r') \xrightarrow{r' \to \infty} K_{An(lj)} \frac{u_{lj(r')}}{r'}, \tag{2.44}$$

where $K^2_{An(lj)}$ $(= S_{An(lj)})$ is the single-particle spectroscopic factor of the configuration A-n with quantum numbers l, j in nucleus B. It is valuable to bear in mind that for a pure single-particle configuration this single-particle

spectroscopic factor (SF) will coincide with the spectroscopic factor obtained from the square of the norm of the radial overlap function. However, this condition does not always hold due to the fact that the overlap function is actually a many-body object. Especially in the nuclear interior where the overlap function has most of its probability and hence contributes significantly to the SF, the single-particle model is no longer a valid approximation. Nonetheless, at large distances the radial dependence of the radial overlap function remains similar to that of the radial wave function [OMNP12]. Introducing the ANC C_{lj} to quantitatively define its asymptotic behavior, the radial overlap function has the format of

$$I^B_{An(lj)}(r') \xrightarrow{r'\to\infty} C_{lj}\frac{W_{-\eta,l+\frac{1}{2}}(2\kappa r')}{r'}. \tag{2.45}$$

Combining Eq. (2.45) and (2.44) and compared with Eq. (2.31), the ANC and SPANC are related by

$$C^2_{lj} = S_{An(lj)}b^2_{lj}. \tag{2.46}$$

Here the ANC is well accepted as an experimentally measurable quantity while the SPANC and single-particle spectroscopic factor are model dependent. Moreover, the ANC is a key part of the halo structure, which gives the strength in the halo. Roughly speaking, if the ANC is small, there cannot be a true halo even if the valence particle is loosely bound. If the ANC is large, the halo will be clear. One important point in this work is to extract the ANC value precisely, which relies heavily on the aforementioned framework.

Similar derivation as above can also be done for the initial channel $d + A$ which reveals the interaction associated with the three-body problem of the proton p, the neutron n and the core A. A series of methods like DWBA [BH61] and ADWA [JS70, JT74] is generated based on the approximation to this three-body wave function and will be discussed in the coming sections. At this step, the corresponding description is denoted as ψ_{dA}.

With all these ingredients, the three-body transition matrix element of the (d,p) stripping reaction can be built in the post form as [GCM14]

$$T_{\rm post}(pB, dA) = \langle \chi^{(-)}_{pB} I^B_{An} | V_{pn} + U_{pA} - U_{pB} | \psi^{(+)}_{dA} \rangle. \tag{2.47}$$

Repeating the above analysis in the prior form, an equivalent expression for the transition matrix element is

$$T_{\rm prior}(pB, dA) = \langle \psi^{(-)}_{pB} | V_{An} + U_{pA} - U_{dA} | \chi^{(+)}_{dA} \varphi_{pn} \rangle \tag{2.48}$$

in which φ_{pn} is the bound wave function of deuteron, $\psi^{(-)}_{pB}$ represents the exact three-body (p, n, A) solution subject to the boundary conditions consisting

of a plane wave (on the p-B coordinate $\mathbf{R}'$) with the final momentum in the detector direction, times the wave function of the system B, plus ingoing waves in all other open channels [GCM14].

Note here that in order to retain consistency through this study the calculations are always performed in the post form unless otherwise specified. Once the transfer amplitude $T_{\rm post}(pB, dA)$ is obtained, the differential cross section can be calculated since it is proportional to the square of that transition matrix element. Now the primary concern is the solution $\psi^{(+)}_{dA}$ with respect to the three-body problem. The way to deal with it gives rise to the following models.

2.4.2 Distorted wave Born approximation (DWBA)

In the DWBA model, the exact solution $\psi^{(+)}_{dA}$ of the three-body system is replaced by its asymptotic condition which can be expressed as a distorted wave $\chi^{(+)}_{dA}(\mathbf{R})$ multiplied by the deuteron bound-state wave function $\varphi_{pn}(\mathbf{r})$. The transition matrix for the (d,p) transfer thus becomes[4]

$$T_{\rm post}(pB, dA) \simeq \langle \chi^{(-)}_{pB}(\mathbf{R}') I^B_{An} | \mathcal{V}_f | \chi^{(+)}_{dA}(\mathbf{R}) \varphi_{pn}(\mathbf{r}) \rangle. \tag{2.49}$$

This approximation is in fact the leading term with respect to the Born series of the transition amplitude (see Sec. 2.1.5). For the sake of probing the nuclear structure with the transfer, namely I^B_{An} in our case, the accuracy of the other terms in Eq. (2.49) should be well determined. As for the interaction term $\mathcal{V}_f$, the magnitudes of two complex potentials U_{pA} and U_{pB} are often similar, producing a cancellation of the remnant term. The remaining part V_{pn} and also the bound-state wave function φ_{pn} depend strongly on a good understanding of the deuteron for which the related interaction mechanism is believed to be well established nowadays. The distorted wave functions $\chi^{(-)}_{pB}$ and $\chi^{(+)}_{dA}$ are generated by the auxiliary potentials U_{pB} and U_{dA} with the corresponding boundary conditions. To make an appropriate choice of the potentials, the phenomenological approach discussed in Sec. 2.2 is used. U_{pB} and U_{dA} then become the optical potentials which are responsible for reproducing the elastic scattering on both channels. Such approach takes into account the effect of other complex reaction processes like fusion and breakup which can remove flux from the elastic channels. In practice, the elastic scattering for the incident channel $(d + A)$ and sometimes even the exit one $(p + B)$ needs to be performed

[4]Similarly, assume that in Eq. (2.48) the three-body solution $\psi^{(-)}_{pB}$ can be approximated by $\chi^{(-)}_{pB}(\mathbf{R}')I^B_{An}$, the transition matrix element becomes in the prior representation,

$$T_{\rm prior}(pB, dA) \simeq \langle \chi^{(-)}_{pB}(\mathbf{R}') I^B_{An} | \mathcal{V}_i | \chi^{(+)}_{dA}(\mathbf{R}) \varphi_{pn}(\mathbf{r}) \rangle$$

which should give identical results as the post form in Eq. (2.49).

and analyzed as a priority in the study of transfer reaction. Generally speaking, when the elastic scattering is dominant in both the incident and outgoing channels, the DWBA is used as a fast and key method to evaluate the (d,p) transfer data and extract the spectroscopic information on nuclear structure [GCM14].

Note that the elastic scattering amplitude is typically related to the asymptotic region of the distorted wave functions, which indicates that the internal part of those wave functions might not be exactly reproduced by these optical potentials. Moreover, even though the breakup effect of deuteron is implicitly considered in the optical potentials, its role during the transfer might still not be sufficiently taken into account. The improvement on this aspect will be introduced within the ADWA.

2.4.3 Adiabatic distorted wave approximation (ADWA)

As mentioned before, the DWBA approach might encounter some difficulties in explaining the (d,p) transfer with its inadequate treatment of the three-body effects, in particular the breakup of the deuteron. In order to include explicitly the contribution from the breakup, an interesting prescription called adiabatic distorted wave approximation (ADWA) was initially proposed by Johnson and Soper [JS70], which is supposed to contain most of the dominant effects in the three-body system while only involving a minor modification of the DWBA framework. This method is based on an adiabatic approximation. By the word 'adiabatic', it means that with a relatively high incident energy the proton-neutron coordinate is seen as fixed during the collision process [GCM14]. As a consequence, the deuteron-target potential $U_{dA}(\mathbf{R},\mathbf{r})$ that generates the wave function $\chi^{(+)}_{dA}(\mathbf{R},\mathbf{r})$ can be built from the sum of each fragment in deuteron interacting with the target as

$$U_{dA}(\mathbf{R},\mathbf{r}) = U_{pA}(R_c) + V_{An}(r'). \tag{2.50}$$

The relevant three-body wave function has a format of $\psi^{(+)}_{dA} \simeq \chi^{(+)}_{dA}(\mathbf{R},\mathbf{r})\varphi_{pn}(\mathbf{r})$. Via this step, the breakup channels are merged with the ground state of the deuteron. Fig. 2.3 schematically illustrates the scheme of coupling behind the ADWA method together with its comparison to the other methods (DWBA, and CDCC-BA which will be introduced in Sec. 2.4.4). Furthermore, assuming that the proton-neutron distance $\mathbf{r}$ is negligible compared to the deuteron-target one $\mathbf{R}$ thanks to the short-range feature of the binding potential $V_{pn}(r)$, one arrives at the zero-range (ZR) version of the ADWA method with the value of $\mathbf{r}$ set to 0. In this situation, the deuteron-target potential is given by

$$U^{ZR}_{dA}(R) = U_{pA}(R) + U_{An}(R), \tag{2.51}$$

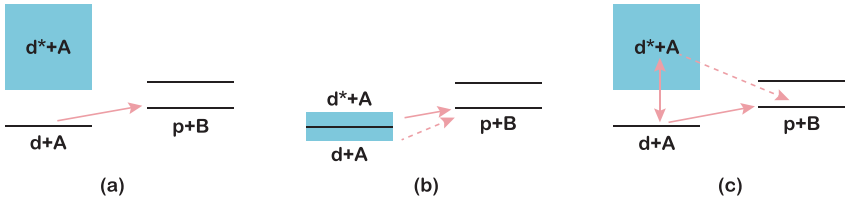

Figure 2.3: Depiction of the coupling schemes assumed in several reaction models to interpret the (*d*,*p*) transfer: (a) DWBA, (b) ADWA, (c) CDCC-BA. Figure adapted from [GCM14].

which relies only on the relative radial distance R between the deuteron and the target A. Under this zero-range limit, the transfer and the scattering are conceived to occur at the same place. Replacing the binding potential V_{An} with the complex optical potential U_{An} here is justified by the adiabatic approach [GCM14]. Later, a finite-range (FR) adiabatic potential as a refinement to the ZR-ADWA formalism has been derived by Johnson and Tandy [JT74]:

$$U_{dA}^{FR} = \frac{\langle \varphi_{pn} | V_{pn}(U_{pA} + U_{An}) | \varphi_{pn} \rangle}{\langle \varphi_{pn} | V_{pn} | \varphi_{pn} \rangle}. \tag{2.52}$$

This gives an averaged value of the potential by folding over the *p*-*n* wave function in the incoming channel. The distorted wave function $\chi_{dA}^{(+)}$ can be completely generated by the less ambiguous nucleon-target optical potentials which have a conventional form for parameterization and get evaluated normally at half of the deuteron incident energy. One factor that could be missing in the adiabatic model is the connection between different final channels. For an enhanced transfer case, the associated elastic scattering might be overestimated by the adiabatic potentials. However, with deuteron, this impact should be quite limited. And due to the outstanding advantages mentioned before, most transfer calculations in the present study will be carried out with either ZR- or FR-ADWA model in the post form using FRESCO (check Appendix A for more details). It is worth mentioning here that it is not legitimate to use the adiabatic deuteron potential in the prior form since such application is justified only when the transition potential contains the vertex function $V_{pn}\varphi_{pn}$, which is the case of the post form.

Dependencies

Moving further, it would be useful to assess the sensitivity of the transfer cross section to several variables so that their influence can be noticed or even controlled during this study. Within the ADWA model, the transfer calculations depend strongly at least on four factors which are the choice of the optical potentials, the incident energy, the Q-value of the reaction and the transferred angular momentum. The following discussion revolves around these points when more concrete results will be presented in the Chapter 3.

- Optical potentials

  Due to the difference in the experimental objects being fitted (energy range, target type) and the selected analysis method, several sets of global optical model potential compilations for the nucleon-target case are available in the literature [VTM$^+$91, KD03]. Directly linked to the generation of the distorted wave functions, the choice of these potential affects both the magnitude and the shape of the calculated cross sections. A recent study has been carried out by Lovell and Nunes [LN18] using the Bayes' theorem to investigate the uncertainties in the transfer predictions originating from the optical potentials as well as from the reaction models.

- Angular momentum transferred

  The influence of transferred angular momentum is deduced from the combination of two distorted wave functions $\chi_{pB}^{(-)}$ and $\chi_{dA}^{(+)}$ in the transition matrix. Considering a (d,p) transfer to a certain bound state of B in which usually low angular momentum transfer is favored, the related matrix element is selectively evaluated with the l value equaling the total angular momentum transferred [Bou13]. Thus, the angular distribution of the transfer probability will experience a shape which is determined by that l value. This feature has been illustrated using momentum matching in Sec. 1.2 in a semi-classical picture.

- Q-value matching

  The reaction Q-value has a strong impact on the magnitude of the differential cross sections. The Q-value matching results in an enhancement of the transfer probability towards a certain nuclear state. It is characterized sometimes as the optimum Q-value when the transfer reaction has the largest cross section. In first approximation for $l = 0$ (i.e., head-on) collisions, the optimum Q-value Q_{opt} is expressed as [HEK$^+$78]

  $$Q_{\text{opt}} \approx E_i\left(\frac{Z_B z_b}{Z_A z_a} - 1\right) \tag{2.53}$$

  with the beam energy E_i while Z and z denote the charges of target and projectile in the initial or final state. In our case of a (d,p) transfer, the Q-

value can be calculated by the difference between the one-neutron separation energy in the deuteron and that in the produced nucleus B as $Q = S_{1n}^{B} - S_{1n}^{d}$. For this kind of transfer of a neutral particle, the maximum cross section will be reached at $Q \approx 0$ MeV according to Eq. (2.53). With the aim of studying purely the influence of binding energy in the calculation, it is necessary to exclude the strong interference caused by the factor of Q-value. Due to its intrinsic connection with the binding energy, it is not always feasible to perform such analysis, but possible with FRESCO. More details will come in Sec. 3.3.

- Beam energy

  Different beam energies lead to diverse combinations of several reaction channels. Thus, as the incident energy changes, we should be aware that the energy-dependent optical potentials which are related to the reaction mechanism also needs to be adjusted. Correspondingly, the magnitude and the shape of the angular distribution of the cross section will also evolve. When the beam energy is decreasing towards the Coulomb barrier, no close approach between the projectile and the target simplifies the theoretical interpretation of the undergoing reaction. Within this condition, an argument that can be drawn is that the observed transfer reaction would most likely be a direct and peripheral one.

2.4.4 Other options

Despite being widely used, the previous transfer models (DWBA and ADWA) are still often questioned and challenged due to the simple approximation made there. A more convincing approach is offered by the continuum-discretized coupled-channel Born approximation (CDCC-BA also called CDCC for simplicity) [GCM14]. The framework of the CDCC method was first introduced by Rawitscher [Raw74] to describe reactions involving the deuteron by taking into account the deuteron breakup effect to all orders. The three-body wave function $\psi_{dA}^{(+)}$ is expanded over the eigenstates of the deuteron Hamiltonian. Since calculating the continuum would imply an integral over the p-n relative linear momentum and hence is not tractable, the idea of Rawitscher was to discretize the continuum into several bin states. The related expression for the three-body wave function is obtained by

$$\psi_{dA}^{(+)} \approx \chi_{dA,0}^{(+)} \varphi_{pn,0} + \sum_{i=1(bin)} \chi_{dA,i}^{(+)} \varphi_{pn,i}, \tag{2.54}$$

where 0 indicates the solution corresponding to the deuteron bound state. The index i includes the p-n angular momentum l and its projection m, representing

Table 2.1: Characteristics of the ADWA method compared to the other methods: DWBA, CDCC and Faddeev-AGS.

Compared to	Property of ADWA
DWBA	• Includes the deuteron breakup • Constructed solely on nucleon-target optical potentials
CDCC	• A simplified CDCC method [ND11] • Good agreement around 10 MeV/A, not for higher beam energies[a] • Less suitable when angular momentum transfer is not zero
Faddeev-AGS	• Compares very well at around 10 MeV/A [UDN12] • Suits the transfer to the loosely-bound nucleus • Agreement deteriorates with increasing beam energy • Not ideal for large angular momentum transfer • Energy dependent with respect to the global OMP

[a] Performed neglecting the spin of the nucleons.

a set of discretized bin states for the deuteron continuum. This model of wave function gives rise to a set of coupled differential equations to solve. With the results being inserted into the transition matrix, the transfer process can no longer be viewed as a direct one like in the DWBA, whereas proceeding via multiple steps from the continuum state of the deuteron as shown in Fig. 2.3. Because of this, this model is more robust than DWBA and ADWA.

As a generalization of the CDCC method, not only the bound states and continuum of the incident channel, but also those of the rearrangement channel can be incorporated within the framework of the coupled reaction channels (CRC). The three-body wave function $\psi^{(+)}$ becomes a superposition of the wave functions which shares a similar format to Eq. (2.54) but corresponds to all the possible mass partitions during the reaction (such as including the bound and unbound states of the pB partition in the transfer). Solving the CRC equations has to deal with the non-local potentials and non-orthogonality terms [GCM14]. This method is especially useful to describe the reaction in which the elastic scattering is not the dominant channel.

The most accurate solution of this three-body problem was formulated by Faddeev [Fad61], which gives a rigorous treatment of the equation expressed as a sum of three components. Each of the components containing a two-body interaction for a given pair of particles are derived in terms of its definite set of Jacobi coordinates. Note the interaction should be the same in all three sets of coordinate systems. The methods discussed in the preceding part can be viewed as an approximate version of the Faddeev formalism [GCM14]. This Faddeev-type method, later formulated as the Alt-Grassberger-Sandhas (AGS,

also known as FAGS) equations [AGS67] to include the Coulomb interaction in few-nucleon reactions, has recently been applied to study (d,p) transfer [Del09]. It also provides a very useful assessment for those approximate methods [ND11, UDN12]. In Ref. [ND11], the adiabatic approximation is compared to the exact Faddeev method for (d,p) reaction, drawing a conclusion that the approximation made in ADWA is more suitable when a small angular momentum is transferred and a loosely-bound nucleus gets produced. A more complete and systematic comparison among ADWA, CDCC and FAGS is performed in Ref. [UDN12].

Compared to the DWBA and ADWA method, the cost of less approximation made in these more complex models (CDCC, CRC and FAGS) is the rapid growth of the computational demands. For a quick estimation without missing the key feature in the transfer, simple reaction models are still sometimes preferred to reveal the nuclear structural information. In this study, we are interested in the transfers that are peripheral, and for which ADWA seems to be an effective approach according to Refs. [ND11, UDN12]. To show more confidence on the choice of the simple method ADWA, its validity is specified in Table 2.1 by the comparison to the other methods. In addition, it would also be interesting in future work to confirm the present results of our study with a more detailed description of the reactions.

Chapter 3

Halo Study with Transfer Calculations

This chapter consists of three sections to introduce the theoretical results with the aim to better understand what kind of information can be extracted from the analysis of transfer data to study halo systems.

The first part reports briefly the framework of the study published in our paper [YC18] attached in Appendix B with some extension. In Sec. 3.1.1, the analysis of the peripherality of the ^{10}Be(d,p) stripping reaction carried out by Schmitt *et al.* [SJB$^+$12, SJA$^+$13] is systematically reviewed at the deuteron energies (E_d) of 21.4, 18, 15, and 12 MeV. This enables us to extract the asymptotic normalization coefficient (ANC) for both bound states in the nucleus ^{11}Be. The discussion afterwards highlights the importance of this analysis method. As a cross check here, the supersymmetry (SuSy) method is used to take another insight into the same topic (see Sec. 3.1.2). Then, the sensitivity of those calculations to the optical potential choice is investigated by comparing the results obtained with two optical potentials (CH89 [VTM$^+$91] and Koning and Delaroche (KD) [KD03]). Furthermore, our developed method is also extended to study the influence of the resonance width for transfers to the first $5/2^+$ resonance of ^{11}Be nucleus.

In Sec. 3.2, the ANC for ^{15}C, which is of astrophysical interest [TBD$^+$06], is extracted using our method from the transfer data of ^{14}C(d,p) at $E_d = 17.06$ MeV provided in Ref. [MBG$^+$11]. It is used as an optimal value to which the additional parameter appearing in the Halo-EFT description of ^{15}C at next-to-leading order (NLO) can be tuned. The related paper [MYC19] is attached in Appendix C.

Eventually, inspired by Prof. Alexandre Obertelli who is an experimentalist within the nuclear-physics group at the TU Darmstadt, the original intention of the third section is to use transfer below the Coulomb barrier to detect possible halos in nuclear excited states. Tentative efforts have been made in this work on the theoretical side to search for a candidate to study the presence of a neutron halo in an excited nuclear state using sub-Coulomb (d,p) transfer in inverse kinematics. With the testing case of ^{95}Sr, the dependencies of the transfer calculations are explored on several aspects, for instance, Q-value, beam energy, one-neutron binding energy and so on.

3.1 ^{10}Be(d,p)^{11}Be transfer reaction

As said before in Sec. 1.1, ^{11}Be is well known for its distinct n+^{10}Be halo structure. The next (n+n+^{9}Be) breakup threshold appears at 7.31 MeV [CNR$^+$16], also making sure that the rich resonance structure at low energies is dominated by the n+^{10}Be single-particle structure. Already many different experimental methods (e.g., β decay [MBA$^+$09], elastic scattering [DPRS$^+$10, DPSM$^+$12], breakup [FNA$^+$04], neutron knockout [ANB$^+$00] and transfer reactions [SJB$^+$12, BPTO$^+$14]) have been carried out with the aim to understand the halo nature of ^{11}Be. Meanwhile, there have also been considerable efforts put forward on the theoretical side to describe the structure and help explain the reactions involving ^{11}Be. Recently, *ab initio* calculations [CNR$^+$16] got improved by including explicitly the description of ^{11}Be as ^{10}Be $+n$ and its continuum effects in the model space.

The main purpose of the work in this section is to test the sensitivity of transfer reaction to the projectile structure using the best simple model of reaction, and look for the best experimental conditions to extract the halo-structure observables, such as ANC. Part of the results has been published in the paper [YC18] attached in Appendix B. As a review and sometimes a supplement to that work, the first part of this section is mainly used to highlight the basic idea and framework of the method. For a short and concise overview, I refer the reader in a hurry to that article.

Experimental details

The experimental data are taken from the paper by Schmitt *et al.* [SJB$^+$12, SJA$^+$13]. The measurement of the ^{10}Be(d,p)^{11}Be transfer reaction was performed in inverse kinematics at the Holifield Radioactive Ion Beam Facility of the Oak Ridge National Laboratory [BBU$^+$11]. The experiment is realized with a ^{10}Be beam at four different lab energies of 107, 90, 75 and 60 MeV impinging on a deuterated polyethylene (CD_2). Thanks to the long half-life

of ^{10}Be ($T_{1/2}$ = (1.387 ± 0.012) Ma [KBF$^+$10]), the source was prepared from a solution of ^{10}Be in hydrochloric acid. The quality of the beam during the runs is significantly improved by the acceleration techniques used to reduce the contamination (< 1%). A relatively high incident intensity of the beam was achieved, being approximately 5×10^6 particles per second. The reaction products are detected by the silicon detector array (SIDAR) [BBB$^+$99] mounted in a lampshade configuration covering the backward laboratory angles ($138° \leqslant \theta \leqslant 165°$) together with the full implementation of the Oak Ridge Rutgers barrel array (ORRUBA) [PCH$^+$07] placed at the forward angular range from 45° to 135°. Due to the fact that the peak of the angular distribution of the protons from the (d,p) reactions is typically located at forward center-of-mass (c.m.) angles when small angular momentum is transferred, most of the data for the transfer channel is collected in the SIDAR array with an energy resolution of ≈ 70 keV.

Numerical inputs

For the ^{10}Be$(d,p)^{11}$Be transfer reaction, the equivalent deuteron incident energy E_d is taken to be 21.4, 18, 15, and 12 MeV [SJA$^+$13]. In our calculations, the finite-range version of the adiabatic potential developed by Johnson and Tandy [JT74] is used to compute the reaction. The nucleon-nucleus optical potentials are obtained from the global parametrization CH89 [VTM$^+$91] without including the spin-orbit terms. Using the FR-ADWA approach, $U_{p-^{10}\mathrm{Be}}$ and $U_{n-^{10}\mathrm{Be}}$ are calculated at half the incident energy $E_d/2$, while the auxiliary potential $U_{p-^{11}\mathrm{Be}}$ is obtained at the proton energy corresponding to the exit channel. For the p-n interaction, the Reid soft-core interaction [Rei68] is chosen to get the appropriate wave function of the deuteron (see Sec. 2.3.1). The transfer calculations are performed with FRESCO [Tho06], and the adiabatic potentials are calculated using the front-end code of TWOFNR [TTIK12].

3.1.1 ANC extraction

Description of ^{11}Be bound states

^{11}Be, as the archetype of a single-neutron halo nucleus, can be modeled as a neutron loosely bound to a ^{10}Be core. Its energy level diagram is shown in Fig. 3.1. With the assumption that the ^{10}Be core is in its ground state (0^+), the $1/2^+$ ground state (g.s.) of ^{11}Be can be described by a $^{10}\mathrm{Be}(0^+)\otimes 1s_{1/2}$ configuration, and the $1/2^-$ excited state (ex.s.) by a $^{10}\mathrm{Be}(0^+)\otimes 0p_{1/2}$ configuration. No core excitation is considered since its effect in this case is generally small. Indeed, there are several sources of core excitation in this reaction. One is arising from the U_{pA} interaction appearing in the transition potential as expressed in Eq. (2.42), whose influence has been investigated to be

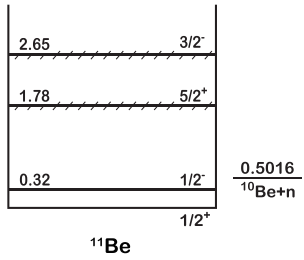

Figure 3.1: Low-energy level diagram for ^{11}Be [NuD19].

Table 3.1: Gaussian parameters of the ^{10}Be-n potentials. The potential depths, SPANCs and root-mean-square radii of the $1s_{1/2}$ ground state and the $0p_{1/2}$ first excited state are shown as well.

Potential	r_0 (fm)	$V_0(g.s.)$ (MeV)	$b_{1s1/2}$ ($\mathrm{fm}^{-1/2}$)	$\langle r^2\rangle^{1/2}$ (fm)	$V_0(ex.s.)$ (MeV)	$b_{0p1/2}$ ($\mathrm{fm}^{-1/2}$)	$\langle r^2\rangle^{1/2}$ (fm)
V_1	0.4	1314.6	0.601	5.29	869.4	0.068	2.82
V_2	0.6	592.3	0.632	5.55	387.3	0.085	3.48
V_3	0.8	337.8	0.664	5.81	218.4	0.100	4.05
V_4	1.0	219.2	0.697	6.08	140.2	0.114	4.55
V_5	1.2	154.4	0.732	6.34	97.7	0.127	5.02
V_6	1.4	115.1	0.769	6.61	72.1	0.140	5.45
V_7	1.6	89.3	0.807	6.88	55.4	0.152	5.86
V_8	1.8	71.6	0.846	7.15	44.0	0.165	6.25
V_9	2.0	58.8	0.888	7.41	35.8	0.177	6.62

negligible ($< 3\%$) according to the study by Gómez-Ramos *et al.* [GRMGCT15]. Another source can occur in the entrance channel (d+^{10}Be), which could be taken into account using a CDCC-BA approach. The corresponding effects have been examined in a couple of works such as Refs. [DRNcvN16] and [GRM17] with its magnitude found to depend mostly on the incident energy. In particular, they are of the order of 10% or less at the energies explored in this work ($E_d < \sim$20 MeV). Following the spirit of Halo EFT, the Gaussian potentials in Eq. (2.32) are adopted to describe the interaction between ^{10}Be and the valence neutron. Nine sets of Gaussian potentials are generated with different widths r_0 starting from 0.4 fm to 2.0 fm. These values are chosen in order to generate a significant change in both the SPANC and the internal part of the wave function.

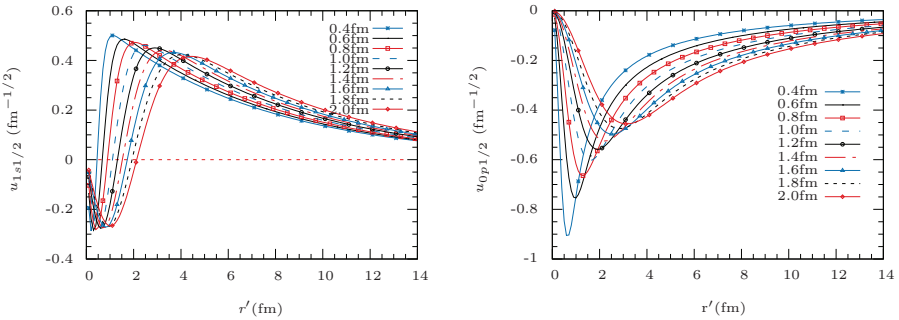

Figure 3.2: Reduced radial wave functions obtained with the nine different Gaussian potentials listed in Table 3.1 for the $1/2^+$ g.s. of ^{11}Be (left) and for the $1/2^-$ ex.s. (right).

Furthermore, we keep the widths to be realistic in a nuclear-physics context: neither ridiculously small (a FWHM of about 1 fm regarding $r_0 = 0.4$ fm) nor too large ($r_0 = 2.0$ fm leads to a FWHM of about the size of the core). The depth V_0 is adjusted to reproduce the neutron binding energy (0.502 MeV for the g.s.; 0.182 MeV for the ex.s.). The relevant parameters are all listed in Table 3.1 alongside the corresponding SPANCs ($b_{1s1/2}$, $b_{0p1/2}$).

Using such potentials, the wave function of the ^{10}Be-n bound states can be calculated. The resulting g.s. and the ex.s. reduced radial wave functions are shown in Fig. 3.2 where the smaller r_0 always leads to the wave function that reaches earlier its asymptotic. To maintain the consistency of the representation, the coordinates of the three-body system in Fig. 2.2 are considered by simply replacing the core A with the nucleus ^{10}Be. Therefore, the symbol of the x-axis in Fig. 3.2 becomes r'. According to the definition in Eq. (2.31), all the wave functions shown here will exhibit a same tail after being scaled by their SPANCs. Via this step, the set of the wave functions can be seen as two parts: one sharing the same asymptotic behavior at large distance and the other being completely different in the internal part. The tail of the wave function is closely linked to the peripherality of the transfer process, i.e., when the reaction is completely peripheral, the transfer differential cross sections should be sensitive only to the value of the ANC without retaining information on the internal region of the wave function. Thus, studying the dependency of the transfer calculations on these different descriptions of ^{11}Be will help safely extract its ANC in a well-defined experimental conditions where peripheral transfer dominates.

In addition to the Gaussian type, in principle this study can be performed with whichever potential one wants. An example with more usual Woods-Saxon

potentials will be shown in Sec. 3.1.3. The use of Gaussian potentials is due to the simplicity (one single variable r_0) and its relation to Halo EFT (see Sec. 2.3.2).

Transfer calculations and analysis

With all those necessary ingredients combined, a series of transfer calculations is carried out for the ^{10}Be(d,p)^{11}Be reaction at E_d = 21.4, 18, 15, and 12 MeV [SJB$^+$12]. Let's start with the plot on the top left corner of Fig. 3.3 to clarify the analysis and the findings. There the first plot (a_1) shows the original angular distribution of the cross sections calculated at 21.4 MeV. With narrower Gaussian potentials (smaller r_0 value), the cross section of the reaction gradually decreases. At forward angles, there exist big variations among the calculated cross sections with different potentials. Dividing the cross sections by the square of the SPANCs generates the plot (b_1). From (a_1) to (b_1), the discrepancies are very much suppressed. Most curves begin to get on top of each other in the forward region except those of r_0 = 0.4 fm, and 0.6 fm. In order to gain quantitative insight into the variation between different distributions after scaling, they are compared to the result at r_0 = 1.4 fm which is at the center of the interval:

$$\mathcal{R}_{r_0/1.4\text{fm}} = \frac{(\frac{d\sigma}{d\Omega})^{\text{th}}_{r_0}/(b_{n_rlj})^2_{r_0}}{(\frac{d\sigma}{d\Omega})^{\text{th}}_{1.4\text{fm}}/(b_{n_rlj})^2_{1.4\text{fm}}} - 1 \tag{3.1}$$

in which the superscript th is short for theoretical results. The index r_0 corresponds to the set of Gaussian potential used for the calculation. The relevant results are presented in the plot (c_1). This plot confirms what has been shown in plots (a_1) and (b_1): at forward angles most of the dependence of the cross section on the description of ^{11}Be is in its SPANC, hence this could be a peripheral region. Then an arbitrary value $\pm$5% (horizontal red dashed lines in Fig. 3.3 (c_1)) is set as the tolerance band to define the peripheral area of the transfer. One sees from this plot that only a small angular region meets this peripheral definition except the cases corresponding to 0.4 fm and 0.6 fm which do not fall in the band at all. For the ^{10}Be$(d,p)^{11}$Be(g.s.) reaction at 21.4 MeV, an angular range of $\theta_{c.m.}$ = 0°-7° is extracted as the peripheral region where the scaling of $b^2_{n_rlj}$ works.

A similar analysis is made for the other three energies to check the evolutionary trend of such angular distribution with the deuteron energy. The plot at each energy is organized following the same logical structure as that at 21.4 MeV. Compared to the previous case, discrepancies among the different curves at 18 MeV start to shrink after scaling by b^2_{nlj}. The peripheral part increases to 10° without taking into account the results of r_0 = 0.4 fm, and 0.6 fm. The region of peripherality is enlarged and improved at 15 MeV since more curves fall within the tolerance band now with a range of $\theta_{c.m.}$ = 0°-20° excluding

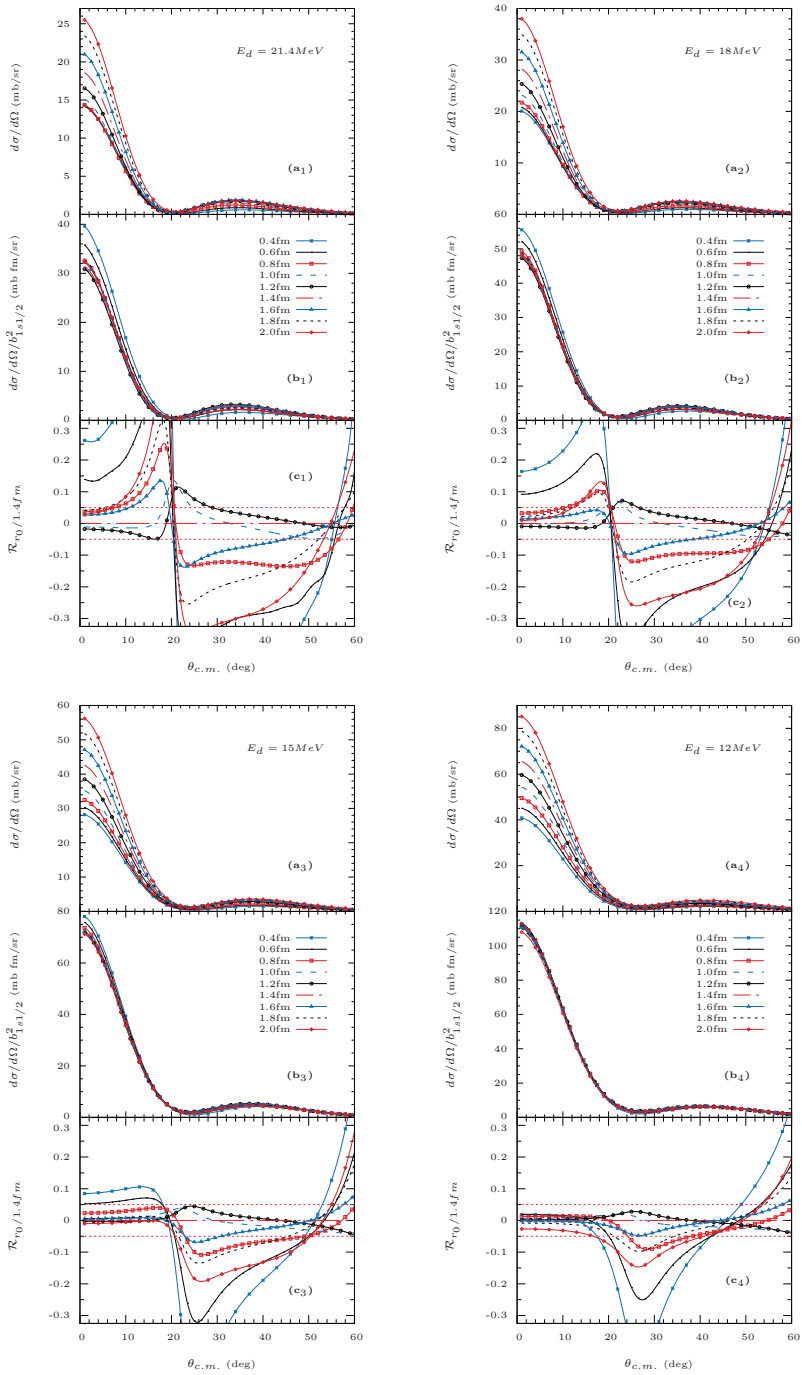

Figure 3.3: Analysis of the differential cross sections of ^{10}Be$(d,p)^{11}$Be to the g.s. of ^{11}Be with incoming deuteron energy of 21.4 MeV (top left), 18 MeV (top right), 15 MeV (bottom left) and 12 MeV (bottom right).

again the calculations performed with $r_0 = 0.4$ fm, and 0.6 fm. Finally, it turns out that the scaling by the square of the SPANC works best at 12 MeV, leading to the most consistent peripheral region. The related angular range there is $\theta_{c.m.} = 0°$-$17°$, which encompasses all the values of r_0 this time.

In summary, two basic conclusions can be drawn at this stage: a) the peripheral region of this transfer reaction is always found at forward angles; b) when the incident energy decreases, the reaction is more peripheral. In addition, as the incident energy decreases, it seems that the average transfer cross section keeps rising. However, this is not always the case. Especially when the incident energy gets close to the Coulomb barrier, the transfer cross section becomes much smaller (see the discussion in Sec. 3.3.3).

Applying the same method to analyze the first excited state of ^{11}Be, I obtain Fig. 3.4. Checking the evolution of the cross sections basically leads to a similar picture, i.e., after scaling by b^2_{nlj}, the differences among the curves at forward angles are well reduced from 21.4 MeV to 12 MeV. But compared to those with the ground state, the results of the excited state always vary in a bigger scope possibly due to its p-wave nature and the relatively larger span of the SPANCs assigned for this state (see Table 3.1). We have to exclude some values of r_0, otherwise no peripheral region can be defined. If only the curves within the $\pm 5\%$ limit are considered, the peripheral region for transfers to the excited state of ^{11}Be is $\theta_{c.m.} = 0°$-$27°$ at $E_d = 21.4$ MeV, $0°$-$30°$ at 18 MeV, $0°$-$34°$ at 15 MeV, and $0°$-$40°$ at 12 MeV.

Results and discussion

Taking use of these obtained peripheral information, the value of the ANC for each bound state can be extracted by performing the χ^2 analysis:

$$\chi^2 = \sum_{i'} \frac{[C^2_{lj} \cdot (\frac{d\sigma}{d\Omega})^{\rm th}_{i'}/b^2_{nlj} - (\frac{d\sigma}{d\Omega})^{\rm exp}_{i'}]^2}{\delta^2_{i'}}, \tag{3.2}$$

where C_{lj} is the ANC obtained for each r_0 by minimizing the χ^2 in the angular range where the reaction is peripheral. Here i' represents all the experimental data points measured in Ref. [SJB$^+$12] within the peripheral region. And the square of experimental error δ'_i determines the weight. The resulting ANCs are shown in Fig. 3.5 as a function of r_0. It can be seen that the extraction of the ANC is more reliable at lower energy for both cases. For 21.4 MeV, the ANC obtained varies with r_0 since at this energy the reaction is less peripheral and the transfer calculation is sensitive to the interior part of the bound-state wave function. There is a problem with the results at 18 MeV which are always smaller than the others. It has been seen in the analysis of Schmitt *et al.* [SJA$^+$13] as well. The reason for that remains unclear. Nevertheless, the most reliable sets of data at 15 MeV, and 12 MeV lead to consistent results, clearly

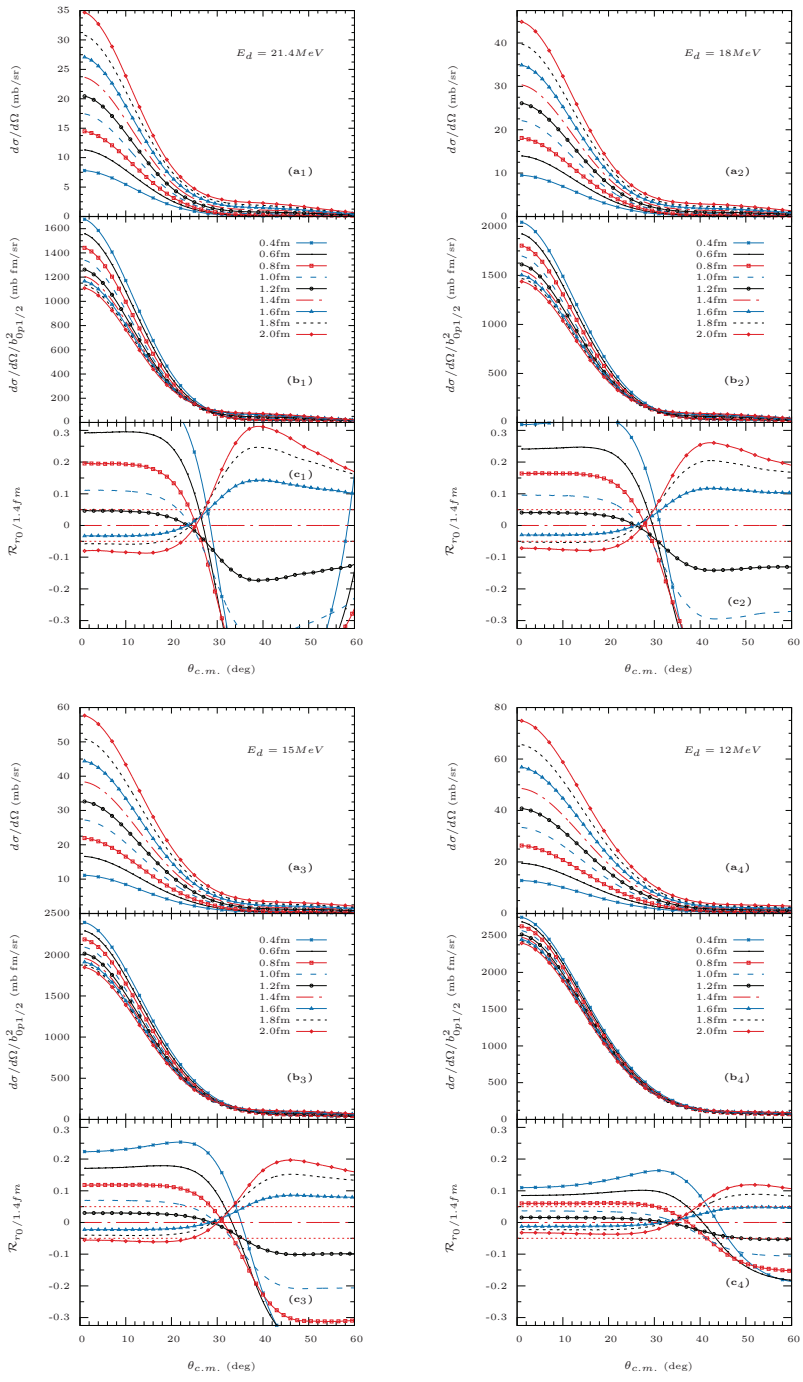

Figure 3.4: Analysis of the differential cross sections of ^{10}Be$(d,p)^{11}$Be to the ex.s. of ^{11}Be with incoming deuteron energy of 21.4 MeV (top left), 18 MeV (top right), 15 MeV (bottom left) and 12 MeV (bottom right).

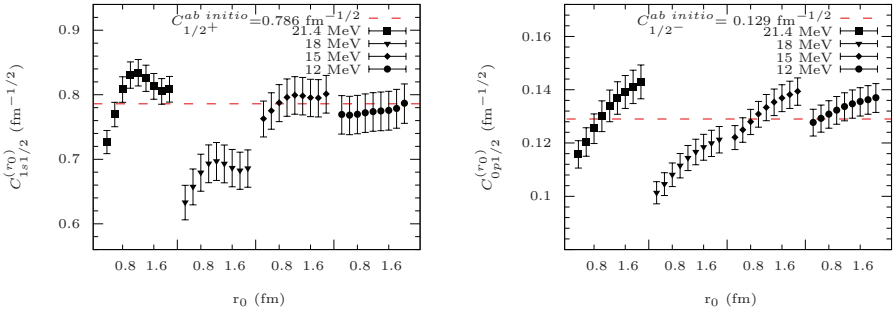

Figure 3.5: ANC extracted for the g.s. (left side) and ex.s. (right side) of ^{11}Be. The *ab initio* result (C_{lj} = 0.786 fm$^{-1/2}$ for g.s. or 0.129 fm$^{-1/2}$ for ex.s.) for comparison is presented by a red dashed line. From left to right in each grid of the horizontal axis, the data points start with the ANC extracted for r_0 = 0.4 fm and end with that for r_0 = 2.0 fm.

reaching a plateau. The only points that are not within the plateau at 15 MeV are the ones falling out of the 5% in the definition of the peripheral region. Based on this analysis, the final value of the ANC is (0.785 ± 0.030) fm$^{-1/2}$ for the g.s. and (0.135 ± 0.005) fm$^{-1/2}$ for the ex.s. In general, the present results are in agreement with the ANCs predicted by the *ab initio* calculation (0.786 fm$^{-1/2}$ for g.s. and 0.129 fm$^{-1/2}$ for ex.s.) [CNR+16]. The associated uncertainty σ is calculated using the formula

$$\sigma = \sqrt{\frac{1}{N}\sum_{i=1}^{N}\sigma_i^2 + \sigma_0^2}, \tag{3.3}$$

which includes the variation represented as σ_0 between the centroids of the estimates obtained with different potential widths and also the uncertainty σ_i of the ANC value extracted by minimization of χ^2 in Eq. (3.2) for each Gaussian potential V_i. N is the total number of the ANC values being considered. Our results are also very close to those found by Belyaeva *et al.* ((0.723 ± 0.016) fm$^{-1/2}$ for the g.s. and (0.133 ± 0.004) fm$^{-1/2}$ for the ex.s. at E_d = 12 MeV) [BPTD+14] using the CRC model. The slight disagreement is mostly due to the fact that in their analysis, they considered the data collected at all angles which are not always within the peripheral region.

In Fig. 3.6, I compare the adjusted theoretical results with the experimental ones. The angular distributions of the cross sections are obtained through multiplying the original results by $C_{lj}^2/(b_{nlj})_{r_0}^2$ (specifically C_{lj} = 0.785 fm$^{-1/2}$

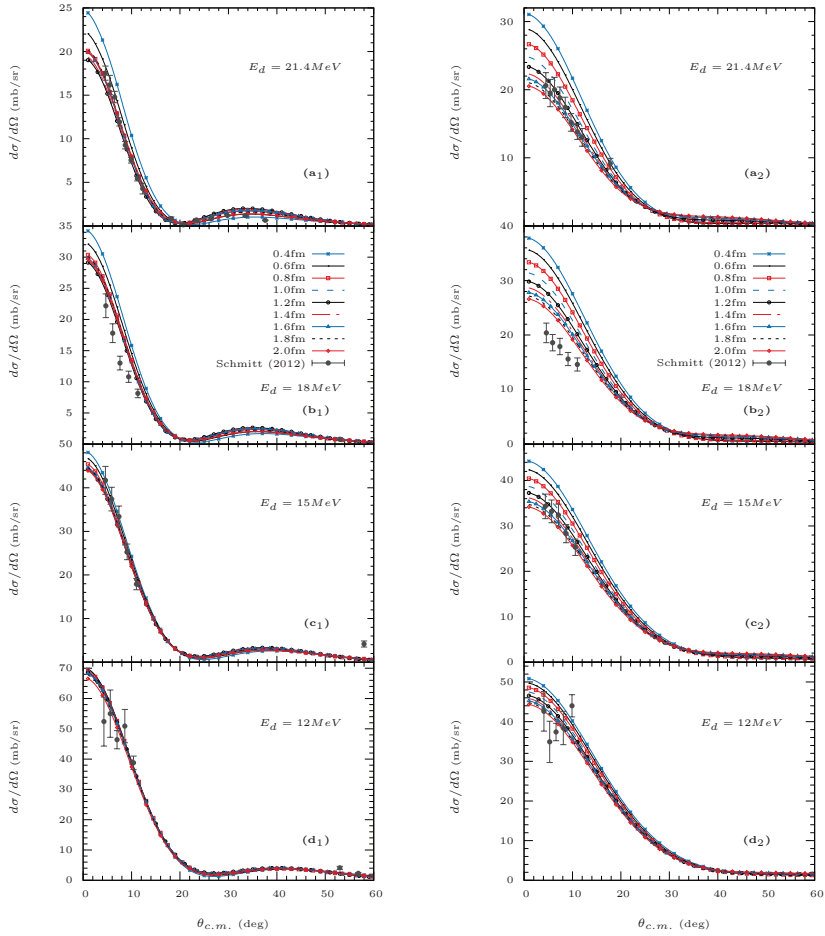

Figure 3.6: The angular distribution of the cross sections for ^{10}Be(d,p)^{11}Be to different states of ^{11}Be at four energies after multiplying by $C_{lj}^2/(b_{nlj})_{r_0}^2$, here $C_{lj} = 0.785$ fm$^{-1/2}$ for the g.s. (left side) or 0.135 fm$^{-1/2}$ for the ex.s. (right side).

for the g.s. and 0.135 $\text{fm}^{-1/2}$ for the ex.s.). In general, the extracted ANC reproduces a good agreement at a low energy between the theoretical results and the experimental data. It gives us confidence on the method developed. Furthermore, if the experimental uncertainty was reduced at $E_d = 12$ MeV, the extracted ANC would be more accurate. Due to the fact that this analysis relies heavily on the accuracy of the experimental data, for obtaining a precise ANC, it would be helpful to do the experimental measurements focusing on the low energies and forward angles.

3.1.2 SuSy test

Similar to the idea developed in Ref. [CN06], an alternative way to check which region of the ^{10}Be-n wave function the transfer reaction probes is to apply the supersymmetry method. As introduced in Sec. 2.3.3, it provides a solution to remove deeply bound state(s) in a partial wave without changing the asymptotics (i.e., ANC of the other bound states and phase shift in the continuum). Via this method, a goal similar as the one presented in the last section is achieved, namely producing a series of wave functions which exhibit the same tail but differ in the internal region. Unlike the previous work, no modification of scaling is needed here. While being normalized, the primary wave function and its SuSy partner(s) naturally share the same identical ANC. If one or more SuSy partners exist, feeding them into the transfer calculations and comparing the obtained cross sections to those calculated with the original wave function could basically tell how the interior of the wave function contributes to the cross sections, and hence reveal the peripherality of the transfer reaction.

Such analysis can be performed with respect to the ground state of ^{11}Be since in the single-particle description of ^{11}Be there is a deeply bound state which can be removed. With the phase-equivalent potential in Eq. (2.37), the SuSy partner corresponding to the wave function of the $1s_{1/2}$ state can be obtained. Both wave functions are displayed in Fig. 3.7. The initial wave function of $1s_{1/2}$ state is constructed using the Gaussian potential with $r_0 = 1.4$ fm set as its width. Compared to that, one node is removed in its $0s_{1/2}$ SuSy partner while the same behavior is kept beyond the distance r' of 4 fm. Considering the subsequent transfer calculations with FRESCO, the numerical settings remain the same as those given at the beginning of Sec. 3.1. The calculated cross sections at two deuteron energies of 21.4 and 12 MeV are plotted in Fig. 3.8. It can be learned from the figure that at $E_d = 21.4$ MeV this transfer is never purely peripheral. As the incident energy decreases to 12 MeV, at forward angles the transfer process depends only on the tail of the wave function which suggests that such process is peripheral in this angular range. These results confirm our previous statement about the conditions when the peripheral transfer is

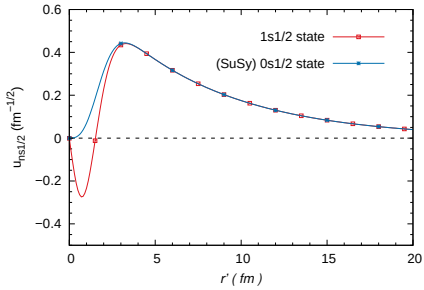

Figure 3.7: The $1s_{1/2}$ radial wave function of ^{10}Be-n bound by 0.502 MeV and its SuSy partner.

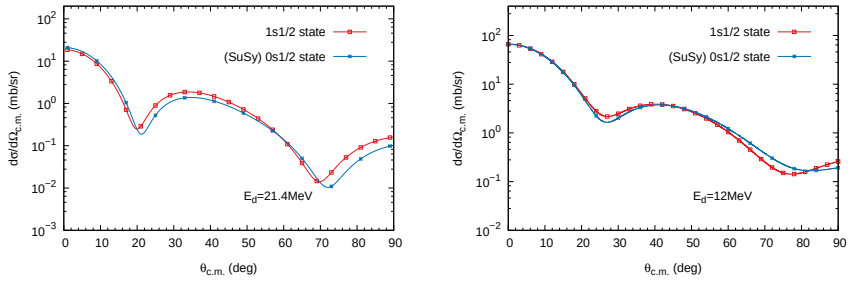

Figure 3.8: ^{10}Be(d,p)^{11}Be reaction calculated at two different deuteron energies using the original wave function and its SuSy partner. Left side: $E_d = 21.4$ MeV; right side: $E_d = 12$ MeV.

favoured, pointing to the same direction (namely at forward angles in the center-of-mass system with a low beam energy) for extracting a reliable ANC value. Besides, the cross sections at large angles are significantly affected by the change in the internal part of the wave functions.

3.1.3 Dependencies

As indicated in Sec. 2.4.3, the accuracy of the transfer calculation depends on several factors. For a specific transfer reaction, usually the Q-value and the transferred angular momentum are fixed. Therefore, mainly the choices of the optical potential and the description of the ^{11}Be ground state are going to be

analyzed here.

Sensitivity to the choice of the optical potentials

The angular distributions of cross sections calculated with ADWA model can depend strongly on the chosen optical potential parameters. In this part, we fix the ^{10}Be-n potential to the Gaussian one with a width $r_0 = 1.4$ fm. By doing that, our interest is to check the influence of the nucleon-nucleus optical potentials on the calculations. In particular, the Koning-Delaroche (KD) potential [KD03] is selected instead of CH89 [VTM$^+$91] to perform this series of analysis. Both are the mostly used potentials in the analysis of transfer reactions [NU12]. In the left panel of Fig. 3.9, a comparison is made between the results obtained using these two parameterizations at $E_d = 12$ MeV. Since the KD potential leads systematically to larger cross sections than the CH89 does, a smaller ANC is expected using the same method (see the right panel of Fig. 3.9). The value of the extracted ANC is (0.755 ± 0.030) fm$^{-1/2}$, not far from the *ab initio* result.

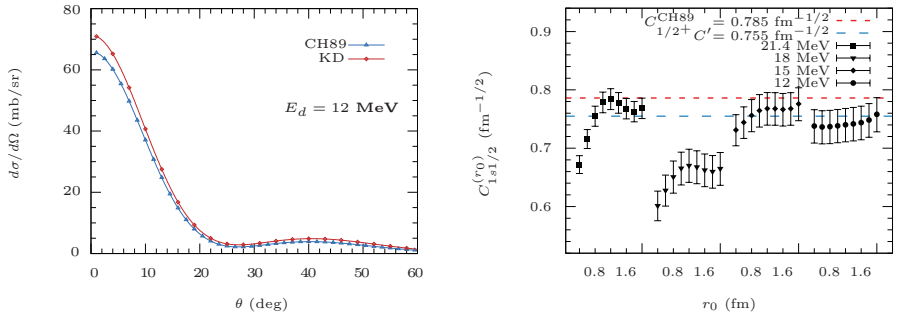

Figure 3.9: Left side: Comparison of the calculated cross sections between using CH89 and KD for ^{10}Be(d,p)^{11}Be at 12 MeV. The Gaussian potential is the set of 1.4 fm for both cases; Right side: ANC extracted for the g.s. of ^{11}Be with KD potentials.

Besides, there are other available options to build such potentials. In order to learn more about the dependence on the potential parameters, the calculations are performed with multiple combinations:

a. Finite-range (FR) adiabatic potential [JT74] built with the CH89 potential and Reid Soft-core [Rei68], abbreviated as FR-CH89, which has been done in Sec. 3.1.1;

b. FR adiabatic potential built with the KD potential and Reid Soft-core, abbreviated as FR-KD;

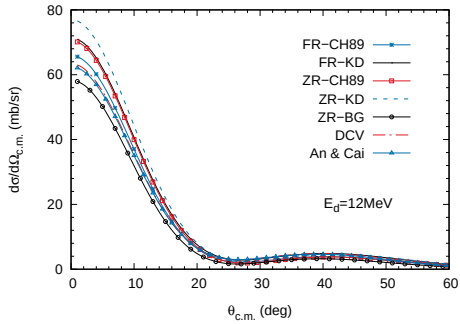

Figure 3.10: Differential cross sections of the ^{10}Be(d,p)^{11}Be(g.s.) reaction obtained using different parameterizations at $E_d = 12$ MeV.

c. Zero-range (ZR) adiabatic potential [JS70] built with the CH89 potential, abbreviated as ZR-CH89;

d. ZR adiabatic potential built with the KD potential, abbreviated as ZR-KD;

e. ZR adiabatic potential built with the nucleon-nucleus potential proposed by Becchetti and Greenlees [BG69], abbreviated as ZR-BG;

f. Global deuteron optical model potential (OMP) of Daehnick *et al.* [DCV80], abbreviated as DCV;

g. Global deuteron OMP of An and Cai [AC06], abbreviated as An & Cai.

The difference in the global parameterizations regarding the incident channel is tested by keeping the CH89 potentials for the exit channel and the core-core interaction since there might be some cancellation of the effect of the potentials if the same parameterization is chosen in all the relevant interactions (not possible for the deuteron OMPs). All the resulting cross sections for transfer to the ground state of ^{11}Be at $E_d = 12$ MeV are shown in Fig. 3.10. Obviously, variations in cross sections are present when using different optical potential parameters. In general, due to the finite-range effect of the deuteron, applying the same nucleon-nucleus parameterization the ZR version of the adiabatic potential gives a larger transfer cross section at forward angles than the FR one does. The smallest cross sections are obtained with ZR-BG in which the nucleon-nucleus potential is less reliable in this case since it has been fitted to a smaller number of cases (mostly heavy targets). Compared to the other results except the one given by the ZR-BG potential, two global deuteron OMPs generate smaller cross sections at forward angles since they effectively take into account more complex reaction processes. In particular, the deuteron OMPs include the deuteron breakup channel in their absorption, whereas the ADWA

Table 3.2: Woods-Saxon parameters of the ^{10}Be-n potentials. The potential depths and SPANCs of the $1s_{1/2}$ ground state are also provided [CN06].

Potential	$V_0(g.s.)$ (MeV)	r_0 (fm)	a (fm)	$b_{1s1/2}$ (fm$^{-1/2}$)
V1	62.96	1.2	0.6	0.829
V2	66.80	1.2	0.5	0.797
V3	59.32	1.2	0.7	0.863
V4	71.81	1.1	0.6	0.818
V5	55.63	1.3	0.6	0.842
V6	57.47	1.25	0.65	0.852

models it adiabatically. Since part of the transfer would come from the breakup of the deuteron with the produced neutron being captured by the target, using a deuteron OMP that treats the breakup as absorption would reduce the transfer cross sections as seen here. Based on this discussion, the major sensitivity of the ANC value is the one shown in Fig. 3.9 since the other choices of optical potentials listed above can be discarded.

Influence of the ^{10}Be-n description

In Sec. 3.1.1, the interaction between ^{10}Be and the neutron in the bound states of ^{11}Be has been simulated by the Gaussian potentials. A general approach to reproduce the effective interaction between these two bodies in the ^{11}Be nucleus is to adopt a Woods-Saxon potential. To study the sensitivity of the transfer calculations to this potential choice, six sets of potential parameters are used. The geometry of the Woods-Saxon potential (r_0, a) is taken from Ref. [CN06]. And the potential depths are adjusted to match the single-neutron separation energy (0.502 MeV) of the ^{11}Be ground state. They are listed in Table 3.2. The calculated wave functions together with the corresponding transfer cross sections are displayed in Fig. 3.11. In order to remain comparable with the previous work, here the transfer calculations are carried out using the FR-ADWA model while the numerical inputs are maintained as those described at the beginning of Sec. 3.1 and only the ^{10}Be-n description gets modified.

There is no doubt that scaling each wave function by its ANC value will generate same tail behavior, resulting in a reduction of the discrepancies existing in the differential cross sections at forward angles. However, using these sets of potential parameters, the values of the SPANCs given in Table 3.2 are very similar to one another, changing by $\sim$8% at the maximum, whereas much larger changes are obtained in the Gaussian case. This lack of significant difference

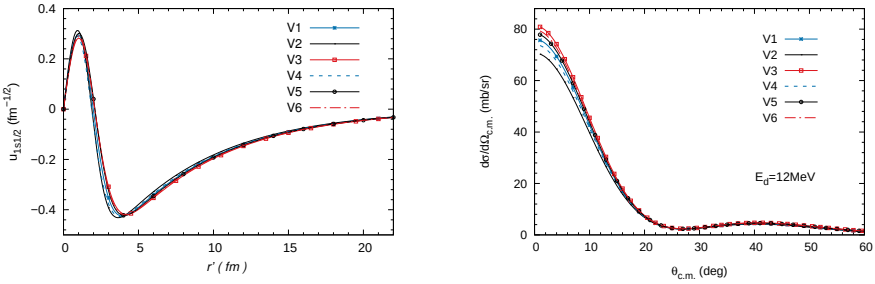

Figure 3.11: Left side: the ^{10}Be-n wave functions obtained with six sets of Woods-Saxon potential parameters; Right side: cross sections calculated for the ^{10}Be(d,p) transfer using those Woods-Saxon potentials.

would make the identification of the peripheral conditions difficult. Note that it is still possible to get a large range of SPANCs using the Woods-Saxon potentials with more extreme parameters. But since a potential is a priori, there is no actual constraint in choosing its type. With two parameters to fix the potential geometry, this certainly brings more work to figure out their influence on the transfer results when without changing the final conclusion the Gaussian potential takes a shortcut on this problem thanks to its simpler expression.

3.1.4 Resonance state

So far in this work, the transfer reaction has only been employed to investigate the bound states of the ^{11}Be nucleus. However, there still exists a possibility that the transferred neutron can populate unbound states of the final nucleus. In particular for the halo nucleus ^{11}Be, such system could easily get into the resonance states. In Schmitt *et al.*'s work [SJA$^+$13], the experimental data for transfer to the first resonance in ^{11}Be is also obtained at several energies. Looking into this part could provide information about the nuclear structure of the resonance and help improve the theoretical model for describing the nuclear many-body systems. Furthermore, the properties of the resonances are of special interest to nuclear astrophysics since many nuclear reactions happening in stellar environments take place through this state.

According to the derivation in Sec. 2.3.4 combined with the previous idea regarding the ANC extraction, the aim in this section is to establish a similar connection between the transfer observables and the energy width of the ^{10}Be-n resonance. The FR-ADWA model is kept for the following transfer calculations

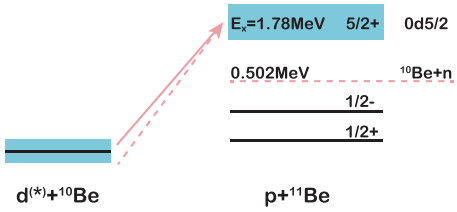

Figure 3.12: Illustration of the coupling scheme used in the ADWA model for transfer to the resonance state.

due to its good capability in calculating the case of (d,p) reactions [GCM14, Cat14] and low computational cost. Considering the transfer to the resonances, the coupling scheme in the ADWA method is shown in the schematic diagram of Fig. 3.12, which basically can be viewed as a one-step transition from the initial state d+^{10}Be to the final state p+^{11}Be.

Within the model presented in Chapter 2, the wave function of this ^{11}Be resonance state is described as an eigenstate of its Hamiltonian. But from the experimental point of view, one has to keep in mind that there is no access to a definite final energy in a practical transfer reaction leading to positive energy states. This means that the measured cross sections are actually integrated over some energy range which is up to at least the resolution of the detection system. In practice, a bin description for the wave function is chosen. A typical form of the bin function is averaged over the momentum k to be square integrable as [TN09]

$$\psi(r) = \sqrt{\frac{2}{\pi N}} \int_{k_1}^{k_2} g(k)\psi_k(r)dk, \tag{3.4}$$

with $N = \int_{k_1}^{k_2} |g(k)|^2 dk$, the upper limit of the momentum k_2 and the lower one k_1 for the bin. The weight function $g(k)$ is set to be $e^{-i\delta_k}\sin(\delta_k)$ for a narrow resonance [Tho06] in our case, where δ_k is the scattering phase shift.

Apart from this description of the resonance, the same settings as those introduced for the potentials at the beginning of Sec. 3.1 are used. Without considering the core excitation, the first resonance of ^{11}Be can be simulated by a $0d_{5/2} \otimes {}^{10}\mathrm{Be}(0^+)$ configuration. Again the Gaussian potential is used in this case to model the interaction between ^{10}Be and the neutron. Six potentials are obtained with different widths r_0 starting from 1.0 fm to 2.0 fm while the depth V_0 is modified to reproduce the resonance energy ($E_{\mathrm{res}} = 1.28$ MeV). The

Table 3.3: Gaussian parameters of the ^{10}Be-n resonance ($E_{\rm res}$ = 1.28 MeV). The Γ widths given by FRESCO are shown as well.

Potential	r_0/fm	V/MeV	Γ/MeV
V1	1.0	303.814	0.0361
V2	1.2	209.241	0.0601
V3	1.4	152.172	0.0917
V4	1.6	115.088	0.1316
V5	1.8	89.622	0.1801
V6	2.0	71.363	0.2381

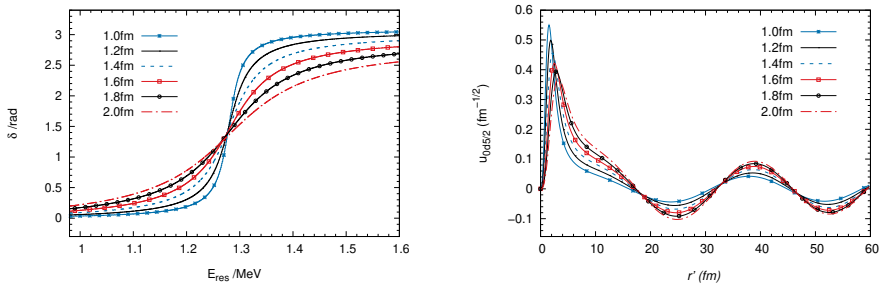

Figure 3.13: Left side: the phase shifts obtained with six different sets of Gaussian potentials for the first resonance of ^{11}Be; Right side: wave functions at $E_{\rm res}$.

potentials with narrower widths are discarded here since they are not really physical and would bring numerical problem when resolving the resonance width in our calculations. The related parameters are all listed in Table 3.3 with the Γ widths. The size of the bin considered in the calculation is matched to its own Γ width. The phase shifts and wave functions for the resonances obtained with these potentials are displayed in Fig. 3.13. We observe the clear signature of a single-particle resonance with a sudden and sharp increase in the phase shift around the resonance energy. The wave function exhibits a significant maximum at small distances of r' and has the usual oscillatory behavior of continuum states at large distances.

Feeding those wave functions into the associated ADWA calculations at different deuteron energies could reveal how the influence of the Γ width on the calculated cross sections evolves with the incident energy. Two cases at E_d = 21.4 MeV and

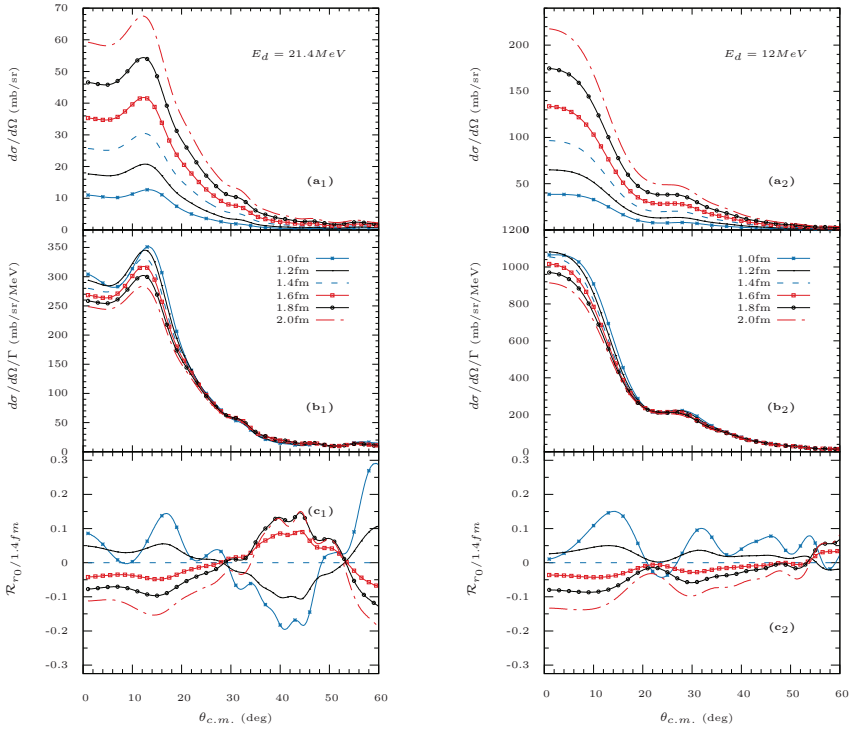

Figure 3.14: Analysis of the differential cross sections of ^{10}Be(d,p) to the first resonance of ^{11}Be with incoming deuteron energy of 21.4 MeV (left side) and 12 MeV (right side).

12 MeV are presented in Fig. 3.14 to illustrate the findings. Referring to what has been carried out with the ANC for bound states, a similar analysis is performed here on the resonance width. In the figures, plot (a_n) ($n = 1$ for $E_d = 21.4$ MeV and $n = 2$ for $E_d = 12$ MeV) shows the angular distribution of the transfer cross sections obtained with different Gaussian potentials; plot (b_n) represents the cross section after being scaled by the corresponding Γ width; plot (c_n) gives the variation of the cross sections relative to those calculated using the potential of $r_0 = 1.4$ fm which leads to an energy width of the resonance that is close to the experimental value (0.1(0.01) MeV) obtained in Refs. [HFA$^+$09, KKP$^+$12]. It is clear that in plot (a_n), the narrower the resonance, the smaller reaction rate. The order of the curves follows the magnitude of the wave functions at about $r' = 10$ fm. Getting the cross sections scaled by the Γ width in plot (b_n) reduces significantly the differences among the curves shown in plot (a_n).

This is not as effective as what was observed for the bound states. But still the effect is similar. After scaling the previous order is inverted, suggesting that the reaction seems to be also sensitive to the internal part of the wave function. Surprisingly, this might indicate that the reaction is less peripheral.

Through the comparison between these two results, one conclusion that can be drawn from the above investigation is that similar to what ANC means to the bound state, the resonance width serves as a signature of the resonance. This is not surprising because both the ANC and the resonance width are related to the residue of the S-matrix as discussed in Ref. [MT99]. However, in general, the calculations at both energies seem to provide the same uncertainty. The peripherality at the low energy is no longer that clear as what has been observed with the ANC. There are several potential factors that could contribute to this situation: the peripherality of the transfer is questionable due to its large angular momentum transferred; the description of the resonance state is a simple approach in a single-particle picture; the ADWA model itself does not include all the necessary coupling forms. It would be dangerous to directly extract the resonance width without studying the above issues. Thus, one of our outlook for the future work is to get more experimental data at low beam energies and test the reliability of the theoretical method for this kind of transfer.

3.2 ^{14}C(*d*,*p*)^{15}C transfer reaction

As a one-neutron halo nucleus, ^{15}C is particularly interesting for physicists since it is involved in reactions that drive the nucleosynthesis such as neutron induced CNO cycles [HWG$^+$02] and inhomogeneous big bang models [AH85, MBG$^+$11]. In this section, the ANCs of the ground state and the first excited state in ^{15}C are extracted via ^{14}C(d,p) transfer using the method introduced in Sec. 3.1. Such value for ^{15}C is very useful to constrain the relevant potential parameters when applying the Halo-EFT description of this nucleus at the next to leading order (NLO) [CPH18]. With this description, it is expected to offer reasonable predictions for various reactions involving the ^{15}C nucleus, such as transfer, breakup at high beam energies and radiative capture [MYC19].

Regarding the ^{14}C(d,p)^{15}C transfer reaction, there have been two experiments performed at relatively low incident energies where we have the best chance to find a peripheral process. One was performed at the University of Notre Dame with the deuteron bombarding energy of 14 MeV [GJB$^+$75]. The other was measured using a momentum-analyzed 17.06 MeV deuteron beam at the Nuclear Physics Institute of the Czech Academy of Sciences [MBG$^+$11]. Due to the fact that the former experiment does not provide enough data points at

forward angles for the analysis, only the data from the latter one are taken into account to extract the ANC value even though being measured at higher beam energy.

The theoretical model chosen for the transfer calculation is again the FR-ADWA. The nucleon-nucleus optical potentials are built with the CH89 global potentials [VTM$^+$91]. The Reid soft core potential [Rei68] is employed for the deuteron bound state. The finite-range version of the deuteron adiabatic potential is obtained with the front-end code of TWOFNR [TTIK12] and the full transfer calculations are carried out using FRESCO [Tho06].

3.2.1 ANC extraction

The introduction of ANC in Eq. (2.45) is to quantitatively define the exponential tail of the bound state wave function. In a purely peripheral transfer, its value determines the overall normalization of its cross sections. In order to extract the ANC as precise as possible, the main task is to find the experimental conditions where the transfer is peripheral and probe only the tail of the wave function. As illustrated in the previous work in Sec. 3.1.1, this can be achieved by studying the sensitivity of the transfer cross sections on different wave functions for the state of the nucleus of interest. From the low-energy level diagram of ^{15}C

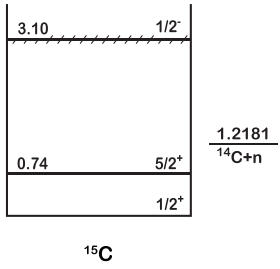

Figure 3.15: Low-energy level diagram for ^{15}C [NuD19].

shown in Fig. 3.15, with the assumption that the ^{14}C core is in its ground state (0+), the $1/2^+$ g.s. of ^{15}C can be described by a $^{14}\mathrm{C}(0+)\otimes 1s_{1/2}$ configuration, and the $5/2^+$ ex.s. by a $^{14}\mathrm{C}(0+)\otimes 0d_{5/2}$ configuration. To simulate the ^{14}C-n interaction at LO of Halo-EFT, several Gaussian potentials are generated to reproduce the measured single-neutron binding energy (1.218 MeV for the g.s. and 0.478 MeV for the first ex.s.) while giving significant changes in the radial wave functions. The detailed parameters of the Gaussian potentials are listed in

Table 3.4: Gaussian parameters of the ^{14}C-n interaction in the $s_{1/2}$ and $d_{5/2}$ waves within ^{15}C. The single-particle ANC (SPANC) and root-mean-square radius for each case are provided as well.

r_0 for g.s. (fm)	$b_{1s1/2}$ (fm$^{-1/2}$)	$\langle r^2\rangle^{1/2}$ (fm)	r_0 for ex.s. (fm)	$b_{0d5/2}$ (fm$^{-1/2}$)	$\langle r^2\rangle^{1/2}$ (fm)
0.6	0.8646	3.81	1.3	0.0355	2.89
0.8	0.9340	4.07	1.4	0.0399	3.09
1.0	1.0083	4.34	1.5	0.0444	3.28
1.2	1.0878	4.61	1.6	0.0492	3.47
1.4	1.1728	4.87	1.7	0.0541	3.66
1.6	1.2636	5.13	1.8	0.0592	3.85
1.8	1.3606	5.39	1.9	0.0646	4.03
2.0	1.4640	5.64	2.0	0.0701	4.21

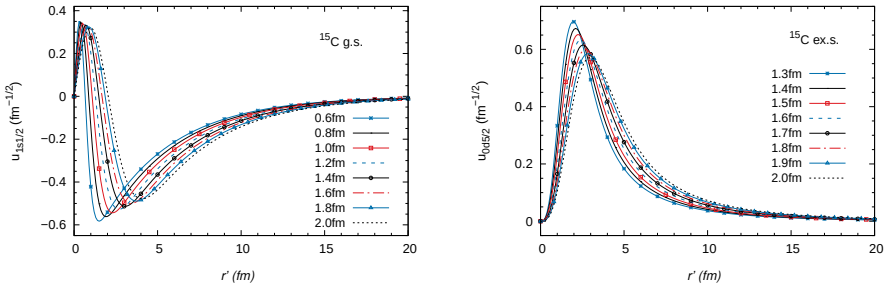

Figure 3.16: Wave functions obtained with eight different sets of Gaussian potentials listed in Table 3.4 for the $1/2^+$ g.s. of ^{15}C (left) and for the $5/2^+$ ex.s. (right).

Table 3.4. The reason to develop the Gaussian potentials for the excited state with a different set of widths is to obtain roughly the same magnitude of change for the single particle ANC compared with that of ground state. The wave functions for the g.s. and ex.s. of ^{15}C obtained using the Gaussian potentials are displayed in Fig. 3.16.

Entering these wave functions into the transfer calculations, the angular distributions are shown in Fig. 3.17 (a_n) (here $n = 1$ for the ground state of ^{15}C and $n = 2$ for its first excited state). After scaling by the square of b_{nlj}, the spread in the cross sections is significantly reduced as shown in Fig. 3.17 (b_n).

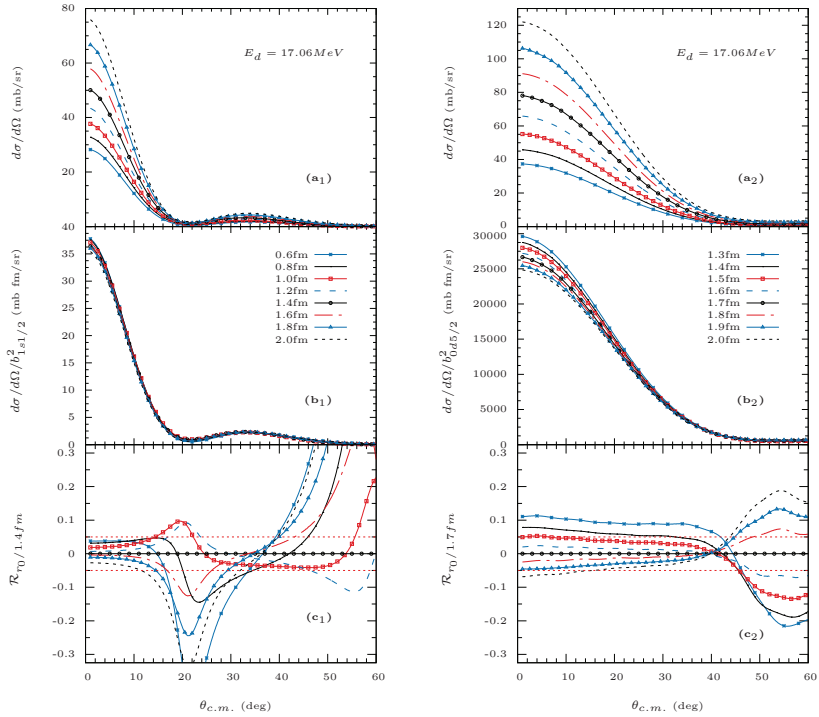

Figure 3.17: Analysis of the differential cross sections of ^{14}C(d,p) transfer to two bound states of ^{15}C with incoming deuteron energy of 17.06 MeV. Left: transfer to the g.s. of ^{15}C. Right: transfer to the first ex.s. of ^{15}C.

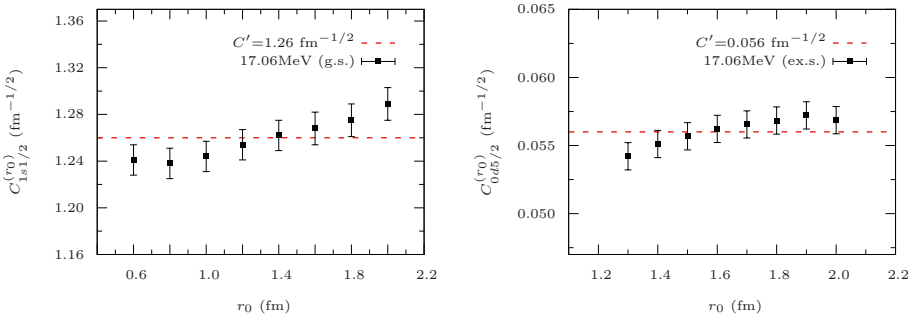

Figure 3.18: Left side: ANCs extracted for the ^{15}C ground state; Right side: ANCs extracted for the ^{15}C first excited state.

Table 3.5: Comparison of the ANC^2 values of the ^{15}C states from the other analysis.

Ref	$C^2_{1s1/2}$ (fm^{-1})	$C^2_{0d5/2}$ ($\times 10^{-3}$ fm^{-1})
[TAC$^+$02][a]	1.48±0.18	
[TBD$^+$06][b]	1.89±0.11	
[SN08][c]	1.74±0.11	
[MBG$^+$11][d]	1.64±0.26	3.55±0.43
[MMT$^+$14][e]	1.88±0.18	4.25±0.38
[Nav18][f]	1.64	2.30
this work	1.59±0.06	3.14±0.11

[a] Knockout data from Refs. [MAB$^+$01] and [SCO$^+$04] were jointly used to extract the ANC [PNM07]. This value should be accurate since the knockout process is mostly peripheral [HC19]. Our result falls exactly within its uncertainty band.
[b] The charge symmetry between ^{15}C and its isobar analog ^{15}F was applied as a model-independent tool to constrain the ANC value. This is strongly dependent on the choice of the width of the ^{15}F resonance considered in the method, which might explain the discrepancy with our value.
[c] This analysis found the related ANC from the Coulomb dissociation data. Our result is compatible with this value. This is not surprising since the Coulomb breakup is peripheral.
[d] The ANCs for both bound states of ^{15}C have been extracted using the (d,p) transfer at $E_d = 17.06$ MeV of which the data is reanalyzed in our work. In their analysis, they considered the data from the entire measured angular range which is not fully peripheral. This could explain the small difference between their results and ours.
[e] The ANCs were determined using the (d,p) reaction as well as a heavy-ion neutron transfer reaction. The experiments were performed at a higher energy ($E_d \approx 24$ MeV) where the transfer is less peripheral. The slight disagreement with our ANC is most likely due to that issue.
[f] These results are obtained in an *ab initio* calculation of ^{15}C performed within the no-core shell model with continuum (NCSMC) by Navrátil *et al.* [Nav18]. For the ground state of ^{15}C, our result is in excellent agreement with their value. The values for the excited state do not match that well possibly due to the d-wave nature. This is consistent with what has been observed in our previous analysis of the ^{10}Be(d,p)^{11}Be transfer in Sec. 3.1.1.

To quantitatively determine within which angular range the process should be strictly peripheral, the major angular dependence is removed by considering the ratio formula of Eq. (3.1). In the case of transfer to the ^{15}C first excited state, the comparative standard is replaced by the set of 1.7 fm rather than that of 1.4 fm. It turns out that most of the curves in Fig. 3.17 (c_n) fall into the

confident peripheral band of 5% at forward angles. For transfer to the ^{15}C g.s., this happens when $\theta_{c.m.} < 10°$. With respect to the excited state, as expected our method works less well since $l = 2$ here. Excluding the most extreme calculations, viz. the ones corresponding to the largest and smallest values of SPANCs, would lead the maximum peripheral angle extend to 44°. Taking use of the χ^2 method based on Eq. (3.2), the ANCs can be extracted from the experimental data [MBG$^+$11] within the peripheral range. The results shown in Fig. 3.18 are quite independent of the value of r_0. Calculating their mean value and standard deviation, the final ANC value inferred is (1.26 ± 0.02) fm$^{-1/2}$ for the ^{15}C ground state and (0.056 ± 0.001) fm$^{-1/2}$ for the first excited state of ^{15}C.

For comparison with previous work on ^{15}C, in Table 3.5 part of the ANC results reported before is presented together with the values extracted in this work. Our analysis is within the error band but on the lower end of most results, and especially shows a good agreement with those provided in Refs. [SN08] and [MBG$^+$11]. Nevertheless, it is still controversial that the error we get is in general small. This could be due to several aspects. One of them is that the systematic uncertainty on the data has not been taken into account in the analysis. And in our case the ANC is always obtained from the experimental data at forward c.m. angles in which a better statistics is presented than at larger angles.

3.3 Searching for halos in nuclear excited states

The results presented in this section have been obtained in collaboration with Prof. Alexandre Obertelli, an experimentalist at the TU Darmstadt. The original idea is to use transfer with small beam energies to detect halo states in the nuclear excited spectrum where the ground state is not a halo state in contrast to the previous case. Up to now, this topic of the halo excited states introduced in Sec. 1.1.1 remains an open question. Through the work in this section, we study theoretically the feasibility of our methodology. As mentioned before, transfer reaction provides an excellent way to investigate the single-particle structure of the nucleus. When the transfer is performed at low incident energies, even below the Coulomb barrier, no close approach between the projectile and the target in this reaction simplifies the interpretation of the reaction mechanism. One of the decisive factors for the transfer rate is the overlap between the asymptotic parts of the wave functions in the initial and final states. Thus in practice, the transfer cross section can be used to derive the tail behavior of the wave function, thereby further indicating whether the nuclear state would exhibit a halo. Due to its well-studied feature, (d,p)

reaction is employed in the following work. The next two questions are to figure out the suitable energy range for conducting the transfer and find a good halo candidate to test the validity and limitations of the method. These questions will be addressed explicitly in the next two sections. Based on that, a systematic study of the interesting transfer will be carried out in Sec. 3.3.3.

3.3.1 Sub-Coulomb transfer

Regarding the incident energy, there are several factors that prompt us to consider sub-Coulomb transfer. Even though the corresponding cross sections would be reduced due to the Coulomb repulsion, the advantage there is that any observed transfer event would most likely be a direct and peripheral one, making a few other channels negligible, such as the compound-nucleus formation. Meanwhile, the distortion of the elastic Coulomb waves by the nuclear potential would be very small. An early review on this method dates back to 1966 by Goldfarb [Gol66]. Fig. 3.19 shows an example of ^{90}Zr(d,p) which is recalculated based on Goldfarb's work [Gol66] to reveal the evolution of transfer angular distribution in a wide range of incident energies. What we have obtained here is basically consistent with Goldfarb's results [Gol66]. All the transitions

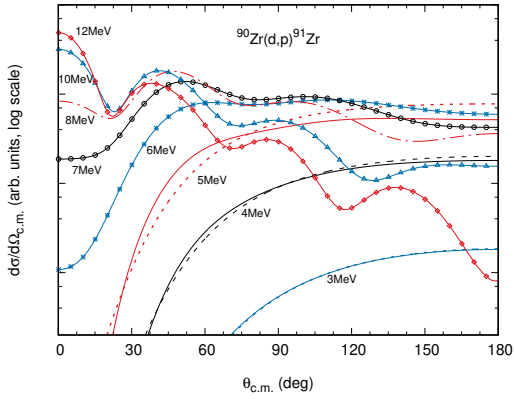

Figure 3.19: Evolution of the angular distributions for the ^{90}Zr(d,p) transfer from sub-Coulomb energies to those well above the Coulomb barrier ($\approx$ 8 MeV). The incident energy of deuteron is marked next to the corresponding line.

are calculated for $l = 0$ using ZR-ADWA model which offers a close result and is easier to manipulate compared to the finite-range version according to our pre-tests (not shown here). For the results obtained at $E_d = 3$, 4 and 5 MeV, the dashed curves correspond to the Coulomb-dominated transfer and

neglect of nuclear absorption and refraction while the solid curves include the full interaction. In a classical physics picture, the Coulomb barrier for the entrance channel is around 8 MeV around which one can easily find a distinct change of the curve shape. Especially below 6 MeV, all the cross sections start to increase monotonically and exhibit a maximum at 180 degrees. At larger incident energies, the familiar diffraction-like peaks appear at forward angles. Another work done by Erskine and his colleagues [EBE62] suggests that the angular distributions for sub-Coulomb stripping probability would be featureless and almost independent of the l-transfer. But this does not mean that the information of the transferred orbital angular momenta will be lost using this method. It has been demonstrated by Hering and Dost [HD68] that applying the sub-Coulomb stripping to assign l-values from the slope of (d,p) excitation functions is adequate. Another interesting finding from the Fig. 5 in Erskine *et al.*'s work [EBE62] is that the less bound the final nucleus is, the higher the transfer cross section becomes. This phenomenon would be a strong asset for us.

3.3.2 Searching for a candidate nucleus

A quick search on a candidate that could host a 1-n halo in one of its excited states is presented in this section. In our case, the ideal candidate should have an excited state with a rather small one-neutron separation energy at medium to heavy mass region with the s orbital occupied. Note that there are two main reasons to concentrate on such mass region. One is that medium to heavy nuclei would have abundant excited states. The other is that compared to the light nuclei the higher charge of these nuclei provides a wider range of beam energy choice in order to perform the transfer below the Coulomb barrier. Considering the above constraints within a simple single-particle structure, the most possible state for the valence neutron in the final product is $2s_{1/2}$ which indicates that the neutron number would be around 50 ± 20 using the prediction of the classical shell model.

A short summary of the searching criteria is: 1) $18 < Z < 60$ (with proton number Z being even); 2) $30 < N < 70$ (with neutron number N being odd); 3) Spin and parity: 1/2+; 4) Binding energy (BE) < 1 MeV at most. Using the experimental data in NNDC [NuD19], the results of this search are listed in Table 3.6. The best case found is the excited state of ^{95}Sr. In this study, I will consider two excited states of ^{95}Sr where the last neutron is bound with either 69.5 keV or 184.4 keV in the associated transfer of ^{94}Sr(d,p) to check its sensitivity to different experimental conditions, and hence learn the feasibility of practical measurements.

Table 3.6: Summary of the possible candidates of the halo excited states. The values including one-neutron separation energy (S_n) for the g.s. and excitation energy (E_x) are taken from [NuD19].

A	Element	N	S_n/keV (g.s.)	E_x/keV	BE/keV (= S_n− E_x)	J^π
63	Ni	35	6837.8	6440.0	397.8	$1/2^+$
95	Sr	57	4348.0	4163.6	184.4	$1/2^+$
95	Sr	57	4348.0	4278.5	69.5	$1/2^+$
95	Sr	57	4348.0	4292.4	55.6	$1/2^+$

3.3.3 Dependencies

In this part, for the aim of understanding better the property of the transfer calculations involving ^{95}Sr, more efforts have been systematically made regarding the investigation of the sensitivity of the cross sections on the nuclear structure and reaction parameters. The crucial factors being tested contain Q-value, nuclear spin and beam energy. In addition, following the nice results obtained for ^{11}Be in Sec. 3.1.2, the SuSy method explained in Sec. 2.3.3 is applied to tell which part of the wave function is probed under certain experimental conditions during the (d,p) transfer since one of the key features coming with the halo nucleus is a significant long-range tail in its wave function.

As mentioned before, the theoretical model chosen for the following transfer calculations is the ZR-ADWA. The settings for the parameters in the calculations are similar to those used before except that the description of the ^{94}Sr-n interaction is simulated by a standard Woods-Saxon potential ($r_0 = 1.25$ fm, $a = 0.65$ fm). Considering the states involved in the test, to give an idea about how they differ from each other, several relevant parameters (like SPANC and rms radius) obtained using the single-particle description of the ^{95}Sr nucleus are listed in Table 3.7. Note the states considered in this test, such as a p-wave state, are not always physically correct. The idea here is to start from a realistic case and then explore the related model space to see what can be inferred from such calculations.

The global optical potential CH89 is employed for the nucleon-nucleus interaction without the spin-orbit terms, while the Reid soft-core potential is used to bind the proton and the neutron in the deuteron. Regarding the incident energy E_d, our initial intention is to bring out the transfer below the Coulomb barrier E_{coul} which is around 7.8 MeV. The lower limit for this energy is imposed by the threshold energy E_{th} ($= -Q\frac{m_a+m_A}{m_A} \geq 0$ in normal kinematics) to make the transfer possible. The relationship can be denoted as $E_{th} < E_d < E_{coul}$. Combined with two interesting excited states of ^{95}Sr (the corresponding Q-value

Table 3.7: Single-particle states of ^{95}Sr considered in the tests. The values of the SPANCs and root-mean-square radii are also offered.

State	BE (keV)	SPANC (fm$^{-1/2}$)	$\langle r^2\rangle^{1/2}$ (fm)
$2s$	69.5	0.460	16.46
	184.4	0.713	11.79
$3s$	69.5	0.476	16.96
	184.4	0.751	12.30
$2p$	69.5	0.175	12.11
	184.4	0.335	9.91
$1d$	69.5	0.024	7.76
	184.4	0.068	7.29

is -2.1551 MeV or -2.0402 MeV), the sub-Coulomb incident energy is set to be 4 MeV as the standard in most of the calculations.

Influence of Q-value

It has been learned in Sec. 2.4.3 that the Q-value could have a significant impact on the magnitude of the cross sections. In FRESCO, this factor can be treated as an independent value that one can manipulate at will. It offers in this way a simple and quick way to compare the cross sections before and after removing the difference in Q-value. In practice, three states ($2s_{1/2}$, $3s_{1/2}$ and

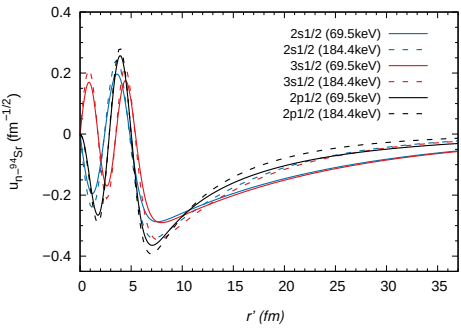

Figure 3.20: Wave functions of ^{94}Sr-n bound in different partial waves and binding energies.

$2p_{1/2}$) bound with two binding energies (69.5 keV and 184.4 keV) are considered to help illustrate our findings. In Fig. 3.20, the wave functions for different combinations of ^{94}Sr-n (see Table 3.7) are plotted. At the same nuclear state,

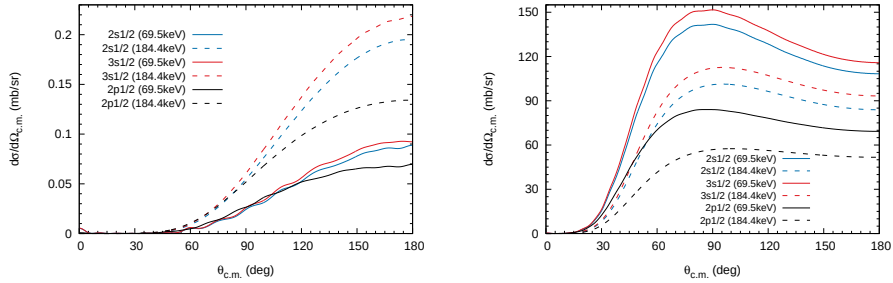

Figure 3.21: Differential cross sections of ^{94}Sr(d,p)^{95}Sr* reaction at $E_d = 4$ MeV with the change of Q-value (left side). On the right side, Q-value is kept as 0 MeV.

the less bound case has a more extended tail beyond 13 fm. With the same binding energy, the tail of s wave function is always higher than that of p wave function due to the presence of a centrifugal barrier. Based on the choice of the Q-value, the cross sections of the ^{94}Sr(d,p)^{95}Sr* transfer at $E_d = 4$ MeV are calculated and organized in two subplots of Fig. 3.21. On the left side of Fig. 3.21, the Q-value varies according to the binding energy. It is clear that the results of BE = 184.4 keV (dashed lines) are always larger than those of BE = 69.5 keV (solid lines). This is because although a lower binding energy leads to an enhanced tail in the reduced radial wave function, a smaller Q-value strongly hinders the transfer. The oscillations observed in some curves are possibly due to numerical problems when encountering a poor Q-value matching [HEK$^+$78]. And the slight difference between the curves of $2s$ and $3s$ states (with the same binding energy) is caused by the difference in their ANC values. After removing the difference in the Q-value as shown on the right side of Fig. 3.21 where all the Q-values are set to 0 MeV, there is a significant increase of the cross sections for the less bound cases. Lowering the threshold energy for the reaction also modifies the shape of the angular distributions. The good news here is that the order of the tail of the wave function which serves as the signature of a halo state can almost be judged by the magnitude of the cross sections. The difference between the results of $2p_{1/2}$(69.5 keV) and $2s_{1/2}$(184.4 keV) (or $3s_{1/2}$(184.4 keV)) would depend on how much range of the tail part gets involved in the calculations, which can be partially checked using the SuSy method (see below).

Influence of the nuclear spin

The aim of this test is to see whether the orbital angular momentum can be distinguished by the transfer cross sections. Here only the spin of the valence

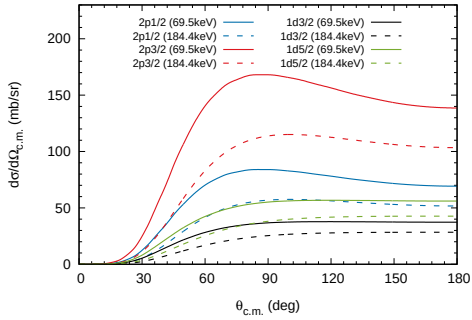

Figure 3.22: Differential cross sections of ^{94}Sr(d,p)^{95}Sr* reaction at $E_d = 4$ MeV with different total spins assigned in the final state.

neutron is changed. The Q-value remains as 0 MeV. Four states ($2p_{1/2}$, $2p_{3/2}$, $1d_{3/2}$ and $1d_{5/2}$) bound with two binding energies (69.5 keV and 184.4 keV) are selected. The calculated transfer cross sections are plotted in Fig. 3.22. With the same binding energy, it turns out that the discrepancy between the cross sections of two states splitting from one orbital angular momentum l can be explained by the total spin j of ^{95}Sr with a relationship of $(2j+1)$. For instance, the ratio of the cross section obtained for the $2p_{3/2}$ state to that for the $2p_{1/2}$ state is close to $(2\times3/2+1)/(2\times1/2+1) = 2$. This is consistent with the derivation given in Ref. [XTG^{+}13] where these information can be extracted separately as the coefficient $C_{\alpha,\beta} = (2j_B + 1)/(2j_A + 1)$ for a stripping reaction (in our case j_A and j_B are the total spins of the ^{94}Sr and ^{95}Sr*). The experience learned from this part is that there is a potential competition between the total spin of the produced nucleus and the tail of the wave functions in determining the magnitude of the transfer probability.

Influence of the incident energy

The effect of incident energy on the transfer cross section is examined here. For the comparison, the transfer calculations are performed at $E_d = 5$ and 8 MeV. The results are displayed in Fig. 3.23. Although a higher incident energy might be able to compensate for the difference in binding energy and hence reduces the effect of Q-value, to ensure the comparability of the results with previous work, 0 MeV is again used as the Q-value. The final states populated in ^{95}Sr contain s and p waves bound with two binding energies. Shifting E_d from 5 MeV to 8 MeV, the cross sections of $2p_{1/2}$ state move beyond those of s states. And considering the s states with $E_d = 8$ MeV, the results obtained using a smaller BE drop below the others. Both phenomena indicate that at higher energies the transfer reaction starts to probe the internal part of the wave function. In

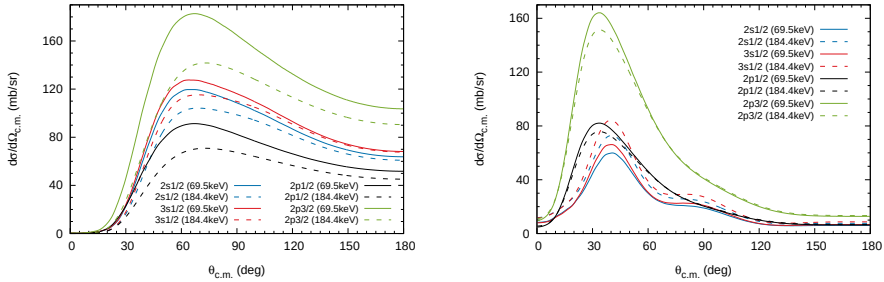

Figure 3.23: ^{94}Sr(d,p) transfer to multiple binding cases of ^{95}Sr* at different deuteron energies with the Q-values set to 0 MeV. Left side: $E_d = 5$ MeV; Right side: $E_d = 8$ MeV.

other words, regarding our case, the cross section is no longer only sensitive to the tail of the wave function with the deuteron energy being above 8 MeV. Repeating the above tests with another Q-value, -2 MeV which is close to the real case, would as expected produce much smaller cross sections (not shown here). But the distribution of the orders of the curves remains similar, which would lead to the same conclusion. This confirms the necessity for this test to be at sub-Coulomb energy in order to study the asymptotic behavior of the wave function.

SuSy test

To clarify which part of the wave function the transfer actually probes, the supersymmetry (SuSy) method is employed here. Via this method, a series of wave functions is generated with the same asymptotic behavior but very different interiors. Feeding them into the transfer calculations and comparing the cross sections will basically tell if the internal part of the wave function is playing a role in determining the results. In this test, the $2s_{1/2}$ state bound by 184.4 keV is taken into account. Instead of considering the binding energy of 69.5 keV which would cause numerical instabilities in the calculations, a higher BE (184.4 keV) is chosen here. Its wave function is plotted together with the associated SuSy partners in Fig. 3.24. In the figure, $2s_{1/2}$ state stands for the original wave function of the $2s_{1/2}$ state having two nodes; removing either the first node corresponding to the deepest Pauli forbidden state or the second one would generate two different $1s_{1/2}$ states indicated by the blue dashed line and the black solid line respectively; $0s_{1/2}$ state is a state in which both nodes are removed.

Fig. 3.25 shows the calculation results of the ^{94}Sr(d,p)^{95}Sr transfer reaction.

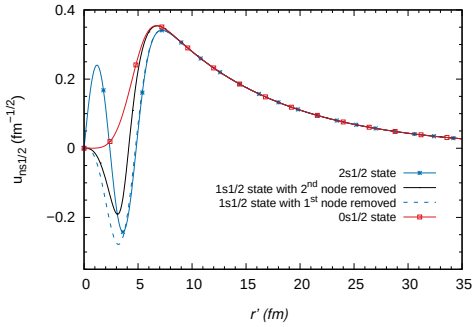

Figure 3.24: SuSy partners of the $2s_{1/2}$ wave functions of ^{94}Sr-n bound by 184.4 keV.

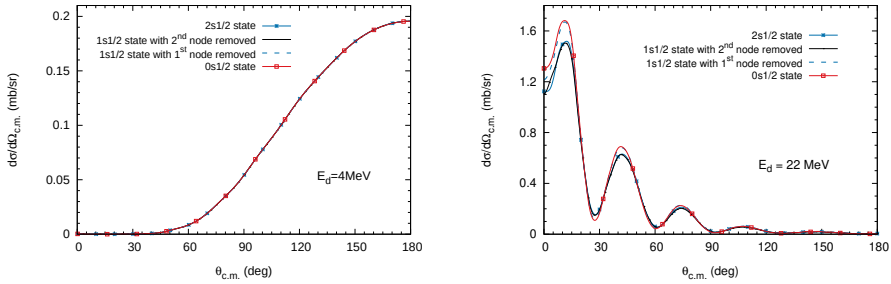

Figure 3.25: ^{94}Sr(d,p) transfer at different deuteron energies using the SuSy partners. Left side: $E_d = 4$ MeV; right side: $E_d = 22$ MeV.

Since just one binding energy is considered in the final state, the same experimental Q-value (-2.0402 MeV) is applied here to approach the real case and will not have any impact on the comparison. Only the influence brought by the internal part of those wave functions is studied. At $E_d = 4$ MeV, all the cross sections are identical to one another in the whole angular range. This confirms the previous idea about the peripherality of the transfer at this energy that only the tail of the wave function is involved in the calculations. When the beam energy moves up to 22 MeV, there exist differences among the curves while the highest peak of cross sections appears at forward angles. It suggests that the internal part of the wave function ($r' < 5$ fm) starts to contribute when the incident energy becomes higher. Similar tests (not shown here) have also been performed starting from the $2p_{1/2}$ wave state, which lead to the same conclusion.

Based on the above tests, it can be figured out that in a peripheral transfer with a low incident energy, viz. sub-Coulomb, the cross sections are sensitive to the tail of the reduced radial wave function (as the simultaneous effect of binding energy and orbital angular momentum in the occupied state). However, other features of the system also play a significant role, which should not be ignored in analyzing the results of actual experiments: the total spin of the final state and the Q-value can reduce the effect of the long-range tail observed in the wave function of a halo state. In our case, the (d,p) transfer taking place at a small incident energy, such as sub-Coulomb transfer, is rather peripheral and therefore will be a clean measure to fetch the probability of the presence of the valence neutron at large distances from the core, i.e., the tail of the wave function. Such extracted information would help identify halo excited states in medium to heavy nuclei. However, some problems remain. The conclusions up to now rely heavily on the prediction power of the adiabatic model being used, which might be questioned at sub-Coulomb beam energy. And the price to pay for carrying out sub-Coulomb transfer is a much smaller cross section. Such low cross sections are rather difficult to measure experimentally and thus would limit the type of nuclei to which this method can be applied. It is not clear that such measurement could be done for the low-intensity beams of radioactive nuclei. On the aspect of the halo candidate, a single-particle description might be too simple an approximation. Thus, there is still room for improvement in our method to test the presence of halos in excited states.

Chapter 4

Investigation of ^{9}Li(*d*,*p*) transfer

This chapter focuses on the recent experimental effort regarding the (d,p) transfer to the ^{9}Li+n resonance followed by my theoretical interpretation.

It starts with the motivation of studying the ^{10}Li structure via the ^{9}Li(d,p) transfer in Sec. 4.1. The experimental campaign IS561 was carried out by the joint force of Aarhus and Madrid nuclear physics group [BFF^{+}12] at HIE-ISOLDE, CERN (European Organization for Nuclear Research). A brief overview of the HIE-ISOLDE facility and the detectors used during the measurement is given in Sec. 4.2. Once the recorded data gets sorted, based on Ref. [Jen17], most of the necessary analysis steps including energy calibration, particle identification, simulation, etc. are reproduced and shown. In this work, two main reaction channels (^{9}Li(d,d) elastic scattering and ^{9}Li(d,p) one-neutron transfer) are of special interests. The relevant results will be extracted and discussed in Sec. 4.4.

In Sec. 4.5, the theoretical framework developed in Sec. 3.1.4 for the transfers to the resonance state is employed to illustrate what structural information can be learned from the experimental data. Due to the unsatisfactory statistics obtained during the aforementioned run, other existing data from Refs. [JMB^{+}06, CDNC^{+}17] are reanalyzed to draw our preliminary conclusion.

4.1 Motivation

The main objective of the experimental program IS561 proposed in Ref. [BFF^{+}12] is to apply the ^{9}Li(t,p) transfer in inverse kinematics to measure the Borromean halo nucleus ^{11}Li which brings, as already introduced in Sec. 1.1, abundant and interesting physics on the aspects of magic number, three-body interaction and shell structure far from stability. A proper understanding of the Borromean halo nucleus ^{11}Li requires sufficient knowledge of the interaction between the ^{9}Li core and neutron since it is one of the important interactions involved within the ^{9}Li+2n model. Besides being a crucial ingredient in the description of the ^{11}Li nucleus, investigating the ^{10}Li system itself can shine light on the puzzle about the nuclear continuum dynamics and help reveal whether the shell inversion between the $1s_{1/2}$ and the $0p_{1/2}$ orbitals in the $N = 7$ isotones (which has been confirmed for the ^{11}Be nucleus) also prevails here [CDNC^{+}17]. Due to these peculiar features, ^{10}Li has already received much attention on both the experimental and theoretical sides. Various techniques have been utilized in past experiments to study the ^{10}Li system, such as fragmentation of ^{18}O [KAG^{+}93, TYA^{+}99] and ^{11}Li [BBBM07], stopped pion absorption reactions [CGK^{+}13], one- and multi-nucleon transfer [WWW^{+}75, YBK^{+}94, ZHN^{+}95, BBG^{+}99, JMB^{+}06, CDNC^{+}17] etc. Tremendous theoretical studies [KI93, TZ94, GFJ02, BPVB18, MCGR19] have been made to address the corresponding structural information hidden in the data.

As the first stage (referred to as IS561A for convenience) of the experiment IS561, ^{9}Li(d,p) transfer was performed in the fall of 2016 at HIE-ISOLDE aiming at providing more data on the ^{10}Li unbound system. With a different incident energy (6.72 MeV/A) compared to the previous similar experiments [SKGa^{+}03, JMB^{+}06, CDNC^{+}17], these data could hopefully provide information on the debatable existence of the s-wave virtual state for the ^{10}Li ground state. Moreover, this run offers an excellent test bed to learn the strengths and weaknesses of the detection system and adjust the associated analysis method, which is essential for the success of the more challenging ^{11}Li case.

4.2 Experimental setup

The production of ^{10}Li in the IS561A is realized in inverse kinematics, namely by bombarding a deuterium target with the ^{9}Li beam. Here it is not feasible to utilize the ^{9}Li nucleus as the target since it is unstable with a half-life $T_{1/2}$= 178.3(4) ms [NuD19]. Thanks to the great development made in the technique of Radioactive Ion Beams (RIBs), the Isotope Separation On-Line

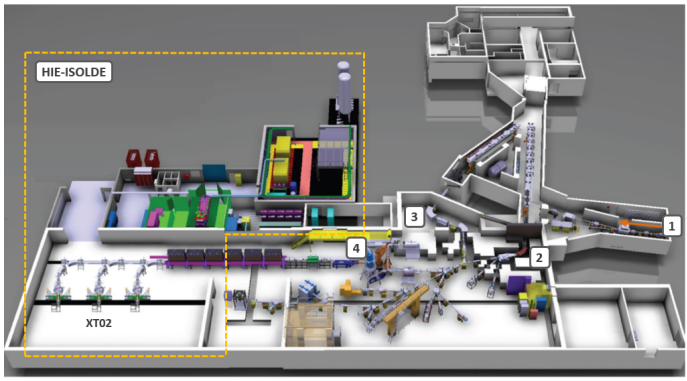

Figure 4.1: Overview of the ISOLDE facility. The components marked with number in the figure are: 1) Injection of the proton beam, 2) GPS, 3) HRS, 4) REX-TRAP and REX-EBIS. The picture is from [Iso19].

(ISOL) method [VD06] is employed at the ISOLDE facility at CERN in order to generate and transport such short-lived radioactive beams. Its principle is to take use of fission, fragmentation and spallation reactions after shooting light particles with high energies on a heavy and thick target, so as to extract the isotope of interest from the target afterwards. In practice at ISOLDE, a proton beam with an energy of 1.4GeV and an average intensity of 2.0 μA delivered by the Proton Synchrotron Booster (PSB) in pulses every 1.2 seconds is used to induce reactions on some hot target, such as a uranium-carbide $^{238}UC_x$. The produced fragments then diffuse through the target material and drift into an ion source where they are ionized by lasers of different wavelengths and transported at an energy of 60 keV to the High Resolution Separator (HRS) or the General Purpose Separator (GPS) for mass separation based on their mass-to-charge ratio A/q as shown in Fig. 4.1. In this experiment, the GPS which has a mass resolving power $m/\Delta m$ of 2400 [Els13] was used. Then this low-energy ion beam is transferred to the post-accelerator REX-ISOLDE (Radioactive beam Experiment at ISOLDE which was installed between 2001 and 2005 [HKB$^+$97]) to get bunched in a Penning trap (REX-TRAP) [SAB$^+$02], charge bred using the REX Electron Beam Ion Source [Wen10] (REX-EBIS) and further accelerated up to 3 MeV/A. With the HIE-ISOLDE (High-Intensity and Energy upgrade of ISOLDE) project, several superconducting modules (three of the five planned ones) were mounted in 2016 [Jen17], which increases the upper limit of the beam energy at ISOLDE up to 7 MeV/A. This energy region meets the desired experimental condition. In our case, the ^{9}Li beam was accelerated to an energy of 6.72 MeV/A. The chosen beam line for carrying out this transfer experiment is the second one called XT02 as shown in Fig. 4.1. At

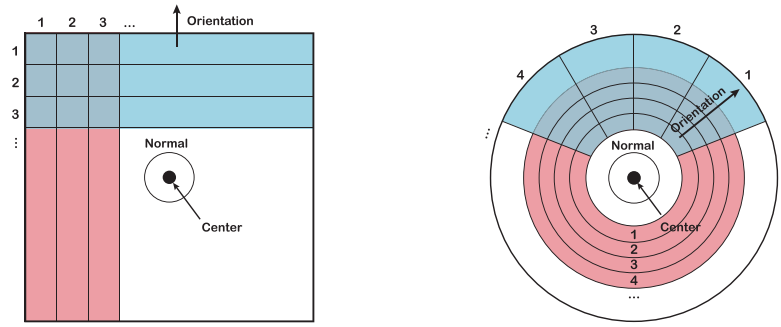

Figure 4.2: Types of DSSDs used in the IS561A experiment. W1 and BB7 have a rectangular shape (as shown on the left side) while S3 is round (right side). Images taken from Ref. [Jen17].

the end of this beam line is the Scattering Experiments Chamber (SEC) [HIE19] inside which the related detection system is installed. For more technical details with respect to different stages of ISOLDE, I refer the interested reader to Refs. [HKS+98, OT99, Bor16, KFPK18].

Detection system

For the detection system in the SEC, its building blocks are two types of silicon detectors: double-sided silicon strip detectors (DSSD) and single-sided unsegmented silicon detectors (also called pad detectors). Whenever a charged particle enters a silicon detector, its energy is gradually transformed into electron-hole pairs. If a bias voltage is applied there, those pairs will start to drift and then be collected with metal contacts to give an output signal. Such signal will then be sampled and stored in a data acquisition system (DAQ), waiting for subsequent analysis. Besides the energy information, the DSSDs can also provide positional information while the unsegmented silicon detectors cannot. This is because of the unique structure that the DSSDs have. In the DSSDs, each side is divided into a number of strips (or rings and spokes for the round case) as shown in Fig. 4.2. The strips on different sides are orthogonal to each other. By recording the same event passing through the strips on both sides, the position where the particle hits the detector can be limited within the range of a certain pixel delimited by the two strips. Further combined with the spatial location of the DSSDs, the kinetic information (direction and energy) of the recorded particle can be measured.

For the IS561A experiment, three basic types of DSSDs are employed to build

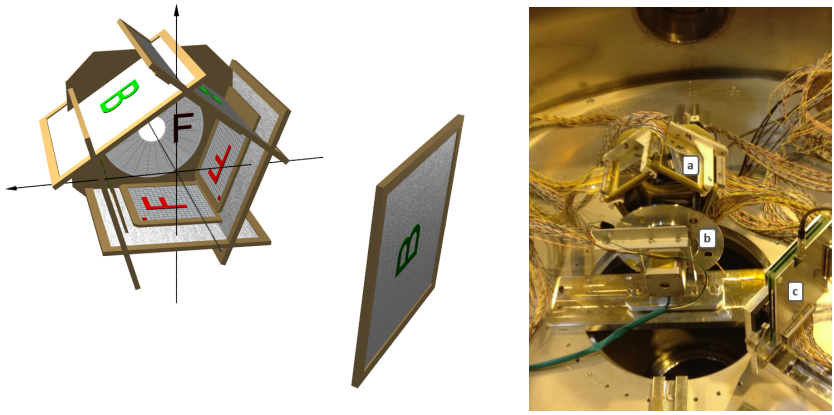

Figure 4.3: CAD drawing (left) using AUSAdraw [AUS19] and actual installation photo (right) of the applied detection array. In the right figure, a target wheel is added at the position (b) while the pentagon array and the backward telescope are placed at (a) and (c), respectively.

the detection array. They are W1 (60 μm thick square detector with 16×16 strips each of width 3 mm), BB7 (60 μm thick square detector with 32×32 strips each of width 1.9 mm) and S3 (1000 μm thick round detector with 24 rings each of width 0.89 mm and 32 spokes) [Jen17]. By putting a thin DSSD in front of a thick silicon pad, a telescope configuration is constructed. This assembly of the detectors is extremely useful for light particle identification since the correlation between the deposited energy in both detectors is rather unique for a certain type of particles. Such technique is also named ΔE-E method which will be discussed more in the next section.

The complete detection setup used in IS561A is shown in Fig. 4.3. Five telescopes (each composed of a DSSD W1 and a pad detector) are placed in a pentagon shape with the S3 attached at the end of the structure. In this measurement, the telescopes are mainly responsible for identifying light ejectiles while the main role of the S3 is to detect the heavy beam-like fragments. Based on the hit pattern of the particles on this symmetric detector, the quality of the beam alignment can be learned. It is also possible to get the beam intensity by collecting the particles from the Rutherford scattering. In addition, combined with the other detectors, one could perform a coincidence analysis to extract reliable reaction events. On the other side of the pentagon structure, another telescope is placed with a BB7 being the front part. The main reason for such placement is in fact that the laboratory backward angles correspond to small c.m. ones where the transfer of interest in this study is favored. Another

Table 4.1: Targets used in the IS561A experiment.

Target	Thickness	Usage
^{197}Au	0.1 μm	Backed by 3.5 μm Mylar to estimate the beam yield
CD_2	8 μm	Main target used for the ^{9}Li+d reaction
CH_2	6 μm	Background measurement for ^{9}Li+p reaction
^{12}C	8.8 μm	Background measurement for ^{9}Li+C reaction

advantage to have detectors within this angular region is to get rid of the interference from the other reaction channels and thus capture a clean transfer spectrum since according to the kinematics only the protons produced by the transfer reaction can reach the laboratory backward angles. A target wheel, which contains several targets as listed in Table 4.1, is mounted in the middle. The support frame for this setup is 3D-printed so that the spatial orientation and relative positions of the detectors are reproduced with good precision.

4.3 Data analysis

The actual duration of the measurement in the IS561A run is about 22.6 hours. After that, a huge amount of raw data was obtained from the detection system. To translate those data into the language of physics, several pre-analysis stages, such as the detector mapping, unpacking, calibration and sorting, are required. Most of these complex and lengthy steps have been done by Jesper Halkjær Jensen, a Ph.D student from the Aarhus university (Denmark). My contribution to this analysis is mainly after the calibration of the acquired spectrum. In

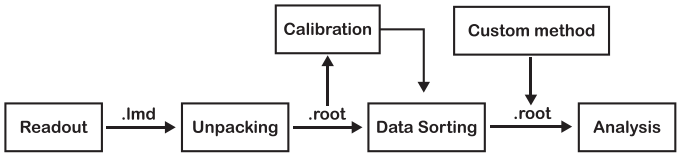

Figure 4.4: Typical routine for the present data analysis based on the AUSAlib pipeline.

order to gain a better understanding of the whole process and make the story complete, the main points of each stage are going to be quickly reviewed based

on Ref. [Jen17]. Fig. 4.4 shows a typical pipeline for this kind of data analysis. The idea behind is to transform the data and its structure to a higher level of abstraction when moving to the next stage.

There is a variety of information written in the raw data, such as the pulse amplitude, timing and so on, regarding the readout signal. At first these stored data have to be unpacked using the program ucesb (unpack & check every single bit) which provides easy access to the various data members and produces ROOT files afterwards. As the name suggests, the ROOT files are dealt with by the ROOT framework which is developed at CERN with rich functionalities for big data processing [ABB+09]. This framework is mainly written in C++ programming language and excels at processing histograms.

Energy calibration

As an intermediate step from the unpacking to the data sorting, energy calibration of the detectors is essential to bridge the gap between digital signal to real energy. To do that, an α source with a well known spectrum is used, typically the ^{148}Gd source and a combined one of ^{239}Pu, ^{241}Am and ^{244}Cm. By placing the source in the target position, a spectrum similar to the one on the left side of Fig. 4.5 is acquired with its x-axis being the number of the raw channels. The channel of the peak position representing the deposited particle

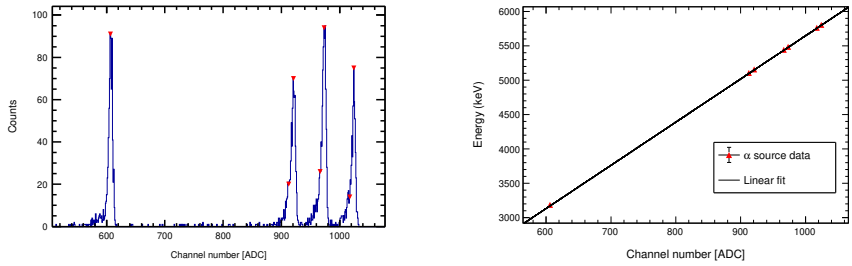

Figure 4.5: An example of the α energy spectra (left side) as measured in one DSSD with the peak position pointed by red triangles and the linear fit (right side) performed using the α source data.

energy is determined by fitting each peak with Gaussian functions. Some of the α sources could deliver more than one energy. Such sub-component might not always be directly visible in the spectrum due to the limited resolution of each strip in the detectors (typically in the order of 15-30 keV for the FWHM). Nevertheless, these unresolved peaks are also taken into account when doing the fitting. Before depositing its energy in the active region of the silicon detector, the α particles have to go through a dead layer on the surface of the detector

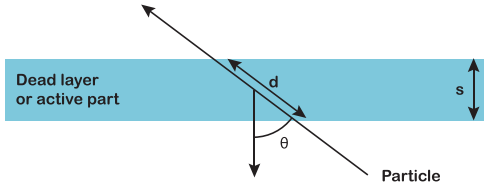

Figure 4.6: Illustration of the situation when the charged particle hits the detector with a certain angle θ and passes through an effective length d.

(about 50 nm thick for the W1 type, 900 nm thick for the BB7 type and 507 nm thick for the S3 one). The actual distance that the particle has penetrated through the dead layer depends on the incoming angle. The correction is made by $d = s/\cos\theta$ as described in Fig. 4.6 where d represents the effective length, s gives the nominal thickness of the dead layer and θ is the angle between the incident particle and the normal to the detector. Since this kind of layer is usually rather thin, the energy loss can be approximated as being proportional to the travelling distance with a coefficient dE/dx giving the energy lost per unit distance. The relationship can be denoted as

$$E_{\text{loss}} = \frac{dE}{dx} d = \frac{dE}{dx} \frac{s}{\cos\theta}, \tag{4.1}$$

in which dE/dx depends on the kinetic energy and type of the incident particle and the material of the dead layer. The value of dE/dx can be obtained from the SRIM program [ZZB10] which offers tabulated ranges of ions carrying different energies in various matters. Likewise, this principle is applicable for particles passing through active area in silicon detector. To implement this correction in the calibration, an average energy loss for each strip is extracted by summing its value in each pixel weighted by the corresponding solid angle Ω_{pixel} relative to that of the strip Ω_{strip}. The formula to calculate the corrected energy E_c from the reference energy of an α particle E_α has the format of [Jen17]

$$E_c = E_\alpha - \sum_{\text{pixels}} E_{\text{loss}} \frac{\Omega_{\text{pixel}}}{\Omega_{\text{strip}}}. \tag{4.2}$$

As for the case of the pad detector, such weighting method does not work since the pad is not segmented. Instead the energy loss is included considering the α particles hitting the center position on the pad. There the nominal thickness is about 2000nm. With these pieces of information, the next step is to perform the conversion between the corrected energy $(E_c)_i$ from a specific α energy and the mean value of the corresponding peak in channel ch_i through a linear fit

$$(E_c)_i = a \cdot ch_i + b, \tag{4.3}$$

where the index i means the different energies brought by the α particles. In practice, the whole process was accomplished with the calibration tool in AUSAlib (Aarhus subatomic library) [AUS19] which is built on top of ROOT and aims at offering a common functionality to ease the sophisticated analysis of the reaction data. However, a problem encountered in this stage is the incomplete mapping between the detector segments and analog-to-digital converter (ADC) channels due to the fact that the connectors for the chamber were newly designed. This issue has been later solved by Jensen using the α distribution in the calibration files and the coincidence events from the reactions [Jen17]. An example of the linear fit for one strip in one DSSD detector is displayed on the right side of Fig. 4.5.

Data sorting

After that, the calibrated data has to be sorted to select the physical events in the DSSDs. A particle will deposit roughly the same amount of energy in both sides of a DSSD when passing through the detector. Based on this simple principle, several cases are abandoned as non-physical events: a) a hit is observed only in one side of the DSSD; b) there exists a significant difference between the energy deposited in the front side of the detector and that in the back side. A particular example for the second situation is the charge sharing effect between strips [MPS+02]. Once a charged particle hits a strip, the strips next to it could possibly be activated to start counting. To get rid of all these

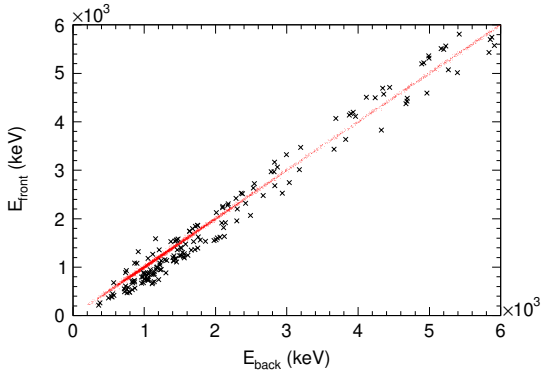

Figure 4.7: Sorting procedure based on the energy deposited in the front and back sides of a DSSD. The data points represented by black cross are excluded due to the matching gate. And only the red dots are left as physical events.

interfering events, the data from both sides of the DSSD have to be matched within a threshold Δ, namely $|E_{\text{front}} - E_{\text{back}}| < \Delta$. The size of the threshold is

up to the resolution of the setup. In this case, 100 keV was chosen to perform the matching. Fig. 4.7 explains how the data sorting looks like in a 2D spectrum. In addition, it is worth mentioning that the main data structure chosen for the further analysis is the TTree-class from ROOT which presents event by event the experimental data via branches. The associated branches can be built for different physical quantities, like particle energy, time stamp, hit position, etc. Thanks to this clear classification and the member functions offered by TTree, the subsequent analysis becomes straightforward and convenient.

Particle identification

On the basis of the energy calibration and the layout of the detectors, it is now possible to distinguish between different kinds of particles using the ΔE-E method. As introduced before, this method requires a thin transmission detector placed in front of a relatively thick stopping one. Thus, the particle is able to penetrate the front detector, depositing a fraction of its energy (ΔE) there by ionization and then be completely stopped in the back detector with an energy E detected. The correlation between those two energies recorded by the front and back detectors can be estimated by the Bethe formula [Bic88]. It has a simplified approximate form of $E\Delta E \propto MZ^2$ (mass number M and charge number Z) for a certain combination of detectors when $\Delta E \ll E$, and hence is unique for a specific particle type. An intuitive way to discriminate the particle type is to draw a 2D plot of ΔE versus E. Again the angular dependence of the energy loss described by Eq. (4.1) needs to be taken into account here. This is because the collected energy by the front detector would vary a lot if the particle arrives with different angles, resulting in a wider band in the 2D plot (see Fig. 4.8(a)) and a worse resolution for identification. To correct for this effect, the original energies $\Delta E = (E_{\mathrm{front}}+E_{\mathrm{back}})/2$ from DSSDs are transformed by

$$\Delta E' = \frac{dE}{dx} s = \Delta E \cdot \cos\theta \tag{4.4}$$

to values $\Delta E'$ which are independent of the incident directions by restoring the situation that all the particles enter the detector orthogonally. To ensure that the total energy is conserved within this correction, the remaining energy is assumed to be absorbed in the back detector, adding an extra term to its measured energy E as

$$E' = E + \Delta E\ (1 - \cos\theta). \tag{4.5}$$

As shown in Fig. 4.8(b) a much tighter ΔE-E spectrum is obtained so that different types of the particles can be better resolved. One can now clearly see the banana-shaped bands for several kinds of particles. The three lower components correspond to three hydrogen isotopes: protons, deuterons and

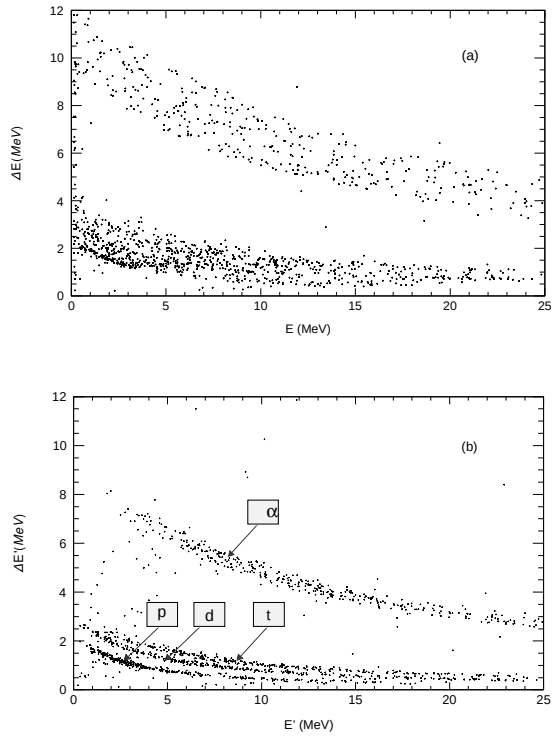

Figure 4.8: ΔE-E plot from one of the telescopes in the forward direction. The subplot (a) does not take into account the angular correction while the subplot (b) does.

tritons while the band of α particles lies well above them. All these residues are produced by the reaction between the ^{9}Li beam and the CD_2 target.

Beam properties

Another important factor to analyze is the quality of the beam. Besides the reported beam energy of 6.72 MeV/A, there are basically two more aspects that need to be determined.

At the first place, it is the geometrical information of the beam, such as its direction, size, etc. In an ideal physics picture, the section of the beam employed in an experiment would be point-like and impinge at the center of the target. Instead, in the real life the structure of the actual beam can be rather complex. It can be broad, angled, shifted or sometimes diffused. Even after a cautious

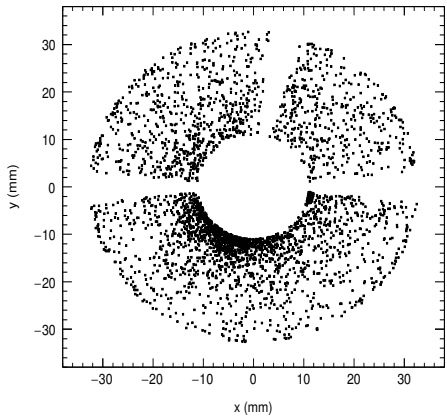

Figure 4.9: Hit pattern of the forward S3 detector during the run with the ^{9}Li beam impinging on the gold target.

collimation and adjustment of the steup, some of those effects still cannot be entirely avoided, which will propagate to the data analysis and introduce some bias later when reconstructing the particle energies and momenta. During the run, due to the difficulties encountered with respect to the beam alignment, the beam was slightly steered to find the optimal position. There have been two periods with two different beam settings. The considered Rutherford scattering between ^{9}Li beam and ^{197}Au target is performed after the first beam tuning. The hit pattern of the forward S3 detector is shown in Fig. 4.9. It can be found that the beam was pointing a bit to the bottom left. One of the common methods to deduce the beam direction [JFB+13] is to use coincident events collected during the measurement. Unfortunately, due to the lack of adequate statistics here, it remains hard to derive the exact beam position by fitting simulations to the data. Furthermore, to make a quick estimation in this case, it is not unrealistic to make use of the simple model considering the fact that the distance from the target to the detector is much larger than the size of the detection area.

The second major feature is the beam intensity which can be estimated using the Rutherford scattering. Having the ^{9}Li beam on a gold target, the angular distribution of the scattered ^{9}Li particles collected in the S3 detector follows the well known Rutherford cross section (see Eq. (2.18)). Its formula can be rewritten in the laboratory system as

$$\frac{d\sigma\left(\theta, E_1\right)}{d\Omega} = \left(\frac{Z_1 Z_2 e^2}{4\pi\epsilon_0 E_1}\right)^2 \frac{(\cos\theta + a)^2}{4a\sin^4\theta} \tag{4.6}$$

with the parameter a equals to $\sqrt{1-\left(\frac{M_1}{M_2}\sin\theta\right)^2}$. The subscripts 1 and 2 are to indicate incident particle and target, respectively. And E_1 thus is the kinetic energy of the beam in the laboratory. Starting from Eq. (2.6), the beam intensity can be deduced from

$$I = \frac{dN}{n\ dt\ \int_{\Omega_{\text{setup}}} \frac{d\sigma(\theta,E_1)}{d\Omega} d\Omega} \tag{4.7}$$

where the Ω_{setup} represents the solid angle covered by the present detector over which the differential Rutherford cross section has to be integrated. Blocked by part of the support structure, the detectable area in the S3 detector is up to the 24^{th} ring if one starts counting from the inner region. Note there is a hole in the center with a radius of 11.0mm. And a gap of 0.1mm exists between two neighbouring rings. The overall integration interval for the lab θ in Ω_{setup} is from 8.15° to 24.28°. The corresponding integrated Rutherford cross section is then 39.9b. In this measurement lasting for 33 minutes, a total count of 298 is recorded after the sorting work. In this energy range, the intrinsic efficiency of the detector is almost 100%. Applying the Laser-on and -off technique on the beam line, it is learned that the contamination in the beam (mainly from $^{12}C^{4+}$) is negligible during this experimental run. Due to the low counting rate, the dead time of the electronics can also be neglected here. Taking into account the omitted area as displayed in Fig. 4.9, finally the beam intensity is estimated to be $7.29(42)\times10^3$ pps, which is consistent with the order of magnitude ($\sim 10^4$ pps) compared to the value received at REX-EBIS. This result could be rather close to the final setting of the beam but will never be the same due to the second beam tuning. For sure a higher statistics could guarantee a better determination of the beam direction. Even with this small amount of data, a heuristic method to resolve the beam position is to rely on the kinematics between the coincidence events from for instance an elastic channel [Jen17], which requires precise knowledge on geometry and energy calibrations of the setup.

Kinematics

The kinematics can be used not only to derive the beam property, but also to reconstruct the excitation energies of the interesting particle and serve as a cross-check for the correction made through the analysis. Considering a two-particle reaction as $A(a,b)B^*$, B represents the product of interest while b is the other ejectile after the interaction between the beam a and the stationary target A. By controlling the experimental conditions, none of the beam, target and ejectile is supposed to be excited but the particle B. The corresponding excitation energy E^* can be derived from the conservation of energy and linear

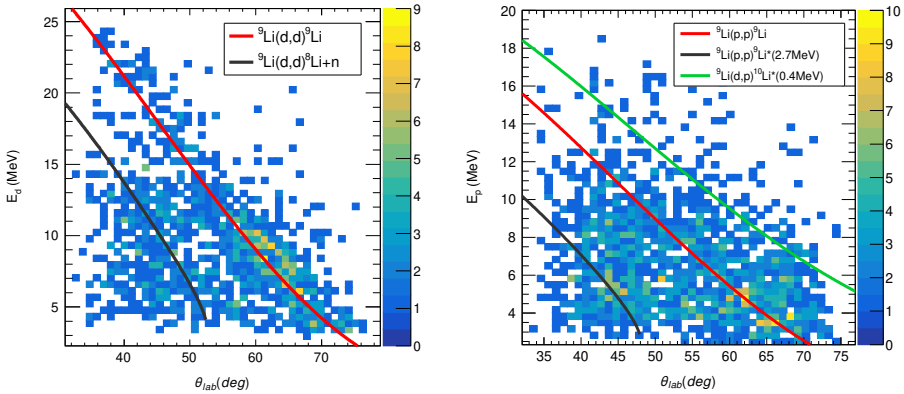

Figure 4.10: Kinetic energy *vs.* lab scattering angle for two identified particles, deuterons (left side) and protons (right side). The theoretical curves are drawn for reference.

momentum,

$$E^* = T_A - T_b - \frac{(\mathbf{p}_A - \mathbf{p}_b)^2}{2m_B} + Q, \tag{4.8}$$

where Q is the ground-state Q-value, T_i, $\mathbf{p}_i$ and m_i are the kinetic energy, momentum and mass of particle i, respectively. With a solid target in our case, the kinetic energy of the ^{9}Li beam has to be corrected with an average value approach to account for the energy loss within the target [KGOY07]. Thus, the effective beam energy is obtained at the half thickness of the target. Regarding the kinetic energy of the light ejectile, it consists of two parts: one measured by a DSSD and the other by the coupled pad detector. Three dead layers (two from both surfaces of the DSSD and one on the front side of the pad detector) are present on the way until the particle gets finally stopped. Let us first derive the energy of the ejectile before entering the pad detector. Since the length of the actual traversed dead layer d can be obtained after the angular correction and the deposited energy E_{pad} is known from the calibration, the particle energy E'_{pad} before hitting the pad detector can be determined using the program SRIM. Using an interpolation method, the range $R(E)$ can be expressed as a continuous function of energy. Based on this, the formula to find the energy E'_{pad} is written as

$$E'_{\mathrm{pad}} = R^{-1}(R(E'_{\mathrm{pad}})) = R^{-1}(R(E_{\mathrm{pad}}) + d), \tag{4.9}$$

in which R^{-1} is the inverted range function [Ref16]. Repeating the similar step twice and adding the energy detected within the DSSD in between, the initial

energy of the ejectile right before entering the detector is obtained. The average beam direction has been deduced by Jensen from the counts in the pentagon array. By fitting the kinematic curves to the data points in the pentagon using the χ^2 method, a reasonable direction under which the beam enters can be extracted. A consistency check has been performed on this point using the Monte Carlo simulation within the toolkit simX [Sim19]. The resolved beam direction (θ, ϕ) is (7.3°, 73.1°) in the spherical coordinate system when the beam line is aligned along the z-axis. Including all the above corrections in the analysis, the plots of kinetic energy E versus the laboratory angle θ for two main ejectiles (deuterons and protons selected from the ΔE-E plot) are displayed in Fig. 4.10 together with several calculated curves. No coincidence measurement between the reaction products is performed in this work for either the (d,d) or the (d,p) channel due to the very limited angular coverage of the detector S3. The interesting events are derived from the light ejectile (deuteron or proton) identified in the pentagon array. In the figure, the elastic component dominates and can be guessed. However, regarding the other channels, we have the feeling that the statistics is not impressive. In particular, no recognizable structure is found for the (d,p) channel of interest. This issue will propagate to the subsequently extracted excitation spectrum.

Excitation spectrum

The excitation energies of the interesting nuclei can be reconstructed using Eq. (4.8) after subtracting the background. Having a ^{9}Li beam impinging on a CD_2 target, the background comes mostly from its interactions with protons (due to the mixing of CH_x) and carbon nuclei. This motivates multiple runs with the targets outlined in Table 4.1. Unfortunately, these measurements have not been successful, giving very few counts that can be used for the background subtraction. In Fig. 4.11, the excitation spectrum of ^{9}Li and the one extracted from the identified protons are presented. In the channel of ^{9}Li, the major peak around 0 MeV belongs to the elastic scattering while the other excitations remain indistinct. By fitting a Gaussian function to the elastic peak, the resolution of the setup in the experiment IS561A can be estimated. The full width at half maximum (FWHM) is measured to be 1108(39) keV, which is almost twice the value (551(4) keV) that was obtained by Jensen in another ^{9}Li experiment [Jen17] with a simpler silicon array. On the one hand, this could be caused by the complexity of the setup, which introduces more uncertainties during the correction. On the other hand, the possible energy and spatial distribution of the beam could also affect significantly the extracted resolution if the related information was not correctly reconstructed. For the ^{10}Li case, according to previous experiments done in Refs. [JMB$^+$06, CDNC$^+$17], a broad peak is expected around the excitation energy of 0.4 MeV where the p-wave component should be dominant. However in our analysis, no clear peak was

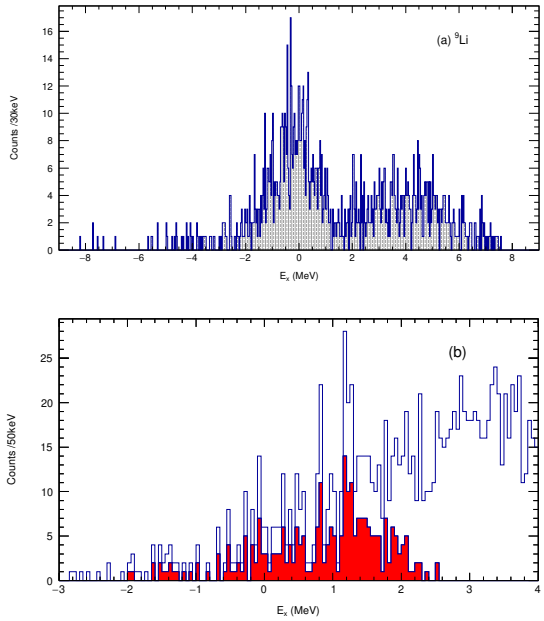

Figure 4.11: Excitation energy spectrum for ^{9}Li in subplot (a). The subplot (b) shows the total excitation spectrum of ^{10}Li and the background. The red zone inside is obtained by projecting the data on the kinematic curve. In this way, it is supposed to contain most of the ^{10}Li events.

observed around that energy region probably due to the low counting rates. Moreover, due to the lack of background measurements, it is not possible for a further analysis of the ^{10}Li channel unless more troubleshooting tests were performed.

4.4 Results and discussion

With the excitation spectrum, it is possible to evaluate the differential cross sections for different channels. Then as already mentioned in Sec. 1.2, the angular distribution of the cross sections can be compared to theoretical predictions in order to extract the transferred angular momentum of the residues and hence infer the populated states in the nucleus of interest.

Most of the ingredients needed as described in Eq. (2.6) are now available.

The purity of the CD_2 target is estimated from Jensen's analysis of another experiment [Jen17]. In addition to that, one more improvement regarding the efficiency of the detector array is employed to calculate the final results since its structure is neither trivial nor symmetric to be calculated by hand. Monte Carlo simulation is applied using simX to account for the problem. The principle behind is to generate N_r^{sim} ($= 10^6$ in practice) events distributed in 4π sr under the same reaction mechanism and a similar resolution and count then the numbers $N_{\mathrm{det}}^{\mathrm{sim}}$ being registered in the detectors. In this way, Eq. (2.6) is transformed to

$$\frac{d\sigma}{d\Omega} = \frac{N_{\mathrm{det}}^{\mathrm{exp}}}{I\ n\ t} \frac{N_r^{\mathrm{sim}}}{N_{\mathrm{det}}^{\mathrm{sim}}}, \tag{4.10}$$

where $N_{\mathrm{det}}^{\mathrm{exp}}$ is the real recorded counts in the experiment which can be derived from the excitation spectrum. And t is the actual duration of the measurement. Another thing we have to be aware of is that most of the previous work is done in the laboratory framework. Considering the convenience for later comparison between experimental and theoretical values, it is necessary to transform the information of angles and energies event by event from the laboratory system to the center-of-mass system. This operation also eliminates the confusion caused by the inverse kinematics. The general method to realize this process is to use the Lorentz transformation within the TLorentzVector class provided by ROOT.

By gating on the ground state of ^{9}Li in the excitation spectrum, the differential cross section for the ^{9}Li(d,d) elastic scattering can be obtained. For theoretical interests, it is helpful to calculate the ratio between the cross sections of the elastic channel and those from the corresponding Rutherford scattering, through which the Coulomb interaction is offset and the nuclear interaction gets highlighted. Thus, in Fig. 4.12, the results of the elastic scattering cross sections relative to the Rutherford ones for ^{9}Li are shown. A theoretical interpretation of these experimental data is performed based on minor modifications to the Daehnick global optical model potential [DCV80] to achieve the best fit using sfresco [Tho06]. The adjusted parameters of the optical model potential are listed in Table 4.2. In general the position of the peak is well fitted with some deviation when reproducing its exact width. In a classical method, the elastic scattering channel always has to be studied at the first stage to account for the effective contribution from different channels. This step is expected to give a better interpretation of, for instance, the transfer data.

In principle, a similar analysis procedure as above can be applied to the ^{10}Li excitation spectrum to extract the (d,p) transfer cross sections. However, there are several problems that have to be solved first. Since the background measurement does not provide enough information to exclude the unrelated events, one way to compensate for that is to rely heavily on the simulation which

Table 4.2: Optical model potential parameters for the ^{9}Li(d,d) elastic scattering at a beam energy of 6.72 MeV/A. The symbols used here are based on Eq. (2.27).

Parameter	V_v (MeV)	r_v (fm)	a_v (fm)	W_v (MeV)	r_w (fm)	a_w (fm)
	92.74	1.15	0.80	0.1	1.33	0.66
Parameter	W_s (MeV)	r_s (fm)	a_s (fm)	V_{so} (MeV)	r_{so} (fm)	a_{so} (fm)
	9.18	1.33	0.66	3.79	1.40	0.59

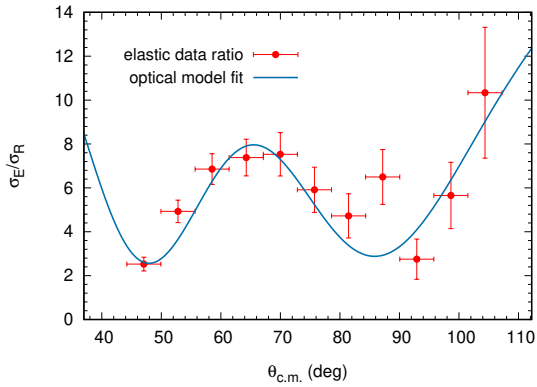

Figure 4.12: Elastic scattering cross section of ^{9}Li(d,d) relative to the corresponding Rutherford cross section at an incident energy of 6.72 MeV per nucleon.

requires a precise knowledge of all the ingredients involved in the experiment, such as beam, target, detector, etc. Even though such simulation is carefully performed, the inevitable fact is the low counting rate according to the rough estimation in Fig. 4.11(b) where no clear peak is observed around the energy region of interest. This directly affects how the energy cut will be made in the excitation spectrum. Usually an alternative option is to focus on the events only detected at backward angles since in this region such transfer is favored and the interference from other channels (like elastic scattering between ^{9}Li and proton) is naturally ruled out due to the kinematics. However the data at backward angles is not really used in our analysis. This is because of the small spatial coverage and insufficient statistics for particle identification. Based on the lessons learned from this experiment, the second and third parts of the experiment IS561 were carried out in 2017 and 2018, in which better results

were expected with an improved setup and a better beam situation [Elo19].

4.5 Theoretical approach

Unfortunately at this stage, no convincing data has been extracted from the IS561A experiment for the ^{9}Li(d,p) channel. However it is still possible to contribute on the theoretical side since several other sets of data are available [SKGa^{+}03, JMB^{+}06, CDNC^{+}17]. In Sec. 3.1.4, I have extended the ADWA framework to apply it in the case of transfer to a resonance state. The wave function of the final resonance state is obtained by a bin discretization of the continuum. To check the universal applicability of this model, the ^{9}Li(d,p) transfer would be a good testing bed since the produced ^{10}Li is an unbound system. I consider the data from two experiments. One was performed at REX-ISOLDE with the ^{9}Li beam energy of 2.4 MeV/A [JMB^{+}06]. The excitation energy spectrum of ^{10}Li is measured up to about 1 MeV in the c.m. angles between 100° and 140°. Being similar to the problem in our measurement, the crucial detection region at backward laboratory angles is excluded in the analysis of these data, because the proton energy in this area is too small to be detectable. Despite this, the experimental results, obtained from the excitation spectrum with an observed resolution (FWHM) of $\sim$ 300 keV, are still reliable to help draw useful conclusion with respect to the role of s-wave and p-wave structures in the ^{10}Li system as in Refs. [JMB^{+}06, MCGR19]. The other was performed with an incident energy of 11.15 MeV/A at TRIUMF [CDNC^{+}17]. In this campaign, Cavallaro *et al.* managed to perform the coincidence measurement between the recoiling protons detected by the LEDA (Louvain-Edinburgh detector array) at backward lab angles from 127° to 152° and the ^{9}Li fragments produced from the breakup of ^{10}Li. This achievement offers the possibility to explore both the transfer reaction and the ^{10}Li system in different experimental conditions.

To perform the associated transfer calculation, several ingredients are needed in the reaction formalism. One of the key inputs is the ^{10}Li structure model. Since in all the cases studied so far in this work the spin of the core is nil and the emphasis of the present study is to test the validity of the method rather than studying the structural information, the potential of Woods-Saxon nature noted as P3 developed in Refs. [CGRM17, GRCM17] is considered. Such potential does not depend explicitly on the spin of the core and only contains the central and spin-orbit terms. The detailed information is clearly explained by Eq. (5) in Ref. [MCGR19]. Centering the $p_{1/2}$ resonance at $E_x = 0.45$ MeV and the virtual $s_{1/2}$ state at $E_x = 0.05$ MeV with an energy width of 1 MeV for both cases, the wave function of this ^{10}Li resonance state can be generated using Eq. (3.4) with a lower bound of 0 MeV and an upper bound of 1 MeV. In addition, the

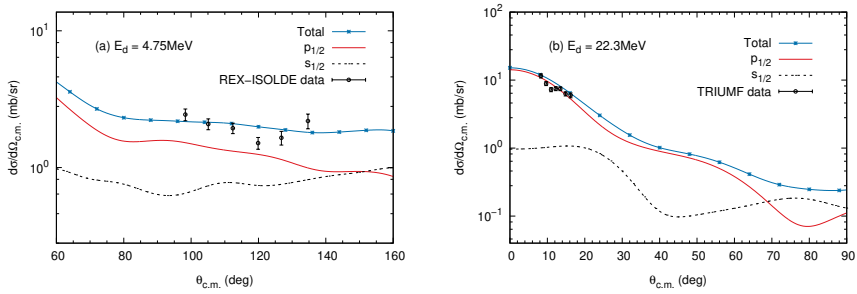

Figure 4.13: Angular distribution of the cross sections for the ^{9}Li(d,p) transfer calculated at $E_d = 4.75$ MeV (left side) and 22.3 MeV (right side) both within the integral region of $E_x < 1$ MeV. The corresponding experimental results are also listed for comparison.

deuteron potential from Johnson and Tandy [JT74] is adopted while the Reid soft-core potential [Rei68] is used to compute the deuteron bound state, and the nucleon-nucleus optical potential is constructed based on the CH89 global potential. Feeding those parameters into the full transfer calculations, the results for two cases at $E_d = 4.75$ MeV and 22.3 MeV are presented in Fig. 4.13.

As a simple model to simulate these transfer cases, the chosen method proves to be rather effective. A similar conclusion as already illustrated in Ref. [MCGR19] where a CDCC-BA model (see Sec. 2.4.4) has been considered can be drawn, i.e., the s-wave state of ^{10}Li has an important role for the transfer at lower energy while its influence becomes negligible for the higher energy experiment. This could be due to two factors according to our previous study. One is the incident energy since a more peripheral transfer is expected when the incident energy decreases resulting in an enhanced contribution of the s wave. The other is the different angular range covered during the two measurements. Usually at very forward c.m. angles a peripheral transfer would exist. However, from the tests performed for the ^{10}Be(d,p) case in Sec. 3.1.2, at the incident energy of ∼11 MeV/A (the TRIUMF experiment) a peripheral transfer considering the ^{9}Li(d,p) reaction should be rarely observed. To verify these two points, it is worth to have a transfer at an incident energy (like 6.72 MeV/A) between the two experiments and focus either on the forward angular range or the backward part, such as IS561A which would in principle give an idea whether the contribution from s wave at backward angles is decreasing or not when the beam energy increases. Moreover, we should admit that the theoretical model used here is far from optimal, in which the spin of ^{9}Li is neglected so that no splitting in the final state of ^{10}Li is considered. In addition, it only simulates a

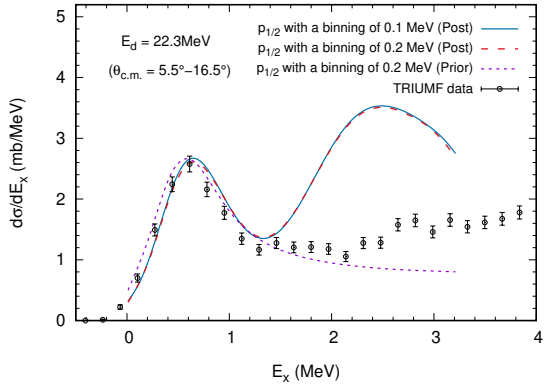

Figure 4.14: Excitation energy spectrum for the ^{9}Li(d,p) transfer reaction at E_d = 22.3 MeV leading to the ^{10}Li system. The theoretical calculations in the post (ADWA using two different binnings) and prior (DWBA) forms are compared to the TRIUMF data.

single-step process and does not include any coupling within the continuum.

The ADWA method is further applied to describe the excitation spectrum as shown in Fig. 4.14. The cross section is integrated over the c.m. angular range from 5.5° to 16.5° covered in the TRIUMF experiment. Similar to the work done in Ref. [MCGR19], the results are convoluted with a Gaussian of FWHM of 0.2 MeV which corresponds to the experimental resolution. With the ADWA model which reduces the couplings in the continuum, it is found that the results of two different binnings (with bin widths of 0.1 and 0.2 MeV) agree with each other. The resonance peak is well reproduced with the sole p wave state, which confirms the previous conclusion obtained from the angular distribution. In the CDCC-BA calculations of Moro *et al.* on these observables [MCGR19], they have obtained a better agreement in the non-resonant region, but a similar agreement in the resonance energy range as ours. This indicates that the ADWA can still be valid and used in the resonance region.

It has been pointed out by Moro that the second bump observed in the non-resonant region is a by-product of the inadequacy of the post form described by Eq. (2.47) for transfers to unbound states since there is no natural cut-off in the transition operator for the final unbound wave function (^{9}Li-n system). In our case, the unbound wave function is represented by a bin function, which would indicate that the transfer calculation can be sensitive to the bin function at large distances. Consequently, the integral involved in the evaluation of

the transition amplitude may not converge or converge slowly with the radial extension of the bin. A convenient way to cure the aforementioned problems is to use the prior form in Eq. (2.48) where the transition operator containing the short-range interaction $V_{n^9\mathrm{Li}}$ will cut the contribution from asymptotic part of the bin function. However, as claimed before in Sec. 2.4.3, adiabatic deuteron potential can no longer be used in this form. Instead, a DWBA calculation in the prior form for such transfer is performed with its results displayed by purple dashed line in Fig. 4.14. The corresponding choice of the parametrization for the potential is mostly the same as in the previous ADWA calculation, apart from the potential of the entrance channel which has been replaced by the Daehnick global potential [DCV80]. As expected, the second bump is eliminated using the prior form.

Chapter 5

Conclusion and outlook

The core topic of this work is to improve the reliability of the nuclear-structure observables inferred from transfer reactions. Through a theoretical analysis of the (d,p) transfer with the produced one-neutron halo nucleus described at leading order of Halo EFT, it has been demonstrated that measuring transfer reactions at low beam energies and forward angles for transfer reaction can ensure the peripherality of the reaction and thus is the best way to obtain a reliable ANC of the interesting nucleus from experimental data. In particular, a systematic re-analysis of the experimental data from Schmitt *et al.*'s work [SJB$^+$12] regarding the ^{10}Be(d,p)^{11}Be transfer reaction at E_d = 21.4, 18, 15 and 12 MeV was performed to extract information on the halo structure of ^{11}Be. Following the concept of Halo EFT, the ^{10}Be-n interaction inside the ^{11}Be nucleus is simulated by Gaussian potentials of different widths to reproduce the single neutron separation energy. These descriptions enable us to obtain very different ^{10}Be-n wave functions but which all exhibit the same asymptotic decay. Based on that, the sensitivity of the transfer cross sections to the short-range physics of the ^{10}Be-n wave function for both bound states in ^{11}Be can be carefully studied. The specific experimental conditions determined for a peripheral (d,p) transfer to the $1s_{1/2}$ ground state of ^{11}Be are $E_d \leqslant 15$ MeV and $\theta < 20°$. Considering the transfer to the first excited state of ^{11}Be, it requires more stringent experimental conditions ($E_d < 10$ MeV) to become peripheral probably because of the centrifugal barrier arising in a p-wave state. By comparison between our theoretical calculations and the experimental data selected in those peripheral regions, the ANC values we obtained are (0.785 ± 0.030) fm$^{-1/2}$ for the ground state and (0.135 ± 0.005) fm$^{-1/2}$ for the first excited state. Incidentally, both results are in excellent agreement with the values predicted by *ab initio* calculations (0.786 fm$^{-1/2}$ for the ground state

and 0.129 $\text{fm}^{-1/2}$ for the excited state) [CNR+16].

As a cross check to the peripheral condition, the supersymmetry (SuSy) method is employed to check how different regions of the wave function contribute to the reaction calculations. With this method, the SuSy partner of the original wave function can be generated, which shares the same asymptotic behavior but exhibits a very different internal part. Feeding those wave functions into the transfer calculations, the results confirm the above findings with respect to the peripherality of the ^{10}Be(d,p) transfer.

This method has then been extended to study another one-neutron halo nucleus: ^{15}C involved in the ^{14}C(d,p) transfer. Fortunately, for this system precise data exist at a low beam energy with enough data points at forward angles to apply our new method. The ANC value obtained in this way are (1.26 ± 0.02) $\text{fm}^{-1/2}$ for the ground state and (0.056 ± 0.001) $\text{fm}^{-1/2}$ for the excited state of ^{15}C. The results are in good agreement with most of the values cited in other studies [TAC+02, TBD+06, SN08, MBG+11, MMT+14], and the slight differences with them can be understood by systematic biases of these methods. Again, the ANC we estimate for the ^{15}C ground state matches perfectly the one predicted in the *ab initio* calculation by Navrátil *et al.* ($C_{1/2^+} = 1.282$ $\text{fm}^{-1/2}$) [Nav18]. Therefore, the present work provides an independent way to test the value obtained in the NCSMC calculation. Relying on the inferred ANC value, it enables us to fit an effective ^{14}C-n interaction at NLO in Halo EFT, which has been used in other reaction calculations, such as Coulomb breakup and radiative capture [MYC19].

These very encouraging outcomes achieved with the adiabatic model led us to perform a similar analysis of transfers to resonant states. The ^{11}Be halo nucleus indeed exhibits a rather narrow resonance above the ^{10}Be-n threshold, which is often described by a neutron resonance in the $d_{5/2}$ partial wave. The goal here is to clarify if the role of the width of the resonance is similar to what has been observed for the ANC in bound states. For this, a series of wave functions has been built from simple Gaussian potentials, which reproduce the resonance at the correct resonant energy (1.28 MeV) but with different energy widths. Difficulties have been encountered when confronting our calculation results to the existing data. On the one hand, the peripheral conditions become less clear due to the increased transfer angular momentum. On the other hand, the reaction model might be too simple to include all the necessary mechanism. A proper simulation of the transfer to the continuum may need a better description of the deuteron breakup. This remains an open question and requires further efforts on both experimental and theoretical aspects.

Another ambitious object we have pursued in collaboration with Prof. Obertelli is the potential use of transfer reactions to study halo structures in the

excitation spectrum of medium to heavy nuclei. Our systematic tests with the hypothetical case of ^{95}Sr show that applying low-energy reactions, i.e., below the Coulomb barrier, gives access to the tail of the wave function. If the associated experimental conditions, such as Q-value, nuclear spin and incident energy, are well controlled, this kind of transfer would serve as a good tool to probe the possible existence of a halo in excited states close to the one-neutron separation threshold. Unfortunately, an inevitable problem of considering the sub-Coulomb transfer in actual application is the relatively small cross section caused by the incident energy and Q-value, which poses a challenge for existing experimental techniques.

In addition to the theoretical work, part of the data analysis has been performed regarding the IS561A experiment to study the ^{9}Li-n resonance via the (d,p) transfer. With the help of Jensen, the elastic-scattering channel of ^{9}Li(d,d) at $E_d = 13.44$ MeV has been obtained and agrees well with theoretical calculations. However, because of low statistics and insufficient background measurements, the extraction of the (d,p) channel remains difficult. Nevertheless, efforts have been made to build the bridge between the capability of the theoretical model and available data of the ^{9}Li(d,p) transfer [JMB^{+}06, CDNC^{+}17]. The outcome suggests that the method we use is a fast and efficient option to simulate the resonance during the transfer. For the non-resonant part, choosing the prior form of the transition matrix instead of the post one would eliminate the weird bump observed there. Besides, in this case couplings within the continuum also need to be properly accounted for, and hence a more complete model of the reaction is required, such as CDCC-BA [Raw74] or Faddeev method [Fad61].

Outlook

As for the test of determining the peripheral conditions, so far we have used only a single Gaussian potential to simulate the final state of the produced nucleus. To make it more realistic, a more complex interaction model, like adding a repulsive core in addition to a mean field or coupling with the core excitation as done in Ref. [GRMGCT15], could be interesting to consider. Instead of a data-based analysis, as already introduced in Ref. [CPH18], the input from an *ab initio* calculation can also be taken to build an effective description of the interesting nucleus under the Halo EFT framework. Furthermore, going beyond NLO in the Halo EFT would provide a way to explore the role of the short-range physics in the internal part of the related wave function.

Regarding the reaction model, the ADWA model has important advantages in calculating the (d,p) transfer. But what remains unclear is the uncertainty in the reaction model related to the inputs (optical potential, etc.). A systematic study on this topic using Bayes' theorem combined with a Markov chain Monte Carlo has been performed in Ref. [LN18]. To better constrain transfer cross sections in

our case, more experimental data and comparison with other advanced models in similar mass and energy regions are definitely needed. For a specific transfer, it could be also useful to carry out a series of similar tests as what we have done in this study to quantify exactly the connection between the experimental conditions and the part of the wave function probed. As mentioned in Sec. 2.2, another interesting topic here is to study the nonlocality effect of the optical potential on the transfer calculations. In the case of transfer to the continuum, there remain multiple tests that can be done to study the effect of the potentials and numerical parameters in calculating the continuum bin state with a certain width. Besides, including the coupling mechanism in the non-resonant region would lead the model to this promising application.

On the experimental side, more precise data is eagerly needed which asks for more advanced detection technique and setup. Especially for the ^{9}Li(d,p) transfer in our case, it can be very useful to detect protons in coincidence with the ^{9}Li fragments produced from the breakup of the corresponding ^{10}Li using an upgraded device which provides a high spatial and energy resolution and a large angular coverage. This is not only about physics but a combined efforts from the aspects of materials science, computer science, engineering, etc. Among the emerging technologies, an active target like the ACTAR TPC has already been a path to follow, which has the power to reconstruct the reaction kinematics in three dimensions with a weak beam intensity (down to 10^3 pps).

Appendix A

FRESCO Input

The computational program FRESCO [Tho88] is a general-purpose reaction code developed by Ian Thompson since 1983. A typical input file of FRESCO is handled in a fortran namelist style, containing five portions,

- & fresco: introducing the parameters in the numerical calculations;
- & partition: inputting all the mass partitions and the channel information;
- & pot: containing all the necessary potentials;
- & overlap: showing the configuration for the composite nucleus;
- & coupling: providing the coupling scheme among different states.

When performing the transfer calculations, some new important parameters need to be added besides the basic information of the reaction. In particular, a non-local kernel, transfer couplings and the amplitudes of all the overlap should be included by introducing *rintp*, *hnl* and others. A specific example of the input for the ^{10}Be(d,p)^{11}Be transfer taking place at $E_d = 21.4$ MeV is given here. Note since the calculation is performed with FR-ADWA model, the deuteron potential for the incident channel is read from outside. The interaction between the valence neutron and the ^{10}Be core in the ^{11}Be nucleus is simulated by a Gaussian potential.

```
Be10(d,p)Be11 @ 21.4 MeV;
NAMELIST
&FRESCO hcm=0.1 rmatch=60 rintp=0.10 hnl=0.05 rnl=10.00 centre=0.0
        jtmin=0.00 jtmax=120 absend=-1.00
        thmin=0.10 thmax=90.00 thinc=0.10
        cutl= 0.00 cutr= 0.00 cutc= 0.00
        it0=1 iter=1 iblock=0
        nnu=36
        xstabl=1
        elab=21.4 /

&PARTITION namep='d' massp=2.0 zp=1
           namet='Be10' masst=10.0 zt=4 nex=-1 /
&STATES jp=1.0 bandp=1 ep=0.0 cpot=1 jt=0.0 bandt=1 et=0.00 /

&PARTITION namep='p' massp=1.0 zp=1
           namet='Be11' masst=11.0 zt=4 qval=-1.7229 nex=1 /
&STATES jp=0.5 bandp=1 ep=0.0 cpot=2 jt=0.5 bandt=1 et=0.00 /
&partition /

&POT kp=1 type=0 shape=0 p(1:3)= 10.00 0.00 1.29 /
&POT kp=1 type=1 shape=9 p(1:2)= 1.0 1.0 /

&POT kp=2 type=0 p(1:3)= 0.00 11.00 1.29 /
&POT kp=2 type=1 p(1:6)= 51.939 1.149 0.690 1.751 1.141 0.690 /
&POT kp=2 type=2 p(1:6)= 0.0000 1.146 0.690 9.500 1.141 0.690 /

&POT kp= 3 type= 1 itt=F shape= 5 p(1:3)= 1.00 0.00 1.00 /
&POT kp= 3 type= 3 itt=F shape= 5 p(1:3)= 1.00 0.00 1.00 /
&POT kp= 3 type= 4 itt=F shape= 5 p(1:3)= 1.00 0.00 1.00 /
&POT kp= 3 type= 7 itt=F shape= 5 p(1:3)= 1.00 0.00 1.00 /

&POT kp=4 type=0 shape=0 p(1:3)= 10.00 0.00 1.29 /
&POT kp=4 type=1 shape=2 p(1:3)= 115.05 0.00 1.9799 /

&POT kp=5 type=0 p(1:3)= 0.00 10.00 1.29 /
&POT kp=5 type=1 p(1:6)= 53.064 1.146 0.690 1.232 1.135 0.690 /
&POT kp=5 type=2 p(1:6)= 0.000 1.146 0.690 9.239 1.135 0.690 /
&pot /

&Overlap kn1=1 kn2=2 ic1=2 ic2=1 in=1 kind=3 nn=1 l=0 lmax=2 sn=0.5 ia=0
         j=0.5 ib=0 kbpot=3 be=2.2246 isc=0 ipc=0 /
&Overlap kn1=3 ic1=1 ic2=2 in=2 kind=0 nn=2 l=0 sn=0.5
         j=0.5 kbpot=4 be=0.5016 isc=0 ipc=0 /
&overlap /

&Coupling icto=-2 icfrom=1 kind=7 ip1=0 ip2=-1 ip3=5 /
&CFP in=1 ib=1 ia=1 kn=1 a=1.00 /
&CFP in=2 ib=1 ia=1 kn=3 a=1.00 /
&CFP /
&coupling /
```

Appendix B

Paper I

This appendix attaches the following published paper, which is part of the work presented in Sec. 3.1.

J. Yang and P. Capel. Systematic analysis of the peripherality of the ^{10}Be$(d,p)^{11}$Be transfer reaction and extraction of the asymptotic normalization coefficient of ^{11}Be bound states. Phys. Rev. C 98, 054602 (2018) [YC18].

Systematic analysis of the peripherality of the ^{10}Be$(d,p)^{11}$Be transfer reaction and extraction of the asymptotic normalization coefficient of ^{11}Be bound states

J. Yang[1,2,*] and P. Capel[1,3,†]

[1]*Physique Nucléaire et Physique Quantique (CP 229), Université libre de Bruxelles (ULB), B-1050 Brussels, Belgium*
[2]*Afdeling Kern-en Stralingsfysica, Celestijnenlaan 200d-bus 2418, B-3001 Leuven, Belgium*
[3]*Institut für Kernphysik, Johannes Gutenberg-Universität Mainz, D-55099 Mainz, Germany*

(Received 5 June 2018; revised manuscript received 30 September 2018; published 2 November 2018)

We reanalyze the experiment of Schmitt *et al.* on the ^{10}Be$(d,p)^{11}$Be transfer reaction [Phys. Rev. Lett. **108**, 192701 (2012)] by exploring the beam-energy and angular ranges at which the reaction is strictly peripheral. We consider the adiabatic distorted wave approximation (ADWA) to model the reaction and use a Halo-EFT description of ^{11}Be to systematically explore the sensitivity of our calculations to the short-range physics of the ^{10}Be-n wave function. We find that by selecting the data at low beam energy and forward scattering angle the calculated cross sections scale nearly perfectly with the asymptotic normalization coefficient (ANC) of the ^{11}Be bound states. Following these results, a comparison of our calculations with the experimental data gives a value of $C_{1s1/2} = 0.785 \pm 0.03\,\mathrm{fm}^{-1/2}$ for the $\frac{1}{2}^+$ ground-state ANC and $C_{0p1/2} = 0.135 \pm 0.005\,\mathrm{fm}^{-1/2}$ for the $\frac{1}{2}^-$ excited state, which are in perfect agreement with the *ab initio* calculations of Calci *et al.*, who obtain $C^{ab\ initio}_{1/2^+} = 0.786\,\mathrm{fm}^{-1/2}$ and $C^{ab\ initio}_{1/2^-} = 0.129\,\mathrm{fm}^{-1/2}$ [Phys. Rev. Lett. **117**, 242501 (2016)].

DOI: 10.1103/PhysRevC.98.054602

I. INTRODUCTION

Halo nuclei [1] constitute a unique class of exotic systems, which are mainly found in the neutron-rich region of the nuclear chart. The halo is a threshold effect observed close to the neutron dripline, in which one or two neutrons are loosely bound to the core of the nucleus. Because of this loose binding, these valence neutrons can tunnel far away into the classically forbidden region and exhibit a high probability of presence at a large distance from the other nucleons. They hence form a sort of diffuse halo around a compact core [2], which significantly increases the matter radius of these nuclei.

Since their discovery in the mid-1980s, halo nuclei have been the subject of many studies in both the nuclear-structure and nuclear-reaction communities. In the former because of the challenge these diffuse nuclei pose to usual nuclear-structure models, like the shell model. In the latter because, due to their short lifetime, they are mostly studied through reactions.

Experimentally, the upgrade of rare isotope beam facilities worldwide provides us with many ways to explore these halo systems. Transfer reaction [3–8] has been an important tool to infer information about these systems for decades. In this reaction, one or several nucleons are transferred between the projectile and target. Because those nucleons populate the valence states of the nucleus, transfer is useful in the analysis of the single-particle structure of nuclei [3,4,8–11]. It is therefore particularly well suited to study halo nuclei [6,10–13].

To extract valuable nuclear-structure information from experimental data, a precise model of the reaction is required. Deuteron-induced reactions, like the one on which this work is focused, are usually described within a three-body model: a proton p, a neutron n, and the nucleus upon which the transfer takes place. Many such models have been developed [3–7]. The Distorted Wave Born Approximation (DWBA) [14] is one of the most used methods to analyze experimental data and extract spectroscopic information about nuclei. However, this method does not properly account for dynamical effects, such as the breakup of the deuteron, therefore alternative formulations have been suggested. Johnson and Soper have introduced the adiabatic distorted wave approximation (ADWA), which, without losing the relative simplicity of the DWBA method, includes a zero-range adiabatic treatment of the deuteron-breakup channel (ZR-ADWA) [15]. Johnson and Tandy have then extended this seminal work to a finite-range version of the ADWA method (FR-ADWA) [16]. For a more accurate inclusion of the deuteron dynamics in the reaction model, the solution of the continuum-discretized coupled-channel approach (CDCC) [17] can be used. In that approach, the projectile-target wave function is expanded upon all the states of the deuteron, including its continuum, which leads to the resolution of a set of coupled equations. More recently, numerical techniques have become available to solve the Faddeev-Alt, Grassberger, and Sandhas (FAGS) equations [18,19], which corresponds to the most accurate framework to describe transfer reactions induced by deuteron within a three-body model [20].

At the Oak Ridge National Laboratory a transfer experiment was performed by Schmitt *et al.* to study the structure of ^{11}Be [10,11]. This nucleus is the archetypical one-neutron

*jiecyang@ulb.ac.be
†pcapel@uni-mainz.de

halo nucleus and, as such, exhibits a strong ^{10}Be-n structure. In this Oak Ridge experiment a neutron is transferred from a deuteron to ^{10}Be to form ^{11}Be: $^{10}\mathrm{Be}(d,p)^{11}\mathrm{Be}$. The two bound states of ^{11}Be have been populated: its $\frac{1}{2}^+$ ground state and $\frac{1}{2}^-$ excited state. Transfer to the $\frac{5}{2}^+$ resonance above the one-neutron threshold has also been measured. The experiment was performed in inverse kinematics with an ultrapure ^{10}Be beam impinging on a CD_2 target at beam energies 107, 90, 75, and 60 MeV, which correspond, in direct kinematics, to, respectively, $E_d = 21.4$, 18, 15, and 12 MeV in the laboratory restframe [11].

The main goal of the present work is to reanalyze this Oak Ridge experiment with a special focus on the sensitivity of the calculations to the ^{10}Be-n wave function in the ^{11}Be bound states. In particular, we look for the best experimental conditions in which the reaction is strictly peripheral, i.e., for which only the tail of the ^{10}Be-n radial wave function affects the theoretical cross sections. Because this tail has a universal behavior [21], but for its normalization, the comparison with the data in these peripheral conditions should enable us to extract this asymptotic normalization constant (ANC) in a model-independent way [12,13,22–26].

To reach this goal, we couple a Halo-EFT description of ^{11}Be [27,28] to the ADWA model of reaction. Thanks to the natural separation of scales in EFT, this provides us with a very systematic way of studying the sensitivity of the cross section to the short-range physics of the overlap wave function. Albeit similar in spirit with Refs. [12,13,24,25], this analysis will enable us to determine the exact conditions of peripherality of the reaction, and hence extract a reliable estimate of the ANC of the bound states of ^{11}Be.

Recently an *ab initio* calculation of ^{11}Be has been performed by Calci *et al.* within the framework of the no-core shell model with continuum (NCSMC) [29]. These calculations provide a fully microscopic prediction of its ANC, to which we will be able to confront our values inferred from the data of Schmitt *et al.* [10,11].

This paper is structured as follows: In Sec. II, we briefly present the three-body model of the reaction and the ADWA, which we use to compute the transfer cross sections. In Sec. III, we introduce the numerical inputs and the descriptions of ^{11}Be we consider in this study. Finally we present the results of our calculations and discuss them in Sec. IV. Our conclusions are drawn in Sec. V.

II. THEORETICAL FRAMEWORK

We consider the stripping reaction $A(d,p)B$ in which a neutron is transferred to a nucleus A (^{10}Be) to form nucleus B (^{11}Be). In a simple physical picture, this transfer reaction can be viewed as a process in which the neutron n from the incident deuteron d populates an unoccupied state in the target nucleus A, producing the composite nucleus described as a two-cluster structure $B = A + n$. To model this reaction, we adopt the three-body model $(A + n + p)$ illustrated in Fig. 1.

In its post form, the transition matrix elements for the reaction reads [4–6]

$$T_{\mathrm{post}}(pB, dA) = \langle \chi^{(-)}_{pB}\varphi_{An}|V_{pn} + U_{pA} - U_{pB}|\psi^{(+)}_{dA}\rangle, \quad (1)$$

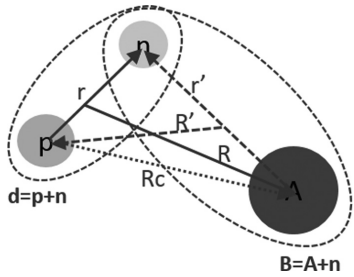

FIG. 1. Illustration of the three-body system with associated coordinates.

where V_{pn} is the potential that simulates the interaction that binds the proton and the neutron into the deuteron and U_{pA} and U_{pB} are optical potentials that simulate the interaction between the proton and the clusters A and B, respectively. The wave function $\psi^{(+)}_{dA}$ describes the three-body system with the condition that the proton and neutron are initially bound into a deuteron that is impinging on A. At the ADWA, it is approximated by

$$\psi^{(+)}_{dA}(\boldsymbol{r}, \boldsymbol{R}) \simeq \chi^{(+)}_{dA}(\boldsymbol{R})\varphi_{pn}(\boldsymbol{r}), \quad (2)$$

where φ_{pn} is the deuteron bound state computed from V_{pn} and $\chi^{(+)}_{dA}$ is the distorted wave describing the scattering of d by A. Following the Johnson and Tandy prescription [16], this wave function is obtained from the optical potential U_{dA} built by averaging A-p and A-n optical potentials over the finite-range deuteron bound state,

$$U_{dA}(R) = \frac{\langle \varphi_{pn}|V_{pn}(U_{pA} + U_{nA})|\varphi_{pn}\rangle}{\langle \varphi_{pn}|V_{pn}|\varphi_{pn}\rangle}. \quad (3)$$

The distorted wave $\chi^{(-)}_{pB}$ appearing in Eq. (1) describes the scattering of p by the cluster B in the outgoing channel of the reaction; it is obtained using the optical potential U_{pB}. The wave function φ_{An} describes the state of the nucleus B formed in the transfer. In this three-body model, it is obtained at the single-particle approximation, in which B is seen as a two-cluster structure, in which a neutron is bound to the core A assumed to be structureless. The A-n interaction is described by a phenomenological potential V_{An}. Following Refs. [30,31], we use a Halo-EFT description of ^{11}Be (see Sec. III A) [27,28]. Within this description, the B bound state is characterized by the quantum numbers $n_{r'}lj$, where $n_{r'}$ is the number of nodes in the radial wave function, l is the orbital angular momentum, and j is obtained from the coupling of l with the spin of the neutron.

The reduced radial wave function has the following asymptotic behavior:

$$u_{n_{r'}lj}(r') \underset{r'\to\infty}{\longrightarrow} b_{n_{r'}lj}\; i\,\kappa_{n_{r'}lj}\, r'\, h_l\big(i\kappa_{n_{r'}lj} r'\big), \quad (4)$$

where h_l is a spherical Hankel function and $\kappa_{n_{r'}lj} = \sqrt{2\mu_{An}|E_{n_{r'}lj}|}/\hbar$, with $|E_{n_{r'}lj}|$ the binding energy of the neutron to the core A and μ_{An} their reduced mass. The parameter $b_{n_{r'}lj}$ is the single-particle ANC (SPANC) defining the

strength of the exponential tail of the A-n bound-state wave function. This SPANC will vary with the geometry of the potential used to simulate the A-n interaction [12,13,21,32]. We will use this property in Sec. IV to assess the sensitivity of the transfer cross section to the ANC.

Being universal, the asymptotic behavior (4) exists also in the actual structure of the nuclei [21] and hence should be reproduced in *ab initio* models, like the NCSMC calculation of Calci *et al.* [29]. However, the true ANC will differ from the SPANC obtained in the phenomenological two-body description of B because of the coupling with the other possible configurations [21]. In the present piece of work, we study how to relate the two and if there are experimental conditions which enable a safe extraction of the ANC for the ^{11}Be bound states from the Oak Ridge experiment [10,11].

The theoretical differential cross section expressed as a function of the relative direction $\Omega = (\theta, \phi)$ between p and B in the outgoing channel $d\sigma_{\rm th}/d\Omega$ is obtained from the square modulus of the transition matrix elements (1). All transfer calculations are performed with the code FRESCO [33]. In the next section, we provide all the details about our choices of the potentials used in this work.

III. TWO-BODY POTENTIALS

A. Description of ^{11}Be

As mentioned in the previous sections, ^{11}Be is the archetype of a one-neutron halo nucleus. It can thus be modeled as a neutron loosely bound to a ^{10}Be core. With the assumption that the ^{10}Be core is in its ground state (0^+), the $\frac{1}{2}^+$ ground state (g.s.) of ^{11}Be can be described by a $^{10}\mathrm{Be}(0^+) \otimes 1s_{1/2}$ configuration, and the $\frac{1}{2}^-$ excited state (e.s.) by a $^{10}\mathrm{Be}(0^+) \otimes 0p_{1/2}$ configuration. In this study, we use a Halo-EFT description of this nucleus at the leading order of the expansion in each of these partial waves [27,28].

Halo EFT provides a systematic treatment of halo nuclei, which exhibit a clear separation of scales: The core of the nucleus (^{10}Be in the present case) is tightly bound and hence compact, whereas the halo neutron is loosely bound and consequently has a very extended wave function. The parameter $R_{\rm core}/R_{\rm halo}$, where $R_{\rm core}$ ($R_{\rm halo}$) is the size of the core (halo) of the nucleus, is thus small (about 0.4 for ^{11}Be). Halo EFT exploits this separation of scales and considers the core and halo neutron as its degrees of freedom. Within Halo EFT, the quantum-mechanical amplitudes are expanded into powers of that parameter (see Ref. [28] for a recent review). This effective theory will break down if the process it describes probes distances smaller than $R_{\rm core}$, or if they lead to the excitation of the core.

Halo EFT is expressed through a Lagrangian that includes all operators up to a given order in this expansion. The interactions that appear in this Lagrangian are thus considered at the limit $R_{\rm core}/R_{\rm halo} \to 0$ and are described by zero-range potentials and their derivatives. The coefficients of these potentials—the low-energy constants of the theory—are free parameters, which are adjusted to reproduce experimental data or outputs of *ab initio* calculations [30]. In the present work, we consider the development at the lowest order using just one contact term, and hence one low-energy constant, per partial wave to simply reproduce the one-neutron separation energy of each bound state of ^{11}Be populated through the transfer reactions measured by Schmitt *et al.* [10,11]. We neglect the possible derivatives of the interaction as well as the higher-order terms [27,28].

To render the interactions numerically tractable, we follow what is done to describe the nucleon-nucleon interaction in EFT [34] and regulate them with a Gaussian, whose range can be varied [30,31],

$$V_{An}(r') = -V_0\, e^{-\frac{r'^2}{2r_0^2}}. \tag{5}$$

This form of the neutron-core potential enables us to easily evaluate the sensitivity of the reaction to the short-range physics, which is believed to take place at distances shorter than the radial range $\sqrt{2}\,r_0$ of these Gaussians. Our goal being to find the experimental conditions under which the reaction is purely peripheral, Halo EFT provides us with a simple and elegant tool to generate, using different values of the Gaussian width r_0, wave functions for the bound states of ^{11}Be that exhibit significantly different radial behaviors. For the reaction to be peripheral, it needs to be sensitive only to the tail of the radial wave function (4). One simple way to find that out is to check that its cross section is proportional to the square of the bound state SPANC $|b_{n,r,lj}|^2$, using different A-n potentials that generate single-particle wave functions with different SPANCs, as was already done in Refs. [12,13,24,25,32]. However, we must also be sure that the reaction is *not* sensitive to the internal part of the wave function. For this, the different wave functions must not only have different SPANCs, but should also exhibit very different radial behavior inside the nucleus.

The Gaussian potential (5) enables us to realize that in a simple way. We consider nine such Gaussian potentials with different widths r_0 ranging from 0.4 to 2.0 fm. The lower end of that range is unphysically small, but it enables us to generate both very small SPANCs and significant changes in the internal part of the wave function. The upper end is chosen so as to avoid distortion in the long-range physics of ^{11}Be [30].

For each width the depth V_0 in the $s_{1/2}$ partial wave is adjusted to reproduce the neutron binding energy: $|E_{1s1/2}| = 0.502\,\mathrm{MeV}$ for the g.s. [35]. We do the same in the $p_{1/2}$ partial wave to describe the $\frac{1}{2}^-$ bound excited state of ^{11}Be, fitting the depth of the central term V_0 to obtain $E_{0p1/2} = -0.182\,\mathrm{MeV}$ [35]. These parameters are listed in Table I with the corresponding SPANCs $b_{1s1/2}$ and $b_{0p1/2}$. This way of doing enables us to generate a very broad range of SPANCs for both the ground and excited bound states of ^{11}Be.

The corresponding reduced radial wave functions are displayed in Figs. 2 and 3 for the g.s. and the e.s., respectively. As desired for this study, we observe that the nine Gaussian potentials provide radial wave functions significantly different from one another. The very narrow potentials lead to wave functions that reach their asymptotic behavior (4) at quite a small radius, viz. $r' \simeq 1$ fm, while the broader ones have their internal behavior developing at much larger distances. The wave function corresponding to $r_0 = 2.0$ fm being similar to what a usual Woods-Saxon potential produces, i.e., with an

TABLE I. Parameters of the Gaussian ^{10}Be-n potentials [see Eq. (5)] adjusted to reproduce the g.s. and e.s. of ^{11}Be. The SPANC $b_{n_r lj}$ obtained for each case is provided as well.

r_0 (fm)	V_0 (g.s.) (MeV)	$b_{1s1/2}$ (fm$^{-1/2}$)	V_0 (e.s.) (MeV)	$b_{0p1/2}$ (fm$^{-1/2}$)
0.4	1314.6	0.601	869.4	0.068
0.6	592.3	0.632	387.3	0.085
0.8	337.8	0.664	218.4	0.100
1.0	219.2	0.697	140.2	0.114
1.2	154.4	0.732	97.7	0.127
1.4	115.1	0.769	72.1	0.140
1.6	89.3	0.807	55.4	0.152
1.8	71.6	0.846	44.0	0.165
2.0	58.8	0.888	35.8	0.177

asymptotic behavior reached at $r' \simeq 5$ fm (see, e.g., Fig. 7 of Ref. [13] or Fig. 6(a) of Ref. [32]). These significant changes in both the SPANCs and in the radial behavior in the interior of the nucleus, will help us assessing the sensitivity of our ^{10}Be$(d,p)^{11}$Be transfer calculations to the radial wave function of the ^{11}Be bound states. In particular, let us note that these wave functions differ very significantly in the surface part of the nucleus—viz. at $r' \sim 2$–3 fm—to which transfer reactions can be sensitive [21,25]. The study of the transfer calculations performed with these very different wave functions will enable us to clearly identify the experimental conditions under which the reaction is purely peripheral.

B. Other optical potentials

The nucleon-nucleus optical potentials used to compute the distorted waves used in Eq. (1) and to build the FR-ADWA d-A potential in Eq. (3) are obtained from the global Chapel Hill parametrization CH89 [36] without including the spin-orbit terms. This potential is energy dependent and hence needs to be adapted as a function of the deuteron energy E_d.

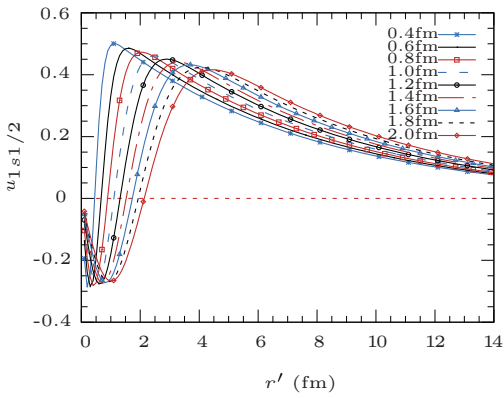

FIG. 2. Reduced radial wave functions $u_{1s1/2}$ of the $\frac{1}{2}^+$ g.s. of ^{11}Be obtained with the nine Gaussian potentials of Table I.

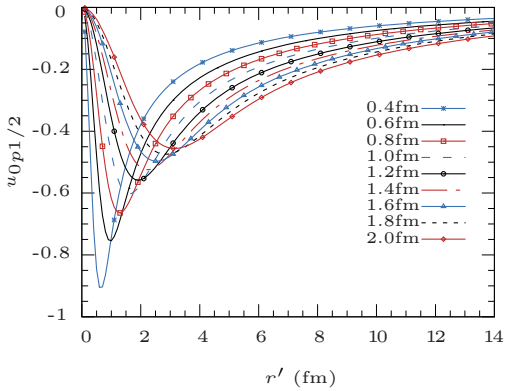

FIG. 3. Reduced radial wave functions $u_{0p1/2}$ of the $\frac{1}{2}^-$ e.s. of ^{11}Be obtained with the nine Gaussian potentials of Table I.

The FR-ADWA potential (3) is obtained by computing $U_{p^{10}\mathrm{Be}}$ and $U_{n^{10}\mathrm{Be}}$ at half the deuteron energy. For that potential, the numerical integration is performed with the front-end code TWOFNR [37].

To test the sensitivity of our calculations to the choice of these optical potentials, we also consider the Koning-Delaroche parametrization [38]. The results of these tests are presented in Sec. IV C.

The Reid soft-core interaction [39] is used as V_{pn}.

IV. RESULTS AND DISCUSSION

Following the experimental conditions of Refs. [10,11], we perform ADWA calculations of the reaction ^{10}Be$(d,p)^{11}$Be at energies $E_d = 21.4$, 18, 15, and 12 MeV. We first consider the transfer towards the g.s. (Sec. IV A) and then towards the e.s. (Sec. IV B). In both cases, we study the experimental conditions for which the reaction is peripheral and accordingly extract an ANC for each of these states, which we then compare to the prediction of the *ab initio* calculations of Calci *et al.* [29].

A. Transfer to ^{11}Be ground state

1. Conditions of peripherality of the reaction

Figure 4(a) displays the differential cross section $d\sigma_{\mathrm{th}}/d\Omega$ for the transfer to the ^{11}Be g.s. computed for the highest experimental deuteron energy $E_d = 21.4$ MeV. The calculations have been performed for the nine $1s_{1/2}$ wave functions shown in Fig. 2 obtained with the potentials of Table I. As expected, we observe a large variation in the results. At forward angle, the cross sections seem to scale with the square of the SPANC $b_{1s1/2}$ (see Table I), as one would expect if the process were purely peripheral [see Eq. (1)]. At larger angle, i.e., in the region of the second peak, the ordering of the curves is inverted, showing that in this angular range, the process is more sensitive to the short-range physics of the

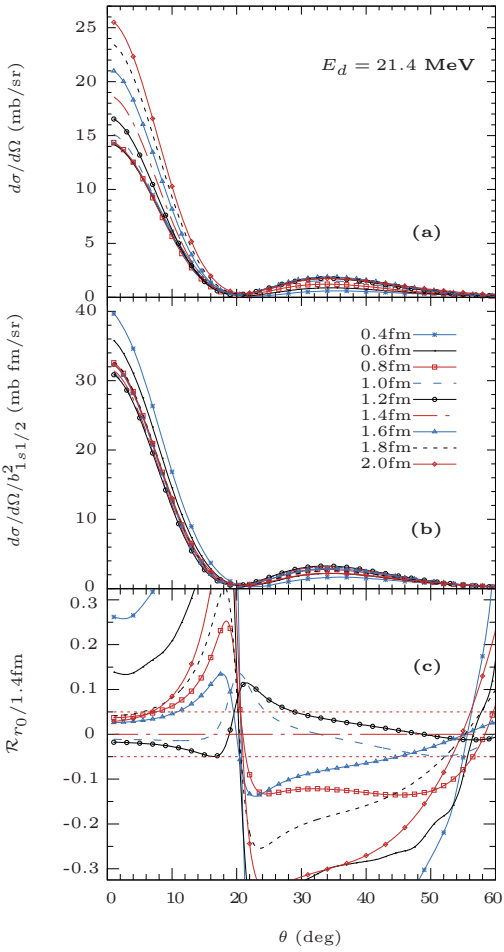

FIG. 4. Analysis of the differential cross sections of ^{10}Be$(d,p)^{11}$Be(g.s.) for a deuteron energy $E_d = 21.4$ MeV. The results of the ADWA calculations are presented for every potential of Table I.

wave function. Therefore, selecting data at small scattering angle might enable us to constrain the g.s. ANC.

To better estimate the sensitivity of our calculations to the SPANC, we have plotted in Fig. 4(b) the transfer cross section divided by $b^2_{1s1/2}$. Accordingly, the spread in the results is significantly reduced at forward angle, confirming our initial impression of Fig. 4(a). In the region of the second maximum, however, it remains similar to what was observed before scaling.

To precisely determine within which angular range the data should be limited to select a strictly peripheral process, we remove the major angular dependence by considering the following ratio:

$$\mathcal{R}_{r_0/1.4\mathrm{fm}}(\theta) = \left(\frac{b^{(1.4\mathrm{fm})}_{n_{r'}lj}}{b^{(r_0)}_{n_{r'}lj}}\right)^2 \frac{\frac{d\sigma^{(r_0)}_{\mathrm{th}}}{d\Omega}}{\frac{d\sigma^{(1.4\mathrm{fm})}_{\mathrm{th}}}{d\Omega}} - 1, \tag{6}$$

where the transfer cross section computed using the ^{10}Be-n Gaussian potential of width r_0 scaled by the square of the SPANC is divided by the result obtained with $r_0 = 1.4$ fm, which is at the center of the range in r_0. The results are displayed in Fig. 4(c). If one excepts the very narrow potentials ($r_0 = 0.4$ fm and $r_0 = 0.6$ fm), we see that all ratios $\mathcal{R}_{r_0/1.4\mathrm{fm}}$ fall very close to one another, confirming the peripherality of the reaction when the data are selected at forward angles. To define an angular range in which the reaction can be considered as peripheral, we consider a maximum of 5% difference [horizontal dotted lines in Fig. 4(c)]. In this case, this happens only at very forward angles, viz. when $\theta < 7^\circ$.

We repeat our calculations and analysis at the other energies at which data were taken [10,11]. The results obtained at $E_d = 18$ MeV are presented in Fig. 5. As at 21.4 MeV, the reaction is peripheral at forward angles. However, the region of peripherality is enlarged up to $\theta < 10^\circ$ and even though the short-range potentials still lead to significant ratios $\mathcal{R}_{r_0/1.4\mathrm{fm}}$, they move closer to the 5% acceptance band. It seems therefore that transfer reactions measured at lower beam energy are more peripheral.

Moving down in energy confirms this trend. At $E_d = 15$ MeV (Fig. 6), the peripherality angular range goes up to 20° and the results obtained with the narrow potentials are now within a mere 10% of the more regular widths. At even lower energy ($E_d = 12$ MeV, Fig. 7), the peripherality at forward angle is even clearer. This can already be seen in Fig. 7(b), and the Fig. 7(c) confirms that all potentials, even the most narrow ones, fall into the peripherality acceptance band for $\theta < 20^\circ$. We therefore conclude that, first, the peripheral area of this transfer reaction is always found at forward angles, and, second, that when the incident energy decreases, the reaction exhibits a more pronounced peripheral character.

2. *Extraction of the ANC of the* ^{11}Be *g.s.*

Now that we know in which conditions the reaction is peripheral (low E_d and forward angles), we extract an ANC by scaling our calculations to the data of Schmitt *et al.* in these exact conditions. For each beam energy, and each potential width r_0, we thus infer an ANC $C^{(r_0)}_{n_{r'}lj}$ from a χ^2 analysis,

$$\chi^2_{(r_0)} = \sum_{i'} \frac{\left[\left(\frac{C^{(r_0)}_{n_{r'}lj}}{b^{(r_0)}_{n_{r'}lj}}\right)^2 \frac{d\sigma^{(r_0)}_{\mathrm{th}}}{d\Omega}\Big|_{i'} - \frac{d\sigma_{\mathrm{exp}}}{d\Omega}\Big|_{i'}\right]^2}{(\delta_{\mathrm{exp}}|_{i'})^2}, \tag{7}$$

where $\delta_{\mathrm{exp}}|_{i'}$ is the experimental uncertainty at angle $\theta_{i'}$ and the sum is limited to the sole data points i' which lie within the peripheral regions defined in the previous section, viz. within the 5% acceptance band.

The ANCs $C^{(r_0)}_{1s1/2}$ obtained by minimizing the sum in Eq. (7) are shown in Fig. 8 as a function of the potential width r_0 (from $r_0 = 0.4$ fm on the left to $r_0 = 2.0$ fm on the right) and are grouped according to the beam energy: $E_d =$

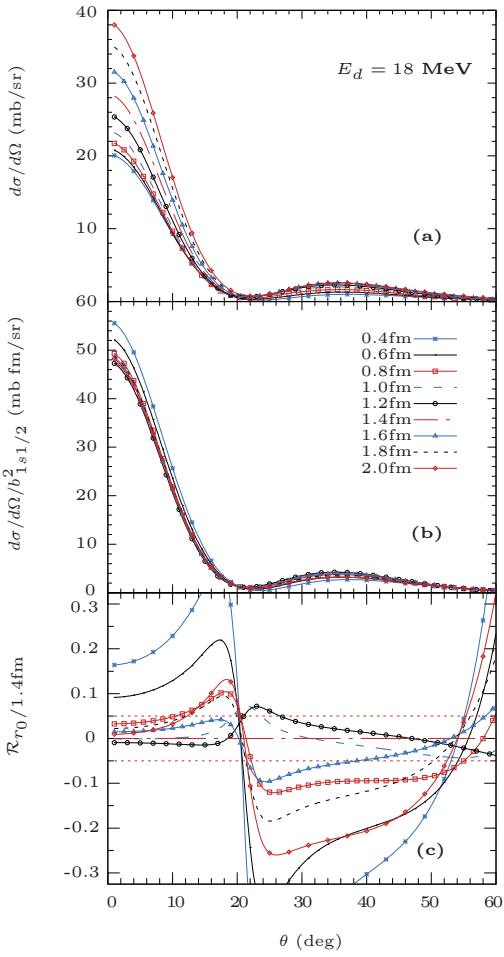

FIG. 5. Same as Fig. 4 for $E_d = 18$ MeV.

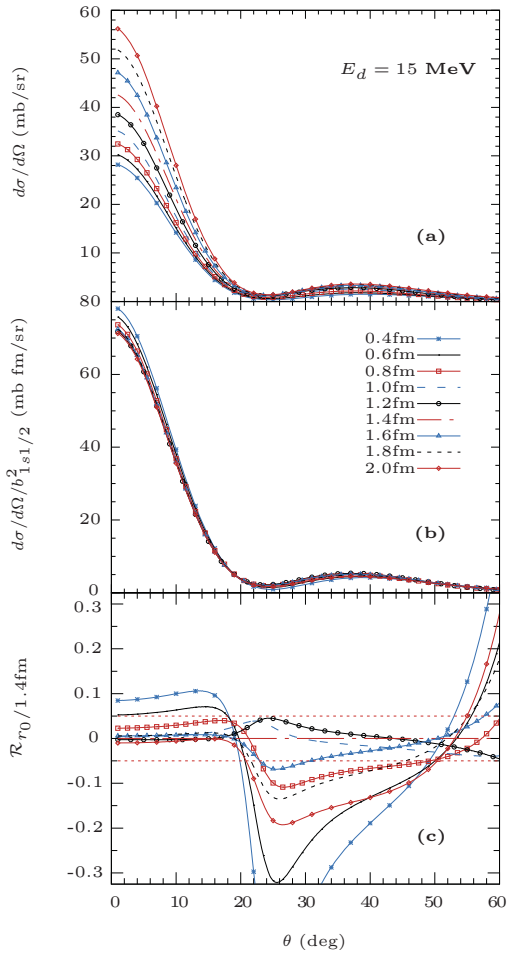

FIG. 6. Same as Fig. 4 for $E_d = 15$ MeV.

21.4 MeV (squares), 18 MeV (triangles), 15 MeV (diamonds), and 12 MeV (circles). The error bars correspond to the uncertainty in the χ^2 minimization.

The extraction of these ANCs is more reliable at low energy: The dependence on r_0 vanishes for the lowest beam energies. At $E_d = 21.4$ MeV, even if one excepts the results obtained with the shortest widths r_0 (first two points), we observe a significant dependence on the potential geometry. This confirms that, at this energy, even when selecting the data at forward angles, the reaction is not completely independent of the internal part of the radial wave function (see Fig. 4). There is a problem with the results at $E_d = 18$ MeV, which are always smaller than at the other beam energies. This has already been seen in Schmitt *et al.*'s analysis [10,11]. The reason for that remains unclear. However, here, too, the dependence of the extracted ANC on r_0 cannot be neglected, and hence that reaction cannot be considered as purely peripheral.

As already seen above, the best results are obtained at $E_d = 15$ and 12 MeV. Especially in the latter case, the ANC is nearly independent on the geometry of the potential, which gives us confidence that the value hence inferred is close to the real one.

To infer the actual ANC from the Oak Ridge data, we thus focus on the two lowest beam energies and select only the calculations that fall within the confidence band of 5% defined in the previous section, which means that we consider all potentials at $E_d = 12$ MeV and the potentials with $r_0 \geqslant 0.8$ fm at $E_d = 15$ MeV. We hence obtain an average of $C_{1s1/2} = 0.785 \pm 0.03\,\mathrm{fm}^{-1/2}$. This value is close to that found by Belyaeva *et al.* [13] with a coupled-reaction channel model of the reaction. More interestingly, it is in excellent

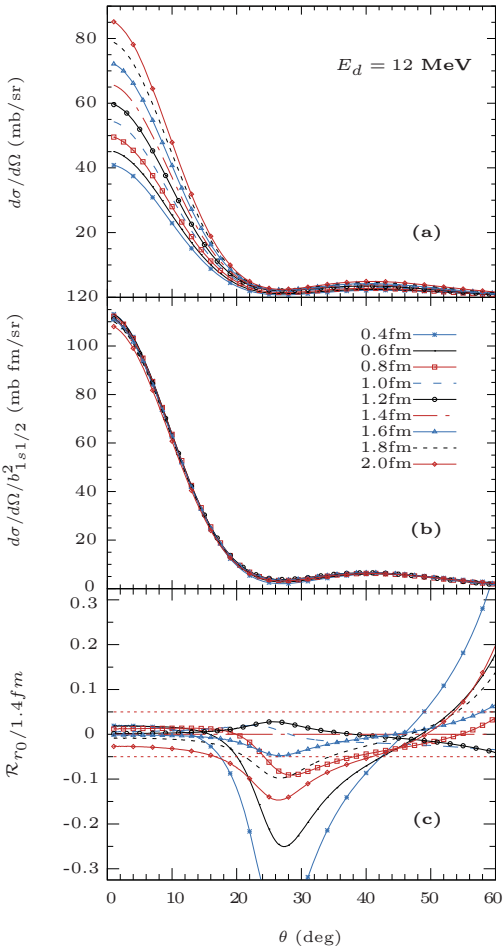

FIG. 7. Same as Fig. 4 for $E_d = 12$ MeV.

agreement with the result obtained by Calci *et al.* within their NCSMC calculation of ^{11}Be structure [29]: $C^{ab\ initio}_{1/2^+} = 0.786\,\mathrm{fm}^{-1/2}$ (dashed line in Fig. 8).

To estimate the accuracy of the inferred ANC, we plot in Fig. 9 the results of our calculations scaled to this value, viz. $(\frac{C_{1s1/2}}{b^{(r_0)}_{1s1/2}})^2 \frac{d\sigma^{(r_0)}_{th}}{d\Omega}$. The agreement with the data improves at lower energy, which confirms the method introduced here. Because this analysis relies a lot on the accuracy of the experimental data, it would be helpful to conduct such experiments focusing on the low energies and forward angles to obtain a more precise ANC.

B. Transfer to the ^{11}Be e.s.

We next apply the same method to the data of Schmitt *et al.* on the ^{11}Be $\frac{1}{2}^-$ e.s. Our results are summarized in

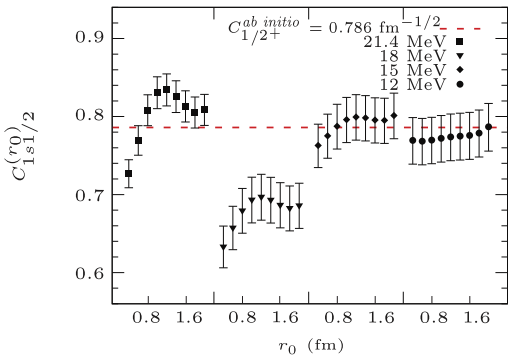

FIG. 8. ANCs extracted for the ground state of ^{11}Be by minimizing the χ^2 (7) for each beam energy and each potential of Table I. The *ab initio* result ($C^{ab\ initio}_{1/2^+} = 0.786\,\mathrm{fm}^{-1/2}$) is displayed for comparison by the dashed line.

Fig. 10. In this case, we observe a much stronger dependence of the results on the potential geometry, and even if it flattens at lowest beam energy, it never becomes negligible at $E_d = 12$ MeV. In our analysis, we have observed a much larger spread of the theoretical cross sections than for the ground state. This is most likely due to the p-wave dominant structure of this state, which, with a nonvanishing centrifugal barrier, forces a large fraction of the wave function to be in the interior of the nucleus, hence leading to transfer reactions that are no longer purely peripheral at these energies.

To infer an ANC from the existing data, we hence focus solely on the set of data at the lowest energy ($E_d = 12$ MeV). As for the g.s. we consider only the calculations which fall within the 5% acceptance band, which excludes the potentials with a width $r_0 \leqslant 0.8$ fm. From this analysis of the data, we obtain an averaged $C_{0p1/2} = 0.135 \pm 0.005\,\mathrm{fm}^{-1/2}$. This value is also comparable to that obtained in Ref. [13] and is close to the *ab initio* value of Calci *et al.* $C^{ab\ initio}_{1/2^-} = 0.129\,\mathrm{fm}^{-1/2}$ [29]. To improve the accuracy of the method, one would need transfer data measured at even lower beam energy. Extrapolating the tendency observed in Fig. 10, it seems that at an energy $E_d < 10$ MeV, the reaction will become purely peripheral, leading to a dependence on r_0 sufficiently negligible to extract a more reliable ANC.

C. The sensitivity to the optical potential choice

All the calculations presented in this work have been obtained using the Chapel Hill (CH89) global nucleon-nucleus optical potential [36]. However, other choices are possible. To estimate the sensitivity of our calculations to this potential choice, we repeat our calculations with the Koning-Delaroche potential (KD) [38]. This analysis is illustrated in Fig. 11 for the transfer reaction ^{10}Be$(d,p)^{11}$Be(g.s.) at $E_d = 12$ MeV. In both cases, we use the Gaussian ^{10}Be-n potential with a width $r_0 = 1.4$ fm.

As already observed in Refs. [10–12], we observe that the KD potential leads to a larger cross section compared

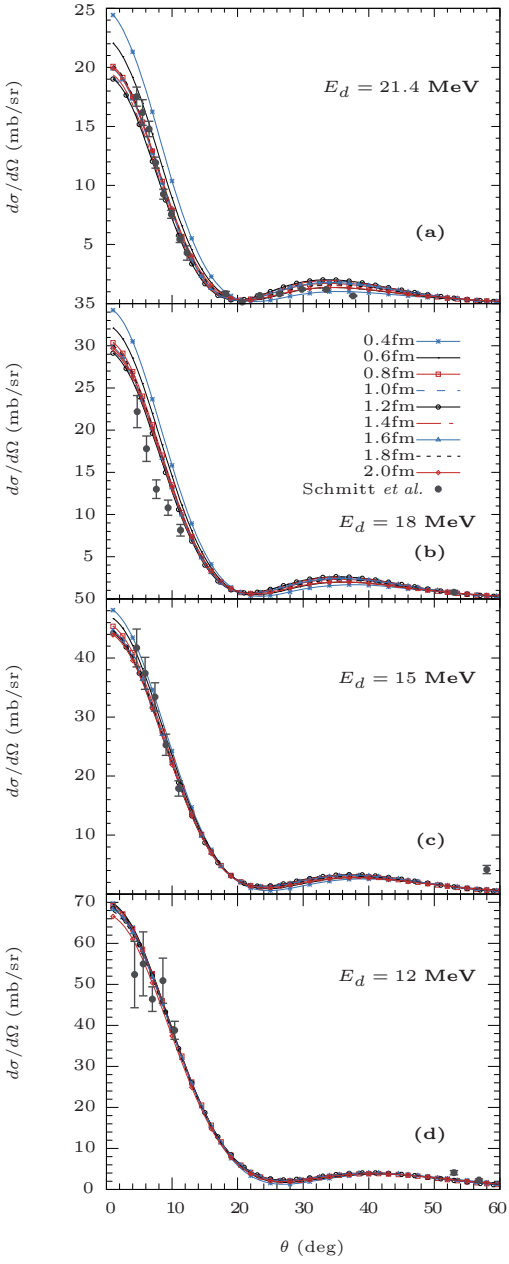

FIG. 9. The angular distribution for ^{10}Be$(d,p)^{11}$Be(g.s.) at all experimental energies after scaling to the ANC obtained by the χ^2 minimization $C_{1s1/2} = 0.785\,\mathrm{fm}^{-1/2}$.

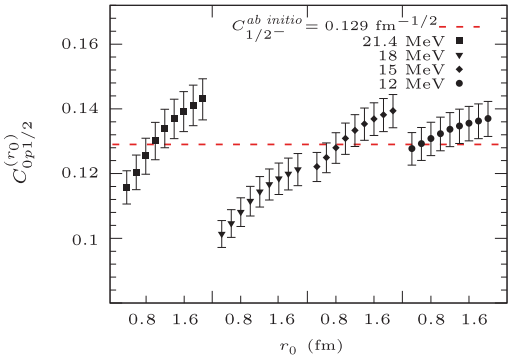

FIG. 10. ANCs extracted for the ^{11}Be e.s. by minimizing the χ^2 (7) for each beam energy and each potential of Table I. The *ab initio* result ($C^{ab\ initio}_{1/2^-} = 0.129\,\mathrm{fm}^{-1/2}$) is displayed for comparison.

to the CH89 one. Besides this change in magnitude of the cross section, the choice of optical potential does not affect the method. Because the cross sections calculated with the KD potential lead systematically to larger cross sections than those with CH89, we obtain a smaller ANC $C^{\mathrm{KD}}_{1s1/2} = 0.755 \pm 0.03\,\mathrm{fm}^{-1/2}$, still in agreement with the *ab initio* prediction.

V. CONCLUSION

Transfer reactions provide an efficient tool to study the single-particle structure of nuclei away from stability [3–8]. They are therefore used to study halo structures, like in ^{11}Be. In a recent experiment, Schmitt *et al.* have measured the ^{10}Be$(d,p)^{11}$Be transfer reaction at $E_d = 21.4$, 18, 15, and 12 MeV [10,11].

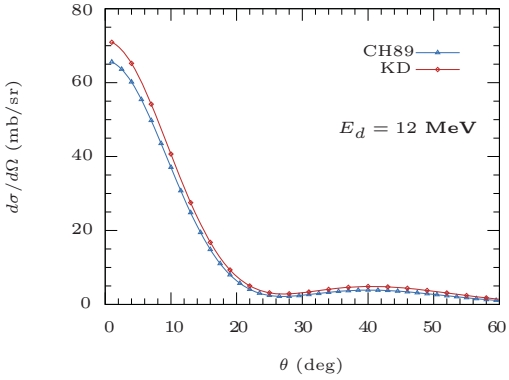

FIG. 11. Influence of the nucleon-nucleus optical potential on the transfer cross section for ^{10}Be$(d,p)^{11}$Be(g.s.) at $E_d = 12$ MeV. The Gaussian ^{10}Be-n potential is chosen with a width $r_0 = 1.4$ fm in both cases.

We have reanalyzed these data within the ADWA model of transfer [16], using a Halo-EFT description of ^{11}Be at leading order [27,28]. This enables us to precisely study the sensitivity of the cross sections to the short-range physics of the ^{10}Be-n wave function of both the g.s. and e.s. of ^{11}Be. Accordingly, we have been able to define the experimental conditions under which the reaction can be considered as peripheral, and hence from which a reliable ANC can be extracted [12,13,22–26].

For the $\frac{1}{2}^+$ g.s. of ^{11}Be, selecting the data at low energy ($E_d \leqslant 15$ MeV) and forward angles ($\theta < 20^\circ$) seems enough. Transfer reactions towards the $\frac{1}{2}^-$ e.s. require a much lower energy to be strictly peripheral, probably because of the existence of the centrifugal barrier in this p-wave dominated bound state. The ideal experimental conditions would actually require $E_d < 10$ MeV.

From the comparison between our calculations and the experimental data selected in these conditions of peripherality, we obtain $C_{1s1/2} = 0.785 \pm 0.03\,\mathrm{fm}^{-1/2}$ in the g.s. and $C_{0p1/2} = 0.135 \pm 0.005\,\mathrm{fm}^{-1/2}$ in the e.s. Both are in excellent agreement with the *ab initio* predictions of Calci *et al.* ($C^{ab\ initio}_{1/2^+} = 0.786\,\mathrm{fm}^{-1/2}$ and $C^{ab\ initio}_{1/2^-} = 0.129\,\mathrm{fm}^{-1/2}$) [29]. This, adding to the fact that the same value of the g.s. ANC leads to excellent agreements with breakup measurements of ^{11}Be [30,31,40], confirm the accuracy of Calci *et al.*'s predictions.

In conclusion, this work suggests a new, systematic and reliable way to extract from transfer measurements the ANC of loosely bound nuclei, e.g., exhibiting a halo. Our study indicates that investigating transfer reactions at low beam energies and forward angles ensures the reaction to be peripheral, and is hence the best way to obtain a reliable ANC from experimental data. This strong constraint on the asymptotics of these nuclei will help investigate the short-range physics of these nuclei as suggested in Refs. [24,25]. In the near future, we plan to apply this method to other systems, like ^{15}C, for which there exist precise data measured at low energy [12,41]. It would also be interesting to see if this idea can be extended to resonances, like the $\frac{5}{2}^+$ state in ^{11}Be.

ACKNOWLEDGMENTS

We thank A. M. Moro and D. Y. Pang for their support in doing the calculation. This project has received funding from the European Union's Horizon 2020 research and innovation programme under Grant Agreement No. 654002, the PRISMA (Precision Physics, Fundamental Interactions and Structure of Matter) Cluster of Excellence, and the Deutsche Forschungsgemeinschaft through the Collaborative Research Center 1044. J.Y. is supported by the China Scholarship Council (CSC). P.C. is supported by the Federal State of Rhineland-Palatinate. This text presents research results of the Belgian Research Initiative on eXotic nuclei (BriX), Program No. P7/12 on interuniversity attraction poles of the Belgian Federal Science Policy Office.

[1] J. Al-Khalili, in *The Euroschool Lectures on Physics with Exotic Beams*, Vol. I (Springer, Berlin/Heidelberg, 2004), pp. 77–112.
[2] P. G. Hansen and B. Jonson, Europhys. Lett. **4**, 409 (1987).
[3] J. Al-Khalili and F. Nunes, J. Phys. G **29**, R89 (2003).
[4] I. J. Thompson and F. M. Nunes, *Nuclear Reactions for Astrophysics* (Cambridge University Press, Cambridge, 2009).
[5] R. C. Johnson, J. Phys. G: Nucl. Part. Phys. **41**, 094005 (2014).
[6] J. G. Camacho and A. M. Moro, in *The Euroschool Lectures on Physics with Exotic Beams*, Vol. IV (Springer, Berlin/Heidelberg, 2014), pp. 39–66.
[7] G. Potel, G. Perdikakis, B. V. Carlson, M. C. Atkinson, W. H. Dickhoff, J. E. Escher, M. S. Hussein, J. Lei, W. Li, A. O. Macchiavelli, A. M. Moro, F. M. Nunes, S. D. Pain, and J. Rotureau, Euro. Phys. J. A **53**, 178 (2017).
[8] K. Wimmer, J. Phys. G **45**, 033002 (2018).
[9] K. L. Jones, A. S. Adekola, D. W. Bardayan, J. C. Blackmon, K. Y. Chae, K. A. Chipps, J. A. Cizewski, L. Erikson, C. Harlin, R. Hatarik, R. Kapler, R. L. Kozub, J. F. Liang, R. Livesay, Z. Ma, B. H. Moazen, C. D. Nesaraja, F. M. Nunes, S. D. Pain, N. P. Patterson, D. Shapira, J. F. S. Jr., M. S. Smith, T. P. Swan, and J. S. Thomas, Nature (London) **465**, 454 (2010).
[10] K. T. Schmitt, K. L. Jones, A. Bey, S. H. Ahn, D. W. Bardayan, J. C. Blackmon, S. M. Brown, K. Y. Chae, K. A. Chipps, J. A. Cizewski, K. I. Hahn, J. J. Kolata, R. L. Kozub, J. F. Liang, C. Matei, M. Matoš, D. Matyas, B. Moazen, C. Nesaraja, F. M. Nunes, P. D. O'Malley, S. D. Pain, W. A. Peters, S. T. Pittman, A. Roberts, D. Shapira, J. F. Shriner, M. S. Smith, I. Spassova, D. W. Stracener, A. N. Villano, and G. L. Wilson, Phys. Rev. Lett. **108**, 192701 (2012).
[11] K. T. Schmitt, K. L. Jones, S. Ahn, D. W. Bardayan, A. Bey, J. C. Blackmon, S. M. Brown, K. Y. Chae, K. A. Chipps, J. A. Cizewski, K. I. Hahn, J. J. Kolata, R. L. Kozub, J. F. Liang, C. Matei, M. Matos, D. Matyas, B. Moazen, C. D. Nesaraja, F. M. Nunes, P. D. O'Malley, S. D. Pain, W. A. Peters, S. T. Pittman, A. Roberts, D. Shapira, J. F. Shriner, M. S. Smith, I. Spassova, D. W. Stracener, N. J. Upadhyay, A. N. Villano, and G. L. Wilson, Phys. Rev. C **88**, 064612 (2013).
[12] M. McCleskey, A. M. Mukhamedzhanov, L. Trache, R. E. Tribble, A. Banu, V. Eremenko, V. Z. Goldberg, Y.-W. Lui, E. McCleskey, B. T. Roeder, A. Spiridon, F. Carstoiu, V. Burjan, Z. Hons, and I. J. Thompson, Phys. Rev. C **89**, 044605 (2014).
[13] T. L. Belyaeva, R. Perez-Torres, A. A. Ogloblin, A. S. Demyanova, S. N. Ershov, and S. A. Goncharov, Phys. Rev. C **90**, 064610 (2014).
[14] G. Satchler, Nucl. Phys. **55**, 1 (1964).
[15] R. C. Johnson and P. J. R. Soper, Phys. Rev. C **1**, 976 (1970).
[16] R. Johnson and P. Tandy, Nucl. Phys. A **235**, 56 (1974).
[17] N. Austern, Y. Iseri, M. Kamimura, M. Kawai, G. Rawitscher, and M. Yahiro, Phys. Rep. **154**, 125 (1987).
[18] L. D. Faddeev, Zh. Eksp. Teor. Fiz. **39**, 1459 (1960) [Sov. Phys. JETP **12**, 1014 (1961)].
[19] E. Alt, P. Grassberger, and W. Sandhas, Nucl. Phys. B **2**, 167 (1967).
[20] A. Deltuva, Phys. Rev. C **79**, 054603 (2009).
[21] N. K. Timofeyuk, J. Phys. G **41**, 094008 (2014).
[22] L. Blokhintsev, E. Dolinskij, and I. Borbej, Fizika Ehlementarnykh Chastits i Atomnogo Yadra **8**, 1189 (1977).

[23] C. A. Gagliardi, R. E. Tribble, A. Azhari, H. Clark, Y.-W. Lui, A. Mukhamedzhanov, A. Sattarov, L. Trache, V. Burjan, J. Cejpek *et al.*, Phys. Rev. C **59**, 1149 (1999).
[24] A. M. Mukhamedzhanov and F. M. Nunes, Phys. Rev. C **72**, 017602 (2005).
[25] D. Y. Pang, F. M. Nunes, and A. M. Mukhamedzhanov, Phys. Rev. C **75**, 024601 (2007).
[26] S. Igamov, M. Nadirbekov, and R. Yarmukhamedov, Phys. At. Nucl. **70**, 1694 (2007).
[27] C. Bertulani, H.-W. Hammer, and U. van Kolck, Nucl. Phys. A **712**, 37 (2002).
[28] H.-W. Hammer, C. Ji, and D. R. Phillips, J. Phys. G **44**, 103002 (2017).
[29] A. Calci, P. Navrátil, R. Roth, J. Dohet-Eraly, S. Quaglioni, and G. Hupin, Phys. Rev. Lett. **117**, 242501 (2016).
[30] P. Capel, D. R. Phillips, and H.-W. Hammer, Phys. Rev. C **98**, 034610 (2018).
[31] P. Capel, V. Durant, L. Huth, H.-W. Hammer, D. R. Phillips, and A. Schwenk, J. Phys. Conf. Ser. **1023**, 012010 (2018).
[32] P. Capel and F. M. Nunes, Phys. Rev. C **73**, 014615 (2006).
[33] I. J. Thompson, Comput. Phys. Rep. **7**, 167 (1988).
[34] A. Kievsky, M. Viviani, M. Gattobigio, and L. Girlanda, Phys. Rev. C **95**, 024001 (2017).
[35] J. Kelley, E. Kwan, J. Purcell, C. Sheu, and H. Weller, Nucl. Phys. A **880**, 88 (2012).
[36] R. Varner, W. Thompson, T. McAbee, E. Ludwig, and T. Clegg, Phys. Rep. **201**, 57 (1991).
[37] J. A. Tostevin, University of Surrey version of computer code TWOFNR, 2008 (M. Toyama, M. Igarashi, and N. Kishida) and computer code FRONT (private communication).
[38] A. Koning and J. Delaroche, Nucl. Phys. A **713**, 231 (2003).
[39] R. V. Reid, Ann. Phys. **50**, 411 (1968).
[40] L. Moschini and P. Capel, arXiv:1807.07537.
[41] J. D. Goss, P. L. Jolivette, C. P. Browne, S. E. Darden, H. R. Weller, and R. A. Blue, Phys. Rev. C **12**, 1730 (1975).

Appendix C

Paper II

This appendix attaches the following published paper, which contains the work presented in Sec. 3.2.

L. Moschini, J. Yang and P. Capel. ^{15}C: From halo effective field theory structure to the study of transfer, breakup, and radiative-capture reactions. Phys. Rev. C 100, 044615 (2019) [MYC19].

^{15}C: From halo effective field theory structure to the study of transfer, breakup, and radiative-capture reactions

Laura Moschini [1,*], Jiecheng Yang [1,2,†] and Pierre Capel [3,1,‡]

[1]*Physique Nucléaire et Physique Quantique (C.P. 229), Université libre de Bruxelles (ULB), 50 avenue F.D. Roosevelt, B-1050 Brussels, Belgium*

[2]*Afdeling Kern-en Stralingsfysica, Celestijnenlaan 200d-bus 2418, 3001 Leuven, Belgium*

[3]*Institut für Kernphysik, Johannes Gutenberg-Universität Mainz, Johann-Joachim-Becher Weg 45, D-55099 Mainz, Germany*

(Received 13 August 2019; revised manuscript received 23 September 2019; published 25 October 2019)

Background: Aside from being a one-neutron halo nucleus, ^{15}C is interesting because it is involved in reactions of relevance for several nucleosynthesis scenarios.

Purpose: The aim of this work is to analyze various reactions involving ^{15}C, using a single structure model based on halo effective field theory (halo EFT) following the excellent results obtained in [P. Capel *et al.*, Phys. Rev. C **98**, 034610 (2018)].

Method: To develop a halo-EFT model of ^{15}C at next to leading order (NLO), we first extract the asymptotic normalization coefficient (ANC) of its ground state by analyzing ^{14}C$(d, p)^{15}$C transfer data at low energy using the method developed in [J. Yang and P. Capel, Phys. Rev. C **98**, 054602 (2018)]. Using the halo-EFT description of ^{15}C constrained with this ANC, we study the ^{15}C Coulomb breakup at high (605 MeV/nucleon) and intermediate (68 MeV/nucleon) energies using eikonal-based models with a consistent treatment of nuclear and Coulomb interactions at all orders, and which take into account proper relativistic corrections. Finally, we study the ^{14}C$(n, \gamma)^{15}$C radiative capture.

Results: Our theoretical cross sections are in good agreement with experimental data for all reactions, thereby assessing the robustness of the halo-EFT model of this nucleus. Since a simple NLO description is enough to reproduce all data, the only nuclear-structure observables that matter are the ^{15}C binding energy and its ANC, showing that all the reactions considered are purely peripheral. In particular, it confirms the value we have obtained for the ANC of the ^{15}C ground state: $\mathcal{C}^2_{1/2^+} = 1.59 \pm 0.06$ fm^{-1}. Our model of ^{15}C provides also a new estimate of the radiative-capture cross section at astrophysical energy: $\sigma_{n,\gamma}(23.3\,\text{keV}) = 4.66 \pm 0.14\,\mu$b.

Conclusions: Including a halo-EFT description of ^{15}C within precise models of reactions is confirmed to be an excellent way to relate the reaction cross sections and the structure of the nucleus. Its systematic expansion enables us to establish how the reaction process is affected by that structure and deduce which nuclear-structure observables are actually probed in the collision. From this, we can infer valuable information on both the structure of ^{15}C and its synthesis through the ^{14}C$(n, \gamma)^{15}$C radiative capture at astrophysical energies.

DOI: 10.1103/PhysRevC.100.044615

I. INTRODUCTION

The nucleus ^{15}C is interesting for various reasons. On a nuclear-structure viewpoint, ^{15}C is one of the best known one-neutron halo nuclei [1,2]. Due to its small one-neutron separation energy [$S_n(^{15}\text{C}) = 1.218$ MeV], the ground state of ^{15}C is mostly described as a two-body structure, in which the valence neutron is loosely bound in a $1s_{1/2}$ orbital to a ^{14}C in its 0^+ ground state. Thanks to its loose binding and the fact that it sits in an $l = 0$ orbital, the valence neutron exhibits a high probability of presence at a large distance from the other nucleons. It therefore forms like a diffuse halo surrounding a compact core [3]. The existence of halos in some nuclei challenges our view of the nucleus, which is usually seen as a compact object with a nucleon density at saturation. Halo nuclei, including ^{15}C, are thus the focus of many experimental and theoretical studies [1,2].

The study of ^{15}C has also applications in nuclear astrophysics. Its synthesis through one-neutron radiative capture by ^{14}C has been suggested to be part of neutron-induced CNO cycles, which take place in the helium-burning zone of asymptotic-giant-branch (AGB) stars [4]. This ^{14}C$(n, \gamma)^{15}$C reaction is also the doorstep to the production of heavy elements in inhomogeneous big-bang nucleosynthesis [5] and it has been shown to be part of possible reaction routes in the nuclear chart during the r process in Type II supernovae [6]. It is therefore necessary to have a reliable estimate of the cross section for this radiative capture at astrophysical energy, and hence to better understand the structure of ^{15}C.

Because ^{15}C exhibits a short lifetime, its structure cannot be probed with usual spectroscopic techniques. This nucleus is therefore mostly studied through reactions. Transfer, such

*laura.moschini@ulb.ac.be
†jiecyang@ulb.ac.be
‡pcapel@uni-mainz.de

as (d, p), measured in both direct and inverse kinematics, has been used to infer the single-particle structure of ^{15}C [7–10]. In breakup, the lose binding of the valence neutron to the core is broken up during the collision of the nucleus on a target, hence revealing its internal core-n structure. Various experimental campaigns have been set up to measure the inclusive breakup—also known as knockout—of ^{15}C on light targets at intermediate beam energies [11–13]. In these measurements, only ^{14}C is detected after the reaction, and information pertaining to the single-particle structure of ^{15}C is inferred from the analysis of the parallel-momentum distribution of the core. In Refs. [14,15], the Coulomb (exclusive) breakup of ^{15}C has been measured. In that case, both the ^{14}C core and the halo neutron are detected in coincidence after the dissociation of the ^{15}C projectile on a Pb target. Being dominated by the Coulomb interaction, this reaction process is rather clean as it exhibits little dependence on the choice of the optical potentials used to describe the nuclear interaction between the projectile constituents (core and n) with the target.

In addition to its interest in the study of the halo structure of ^{15}C, Coulomb breakup has also been suggested as an indirect method to deduce the cross section for the ^{14}C$(n, \gamma)^{15}$C radiative capture at low energies [16,17]. The idea behind the Coulomb-breakup method is that this dissociation, which is often described as resulting from the exchange of virtual photons between the projectile and the heavy target [18], can be seen as the time-reversed reaction of the radiative capture, where a (real) photon is emitted following the capture of a neutron by the core. Later analyses have shown that the breakup process is not that simple and that higher-order effects spoil this nice picture [19,20]. However, it has been suggested that the Coulomb-breakup measurements could be used to infer the asymptotic normalization coefficient (ANC) of the ^{15}C ground-state wave function [21]. However, due to the aforementioned higher-order effects, a precise model of the reaction is needed in the analysis of the reaction [21–23]. Because the radiative capture ^{14}C$(n, \gamma)^{15}$C is a purely peripheral process [24], a reliable estimate of this ANC can then be used to compute its cross section. Following Ref. [24], it has also been suggested to rely on the strong sensitivity of transfer reaction to the single-particle structure of the nucleus to measure the ANC of the ^{15}C ground-state wave function for that purpose [10]. Since the radiative capture ^{14}C$(n, \gamma)^{15}$C has been measured directly by Reifarth *et al.* [25], the ^{15}C case provides the opportunity to test the validity of the different indirect methods listed above.

In the present work, we reanalyze the transfer [7,10], Coulomb-breakup [14,15], and radiative-capture [25] measurements using one single description of the one-neutron halo nucleus ^{15}C. For this, we follow the recent idea developed in Ref. [26] and include, within precise models of reactions, a description of the nucleus based on halo effective field theory (halo EFT) [27] (see Ref. [28] for a recent review). Halo EFT exploits the natural separation of scales that is observed in halo nuclei—viz. the difference between the small size of the core $R_{\rm core}$ and the large extension of the halo $R_{\rm halo}$—to build an effective Hamiltonian constructed as an expansion in powers of the small parameter $R_{\rm core}/R_{\rm halo}$. This allows us to introduce, order by order, the different nuclear-structure parameters in the description of the nucleus within the reaction models, and thereby to deduce how each of them affects the reaction processes. This puts a strong constraint on what can be learned about the structure of ^{15}C from transfer and breakup experiments and how this nuclear-structure information relates to the direct radiative-capture capture measurement of Ref. [25].

This paper is structured as follows. In Sec. II we introduce the halo-EFT description of ^{15}C and explain how it is fitted at next to leading order (NLO). Using this description, we reanalyze transfer measurements at $E_d = 14$ [7] and 17.06 MeV [10] in Sec. III. In Sec. IV we use the same ^{15}C structure to study its breakup at high (605 MeV/nucleon [14]) and intermediate (68 MeV/nucleon [15]) energy. In Sec. V, we study the ^{14}C$(n, \gamma)^{15}$C radiative capture [25]. Finally, in Sec. VI, we summarize our results and provide the outlook for future work.

II. HALO-EFT DESCRIPTION OF ^{15}C

A. Single-particle structure of ^{15}C

Being a one-neutron halo nucleus, ^{15}C can be modeled as a neutron loosely bound to a ^{14}C core. With the assumption that the ^{14}C core is in its ground state (0^+), the $\frac{1}{2}^+$ ground state (g.s.) of ^{15}C can be described by a $^{14}\text{C}(0^+) \otimes 1s_{1/2}$ configuration and its $\frac{5}{2}^+$ excited state (e.s.) by a $^{14}\text{C}(0^+) \otimes 0d_{5/2}$. These states have an energy relative to the one-neutron threshold of $E_{\rm g.s.} = -1.218$ MeV and $E_{\rm e.s.} = -0.478$ MeV, respectively.

To model this system, the core A of mass m_A and charge $Z_A e$ is assumed to be of spin and parity 0^+ and we neglect its internal structure. The halo nucleus $B = A + n$ is thus of mass $m_B = m_A + m_n$, with m_n the neutron mass, and charge $Z_B e = Z_A e$. Such a two-body structure is described by the internal Hamiltonian

$$H_0 = -\frac{\hbar^2 \Delta}{2\mu_{An}} + V_{An}(\boldsymbol{r}), \tag{1}$$

where $\boldsymbol{r}$ is the A-n relative coordinate, $\mu_{An} = m_A m_n/m_B$ is their reduced mass, and V_{An} is the effective potential simulating their interaction. In partial wave $l\,jm$, the eigenstates of H_0 read

$$H_0\, \varphi_{l\,jm}(E_{lj}, \boldsymbol{r}) = E_{lj}\, \varphi_{l\,jm}(E_{lj}, \boldsymbol{r}), \tag{2}$$

where j is the total angular momentum resulting from the coupling of the orbital angular momentum l with the spin of the halo neutron and m is its projection. The eigenstates of H_0 of negative energy $E_{n'lj}$ are discrete and correspond to the bound states of the two-body model of the projectile B. These include physical A-n bound states of the system as well as Pauli forbidden states, which simulate the presence of neutrons within the core A. We enumerate them by adding the number of nodes in the radial wave function n' to the other quantum numbers. They are normed to unity and their reduced radial wave function behaves asymptotically as

$$u_{n'lj}(r) \underset{r\to\infty}{\longrightarrow} b_{n'lj}\, ik_{n'lj} r\, h_l^{(1)}(ik_{n'lj} r), \tag{3}$$

where $\hbar k_{n'lj} = \sqrt{2\mu_{An}|E_{n'lj}|}$, with $|E_{n'lj}|$ the A-n binding energy, and $h_l^{(1)}$ is a spherical Bessel function of the third

kind [29]. The single-particle asymptotic normalization constant (SPANC) $b_{n'lj}$ defines the strength of the exponential tail of the A-n bound-state wave function [30]. This SPANC will vary with the geometry of the potential used to simulate the A-n interaction [31–34]. The asymptotic behavior (3) is universal, therefore it exists also in the actual structure of the nucleus, viz. in the overlap wave function obtained within a microscopic calculation of the nucleus [33,35]. Being affected by the inherent couplings between the different configurations in the actual structure of the nucleus, in particular those involving the core in one of its excited states, the true asymptotic normalization constant (ANC) of the overlap wave function of the physical state of spin and parity J^π corresponding to the configuration in which the core is in its 0^+ ground state, $\mathcal{C}_{J^\pi}$, differs from the SPANC $b_{n'lj}$ obtained in the effective single-particle description considered here [33,35].

The positive-energy states describe the A-n continuum, i.e., the broken-up projectile. Their reduced radial parts are normalized according to

$$u_{klj} \underset{r\to\infty}{\longrightarrow} kr[\cos\delta_{lj}\; j_l(kr) + \sin\delta_{lj}\; n_l(kr)], \tag{4}$$

where δ_{lj} is the phase shift at energy E_{lj} and $\hbar k = \sqrt{2\mu_{An}E_{lj}}$; j_l and n_l are spherical Bessel functions of the first and second kinds, respectively [29].

As mentioned above, the A-n interaction is described by an effective potential V_{An}. In this study, following the idea developed in Ref. [26], this potential is built within a halo-EFT description of the nucleus [27,28]. At the leading order (LO), this interaction consists of a simple contact term within the sole s wave. As usual, this interaction is regularized with a Gaussian

$$V_{An}^{\rm LO}(r) = V_0^{s1/2} e^{-\frac{r^2}{2r_0^2}}. \tag{5}$$

The range of the Gaussian r_0 corresponds to the scale of the short-range physics neglected in this halo-EFT description. Changing its value will enable us to generate different single-particle wave functions to describe the ^{14}C-n system and hence test the sensitivity of our reaction calculations to the internal part of the wave function of the projectile. At LO, the only free parameter $V_0^{s1/2}$ is adjusted to reproduce $E_{\rm g.s.} = -1.218$ MeV within a $1s_{1/2}$ orbit.

At next-to-leading order (NLO), the interaction is extended up to the p waves and contains, in addition to the contact term its second-order derivative. For simplicity, we follow Ref. [26] and use the equivalent following parametrization of the interaction:

$$V_{An}^{\rm NLO}(r) = V_0^{lj} e^{-\frac{r^2}{2r_0^2}} + V_2^{lj} r^2 e^{-\frac{r^2}{2r_0^2}}. \tag{6}$$

To constrain the potential parameters $V_0^{s1/2}$ and $V_2^{s1/2}$ in the s wave, we need two structure observables: in addition to the binding energy of the state, we also use its ANC. Various groups have estimated this ANC from reaction data [10,21,24,31,36,37]. In this work, we use the method presented in Ref. [38] to deduce this ANC from low-energy transfer data selected at forward angle (see Sec. II B).

Unlike ^{11}Be, ^{15}C does not exhibit any low-lying bound or resonant $\frac{3}{2}^-$ or $\frac{1}{2}^-$ states to which we could fit the effective interaction (6) in the p waves. Therefore, true to the spirit of halo EFT, we set this interaction to 0 in the $p_{3/2}$ and $p_{1/2}$ partial waves. Interestingly, this treatment is in agreement with preliminary results obtained in an *ab initio* calculation of ^{15}C performed within the no-core shell model with continuum (NCSMC), which predicts negligible phase shifts at low ^{14}C-n energies in both p waves [39].

At NLO, the interaction V_{An} is nil in higher partial waves. Since the $\frac{5}{2}^+$ excited bound state of ^{15}C plays a role in the radiative capture (see Sec. V), we follow the idea of Ref. [26] and go beyond NLO to include a $0d_{5/2}$ state at $E_{\rm e.s.} = -0.478$ MeV. The potential in that partial wave is chosen similar to that of Eq. (6). We fit the depths $V_0^{d5/2}$ and $V_2^{d5/2}$ to reproduce the experimental binding energy of the $\frac{5}{2}^+$ state and the ANC deduced from transfer data.

B. Extraction of the ANC of the ^{15}C bound states from the analysis of low-energy transfer reactions

To obtain a reliable estimate of the ANC of both bound states of ^{15}C, we follow the idea developed in Ref. [38] and reanalyze ^{14}C$(d,p)^{15}$C transfer data. In that reference, it was found that (d,p) transfer reactions are purely peripheral when they are performed at low beam energy (viz. $E_d \lesssim 15$ MeV) and when the data are selected at forward angles. Within these experimental conditions, the transfer cross section scales perfectly with the square of the final-state ANC $\mathcal{C}^2_{J^\pi}$. That value can then be reliably extracted from a comparison between reaction calculations performed using a single-particle description of the nucleus similar to the one presented in Sec. II A and experimental data [38].

We therefore need ^{14}C$(d,p)^{15}$C transfer data measured at low energies, and which contain enough data points at forward angles for this extraction of the ANC of ^{15}C to be statistically meaningful. Two experiments satisfying the low-energy condition have been performed: one at the University of Notre Dame at $E_d = 14$ MeV [7], and another at the Nuclear Physics Institute of the Czech Academy of Sciences at $E_d = 17.06$ MeV [10]. Unfortunately, the former contains only one point at $\theta < 15^\circ$, which we deem not enough for this extraction. Fortunately, although performed at a slightly higher energy, the latter experiment contains six points at $\theta < 12^\circ$, which seems enough to constrain the ANC within proper peripheral conditions (see below).

Following the method presented in Ref. [38], we couple a leading-order (LO) halo-EFT description of ^{15}C with a finite-range adiabatic distorted wave approximation (FR-ADWA) model [40]. This model provides a reliable description of transfer reactions at these energies [41,42]. As in Ref. [38], we consider the CH89 global potential [43] to generate the optical potentials in the incoming (d-^{14}C) and outgoing (p-^{15}C) channels. The Reid soft-core potential [44] is used to compute the deuteron bound state. The deuteron adiabatic potentials are obtained with the front-end code of TWOFNR [45] and the transfer calculations are performed using FRESCO [46]. We illustrate here the results for the ground state, the method to extract the ANC of the excited state is analogous, though less efficient because it corresponds to a d ^{14}C-n bound state (see Ref. [38] for the details).

TABLE I. Potentials describing $^{14}C + n$ g.s. at LO [see Eq. (5)] and corresponding single-particle asymptotic normalization constant (SPANC) $b^{(r_0)}_{1s1/2}$. They are adjusted on the one-neutron binding energy.

r_0 (fm)	$V_0^{s1/2}$ (MeV)	$b^{(r_0)}_{1s1/2}$ (fm$^{-1/2}$)
0.6	−591.05	0.865
0.8	−339.87	0.934
1.0	−222.43	1.01
1.2	−157.95	1.09
1.4	−118.68	1.17
1.6	−92.933	1.26
1.8	−75.095	1.36
2.0	−62.212	1.46

We first build eight Gaussian potentials at the LO of halo EFT [see Eq. (5)] considering different ranges r_0 between 0.6 fm and 2.0 fm. For each width the depth $V_0^{s1/2}$ is adjusted to reproduce the neutron binding energy in the ^{15}C final state (see Table I). These potentials provide different single-particle radial wave functions $u_{1s1/2}$ with very different SPANCs $b^{(r_0)}_{1s1/2}$, but also a significant change in the surface part of the nucleus, i.e., in the range $2\,\text{fm} \lesssim r \lesssim 4$ fm, see Fig. 1. This is the corner stone of the method developed in Ref. [38], because it is known that transfer reactions can be sensitive to that region [33,37]. Using single-particle wave functions that strongly differ, not only in their SPANC, but also in their shape within that surface region will enable us to accurately determine the conditions under which the reaction is purely peripheral, and thus under which a reliable estimate of the actual ANC of the nucleus can be inferred.

With this input, we compute within the FR-ADWA [40] the corresponding theoretical differential cross section $d\sigma_{\text{th}}/d\Omega$ for the transfer to the ^{15}C g.s. at $E_d = 17.06$ MeV [10], expressed as a function of the relative direction $\Omega = (\theta, \phi)$ between the proton and the ^{15}C in the outgoing channel. These results are displayed in Fig. 2(a) for the eight g.s. wave functions shown in Fig. 1. At forward angles, the cross

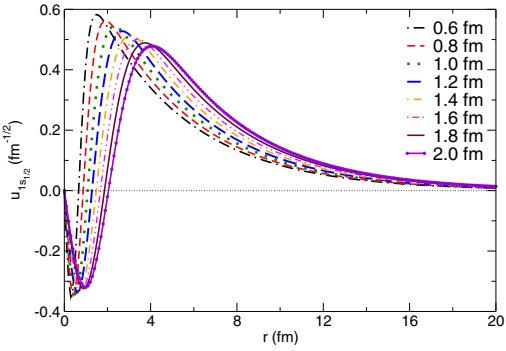

FIG. 1. Reduced radial wave functions of the ^{15}C g.s. obtained with LO Gaussian potentials of Table I.

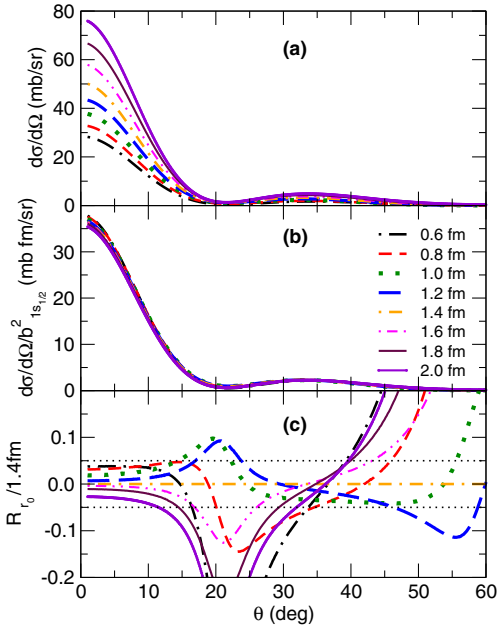

FIG. 2. Analysis of the differential cross section of $^{14}C(d, p)^{15}C$ (g.s.) for the deuteron energy $E_d = 17.06$ MeV. The results of the FR-ADWA calculations are presented for every wave function of Fig. 1.

sections exhibit a huge sensitivity to the choice of the ^{14}C-n wave function. They seem to scale with the square of the SPANC, as one would expect if the process were purely peripheral [38]. To confirm this, we have plotted the transfer cross section scaled by $b^2_{1s1/2}$ in Fig. 2(b). In this way, the spread in the results is significantly reduced at forward angles.

To precisely determine within which angular range the data should be limited to select strictly peripheral conditions, we remove the major angular dependence by considering the ratio

$$\mathcal{R}_{r_0/1.4\,\text{fm}}(\theta) = \left(\frac{b^{(1.4\,\text{fm})}_{n'lj}}{b^{(r_0)}_{n'lj}}\right)^2 \frac{d\sigma^{(r_0)}_{\text{th}}/d\Omega}{d\sigma^{(1.4\,\text{fm})}_{\text{th}}/d\Omega} - 1, \qquad (7)$$

where the transfer cross section computed using the ^{14}C-n Gaussian potential of range r_0, scaled by the square of the corresponding SPANC $b^{(r_0)}_{1s1/2}$, is divided by the result obtained with $r_0 = 1.4$ fm, which is at the center of the range in r_0. The results are displayed in Fig. 2(c). We see that all ratios $\mathcal{R}_{r_0/1.4\,\text{fm}}$ fall very close to one another at small angles, confirming the peripherality of the reaction when data measured at low beam energy are selected in the forward direction. To define an angular range in which the reaction can be considered as peripheral, we consider a maximum of 5% difference [horizontal black dotted lines in Fig. 2(c)]. In this case, this happens only at very forward angles, viz. when $\theta <$ 12°. There are six data points within this angular region in this

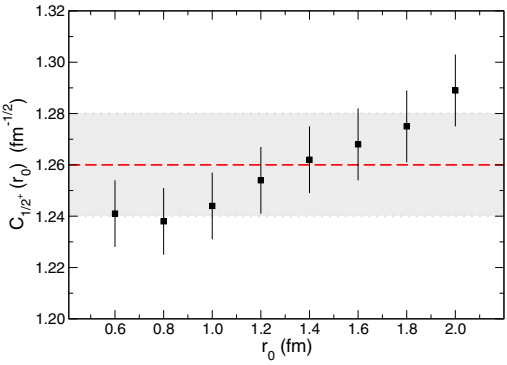

FIG. 3. ANCs extracted for the ^{15}C g.s. for each wave function of Fig. 1. Our recommended value is displayed by the horizontal red dashed line (the gray band represents its uncertainty).

experiment [10]. Note that there is no data available within this angular range in the case of the experiment performed at the lower energy $E_d = 14$ MeV [7].

Having determined the angular region within which the process is purely peripheral, we extract the value of the ANC $\mathcal{C}_{1/2^+}(r_0)$ for each of the single-particle wave functions shown in Fig. 1. This is done by scaling, through a χ^2 minimization, the corresponding theoretical cross section to the data selected at $\theta < 12^\circ$ [38]. The ANCs $\mathcal{C}_{1/2^+}(r_0)$ obtained in this way are shown in Fig. 3 as a function of the potential width r_0. The error bars correspond to the uncertainty in the χ^2 minimization. Despite the huge changes in the radial wave functions observed in Fig. 1, the ANCs extracted are nearly independent of r_0; they fall within 4% from each other. This is similar to what was obtained for ^{11}Be (see Fig. 8 of Ref. [38]), hence confirming the validity of the method.

To deduce an estimate of the actual ANC $\mathcal{C}_{1/2^+}$, we average the $\mathcal{C}_{1/2^+}(r_0)$ results and get $\mathcal{C}_{1/2^+} = 1.26 \pm 0.02$ fm$^{-1/2}$ ($\mathcal{C}^2_{1/2^+} = 1.59 \pm 0.06$ fm^{-1}) displayed as the horizontal red dashed line and gray band in Fig. 3. Following the same process, we obtain for the e.s. an estimate of the ANC of $\mathcal{C}_{5/2^+} = 0.056 \pm 0.001$ fm$^{-1/2}$.

We compare our estimate with values extracted from the analysis of other experiments in Table II. Though on the lower end of the range, the ANC we obtain agrees with most of the others. Our value is within the uncertainty band of the ANC extracted from knockout measurements in Ref. [36], which is not surprising because that reaction is mostly peripheral [47]. Compared to the value extracted from the width of the $\frac{1}{2}^+$ ground state of the proton-unbound mirror nucleus ^{15}F, our $\mathcal{C}_{1/2^+}$ seems too low. However, as explained in Ref. [48], that resonant state being quite broad, its width used in this analysis might be marred with significant uncertainty. In Ref. [37], Pang *et al.* have used the aforementioned ^{14}C$(d, p)^{15}$C transfer data measured at $E_d = 14$ MeV [7], which have not enough points at forward angles to be purely peripheral. Its large value is most likely due to that issue. Note also that the normalization of the $E_d = 14$ MeV data has been questioned in Ref. [10]. Interestingly, we are in excellent agreement with the value obtained by Summers and Nunes in their analysis [21] of the Coulomb-breakup cross section of ^{15}C measured at RIKEN [15]. Since this reaction is very peripheral [23,49], this is not surprising (see Sec. IV B). Our ANC is also perfectly compatible with the value extracted from the same data at $E_d = 17.06$ MeV in Ref. [10]. The $\mathcal{C}_{1/2^+}$ we have obtained is on the lower end of the uncertainty range of the value extracted from the ^{13}C(^{14}C, ^{15}C)^{12}C and $d(^{14}$C, $p)^{15}$C transfer experiments in Ref. [31]. However, these experiments have been performed at energies corresponding to $E_d \approx 24$ MeV, where the reaction is not fully peripheral [38], which may explain the slight disagreement with our ANC.

TABLE II. Comparison of $\mathcal{C}^2_{1/2^+}$ inferred for the ^{15}C g.s. from various works.

$\mathcal{C}^2_{1/2^+}$ (fm^{-1})	Ref.	Method
1.48 ± 0.18	[36]	Knockout
1.89 ± 0.11	[24]	Mirror symmetry
2.14	[37]	Transfer
1.74 ± 0.11	[21]	Coulomb breakup
1.64 ± 0.26	[10]	Transfer
1.88 ± 0.18	[31]	Transfer
1.59 ± 0.06	this work	Transfer

The value we have obtained from the method developed in Ref. [38] is therefore in good agreement with most of the values cited in the literature, and the differences we observe with previous analyses can be explained from uncertainties in these analyses. Incidentally, as was observed in our previous analysis of the ^{10}Be$(d, p)^{11}$Be transfer [38], this ANC for the ground state of ^{15}C is in excellent agreement with the $\mathcal{C}^2_{1/2^+} = 1.644$ fm^{-1} obtained by Navrátil *et al.* in the aforementioned *ab initio* calculation of this one-neutron halo nucleus [39]. The present work will therefore provide a stringent test of the value predicted in that NCSMC calculation.

C. Halo-EFT description of ^{15}C at NLO

Having inferred a reliable value of the ANC for the ^{15}C g.s., we can now proceed as suggested in Ref. [26] and adjust a NLO halo-EFT potential (6) to describe this nucleus within our reaction models. In the $s_{1/2}$ partial wave, the two depths of the Gaussian potential are fitted to reproduce the experimental binding energy of the halo neutron to the core and our ANC. As in Refs. [26,50], we perform this fit for three different ranges r_0 to test the sensitivity of our reaction calculations to the short-range physics of the ^{14}C-n overlap wave function. The depths obtained by these fits are listed in Table III.

As mentioned earlier, the interaction in the p wave is set to zero, in agreement with preliminary results of the *ab initio* calculations [39]. In Table III, we also provide the depths for ^{14}C-n potentials in the $d_{5/2}$ partial wave, which are fitted to reproduce the binding energy and ANC of the $\frac{5}{2}^+$ excited bound state of ^{15}C. This goes beyond the NLO of halo EFT,

TABLE III. Potentials describing $^{14}\mathrm{C}+n$ g.s. and e.s. [see Eq. (6)]. They are adjusted on the corresponding one-neutron binding energy and ANC.

r_0 (fm)	$V_0^{s1/2}$ (MeV)	$V_2^{s1/2}$ (MeV fm^{-2})	$V_0^{d5/2}$ (MeV)	$V_2^{d5/2}$ (MeV fm^{-2})
1.2	−3.1995	−71.3	169.299	−92.368
1.5	−92.814	−2.70	−91.000	−9.000
2.0	−80.827	2.70	−94.916	2.53

but it will enable us to check the influence of the presence of that state in the ^{15}C spectrum in reaction calculations [26].

Figure 4 displays the $1s_{1/2}$ single-particle radial wave functions generated by the three potentials of Table III. By construction, they exhibit the identical behavior in the asymptotic region, viz. for $r \gtrsim 4$ fm. However, as expected, the three wave functions exhibit significant differences at short distances, which will enable us to test the sensitivity to the short-range physics of ^{15}C of the various reactions we consider in the following.

III. TRANSFER REACTION ^{14}C$(d, p)^{15}$C

We start our analysis of the reactions involving ^{15}C using the NLO description developed in Sec. II C by looking at how it behaves in transfer reactions. We consider the low-energy reactions measured at $E_d = 17.06$ MeV [10] and $E_d = 14$ MeV [7]. We use the same FR-ADWA model [40] and potentials employed to extract the ANC in the previous section.

Figure 5 displays the cross sections for the $^{14}\mathrm{C}(d, p)^{15}\mathrm{C}$ transfer reaction obtained at [Fig. 5(a)] $E_d = 17.06$ MeV and [Fig. 5(b)] $E_d = 14$ MeV. The results of the FR-ADWA calculations for each of the three ranges of the Gaussian NLO potential (6) are shown in the same colors and line types as the corresponding radial wave functions in Fig. 4. The green band shows the uncertainty in the cross sections, obtained with the Gaussian potential of range $r_0 = 1.5$ fm, related to the uncertainty in the ANC we have extracted in Sec. II B. For comparison, we also show the results obtained with the LO description of ^{15}C using $r_0 = 1.4$ fm (purple dashed line).

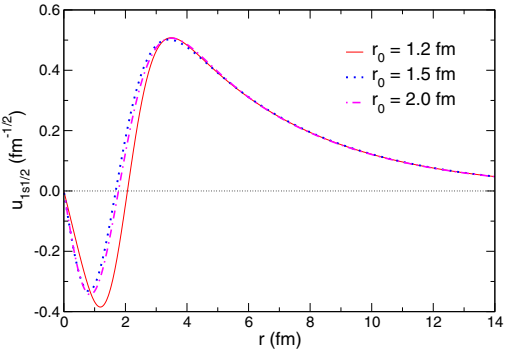

FIG. 4. Reduced radial wave functions of the ^{15}C g.s. obtained with the NLO halo EFT potentials of Table III.

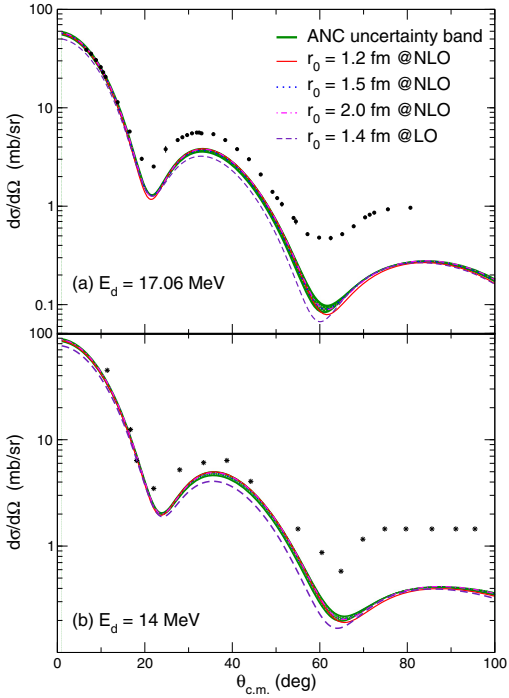

FIG. 5. Cross sections for the $^{14}\mathrm{C}(d, p)^{15}\mathrm{C}$ transfer reaction obtained at (a) $E_d = 17.06$ MeV and (b) $E_d = 14$ MeV. FR-ADWA calculations performed with the NLO descriptions of ^{15}C of Sec. II C are compared to experimental data from (a) Ref. [10] and (b) Ref. [7]. The green band shows the effect of the uncertainty on the ANC upon the calculation.

At $E_d = 17.06$ MeV, without much surprise, the agreement of our NLO calculations with the data is perfect at forward angle since this is the region within which the fit has been performed in Sec. II B. The transfer cross section obtained with the LO description of ^{15}C misses the data by a factor that corresponds to the value of the ANC, which is not fitted at this order. This confirms the importance of fitting both the energy and the ANC of the bound state to correctly reproduce the data. All three NLO ^{14}C-n potentials provide the same cross section in the angular range of peripherality of the reaction, viz. $\theta < 12^\circ$. The agreement between the different wave functions actually extends beyond that range. At larger angles, however, the transfer cross sections obtained with the three different single-particle $1s_{1/2}$ wave functions differ from one another, confirming that, at large angles, the reaction is sensitive to the short-range physics in ^{15}C. The uncertainty band encompasses the error bars of the forward-angle data, but cannot explain the discrepancy between our calculations and

the experimental points at large angles. This shows the limit of the present approach: Halo-EFT provides a proper low-energy—viz. large distances—description of the projectile, but, by construction, does not account for the details of the internal part of the ^{15}C wave function. Hopefully, including a more precise wave function of the projectile could improve the description of the data at large angles. This could be done, e.g., using the overlap wave function provided by the *ab initio* calculation of Navrátil *et al.* [39]. Alternatively, one could use a more elaborated two-body model of ^{15}C, e.g., including core excitation [51].

IV. COULOMB BREAKUP OF ^{15}C

We now turn to the Coulomb breakup of ^{15}C. As mentioned in Sec. I, this reaction has been measured on a lead target twice at two different energies. First at GSI at 605 MeV/nucleon by Datta Pramanik *et al.* [14] and second at RIKEN at 68 MeV/nucleon by Nakamura and his collaborators [15]. These two experiments are similar to those performed previously on the one-neutron halo nucleus ^{11}Be [52,53], which were recently successfully analyzed using a halo-EFT description of ^{11}Be [26,50]. We therefore follow these references and apply the same models of the reaction using the NLO description of ^{15}C detailed in Sec. II C.

A. Breakup of ^{15}C on lead at 605 MeV/nucleon

To analyze the breakup cross section of ^{15}C measured on Pb at GSI at 605 MeV/nucleon [14], we follow what we did in Ref. [50] and use an eikonal-based model of the reaction [54,55], which properly accounts for special relativity.

In that model, the projectile B is described by the two-body system introduced in Sec. II: a core A, to which a neutron n is loosely bound, and which interact through the NLO halo-EFT potential adjusted in Sec. II C. The target T is seen as a structureless body of mass m_T and charge $Z_T e$, which interacts with the projectile constituents A and n through the potentials V_{AT} and V_{nT}, respectively. We solve the problem within the Jacobi set of coordinates composed of the internal coordinate of the projectile $\boldsymbol{r}$ [see Eq. (1)] and the relative coordinate of the projectile center of mass to the target $\boldsymbol{R}$. The latter is explicitly decomposed into its longitudinal Z and transverse $\boldsymbol{b}$ components relative to the incoming beam axis.

At this high beam energy, the use of the eikonal approximation is fully justified as well as the usual adiabatic—or sudden—treatment of the projectile dynamics during the reaction, i.e., we neglect the change in the projectile internal energy in comparison with its kinetic energy. To properly account for special relativity, we follow Satchler [56] and derive the eikonal wave function, which describes the projectile-target relative motion, from the Klein-Gordon equation expressed within the B-T center-of-momentum (CM) frame [56,57]. Within this description of the reaction, the three-body wave function exhibits the following asymptotic behavior

$$\Psi^{(m_0)}(\boldsymbol{R},\boldsymbol{r}) \underset{Z\to+\infty}{\longrightarrow} e^{iK_0 Z} e^{i\chi(\boldsymbol{b},\boldsymbol{r})} \varphi_{n'_0 l_0 j_0 m_0}(\boldsymbol{r}), \tag{8}$$

where $\hbar K_0$ is the initial B-T momentum, χ is the eikonal phase that accounts for the interaction between the target and the projectile constituents, and $\varphi_{n'_0 l_0 j_0 m_0}$ is the wave function of the projectile ground state, in which it is assumed to be initially. Formally, the eikonal phase χ reads [54,55]

$$\chi(\boldsymbol{b},\boldsymbol{r}) = -\frac{1}{\hbar v}\int_{-\infty}^{\infty} [V_{AT}(\boldsymbol{R},\boldsymbol{r}) + V_{nT}(\boldsymbol{R},\boldsymbol{r})]\, dZ, \tag{9}$$

where v is the B-T relative velocity. This phase can be interpreted semiclassically by seeing the projectile B following a straight-line trajectory at fixed impact parameter $\boldsymbol{b}$ along which its wave function accumulates a complex phase due to its interaction with the target. It is composed of three terms: $\chi = \chi^C_{BT} + \chi^C + \chi^N$. The first $\chi^C_{BT}(b) = 2\eta \ln(K_0 b)$, with $\eta = Z_B Z_T e^2/4\pi\epsilon_0 \hbar v$, the Sommerfeld parameter of the reaction, simply describes the Coulomb scattering of the projectile by the target [58]. It does not depend on $\boldsymbol{r}$, and hence does not contribute to the breakup of B. The second

$$\chi^C(\boldsymbol{b},\boldsymbol{r}) = \eta\int_{-\infty}^{\infty}\left(\frac{1}{\left|\boldsymbol{R} - \frac{m_n}{m_B}\boldsymbol{r}\right|} - \frac{1}{R}\right) dZ \tag{10}$$

is the Coulomb term that contributes to the excitation of the projectile. This phase diverges because the infinite range of the Coulomb interaction is not compatible with the sudden approximation, which assumes that the collision takes place in a short time. To solve this issue, we use the Coulomb correction to the eikonal model (CCE) detailed in Refs. [59,60]. In that correction, the diverging eikonal Coulomb phase (10) is replaced at the first order by the first order of the perturbation theory [60]

$$e^{i\chi^C} \to e^{i\chi^C} - i\chi^C + i\chi^{\mathrm{FO}}. \tag{11}$$

For the first-order estimate of the Coulomb phase, we consider the relativistic expression limited to the E1 term [18]

$$\chi^{\mathrm{FO}}(\boldsymbol{b},\boldsymbol{r}) = -\eta\frac{m_n}{m_B}\frac{2\omega}{\gamma v}\left[K_1\left(\frac{\omega b}{\gamma v}\right)\frac{\boldsymbol{b}\cdot\boldsymbol{r}}{b} + i\frac{1}{\gamma}K_0\left(\frac{\omega b}{\gamma v}\right)Z\right], \tag{12}$$

where $\gamma = 1/\sqrt{1 - v^2/c^2}$.[1]

The third term of the eikonal phase χ^N corresponds to the nuclear interaction. At low and intermediate energies, it is usually described by optical potentials fitted to reproduce elastic-scattering cross sections. At high energy, and especially for exotic nuclei, it is difficult to find appropriate potentials. Therefore, we rely on the optical limit approximation (OLA) of the Glauber theory [54,58], which has been successfully used in previous studies [50,61]. In that approximation, the nuclear eikonal phase is obtained by averaging a profile function Γ_{NN}, which simulates the nucleon-nucleon

[1]Note the difference with Ref. [50], where we had considered for the calculation of γ the velocity of the projectile in the CM rest frame. Note also the correct formulation of our equation (12) with the $1/\gamma$ factor (check Eq. (2.15) of Ref. [18]). These corrections have little effect on our results.

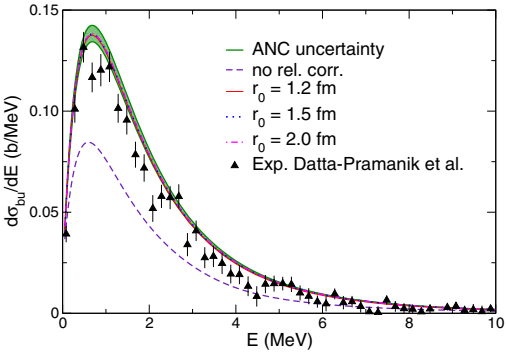

FIG. 6. Breakup cross section of ^{15}C on Pb at 605 MeV/nucleon as a function of the relative energy E between the ^{14}C core and the neutron after dissociation. The results are obtained with the NLO halo-EFT ^{14}C-n interactions listed in Tab. III. The green band represents the uncertainty on the ^{15}C g.s. ANC. For comparison with the GSI data of Ref. [14], the theoretical predictions have been folded with the experimental energy resolution [52]. The result of the calculation without relativistic correction is shown as the purple dashed line.

interaction, over the density of the colliding nuclei

$$\chi_{xT}^{\mathrm{OLA}}(\boldsymbol{b}_x) = i \iint \rho_T(\boldsymbol{r}')\rho_x(\boldsymbol{r}'')\Gamma_{NN}(\boldsymbol{b} - \boldsymbol{s}' + \boldsymbol{s}'')d\boldsymbol{r}''d\boldsymbol{r}', \tag{13}$$

where x stands for either A or n, the two constituents of the projectile, and where $\boldsymbol{s}'$ and $\boldsymbol{s}''$ are the transverse components of the internal coordinate of the target ($\boldsymbol{r}'$) and x ($\boldsymbol{r}''$), respectively. In our three-body model of the reaction, the nuclear eikonal phase thus reads

$$\chi^N(\boldsymbol{b}, \boldsymbol{r}) = \chi_{AT}^{\mathrm{OLA}}(\boldsymbol{b}_A) + \chi_{nT}^{\mathrm{OLA}}(\boldsymbol{b}_n). \tag{14}$$

We consider the usual form of the profile function

$$\Gamma_{NN}(b) = \frac{1 - i\alpha_{NN}}{4\pi\beta_{NN}}\sigma^{\mathrm{tot}} e^{-\frac{b^2}{2\beta_{NN}}}, \tag{15}$$

where σ^{tot} is the total cross section for the NN collision, α_{NN} corresponds to the ratio of the real to the imaginary part of the NN-scattering amplitude, and β_{NN} is the slope of NN elastic differential cross section. These parameters are isospin dependent, which means that, in practice, the OLA phase (13) splits into four terms. For the parameters of Eq. (15) we use the values provided in Ref. [62] for an energy of 650 MeV. The densities used in Eq. (13) for the ^{14}C core and the ^{208}Pb target are approximated by the two-parameter Fermi distributions of Ref. [63], in which the authors study a systematization of nuclear densities based on charge distributions extracted from electron-scattering experiments as well as on theoretical densities derived from Dirac-Hartree-Bogoliubov calculations. For ρ_n, we consider a Dirac δ function.

The breakup cross sections obtained with this model of reaction are displayed in Fig. 6 as a function of the relative energy E between the ^{14}C core and the neutron after dissociation. To enable the comparison with the experimental data of Ref. [14], all theoretical cross sections have been folded with the experimental energy resolution, which we have considered identical to the one provided by Palit *et al.* in the analysis of the Coulomb breakup of ^{11}Be measured at GSI [52]. The calculations performed with all three ^{14}C-n potentials listed in Table III are shown. The sensitivity of our calculations to the uncertainty in the ^{15}C g.s. ANC extracted in Sec. II B is shown by the green band. The result of the calculation obtained without relativistic corrections is displayed as the purple dashed line. This clearly demonstrates the significance of these corrections at this beam energy.

Let us first note that our theoretical predictions are in excellent agreement with the data at all energies. As expected, we do not note any appreciable difference between the calculations performed with the different halo-EFT wave functions (see Fig. 4). This result confirms that this reaction is purely peripheral, in the sense that it is sensitive only to the tail of the projectile wave function and not to its interior. The excellent agreement with the data observed in this reaction observable suggests that the ANC we have extracted from the transfer data, combined with the choice of a nil interaction in the p ^{14}C-n partial waves, is valid structurewise [23]. Accordingly, the predictions of the *ab initio* calculations of Navrátil *et al.* seem correct [39].

In a subsequent test, we have analyzed how the inclusion of the ^{15}C e.s.—described here as a $0d_{5/2}$ bound state (see Sec. II A)—affects our breakup calculations. The presence of that state in the ^{15}C spectrum has no significant effect upon this reaction process; calculations performed with the halo-EFT descriptions of ^{15}C beyond NLO, which include this state, are nearly identical to those shown in Fig. 6. This is reminiscent of what has been observed in Ref. [26] in the analysis of the RIKEN Coulomb-breakup experiment of ^{11}Be [53], in which the presence of the $\frac{5}{2}^+$ resonance, also described within the $d_{5/2}$ partial wave, is barely noticeable in the cross section. This result is not surprising in a reaction that is strongly dominated by an E1 transition from the s bound state towards the p continuum. The existence of a d state in the low-energy spectrum of the projectile is more clearly seen in nuclear-dominated reactions, where quadrupole transitions are more significant [26,47]. Therefore, for this Coulomb-dominated reaction, a halo-EFT expansion limited to NLO is sufficient: the d bound state would actually appear only at the next order (i.e., next-to-next-to-leading order, N^{2}LO), and it has nearly no influence in our breakup calculations. This hence suggests that staying at NLO with a potential fitted to the ANC and binding energy of the g.s. in the s wave and a nil potential in the p wave, is enough to describe the experimental energy distributions for the breakup of ^{15}C.

B. Breakup of ^{15}C on lead at 68 MeV/nucleon

The Coulomb breakup of ^{15}C has also been measured on Pb at RIKEN at 68 MeV/nucleon by Nakamura *et al.* [15]. To reanalyze these data using the halo-EFT description of ^{15}C developed in Sec. II C, we consider the dynamical eikonal approximation (DEA) [64,65]. This model of reaction is

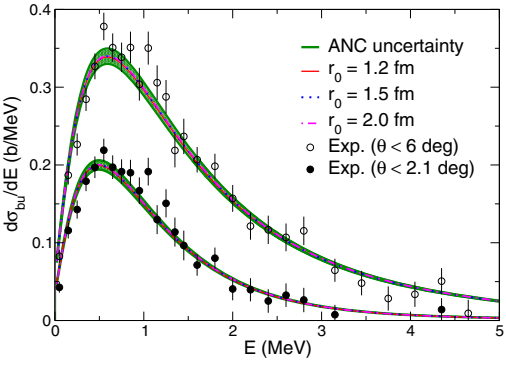

FIG. 7. Breakup cross section of ^{15}C on Pb target at 68 MeV/nucleon at two angular cuts plotted as a function of the relative energy E between the ^{14}C core and the neutron after dissociation. Results obtained with the different halo-EFT ^{14}C-n interactions listed in Table III are shown. For comparison with the RIKEN data of Ref. [15], the theoretical predictions have been folded with the experimental energy resolution.

also based on the eikonal approximation, however, it does not include the usual adiabatic approximation, which means that it properly includes the dynamics of the projectile during the collision, which has been shown to matter at this intermediate beam energy [19–22]. Besides having proved to be very efficient in the description of various observables measured in the breakup of one-neutron [65] and one-proton [66] halo nuclei, the model has been shown to be in excellent agreement with other breakup models on this very reaction [67].

Following Ref. [26], we include the ^{14}C-n halo-EFT potentials within the DEA and compute the breakup cross section at the RIKEN energy. To describe the nuclear interaction between the projectile constituents and the target, we follow Ref. [67] and consider optical potentials found in the literature. The ^{14}C-Pb potential is obtained from the scaling of an ^{16}O-Pb potential fitted to reproduce the elastic-scattering cross section of these nuclei at 94 MeV/nucleon [68]. We simply scale the radius of the potential by $0.987 = (14^{1/3} + 208^{1/3})/(16^{1/3} + 208^{1/3})$ to account for the mass difference between ^{16}O and ^{14}C and ignore the difference in beam energy. We use the Bechetti and Greenlees global nucleon-target optical potential to simulate the n-Pb interaction [69]. Note that the details of these interactions are provided in the Supplemental Material of Ref. [67].

The results of these calculations are shown in Fig. 7 as a function of the ^{14}C-n continuum energy E. We consider the two angular cuts under which the experimental data have been measured, i.e., $\theta < 6^\circ$, which includes the entire significant angular range, and $\theta < 2.1^\circ$, the forward-angle selection. To allow for a direct comparison with the data of Ref. [15], the results of our calculations have been folded with the experimental energy resolution. The green band shows the effect of the uncertainty on the ANC.

As in our analysis of the GSI experiment [14], we obtain an excellent agreement with the data on the whole energy spectrum. All three NLO ^{14}C-n potentials lead to identical cross sections showing that, at this energy also, the reaction is purely peripheral and that the ANC we have extracted from the low-energy transfer data and the nil phase shift in the ^{14}C-n p waves are consistent with this other set of data. Our analysis hence independently confirms the value of the ANC extracted by Summers and Nunes from this same Coulomb-breakup cross section [21]. The slightly larger ANC they have obtained (see line 4 of Table II) is probably due to their use of a nonzero interaction in the p wave, which tends to reduce these contributions to the breakup [23,26,34]. Since there is no experimental observable upon which to constrain the phase shift in these partial waves, we have to rely on theoretical hypotheses. We have made a choice consistent with what we have done in the ^{11}Be case [26] and with preliminary *ab initio* predictions [39]. As shown in Ref. [23], for the Coulomb breakup of loosely bound s wave nuclei, it is the combination of ANC in the g.s. and phase shift in the p continuum that matters, especially at low energy E in the ^{14}C-n continuum and forward scattering angle. The excellent agreement with the data displayed in Figs. 5, 6, and 7 justifies our choice. However, the uncertainty in the data is not sufficiently small to disprove the choice made in Ref. [21]. Using their choice of ^{14}C-n potentials would most likely provide as good an agreement with experiment as ours. Incidentally, this also confirms the *ab initio* prediction of Navrátil *et al.* for the ANC of the ^{15}C g.s.

In addition to these NLO calculations, we have also performed another set of calculations going beyond NLO by including the e.s. in the ^{15}C spectrum as a $0d_{5/2}$ bound state. The results, not shown here for clarity, are identical to those displayed in Fig. 7, confirming that in Coulomb-dominated reactions the details in the description of the d waves are irrelevant, and that an NLO halo-EFT description of the projectile is sufficient.

V. RADIATIVE CAPTURE ^{14}C$(n,\gamma)^{15}$C

As mentioned in Sec. I, the radiative capture of a neutron by ^{14}C to form a ^{15}C nucleus [^{14}C$(n,\gamma)^{15}$C] plays a significant role in various astrophysical sites, from the possible inhomogeneous big-bang nucleosynthesis [5] to neutron-induced CNO cycles in AGB stars [4] and possible role in Type II supernovae [6]. It is therefore useful for models of these astrophysical phenomena to have a reliable estimate of this reaction rate. Unfortunately it is difficult to measure directly: both reactants are radioactive and, although ^{14}C targets can be provided, obtaining purely monochromatic neutron beams is not simple. This is why indirect techniques, such as the Coulomb-breakup method [16,17], have been proposed. Nevertheless, recently, Reifarth *et al.* have taken up the gauntlet and performed a direct measure of this radiative capture [25].

In Sec. IV, we have shown that the halo-EFT description of ^{15}C at NLO was sufficient to describe the breakup cross sections measured at GSI [14] and RIKEN [15]. As expected from the analyses published in Refs. [21–23], this model of ^{15}C should also provide a good estimate for the

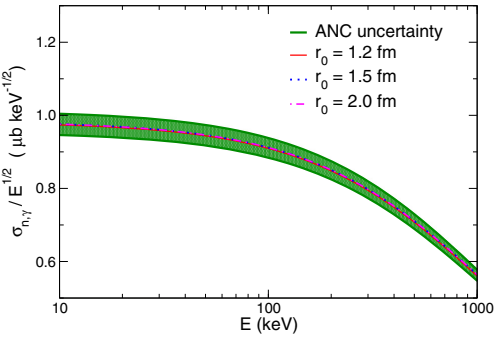

FIG. 8. Cross section for the radiative-capture ^{14}C$(n,\gamma)^{15}$C. The green band shows the uncertainty related to the ANC extracted from transfer data.

TABLE IV. Radiative-capture cross sections measured by Reifarth *et al.* [25] and the theoretical results obtained with the halo-EFT description of ^{15}C developed in Sec. II C. Our calculations include the small contribution of the capture to the excited $\frac{5}{2}^+$ of ^{15}C described beyond NLO and are obtained after averaging over the energy distribution of the neutrons within the beams used in the experiment. The theoretical uncertainty corresponds to the uncertainty on the ANC we have extracted for the ^{15}C g.s. The sensitivity to the choice of the range of the Gaussian potential r_0 is not seen at the level of precision displayed here.

E (keV)	$\sigma^{\rm exp}_{n,\gamma}$ (μb) [25]	$\sigma^{\rm th}_{n,\gamma}$ (μb)
23.3	7.1 ± 0.5	5.8 ± 0.2
150	10.7 ± 1.2	10.6 ± 0.3
500	17.0 ± 1.5	15.4 ± 0.4
800	15.8 ± 1.6	16.7 ± 0.5

radiative-capture cross section at low energy. In this section, we compare our prediction with the data of Reifarth *et al.* [25].

The radiative-capture ^{14}C$(n,\gamma)^{15}$C is dominated by the E1 transition from the p waves in the ^{14}C-n continuum towards the $1s_{1/2}$ ground state of ^{15}C. A small contribution comes also from the capture from the p continuum waves to the $0d_{5/2}$ excited state of the nucleus. Since these two contributions cannot be disentangled in the experiment of Reifarth *et al.* we use the halo-EFT description of ^{15}C beyond NLO to include this excited state in our model of the reaction. To perform the calculations, we proceed as in Ref. [23].

The radiative-capture cross section obtained in this way is displayed in Fig. 8 as a function of the relative energy E between the neutron and the ^{14}C nucleus in the entrance channel. The three ^{14}C-n Gaussian potentials provide identical cross sections, confirming that this reaction is purely peripheral [24]. The effect of the ANC uncertainty is shown by the green band. The contribution due to the capture towards the $0d_{5/2}$ e.s. is, as observed elsewhere [22,23,25], of the order of 5%. The details of the description of this state, and especially the accuracy of its ANC extracted from transfer data, are thus completely negligible in this analysis. We have checked that the contribution of the E2 term to the radiative capture is orders of magnitude lower than the E1. The cross section displayed in Fig. 8 is in excellent agreement with prior predictions [21,23,24,70] and the *ab initio* prediction of Navrátil *et al.* [39]. It is however slightly lower than what has been obtained in the analysis of the direct experiment [25].

To properly confront these results with the data measured by Reifarth *et al.* [25], we need to account for the distribution of the neutron energy in the incoming beam [71]. The values averaged over the neutron distributions shown in Fig. 3 of Ref. [25] are provided in Table IV alongside the experimental data. The experimental values are the ones provided in Table V of Ref. [25]. The theoretical cross sections are the one obtained using the ^{14}C-n potentials listed in Table III of the present article. These values include the small contribution of the capture to the $0d_{5/2}$ bound state that simulates the $\frac{5}{2}^+$ e.s. of ^{15}C. The uncertainty provided for the theoretical value corresponds to the uncertainty on the ANC of the g.s. of ^{15}C. The sensitivity to the range r_0 of the Gaussian potential (6) is smaller than the precision provided here.

Our theoretical predictions are usually in good agreement with the experimental values of Reifarth *et al.* [25]. The only significant difference is observed at the lowest energy point, where our prediction lies two standard deviations lower than the measured cross section. This seems to be an issue for most of the indirect estimates of this cross section [21–24,70]. Therefore, either there is some new physics not considered in the single-particle descriptions used in these references and in the present study, or there is some systematic uncertainty, which has not been well accounted for in the analysis of the experiment. The cross section we derive from our halo-EFT description of ^{15}C at the single astrophysical energy $E = 23.3$ keV is $\sigma_{n,\gamma}(23.3\,\text{keV}) = 4.66 \pm 0.14\,\mu$b, which is slightly lower than what other groups obtain [21,25,33].

Within our study, this is the only one oddity in the analysis of various reaction observables, which are all peripheral, and in particular with Coulomb-breakup cross sections, which are sensitive to the same nuclear-structure observables as the radiative capture, viz. the ANC of the g.s. of ^{15}C and the phase shift in the ^{14}C-n p waves [23]. We therefore believe that they are well constrained within our model of ^{15}C. The E1 strength this model predicts, and upon which both the Coulomb-breakup and the radiative-capture cross sections depend, should thus be quite reliable. Figure 9 provides this $dB(\text{E1})/dE$ as a function of the relative energy E between the ^{14}C and the neutron in the continuum. The value we obtain from our NLO ^{14}C-n potentials are compared with the E1 strength inferred from the Coulomb-breakup measurement by Nakamura *et al.* [15]. We observe that the latter is systematically lower than the $dB(\text{E1})/dE$ deduced from our halo-EFT model of ^{15}C, even though we are in perfect agreement with their Coulomb-breakup cross sections (see Fig. 7). This difference is due to higher-order effects, which are neglected in the analysis of the RIKEN data. As already shown in Refs. [21–23], these effects are significant and cannot be ignored in the reaction model. This is the reason why the RIKEN prediction of the cross section for the radiative

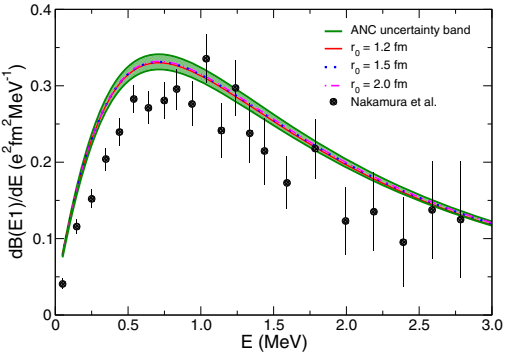

FIG. 9. Electric dipole strength deduced from the halo-EFT structure of ^{15}C at NLO, compared to the E1 strength inferred by Nakamura *et al.*[15]. For a better comparison, our calculation has been folded with the experimental resolution.

capture ^{14}C$(n,\gamma)^{15}$C underestimates the direct measurement or Reifarth *et al.* (see Fig. 3 of Ref. [15]). A comparison with that observable within the *ab initio* model of Navrátil *et al.* would be interesting to confirm our prediction.

VI. SUMMARY AND OUTLOOK

The exotic nucleus ^{15}C raises interests in various fields. It exhibits a one-neutron halo [1,2], and its synthesis through the radiative capture of a neutron by ^{14}C takes place in various astrophysical sites [4–6]. It is therefore interesting to better understand its structure and to provide astrophysicists with reliable cross sections for the radiative capture ^{14}C$(n,\gamma)^{15}$C at low energies.

In this work, we have reanalyzed various reactions involving ^{15}C using one single description of that nucleus. Following the work initiated in Ref. [26], we have considered a halo-EFT description of that one-neutron halo nucleus. Once coupled to a precise model of reactions, this very systematic expansion enables us to accurately determine the observables that affect the reaction process and hence, which can be probed through experimental measurements [26,38,50].

Using a LO halo-EFT Hamiltonian (5), we have reanalyzed the ^{14}C$(d,p)^{15}$C transfer data at low energy [10] within the framework of the FR-ADWA [40]. Following the results of Ref. [38], focusing on the forward-angle region enables us to select purely peripheral data, from which a reliable estimate of the ANC of the g.s. of ^{15}C has been inferred. The value obtained $\mathcal{C}_{1/2^+} = 1.26 \pm 0.02$ fm$^{-1/2}$ ($\mathcal{C}^2_{1/2^+} = 1.59 \pm 0.06$ fm^{-1}) is in good agreement with previous work [10,21,24,31,36,37] and with preliminary *ab initio* predictions [39].

The ANC hence obtained coupled to the binding energy of the valence neutron to the ^{14}C provides us with two nuclear-structure observables, upon which we have constrained a halo-EFT Hamiltonian at NLO. This Hamiltonian has then be used within precise models of reactions to reanalyze transfer data [7,10], Coulomb-breakup cross sections measured at high [14] and intermediate [15] energies, and cross sections for the radiative capture ^{14}C$(n,\gamma)^{15}$C [25]. In all cases, we observe a very good agreement with experiment without the need for any additional adjustment.

By showing that all these experiments can be described at the NLO of the halo-EFT expansion, these analyses indicate that the core-neutron binding energy and the ground-state ANC are the sole nuclear-structure observables that need to be constrained to reproduce these data. These reactions are therefore purely peripheral, in the sense that they probe only the tail of the projectile wave function and not its interior. Especially, no need is found for a renormalization of the projectile wave function, confirming that no spectroscopic factor can be extracted from such measurements [26,49]. Going beyond NLO, we have found that the presence of the bound excited state of ^{15}C in its description has no effect in Coulomb-breakup calculations.

From this NLO description of ^{15}C we have been able to infer a reliable estimate of the E1 strength from the $\frac{1}{2}^+$ ground state of ^{15}C to its ^{14}C-n continuum. This $dB(\mathrm{E1})/dE$ leads to excellent agreement with the measurements of both the ^{15}C Coulomb breakup [14,15] and the radiative capture ^{14}C$(n,\gamma)^{15}$C [25]. Accordingly, we suggest as a cross section for the latter process at astrophysical energy the value $\sigma_{n,\gamma}(23.3\,\mathrm{keV}) = 4.66 \pm 0.14\,\mu$b.

The excellent results obtained within this framework confirms the interest of coupling a halo-EFT description of the nucleus to existing precise models of reactions [26]. They also drive us to extend this idea to other reactions, such as knockout [47]. Hopefully, the model developed herein and in Ref. [26] will enable us to reproduce existing data on ^{15}C and ^{11}Be [11–13]. We also plan to apply this model to other halo nuclei, such as ^{19}C and ^{31}Ne.

ACKNOWLEDGMENTS

This project has received funding from the European Union's Horizon 2020 research and innovation programme under Grant Agreement No. 654002, the Deutsche Forschungsgemeinschaft within the Collaborative Research Centers 1044 and 1245, and the PRISMA (Precision Physics, Fundamental Interactions and Structure of Matter) Cluster of Excellence. J.Y. is supported by the China Scholarship Council (CSC). P.C. acknowledges the support of the State of Rhineland-Palatinate.

[1] I. Tanihata, J. Phys. G **22**, 157 (1996).
[2] K. Riisager, Phys. Scr. **2013**, 014001 (2013).
[3] P. G. Hansen and B. Jonson, Europhys. Lett. **4**, 409 (1987).
[4] M. Wiescher, J. Görres, and H. Schatz, J. Phys. G **25**, R133 (1999).
[5] T. Kajino, G. J. Mathews, and G. M. Fuller, Astrophys. J. **364**, 7 (1990).

[6] M. Terasawa, K. Sumiyoshi, T. Kajino, G. J. Mathews, and I. Tanihata, Astrophys. J. **562**, 470 (2001).

[7] J. D. Goss, P. L. Jolivette, C. P. Browne, S. E. Darden, H. R. Weller, and R. A. Blue, Phys. Rev. C **12**, 1730 (1975).

[8] F. Cecil, J. Shepard, R. Anderson, R. Peterson, and P. Kaczkowski, Nucl. Phys. A **255**, 243 (1975).

[9] G. Murillo, S. Sen, and S. Darden, Nucl. Phys. A **579**, 125 (1994).

[10] A. M. Mukhamedzhanov, V. Burjan, M. Gulino, Z. Hons, V. Kroha, M. McCleskey, J. Mrázek, N. Nguyen, F. M. Nunes, Š. Piskoř, S. Romano, M. L. Sergi, C. Spitaleri, and R. E. Tribble, Phys. Rev. C **84**, 024616 (2011).

[11] J. A. Tostevin, D. Bazin, B. A. Brown, T. Glasmacher, P. G. Hansen, V. Maddalena, A. Navin, and B. M. Sherrill, Phys. Rev. C **66**, 024607 (2002).

[12] E. Sauvan, F. Carstoiu, N. A. Orr, J. S. Winfield, M. Freer, J. C. Angélique, W. N. Catford, N. M. Clarke, N. Curtis, S. Grévy, C. Le Brun, M. Lewitowicz, E. Liégard, F. M. Marqués, M. MacCormick, P. Roussel-Chomaz, M.-G. Saint Laurent, and M. Shawcross, Phys. Rev. C **69**, 044603 (2004).

[13] D. Q. Fang, T. Yamaguchi, T. Zheng, A. Ozawa, M. Chiba, R. Kanungo, T. Kato, K. Morimoto, T. Ohnishi, T. Suda, Y. Yamaguchi, A. Yoshida, K. Yoshida, and I. Tanihata, Phys. Rev. C **69**, 034613 (2004).

[14] U. Datta Pramanik, T. Aumann, K. Boretzky, B. Carlson, D. Cortina, T. Elze, H. Emling, H. Geissel, A. Grünschloß, M. Hellström, S. Ilievski, J. Kratz, R. Kulessa, Y. Leifels, A. Leistenschneider, E. Lubkiewicz, G. Münzenberg, P. Reiter, H. Simon, K. Sümmerer, E. Wajda, and W. Walus, Phys. Lett. B **551**, 63 (2003).

[15] T. Nakamura, N. Fukuda, N. Aoi, N. Imai, M. Ishihara, H. Iwasaki, T. Kobayashi, T. Kubo, A. Mengoni, T. Motobayashi, M. Notani, H. Otsu, H. Sakurai, S. Shimoura, T. Teranishi, Y. X. Watanabe, and K. Yoneda, Phys. Rev. C **79**, 035805 (2009).

[16] G. Baur, C. Bertulani, and H. Rebel, Nucl. Phys. A **458**, 188 (1986).

[17] G. Baur, K. Hencken, and D. Trautmann, Prog. Part. Nucl. Phys. **51**, 487 (2003).

[18] A. Winther and K. Alder, Nucl. Phys. A **319**, 518 (1979).

[19] H. Esbensen, G. F. Bertsch, and K. A. Snover, Phys. Rev. Lett. **94**, 042502 (2005).

[20] P. Capel and D. Baye, Phys. Rev. C **71**, 044609 (2005).

[21] N. C. Summers and F. M. Nunes, Phys. Rev. C **78**, 011601(R) (2008); **78**, 069908(E) (2008).

[22] H. Esbensen, Phys. Rev. C **80**, 024608 (2009).

[23] P. Capel and Y. Nollet, Phys. Rev. C **96**, 015801 (2017).

[24] N. K. Timofeyuk, D. Baye, P. Descouvemont, R. Kamouni, and I. J. Thompson, Phys. Rev. Lett. **96**, 162501 (2006).

[25] R. Reifarth, M. Heil, C. Forssén, U. Besserer, A. Couture, S. Dababneh, L. Dörr, J. Görres, R. C. Haight, F. Käppeler, A. Mengoni, S. O'Brien, N. Patronis, R. Plag, R. S. Rundberg, M. Wiescher, and J. B. Wilhelmy, Phys. Rev. C **77**, 015804 (2008).

[26] P. Capel, D. R. Phillips, and H.-W. Hammer, Phys. Rev. C **98**, 034610 (2018).

[27] C. Bertulani, H.-W. Hammer, and U. van Kolck, Nucl. Phys. A **712**, 37 (2002).

[28] H.-W. Hammer, C. Ji, and D. R. Phillips, J. Phys. G **44**, 103002 (2017).

[29] M. Abramowitz and I. A. Stegun, *Handbook of Mathematical Functions* (Dover, New York, 1970).

[30] L. D. Blokhintsev, I. Borbei, and E. Dolinskii, Fizika Ehlementarnykh Chastits i Atomnogo Yadra **8**, 1189 (1977).

[31] M. McCleskey, A. M. Mukhamedzhanov, L. Trache, R. E. Tribble, A. Banu, V. Eremenko, V. Z. Goldberg, Y.-W. Lui, E. McCleskey, B. T. Roeder, A. Spiridon, F. Carstoiu, V. Burjan, Z. Hons, and I. J. Thompson, Phys. Rev. C **89**, 044605 (2014).

[32] T. L. Belyaeva, R. Perez-Torres, A. A. Ogloblin, A. S. Demyanova, S. N. Ershov, and S. A. Goncharov, Phys. Rev. C **90**, 064610 (2014).

[33] N. K. Timofeyuk, J. Phys. G **41**, 094008 (2014).

[34] P. Capel and F. M. Nunes, Phys. Rev. C **73**, 014615 (2006).

[35] P. Capel, P. Danielewicz, and F. M. Nunes, Phys. Rev. C **82**, 054612 (2010).

[36] L. Trache, A. Azhari, F. Carstoiu, C. A. Gagliardi, A. M. Mukhamedzhanov, X. D. Tang, R. E. Tribble, and S. Zhou, Tex. A & M Cyclotron Prog. Rep. **I**, 16 (2002).

[37] D. Y. Pang, F. M. Nunes, and A. M. Mukhamedzhanov, Phys. Rev. C **75**, 024601 (2007).

[38] J. Yang and P. Capel, Phys. Rev. C **98**, 054602 (2018).

[39] P. Navrátil (private communication).

[40] R. Johnson and P. Tandy, Nucl. Phys. A **235**, 56 (1974).

[41] F. M. Nunes and A. Deltuva, Phys. Rev. C **84**, 034607 (2011).

[42] N. J. Upadhyay, A. Deltuva, and F. M. Nunes, Phys. Rev. C **85**, 054621 (2012).

[43] P. R. Varner, W. Thompson, T. McAbee, E. Ludwig, and T. Clegg, Phys. Rep. **201**, 57 (1991).

[44] R. V. Reid, Ann. Phys. (NY) **50**, 411 (1968).

[45] M. Igarashi and M. Toyama, Computer program TWOFNR, University of Surrey version, 2008.

[46] I. J. Thompson, Comput. Phys. Rep. **7**, 167 (1988).

[47] C. Hebborn and P. Capel, arXiv:1906.07660 [nucl-th].

[48] A. M. Mukhamedzhanov, B. F. Irgaziev, V. Z. Goldberg, Y. V. Orlov, and I. Qazi, Phys. Rev. C **81**, 054314 (2010).

[49] P. Capel and F. M. Nunes, Phys. Rev. C **75**, 054609 (2007).

[50] L. Moschini and P. Capel, Phys. Lett. B **790**, 367 (2019).

[51] M. Gómez-Ramos, A. M. Moro, J. Gómez-Camacho, and I. J. Thompson, Phys. Rev. C **92**, 014613 (2015).

[52] R. Palit, P. Adrich, T. Aumann, K. Boretzky, B. V. Carlson, D. Cortina, U. Datta Pramanik, T. W. Elze, H. Emling, H. Geissel, M. Hellström, K. L. Jones, J. V. Kratz, R. Kulessa, Y. Leifels, A. Leistenschneider, G. Münzenberg, C. Nociforo, P. Reiter, H. Simon, K. Sümmerer, and W. Walus (LAND/FRS Collaboration), Phys. Rev. C **68**, 034318 (2003).

[53] N. Fukuda, T. Nakamura, N. Aoi, N. Imai, M. Ishihara, T. Kobayashi, H. Iwasaki, T. Kubo, A. Mengoni, M. Notani, H. Otsu, H. Sakurai, S. Shimoura, T. Teranishi, Y. X. Watanabe, and K. Yoneda, Phys. Rev. C **70**, 054606 (2004).

[54] R. Glauber, in *Lectures in Theoretical Physics*, edited by W. Brittin and L. Dunham, Vol. 1 (Interscience, New York, 1959), p. 315.

[55] D. Baye and P. Capel, Breakup reaction models for two- and three-cluster projectiles, in *Clusters in Nuclei, Vol. 2*, Lecture Notes in Physics, Vol. 848, edited by C. Beck (Springer, Heidelberg, 2012), pp. 121–163.

[56] G. R. Satchler, Nucl. Phys. A **540**, 533 (1992).

[57] D.-Y. Pang, Chin. Phys. C **38**, 024104 (2014).

[58] C. Bertulani and P. Danielewicz, *Introduction to Nuclear Reactions* (Institute of Physics Publishing, Bristol, 2004).

[59] J. Margueron, A. Bonaccorso, and D. Brink, Nucl. Phys. A **720**, 337 (2003).

[60] P. Capel, D. Baye, and Y. Suzuki, Phys. Rev. C **78**, 054602 (2008).
[61] W. Horiuchi, Y. Suzuki, P. Capel, and D. Baye, Phys. Rev. C **81**, 024606 (2010).
[62] B. Abu-Ibrahim, W. Horiuchi, A. Kohama, and Y. Suzuki, Phys. Rev. C **77**, 034607 (2008).
[63] L. C. Chamon, B. V. Carlson, L. R. Gasques, D. Pereira, C. De Conti, M. A. G. Alvarez, M. S. Hussein, M. A. Cândido Ribeiro, E. S. Rossi, and C. P. Silva, Phys. Rev. C **66**, 014610 (2002).
[64] D. Baye, P. Capel, and G. Goldstein, Phys. Rev. Lett. **95**, 082502 (2005).
[65] G. Goldstein, D. Baye, and P. Capel, Phys. Rev. C **73**, 024602 (2006).
[66] G. Goldstein, P. Capel, and D. Baye, Phys. Rev. C **76**, 024608 (2007).
[67] P. Capel, H. Esbensen, and F. M. Nunes, Phys. Rev. C **85**, 044604 (2012).
[68] P. Roussel-Chomaz, N. Alamanos, F. Auger, J. Barrette, B. Berthier, B. Fernandez, L. Papineau, H. Doubre, and W. Mittig, Nucl. Phys. A **477**, 345 (1988).
[69] F. D. Becchetti and G. W. Greenlees, Phys. Rev. **182**, 1190 (1969).
[70] G. Rupak, L. Fernando, and A. Vaghani, Phys. Rev. C **86**, 044608 (2012).
[71] P. Capel and Y. Nollet, Phys. Rev. C **98**, 019906(E) (2018).

Bibliography

[AB92] L. U. Ancarani and D. Baye. Iterative supersymmetric construction of phase-equivalent potentials. *Phys. Rev. A*, 46:206–216, Jul 1992.

[AB95] S. M. Austin and G. F. Bertsch. Halo nuclei. *Sci. Am.*, 272(6):90–95, 1995.

[ABB+09] I. Antcheva, M. Ballintijn, B. Bellenot, M. Biskup, R. Brun, N. Buncic, Ph. Canal, D. Casadei, O. Couet, V. Fine, L. Franco, G. Ganis, A. Gheata, D. Gonzalez Maline, M. Goto, J. Iwaszkiewicz, A. Kreshuk, D. Marcos Segura, R. Maunder, L. Moneta, A. Naumann, E. Offermann, V. Onuchin, S. Panacek, F. Rademakers, P. Russo, and M. Tadel. ROOT — A C++ framework for petabyte data storage, statistical analysis and visualization. *Comput. Phys. Commun.*, 180(12):2499 – 2512, 2009. 40 YEARS OF CPC: A celebratory issue focused on quality software for high performance, grid and novel computing architectures.

[ABBN+18] Y. Ayyad, D. Bazin, S. Beceiro-Novo, M. Cortesi, and W. Mittig. Physics and technology of time projection chambers as active targets. *Eur. Phys. J. A*, 54(10):181, Oct 2018.

[AC06] H. An and C. Cai. Global deuteron optical model potential for the energy range up to 183 MeV. *Phys. Rev. C*, 73:054605, May 2006.

[ADE+02] G. D. Alkhazov, A. V. Dobrovolsky, P. Egelhof, H. Geissel, H. Irnich, A. V. Khanzadeev, G. A. Korolev, A. A. Lobodenko, G. Münzenberg, M. Mutterer, S. R. Neumaier, W. Schwab, D. M. Seliverstov, T. Suzuki, and A. A. Vorobyov. Nuclear matter distributions in the ^{6}He and ^{8}He nuclei from differential cross

sections for small-angle proton elastic scattering at intermediate energy. *Nucl. Phys. A*, 712(3):269 – 299, 2002.

[AGS67] E. O. Alt, P. Grassberger, and W. Sandhas. Reduction of the three-particle collision problem to multi-channel two-particle lippmann-schwinger equations. *Nucl. Phys. B*, 2(2):167 – 180, 1967.

[AH85] J. H. Applegate and C. J. Hogan. Relics of cosmic quark condensation. *Phys. Rev. D*, 31:3037–3045, Jun 1985.

[AIK+87] N. Austern, Y. Iseri, M. Kamimura, M. Kawai, G. Rawitscher, and M. Yahiro. Continuum-discretized coupled-channels calculations for three-body models of deuteron-nucleus reactions. *Phys. Rep.*, 154(3):125 – 204, 1987.

[AK04] J. Al-Khalili. An introduction to halo nuclei. *The Euroschool Lectures on Physics with Exotic Beams, Vol. I*, pages 77–112, 2004.

[ANB+00] T. Aumann, A. Navin, D. P. Balamuth, D. Bazin, B. Blank, B. A. Brown, J. E. Bush, J. A. Caggiano, B. Davids, T. Glasmacher, V. Guimarães, P. G. Hansen, R. W. Ibbotson, D. Karnes, J. J. Kolata, V. Maddalena, B. Pritychenko, H. Scheit, B. M. Sherrill, and J. A. Tostevin. One-Neutron Knockout from Individual Single-Particle States of ^{11}Be. *Phys. Rev. Lett.*, 84:35–38, Jan 2000.

[AS64] M. Abramowitz and I. A. Stegun. *Handbook of Mathematical Functions with Formulas, Graphs, and Mathematical Tables*. Dover, New York, ninth dover printing, tenth gpo printing edition, 1964.

[Aus70] N. Austern. *Direct nuclear reaction theories*. Interscience monographs and texts in physics and astronomy. Wiley-Interscience, 1970.

[AUS19] Aarhus Subatomic Library (AUSAlib). `https://git.kern.phys.au.dk/ausa/ausalib/wikis/home`, Accessed: Jul 2019.

[AW95] G. Audi and A. H. Wapstra. The 1995 update to the atomic mass evaluation. *Nucl. Phys. A*, 595(4):409 – 480, 1995.

[BAG+08] C. Bachelet, G. Audi, C. Gaulard, C. Guénaut, F. Herfurth, D. Lunney, M. de Saint Simon, and C. Thibault. New binding energy for the two-neutron halo of ^{11}Li. *Phys. Rev. Lett.*, 100:182501, May 2008.

[BBB+99] D. W. Bardayan, J. C. Blackmon, C. R. Brune, A. E. Champagne, A. A. Chen, J. M. Cox, T. Davinson, V. Y. Hansper, M. A. Hofstee, B. A. Johnson, R. L. Kozub, Z. Ma, P. D. Parker, D. E. Pierce, M. T. Rabban, A. C. Shotter, M. S. Smith, K. B. Swartz, D. W. Visser, and P. J. Woods. Observation of the Astrophysically Important 3^+ State in ^{18}Ne via Elastic Scattering of a Radioactive ^{17}F Beam from ^{1}H. *Phys. Rev. Lett.*, 83:45–48, Jul 1999.

[BBBM07] G. Blanchon, A. Bonaccorso, D. M. Brink, and N. Vinh Mau. ^{10}Li spectrum from ^{11}Li fragmentation. *Nucl. Phys. A*, 791(3):303 – 312, 2007.

[BBG+99] H. G. Bohlen, A. Blazevic, B. Gebauer, W. Von Oertzen, S. Thummerer, R. Kalpakchieva, S. M. Grimes, and T. N. Massey. Spectroscopy of exotic nuclei with multi-nucleon transfer reactions. *Prog. Part. Nucl. Phys.*, 42:17 – 26, 1999.

[BBU+11] J. R. Beene, D. W. Bardayan, A. Galindo Uribarri, C. J. Gross, K. L. Jones, J. F. Liang, W. Nazarewicz, D. W. Stracener, B. A. Tatum, and R. L. Varner. ISOL science at the holifield radioactive ion beam facility. *J. Phys. G*, 38(2):024002, Jan 2011.

[BDB77] L. D. Blokhintsev, E. I. Dolinskij, and I. Borbej. Nuclear vertex functions. *Fiz. Elem. Chastits At. Yadra*, 8(6):1189–1245, 1977.

[BFF+12] M. J. G. Borge, L. M. Fraile, H. O. U. Fynbo, J. Gomez Camacho, J. Johansen, H. T. Johansson, B. Jonson, R. Krücken, J. Kurcewicz, I. Martel, A. Moro, D. Mücher, T. Nilsson, G. Nyman, R. Raabe, G. Randisi, K. Riisager, S. Sambi, AM. Sanchez-Benitez, and O. Tengblad. Transfer reactions at the neutron dripline with triton target. Technical Report CERN-INTC-2012-060. INTC-P-361, CERN, Geneva, Oct 2012.

[BFG+89] L. Bianchi, B. Fernandez, J. Gastebois, A. Gillibert, W. Mittig, and J. Barrette. SPEG: An energy loss spectrometer for GANIL. *Nucl. Instrum. Methods Phys. Res. A*, 276(3):509 – 520, 1989.

[BG69] F. D. Becchetti and G. W. Greenlees. Nucleon-nucleus optical-model parameters, A $>$ 40, E $<$ 50 MeV. *Phys. Rev.*, 182:1190–1209, Jun 1969.

[BGC+08] G. Brunetti, S. Giacintucci, R. Cassano, W. Lane, D. Dallacasa, T. Venturi, N. E. Kassim, G. Setti, W. D. Cotton, and

M. Markevitch. A low-frequency radio halo associated with a cluster of galaxies. *Nature*, 455:944, 2008.

[BGK+12] V. Bildstein, R. Gernhäuser, T. Kröll, R. Krücken, K. Wimmer, P. Van Duppen, M. Huyse, N. Patronis, R. Raabe, and T-REX Collaboration. T-REX. *Eur. Phys. J. A*, 48(6):85, Jun 2012.

[BH61] B. Buck and P. E. Hodgson. The analysis of (d, p) stripping reactions by the distorted wave born approximation. *Philos. Mag.*, 6(71):1371–1384, 1961.

[BHvK02] C. A. Bertulani, H.-W. Hammer, and U. van Kolck. Effective field theory for halo nuclei: shallow p-wave states. *Nucl. Phys. A*, 712(1):37 – 58, 2002.

[Bic88] H. Bichsel. Straggling in thin silicon detectors. *Rev. Mod. Phys.*, 60:663–699, Jul 1988.

[Bla06] K. Blaum. High-accuracy mass spectrometry with stored ions. *Phys. Rep.*, 425(1):1 – 78, 2006.

[Bor16] M. J. G. Borge. Highlights of the ISOLDE facility and the HIE-ISOLDE project. *Nucl. Instrum. Methods Phys. Res. B*, 376:408 – 412, 2016. Proceedings of the XVIIth International Conference on Electromagnetic Isotope Separators and Related Topics (EMIS2015), Grand Rapids, MI, U.S.A., 11-15 May 2015.

[Bou13] J. Bouma. Elastic scattering and cluster-transfer reactions of ^{98}Rb on ^{7}Li at REX-ISOLDE. Master's thesis, KU Leuven, 2013.

[BPTD+14] T. L. Belyaeva, R. Perez-Torres, A. S. Demyanova, S. A. Goncharov, and A. A. Ogloblin. Neutron asymptotic normalization coefficients and halo radii of the first excited states of ^{13}C and ^{11}Be. *EPJ Web Conf.*, 66:03009, 2014.

[BPTO+14] T. L. Belyaeva, R. Perez-Torres, A. A. Ogloblin, A. S. Demyanova, S. N. Ershov, and S. A. Goncharov. Determination of neutron halo radii in the first excited states of ^{13}C and ^{11}Be with the asymptotic normalization coefficients method. *Phys. Rev. C*, 90:064610, Dec 2014.

[BPVB18] F. Barranco, G. Potel, E. Vigezzi, and R. A. Broglia. The ^{9}Li(d,p) reaction, a specific probe of ^{10}Li, paradigm of parity-inverted nuclei around $N = 6$ closed shell. 2018.

[BS95] V. G. Bagrov and B. F. Samsonov. Darboux transformation, factorization, and supersymmetry in one-dimensional quantum mechanics. *Theor. Math. Phys.*, 104(2):1051–1060, Aug 1995.

[BSM+16] C. A. Bertulani, Shubhchintak, A. Mukhamedzhanov, A. S. Kadyrov, A. Kruppa, and D. Y. Pang. Indirect methods in nuclear astrophysics. *J. Phys.: Conf. Ser*, 703:012007, Apr 2016.

[BSPMS14] D. Baye, J.-M. Sparenberg, A. M. Pupasov-Maksimov, and B. F. Samsonov. Single- and coupled-channel radial inverse scattering with supersymmetric transformations. *J. Phys. A: Math. Theor.*, 47(24):243001, Jun 2014.

[BT18] G. Benedek and J. P. Toennies. *Resonances and Critical Kinematic Effects*, pages 305–336. Springer Berlin Heidelberg, Berlin, Heidelberg, 2018.

[But50] S. T. Butler. On angular distributions from (d, p) and (d, n) nuclear reactions. *Phys. Rev.*, 80:1095–1096, Dec 1950.

[Cat02] W. N. Catford. Nucleon transfer studies with radioactive beams. *Nucl. Phys. A*, 701(1):1 – 6, 2002. 5th International Conference on Radioactive Nuclear Beams.

[Cat14] W. N. Catford. *What Can We Learn from Transfer, and How Is Best to Do It?*, pages 67–122. Springer Berlin Heidelberg, Berlin, Heidelberg, 2014.

[CD61] R. F. Christy and I. Duck. γ rays from an extranuclear direct capture process. *Nucl. Phys.*, 24(1):89 – 101, 1961.

[CDNC+17] M. Cavallaro, M. De Napoli, F. Cappuzzello, S. E. A. Orrigo, C. Agodi, M. Bondí, D. Carbone, A. Cunsolo, B. Davids, T. Davinson, A. Foti, N. Galinski, R. Kanungo, H. Lenske, C. Ruiz, and A. Sanetullaev. Investigation of the ^{10}Li shell inversion by neutron continuum transfer reaction. *Phys. Rev. Lett.*, 118:012701, Jan 2017.

[CF10] B. Cheal and K. T. Flanagan. Progress in laser spectroscopy at radioactive ion beam facilities. *J. Phys. G*, 37(11):113101, Sep 2010.

[CGK+13] B. A. Chernyshev, Yu. B. Gurov, V. S. Karpukhin, L. Yu. Korotkova, S. V. Lapushkin, R. V. Pritula, and V. G. Sandukovsky. Spectroscopy of the heavy lithium isotopes $^{10-12}$Li. *Eur. Phys. J. A*, 49(6):68, Jun 2013.

[CGRM17] J. Casal, M. Gómez-Ramos, and A. M. Moro. Description of the ^{11}Li$(p,d)^{10}$Li transfer reaction using structure overlaps from a full three-body model. *Phys. Lett. B*, 767:307 – 313, 2017.

[CJF97] A. Cobis, A. S. Jensen, and D. V. Fedorov. The simplest strange three-body halo. *J. Phys. G*, 23(4):401, 1997.

[CKS95] F. Cooper, A. Khare, and U. Sukhatme. Supersymmetry and quantum mechanics. *Phys. Rept.*, 251:267–385, 1995.

[CLG19] X.-N. Cao, Q. Liu, and J.-Y. Guo. Prediction of halo structure in nuclei heavier than ^{37}Mg with the complex momentum representation method. *Phys. Rev. C*, 99:014309, Jan 2019.

[CMP16] P. Campbell, I. D. Moore, and M. R. Pearson. Laser spectroscopy for nuclear structure physics. *Prog. Part. Nucl. Phys.*, 86:127 – 180, 2016.

[CN06] P. Capel and F. M. Nunes. Influence of the projectile description on breakup calculations. *Phys. Rev. C*, 73:014615, Jan 2006.

[CNR+16] A. Calci, P. Navrátil, R. Roth, J. Dohet-Eraly, S. Quaglioni, and G. Hupin. Can *ab initio* theory explain the phenomenon of parity inversion in ^{11}Be? *Phys. Rev. Lett.*, 117:242501, Dec 2016.

[Coh71] B. L. Cohen. *Concepts of Nuclear Physics.* McGraw-Hill series in fundamentals of physics. Tata McGraw-Hill, 1971.

[CPH18] P. Capel, D. R. Phillips, and H. W. Hammer. Dissecting reaction calculations using halo effective field theory and *ab initio* input. *Phys. Rev. C*, 98(3):034610, 2018.

[CPS09] L. Corradi, G. Pollarolo, and S. Szilner. Multinucleon transfer processes in heavy-ion reactions. *J. Phys. G*, 36(11):113101, Sep 2009.

[DAA+06] A. V. Dobrovolsky, G. D. Alkhazov, M. N. Andronenko, A. Bauchet, P. Egelhof, S. Fritz, H. Geissel, C. Gross, A. V. Khanzadeev, G. A. Korolev, G. Kraus, A. A. Lobodenko, G. Münzenberg, M. Mutterer, S. R. Neumaier, T. Schäfer, C. Scheidenberger, D. M. Seliverstov, N. A. Timofeev, A. A. Vorobyov, and V. I. Yatsoura. Study of the nuclear matter distribution in neutron-rich Li isotopes. *Nucl. Phys. A*, 766:1 – 24, 2006.

[DC19] W. H. Dickhoff and R. J. Charity. Recent developments for the optical model of nuclei. *Prog. Part. Nucl. Phys.*, 105:252 – 299, 2019.

[DCV80] W. W. Daehnick, J. D. Childs, and Z. Vrcelj. Global optical model potential for elastic deuteron scattering from 12 to 90 MeV. *Phys. Rev. C*, 21:2253–2274, Jun 1980.

[Del09] A. Deltuva. Three-body direct nuclear reactions: Nonlocal optical potential. *Phys. Rev. C*, 79:021602, Feb 2009.

[DFS+11] C. Aa. Diget, S. P. Fox, A. Smith, S. Williams, M. Porter-Peden, L. Achouri, P. Adsley, H. Al-Falou, R. A. E. Austin, G. C. Ball, J. C. Blackmon, S. Brown, W. N. Catford, A. A. Chen, J. Chen, R. M. Churchman, J. Dech, D. Di. Valentino, M. Djongolov, B. R. Fulton, A. Garnsworthy, G. Hackman, U. Hager, R. Kshetri, L. Kurchaninov, A. M. Laird, J. P. Martin, M. Matos, J. N. Orce, N. A. Orr, C. J. Pearson, C. Ruiz, F. Sarazin, S. Sjue, D. Smalley, C. E. Svensson, M. Taggart, E. Tardiff, and G. L. Wilson. SHARC: Silicon highly-segmented array for reactions and coulex used in conjunction with the TIGRESS γ-ray spectrometer. *J. Instrum*, 6(02):P02005–P02005, Feb 2011.

[DMS+07] C. E. Demonchy, W. Mittig, H. Savajols, P. Roussel-Chomaz, M. Chartier, B. Jurado, L. Giot, D. Cortina-Gil, M. Caamaño, G. Ter-Arkopian, A. Fomichev, A. Rodin, M. S. Golovkov, S. Stepantsov, A. Gillibert, E. Pollacco, A. Obertelli, and H. Wang. MAYA, a gaseous active target. *Nucl. Instrum. Methods Phys. Res. A*, 573(1):145 – 148, 2007. Proceedings of the 7th International Conference on Position-Sensitive Detectors.

[DPRS+10] A. Di Pietro, G. Randisi, V. Scuderi, L. Acosta, F. Amorini, M. J. G. Borge, P. Figuera, M. Fisichella, L. M. Fraile, J. Gomez-Camacho, H. Jeppesen, M. Lattuada, I. Martel, M. Milin, A. Musumarra, M. Papa, M. G. Pellegriti, F. Perez-Bernal, R. Raabe, F. Rizzo, D. Santonocito, G. Scalia, O. Tengblad, D. Torresi, A. Maira Vidal, D. Voulot, F. Wenander, and M. Zadro. Elastic scattering and reaction mechanisms of the halo nucleus ^{11}Be around the coulomb barrier. *Phys. Rev. Lett.*, 105:022701, Jul 2010.

[DPSM+12] A. Di Pietro, V. Scuderi, A. M. Moro, L. Acosta, F. Amorini, M. J. G. Borge, P. Figuera, M. Fisichella, L. M. Fraile, J. Gomez-Camacho, H. Jeppesen, M. Lattuada, I. Martel, M. Milin, A. Musumarra, M. Papa, M. G. Pellegriti, F. Perez-Bernal,

R. Raabe, G. Randisi, F. Rizzo, G. Scalia, O. Tengblad, D. Torresi, A. Maira Vidal, D. Voulot, F. Wenander, and M. Zadro. Experimental study of the collision ^{11}Be + ^{64}Zn around the Coulomb barrier. *Phys. Rev. C*, 85:054607, May 2012.

[DRNcvN16] A. Deltuva, A. Ross, E. Norvaišas, and F. M. Nunes. Role of core excitation in (d, p) transfer reactions. *Phys. Rev. C*, 94:044613, Oct 2016.

[DSM+90] T. Davinson, A. C. Shotter, E. W. Macdonald, S. V. Springham, P. Jobanputra, A. J. Stephens, and S. L. Thomas. Development of a silicon strip detector array for nuclear structure physics. *Nucl. Instrum. Methods Phys. Res. A*, 288(1):245 – 249, 1990. Proceedings of the Fifth European Symposium on Semiconductors Detectors.

[EBE62] J. R. Erskine, W. W. Buechner, and H. A. Enge. ^{209}Bi$(d, p)^{210}$Bi Reaction at Low Bombarding Energies and with High Resolution. *Phys. Rev.*, 128:720–728, Oct 1962.

[Efi70] V. Efimov. Energy levels arising from resonant two-body forces in a three-body system. *Phys. Lett. B*, 33(8):563 – 564, 1970.

[Elo19] IS561 ELOG. `https://elog.kern.phys.au.dk/IS561/220`, Accessed: Jul 2019.

[Els13] J. Elseviers. *Probing the semi-magicity of ^{68}Ni via the ^{66}Ni(t,p)^{68}Ni two-neutron transfer reaction in inverse kinematics*. PhD thesis, KU Leuven, Nov 2013.

[End77] P. M. Endt. Spectroscopic factors for single-nucleon transfer in the A = 21–44 region. *At. Data Nucl. Data Tables*, 19(1):23 – 61, 1977.

[ENS18] ENSDF: Evaluated nuclear structure data file. `https://www.nndc.bnl.gov/ensdf/index.jsp`, Dec 2018.

[ES08] J. Eberth and J. Simpson. From Ge(Li) detectors to gamma-ray tracking arrays–50 years of gamma spectroscopy with germanium detectors. *Prog. Part. Nucl. Phys.*, 60(2):283 – 337, 2008.

[FAB+10] S. J. Freeman, A. Andreyev, B. B. Back, V. Bildstein, P. A. Butler, W. N. Catford, J. Cederkall, G. Chapman, D. Di Julio, C. R. Hoffman, M. Huyse, D. Jenkins, B. P. Kay, T. Kröll, R. Krücken, D. Müncher, N. Nowak, R. Raabe, J. P. Schiffer, J. S.

Thomas, P. Van Duppen, R. Wadsworth, N. Warr, K. Wimmer, and A. H. Wuosmaa. Letter of Intent to the ISOLDE and Neutron Time-of-Flight Experiments Committee for experiments with HIE-ISOLDE: A HELIcal Orbit Spectrometer (HELIOS) for HIE-ISOLDE. Technical Report CERN-INTC-2010-031. INTC-I-099, CERN, Geneva, May 2010.

[Fad61] L. D. Faddeev. Scattering theory for a three particle system. *Sov. Phys. JETP*, 12:1014–1019, 1961. [Zh. Eksp. Teor. Fiz. 39, 1459 (1960)].

[FNA+04] N. Fukuda, T. Nakamura, N. Aoi, N. Imai, M. Ishihara, T. Kobayashi, H. Iwasaki, T. Kubo, A. Mengoni, M. Notani, H. Otsu, H. Sakurai, S. Shimoura, T. Teranishi, Y. X. Watanabe, and K. Yoneda. Coulomb and nuclear breakup of a halo nucleus ^{11}Be. *Phys. Rev. C*, 70:054606, Nov 2004.

[Gal88] T. F. Gallagher. Rydberg atoms. *Rep. Prog. Phys.*, 51(2):143, 1988.

[GCM14] J. Gómez Camacho and A. M. Moro. *A Pedestrian Approach to the Theory of Transfer Reactions: Application to Weakly-Bound and Unbound Exotic Nuclei*, pages 39–66. Springer Berlin Heidelberg, Berlin, Heidelberg, 2014.

[GFJ02] E. Garrido, D. V. Fedorov, and A. S. Jensen. The ^{10}Li spectrum and the ^{11}Li properties. *Nucl. Phys. A*, 700(1):117 – 141, 2002.

[Gie97] F. Gieres. *Symmetries in Physics:*. Editions Frontières, 1997.

[GJB+75] J. D. Goss, P. L. Jolivette, C. P. Browne, S. E. Darden, H. R. Weller, and R. A. Blue. Angular distribution measurements for ^{14}C$(d,p)^{15}$C and the level structure of ^{15}C. *Phys. Rev. C*, 12:1730–1738, Dec 1975.

[GKK+99] W. Geithner, S. Kappertz, M. Keim, P. Lievens, R. Neugart, L. Vermeeren, S. Wilbert, V. N. Fedoseyev, U. Köster, V. I. Mishin, V. Sebastian, and ISOLDE Collaboration. Measurement of the magnetic moment of the one-neutron halo nucleus ^{11}Be. *Phys. Rev. Lett.*, 83:3792–3795, Nov 1999.

[GL71] Yu. A. Golfand and E. P. Likhtman. Extension of the Algebra of Poincare Group Generators and Violation of p Invariance. *JETP Lett.*, 13:323–326, 1971. [Pisma Zh. Eksp. Teor. Fiz. 13, 452 (1971)].

[Gle04] N. K. Glendenning. *Direct Nuclear Reactions*. WORLD SCIENTIFIC, 2004.

[Gol66] L. J. B. Goldfarb. Lectures in theoretical physics. 1966.

[GRCM17] M. Gómez-Ramos, J. Casal, and A. M. Moro. Linking structure and dynamics in (p, pn) reactions with Borromean nuclei: The $^{11}\mathrm{Li}(p, pn)^{10}\mathrm{Li}$ case. *Phys. Lett. B*, 772:115 – 120, 2017.

[GRM17] M. Gómez-Ramos and A. M. Moro. Influence of target deformation and deuteron breakup in (d, p) transfer reactions. *Phys. Rev. C*, 95:044612, Apr 2017.

[GRMGCT15] M. Gómez-Ramos, A. M. Moro, J. Gómez-Camacho, and I. J. Thompson. Transfer induced by core excitation within an extended distorted-wave born approximation method. *Phys. Rev. C*, 92:014613, Jul 2015.

[GS18] D. J. Griffiths and D. F. Schroeter. *Introduction to quantum mechanics*. Cambridge University Press, 2018.

[GVO01] M. Garçon and J. W. Van Orden. *The Deuteron: Structure and Form Factors*, pages 293–378. Springer US, Boston, MA, 2001.

[Ham17] I. Hamamoto. Examining possible neutron-halo nuclei heavier than $^{37}\mathrm{Mg}$. *Phys. Rev. C*, 95:044325, Apr 2017.

[HC19] Chloë Hebborn and Pierre Capel. Sensitivity of one-neutron knockout to the nuclear structure of halo nuclei. *arXiv e-prints*, page arXiv:1906.07660, Jun 2019.

[HD68] W.R. Hering and M. Dost. On the l-dependence of stripping excitation functions. *Nucl. Phys. A*, 111(3):561 – 568, 1968.

[Hei27] W. Heisenberg. Über den anschaulichen inhalt der quantentheoretischen kinematik und mechanik. *Z. Phys.*, 43(3):172–198, Mar 1927.

[HEK+78] W. Henning, Y. Eisen, H.-J. Körner, D. G. Kovar, J. P. Schiffer, S. Vigdor, and B. Zeidman. Optimum Q value in heavy-ion-induced neutron transfer at the Coulomb barrier. *Phys. Rev. C*, 17:2245–2247, Jun 1978.

[HFA+09] P. J. Haigh, M. Freer, N. I. Ashwood, T. Bloxham, N. Curtis, P. McEwan, H. G. Bohlen, T. Dorsch, Tz. Kokalova, Ch. Schulz, and C. Wheldon. Neutron decay widths of excited states of $^{11}\mathrm{Be}$. *Phys. Rev. C*, 79:014302, Jan 2009.

[HIE19] About HIE-ISOLDE. `https://hie-isolde-project.web.cern.ch/about-hie-isolde`, Accessed: Jul 2019.

[HJ87] P. G. Hansen and B. Jonson. The neutron halo of extremely neutron-rich nuclei. *Europhys. Lett.*, 4(4):409, 1987.

[HJJ95] P. G. Hansen, A. S. Jensen, and B. Jonson. Nuclear halos. *Annu. Rev. Nucl. Part. Sci.*, 45(1):591–634, 1995.

[HJP17] H.-W. Hammer, C. Ji, and D. R. Phillips. Effective field theory description of halo nuclei. *J. Phys. G*, 44(10):103002, 2017.

[HKB+97] D. Habs, O. Kester, G. Bollen, L. Liljeby, K. G. Rensfelt, D. Schwalm, R. von Hahn, G. Walter, and P. Van Duppen. The REX-ISOLDE project. *Nucl. Phys. A*, 616:29–38. 9 p, 1997.

[HKS+98] D. Habs, O. Kester, T. Sieber, A. Kolbe, J. Ott, G. Bollen, F. Ames, D. Schwalm, R. von Hahn, R. Repnow, H. Podlech, A. Schempp, U. Ratzinger, L. Liljeby, K.-G. Rensfelt, F. Wenander, B. Jonsson, G. Nyman, P. Van Duppen, M. Huyse, A. Richter, G. Shrieder, G. Walter, and REX-ISOLDE collaboration. The REX-ISOLDE project. *Nucl. Instrum. Methods Phys. Res. B*, 139(1):128 – 135, 1998.

[HM53] J. Horowitz and A. M. L. Messiah. The mechanism of stripping reactions. *Phys. Rev.*, 92:1326–1327, Dec 1953.

[Hod84] P. E. Hodgson. The neutron optical potential. *Rep. Prog. Phys.*, 47(6):613–654, Jun 1984.

[HWG+02] A. Horvath, J. Weiner, A. Galonsky, F. Deak, Y. Higurashi, K. Ieki, Y. Iwata, A. Kiss, J. J. Kolata, Z. Seres, J. von Schwarzenberg, H. Schelin, S. Takeuchi, S. Typel, and R. E. Warner. Cross Section for the Astrophysical ^{14}C(n, γ)^{15}C Reaction via the Inverse Reaction. *Astrophys. J.*, 570(2):926–933, May 2002.

[Iac85] F. Iachello. Supersymmetry in nuclear physics. *Physica D*, 15(1):85 – 98, 1985.

[Iso19] ISOLDE facility. `http://isolde.web.cern.ch/facility`, Accessed: Jul 2019.

[JA14] D. H. Jakubassa-Amundsen. DWBA theory for elastic scattering of polarized electrons from heavy unpolarized nuclei. *J. Phys. G*, 41(7):075103, Apr 2014.

[Jen17] J. H. Jensen. Experimental study of neutron-rich Li isotopes: Progress report. Private Communication, 2017.

[JFB+13] J. G. Johansen, M. A. Fraser, V. Bildstein, T. Kröll, R. Raabe, K. Riisager, D. Voulot, and K. Wimmer. Characterization of low energy radioactive beams using direct reactions. *Nucl. Instrum. Methods Phys. Res. A*, 714:176 – 187, 2013.

[JMB+06] H. B. Jeppesen, A. M. Moro, U. C. Bergmann, M. J. G. Borge, J. Cederkäll, L. M. Fraile, H. O. U. Fynbo, J. Gómez-Camacho, H. T. Johansson, B. Jonson, M. Meister, T. Nilsson, G. Nyman, M. Pantea, K. Riisager, A. Richter, G. Schrieder, T. Sieber, O. Tengblad, E. Tengborn, M. Turrión, and F. Wenander. Study of ^{10}Li via the ^{9}Li(^{2}H, p) reaction at REX-ISOLDE. *Phys. Lett. B*, 642(5):449 – 454, 2006.

[Jon04] B. Jonson. Light dripline nuclei. *Phys. Rep.*, 389(1):1 – 59, 2004.

[JR00] A. S. Jensen and K. Riisager. Towards necessary and sufficient conditions for halo occurrence. *Phys. Lett. B*, 480(1):39 – 44, 2000.

[JRFG04] A. S. Jensen, K. Riisager, D. V. Fedorov, and E. Garrido. Structure and reactions of quantum halos. *Rev. Mod. Phys.*, 76:215–261, Feb 2004.

[JS70] R. C. Johnson and P. J. R. Soper. Contribution of deuteron breakup channels to deuteron stripping and elastic scattering. *Phys. Rev. C*, 1:976–990, Mar 1970.

[JT74] R. C. Johnson and P. C. Tandy. An approximate three-body theory of deuteron stripping. *Nucl. Phys. A*, 235(1):56 – 74, 1974.

[KAB+03] V. Kroha, A. Azhari, P. Bém, V. Burjan, C. A. Gagliardi, A. M. Mukhamedzhanov, J. Novák, Š. Piskoř, E. Šimečková, X. Tang, L. Trache, R. E. Tribble, and J. Vincour. Asymptotic normalization coefficients in nuclear astrophysics. *Nucl. Phys. A*, 719:C119 – C122, 2003.

[KAG+93] R. A. Kryger, A. Azhari, A. Galonsky, J. H. Kelley, R. Pfaff, E. Ramakrishnan, D. Sackett, B. M. Sherrill, M. Thoennessen, J. A. Winger, and S. Yokoyama. Neutron decay of ^{10}Li produced by fragmentation. *Phys. Rev. C*, 47:R2439–R2442, Jun 1993.

[KAKR09] N. Keeley, N. Alamanos, K. W. Kemper, and K. Rusek. Elastic scattering and reactions of light exotic beams. *Prog. Part. Nucl. Phys.*, 63(2):396 – 447, 2009.

[Kar75] P. J. Karol. Nucleus-nucleus reaction cross sections at high energies: Soft-spheres model. *Phys. Rev. C*, 11:1203–1209, Apr 1975.

[KBF+10] G. Korschinek, A. Bergmaier, T. Faestermann, U.C. Gerstmann, K. Knie, G. Rugel, A. Wallner, I. Dillmann, G. Dollinger, Ch. Lierse von Gostomski, K. Kossert, M. Maiti, M. Poutivtsev, and A. Remmert. A new value for the half-life of ^{10}Be by Heavy-Ion Elastic Recoil Detection and liquid scintillation counting. *Nucl. Instrum. Methods Phys. Res. B*, 268(2):187 – 191, 2010.

[KD03] A. J. Koning and J. P. Delaroche. Local and global nucleon optical models from 1 keV to 200 MeV. *Nucl. Phys. A*, 713(3):231 – 310, 2003.

[KEF+94] G. Kraus, P. Egelhof, C. Fischer, H. Geissel, A. Himmler, F. Nickel, G. Münzenberg, W. Schwab, A. Weiss, J. Friese, A. Gillitzer, H. J. Körner, M. Peter, W. F. Henning, J. P. Schiffer, J. V. Kratz, L. Chulkov, M. Golovkov, A. Ogloblin, and B. A. Brown. Proton inelastic scattering on ^{56}Ni in inverse kinematics. *Phys. Rev. Lett.*, 73:1773–1776, Sep 1994.

[KFPK18] Y. Kadi, M. A. Fraser, and A. Papageorgiou-Koufidou. *HIE-ISOLDE: technical design report for the energy upgrade.* CERN Yellow Reports: Monographs. CERN, Geneva, May 2018.

[KGOY07] S. Kutlu, R. T. Güray, N. Özkan, and C. Yalçin. Calculation of Effective Beam Energy Depending on the Target Thickness in Applications of Nuclear Astrophysics. *AIP Conf. Proc.*, 899(1):547–547, 2007.

[KH16] B. Kay and C. Hoffman. The (d,p) reaction on ^{206}Hg. Technical Report CERN-INTC-2016-056. INTC-CLL-026, CERN, Geneva, Oct 2016.

[KHH+16] R. Kanungo, W. Horiuchi, G. Hagen, G. R. Jansen, P. Navrátil, F. Ameil, J. Atkinson, Y. Ayyad, D. Cortina-Gil, I. Dillmann, A. Estradé, A. Evdokimov, F. Farinon, H. Geissel, G. Guastalla, R. Janik, M. Kimura, R. Knöbel, J. Kurcewicz, Yu. A. Litvinov, M. Marta, M. Mostazo, I. Mukha, C. Nociforo, H. J. Ong, S. Pietri, A. Prochazka, C. Scheidenberger, B. Sitar, P. Strmen,

Y. Suzuki, M. Takechi, J. Tanaka, I. Tanihata, S. Terashima, J. Vargas, H. Weick, and J. S. Winfield. Proton distribution radii of $^{12-19}$C illuminate features of neutron halos. *Phys. Rev. Lett.*, 117:102501, Sep 2016.

[KI93] K. Katō and K. Ikeda. Analysis of ^{9}Li + n Resonances in ^{10}Li by Complex Scaling Method: Interaction between ^{9}Li and Neutron. *Prog. Theor. Phys.*, 89(3):623–637, Mar 1993.

[KKP+12] J. H. Kelley, E. Kwan, J. E. Purcell, C. G. Sheu, and H. R. Weller. Energy levels of light nuclei A = 11. *Nucl. Phys. A*, 880:88 – 195, 2012.

[KKT86] M. Kawai, M. Kamimura, and K. Takesako. Chapter V. Coupled-Channels Variational Method for Nuclear Breakup and Rearrangement Processes. *Prog. Theor. Phys. Supp.*, 89:118–135, Apr 1986.

[LBC+17] A. E. Lovell, P.-L. Bacq, P. Capel, F. M. Nunes, and L. J. Titus. Energy dependence of nonlocal optical potentials. *Phys. Rev. C*, 96:051601, Nov 2017.

[LBS97] G. Lévai, D. Baye, and J.-M. Sparenberg. Phase-equivalent potentials from supersymmetry: analytical results for a natanzon-class potential. *J. Phys. A: Math. Gen.*, 30(23):8257–8271, Dec 1997.

[LCL+10] M. Labiche, W. N. Catford, R. C. Lemmon, C. N. Timis, R. Chapman, N. A. Orr, B. Fernández-Domínguez, G. Moores, N. L. Achouri, N. Amzal, S. Appleton, N. I. Ashwood, T. D. Baldwin, M. Burns, L. Caballero, J. Cacitti, J. M. Casadjian, M. Chartier, N. Curtis, K. Faiz, G. de France, M. Freer, J. M. Gautier, W. Gelletly, G. Iltis, B. Lecornu, X. Liang, C. Marry, Y. Merrer, L. Olivier, S. D. Pain, V. F. E. Pucknell, B. Raine, M. Rejmund, B. Rubio, F. Saillant, H. Savajols, O. Sorlin, K. Spohr, Ch. Theisen, G. Voltolini, and D. D. Warner. TIARA: A large solid angle silicon array for direct reaction studies with radioactive beams. *Nucl. Instrum. Methods Phys. Res. A*, 614(3):439 – 448, 2010.

[LLL33] E. O. Lawrence, M. S. Livingston, and G. N. Lewis. The emission of protons from various targets bombarded by deutons of high speed. *Phys. Rev.*, 44:56–56, Jul 1933.

[LN18] A. E. Lovell and F. M. Nunes. Constraining transfer cross sections using bayes' theorem. *Phys. Rev. C*, 97:064612, Jun 2018.

[MAB+01] V. Maddalena, T. Aumann, D. Bazin, B. A. Brown, J. A. Caggiano, B. Davids, T. Glasmacher, P. G. Hansen, R. W. Ibbotson, A. Navin, B. V. Pritychenko, H. Scheit, B. M. Sherrill, M. Steiner, J. A. Tostevin, and J. Yurkon. One-nucleon knockout reactions: The test case ^{15}C and the single-particle structure of ^{16,17,19}C. *Nucl. Phys. A*, 682(1):332 – 338, 2001.

[MBA+09] M. Madurga, M. J. G. Borge, M. Alcorta, L. M. Fraile, H. O. U. Fynbo, B. Jonson, O. Kirsebom, G. Martínez-Pinedo, T. Nilsson, G. Nyman, A. Perea, A. Poves, K. Riisager, O. Tengblad, E. Tengborn, and J. Van der Walle. Evidence of a new state in ^{11}Be observed in the ^{11}Li β-decay. *Phys. Lett. B*, 677(5):255 – 259, 2009.

[MBG+11] A. M. Mukhamedzhanov, V. Burjan, M. Gulino, Z. Hons, V. Kroha, M. McCleskey, J. Mrázek, N. Nguyen, F. M. Nunes, Š. Piskoř, S. Romano, M. L. Sergi, C. Spitaleri, and R. E. Tribble. Asymptotic normalization coefficients from the ^{14}C$(d,p)^{15}$C reaction. *Phys. Rev. C*, 84:024616, Aug 2011.

[MCGR19] A. M. Moro, J. Casal, and M. Gómez-Ramos. Investigating the ^{10}Li continuum through ^{9}Li$(d,p)^{10}$Li reactions. *Phys. Lett. B*, 793:13 – 18, 2019.

[MF77] N. J. McGurk and H. Fiedeldey. The deuteron wave function at short range and the triton. *Nucl. Phys. A*, 281(2):310 – 324, 1977.

[MJ55] M. G. Mayer and J. H. D. Jensen. *Elementary Theory of Nuclear Shell Structure*. Structure of matter series. John Wiley & Sons, 1955.

[MKM+97] R. Morlock, R. Kunz, A. Mayer, M. Jaeger, A. Müller, J. W. Hammer, P. Mohr, H. Oberhummer, G. Staudt, and V. Kölle. Halo Properties of the First $1/2^+$ State in ^{17}F from the ^{16}O$(p,\gamma)^{17}$F Reaction. *Phys. Rev. Lett.*, 79:3837–3840, Nov 1997.

[MLSO97] W. Mittig, A. Lépine-Szily, and N. A. Orr. Mass measurement far from stability. *Annu. Rev. Nucl. Part. Sci.*, 47(1):27–66, 1997.

[MMT+14] M. McCleskey, A. M. Mukhamedzhanov, L. Trache, R. E. Tribble, A. Banu, V. Eremenko, V. Z. Goldberg, Y.-W. Lui, E. McCleskey, B. T. Roeder, A. Spiridon, F. Carstoiu, V. Burjan, Z. Hons, and I. J. Thompson. Determination of the asymptotic normalization coefficients for $^{14}C + n \leftrightarrow {}^{15}C$, the $^{14}C(n,\gamma)^{15}C$ reaction rate, and evaluation of a new method to determine spectroscopic factors. *Phys. Rev. C*, 89:044605, Apr 2014.

[MPS+02] K. Mathieson, M. S. Passmore, P. Seller, M. L. Prydderch, V. O'Shea, R. L. Bates, K. M. Smith, and M. Rahman. Charge sharing in silicon pixel detectors. *Nucl. Instrum. Methods Phys. Res. A*, 487(1):113 – 122, 2002. 3rd International Workshop on Radiation Imaging Detectors.

[MSV+07] P. Mueller, I. A. Sulai, A. C. C. Villari, J. A. Alcántara-Núñez, R. Alves-Condé, K. Bailey, G. W. F. Drake, M. Dubois, C. Eléon, G. Gaubert, R. J. Holt, R. V. F. Janssens, N. Lecesne, Z.-T. Lu, T. P. O'Connor, M.-G. Saint-Laurent, J.-C. Thomas, and L.-B. Wang. Nuclear charge radius of ^{8}He. *Phys. Rev. Lett.*, 99:252501, Dec 2007.

[MT99] A. M. Mukhamedzhanov and R. E. Tribble. Connection between asymptotic normalization coefficients, subthreshold bound states, and resonances. *Phys. Rev. C*, 59:3418–3424, 1999.

[MYC19] L. Moschini, J. Yang, and P. Capel. ^{15}C: From halo effective field theory structure to the study of transfer, breakup, and radiative-capture reactions. *Phys. Rev. C*, 100:044615, Oct 2019.

[MZ15] J. Meng and S. G. Zhou. Halos in medium-heavy and heavy nuclei with covariant density functional theory in continuum. *J. Phys. G*, 42(9):093101, 2015.

[Nav18] P. Navrátil. Private Communication, 2018.

[NBB+08] R. Neugart, D. L. Balabanski, K. Blaum, D. Borremans, P. Himpe, M. Kowalska, P. Lievens, S. Mallion, G. Neyens, N. Vermeulen, and D. T. Yordanov. Precision measurement of ^{11}Li moments: Influence of halo neutrons on the ^{9}Li core. *Phys. Rev. Lett.*, 101:132502, Sep 2008.

[ND11] F. M. Nunes and A. Deltuva. Adiabatic approximation versus exact Faddeev method for (d,p) and (p,d) reactions. *Phys. Rev. C*, 84:034607, Sep 2011.

[Nou24] B. V. Noumerov. A Method of Extrapolation of Perturbations. *Mon. Not. R. Astron. Soc.*, 84(8):592–602, Jun 1924.

[NQH+16] P. Navrátil, S. Quaglioni, G. Hupin, C. Romero-Redondo, and A. Calci. Unified *ab initio* approaches to nuclear structure and reactions. *Phys. Scr.*, 91(5):053002, Apr 2016.

[NS71] A. Neveu and J. H. Schwarz. Factorizable dual model of pions. *Nucl. Phys. B*, 31:86–112, 1971.

[NTicv+09] W. Nörtershäuser, D. Tiedemann, M. Žáková, Z. Andjelkovic, K. Blaum, M. L. Bissell, R. Cazan, G. W. F. Drake, Ch. Geppert, M. Kowalska, J. Krämer, A. Krieger, R. Neugart, R. Sánchez, F. Schmidt-Kaler, Z.-C. Yan, D. T. Yordanov, and C. Zimmermann. Nuclear charge radii of ^{7,9,10}Be and the one-neutron halo nucleus ^{11}Be. *Phys. Rev. Lett.*, 102:062503, Feb 2009.

[NU12] F. M. Nunes and N. J. Upadhyay. Status of reaction theory for studying rare isotopes. *J. Phys.: Conf. Ser.*, 403:012029, 2012.

[NuD19] National nuclear data center, information extracted from the nudat 2 database. `https://www.nndc.bnl.gov/nudat2/chartNuc.jsp`, 2019.

[OKS+94] A. Ozawa, T. Kobayashi, H. Sato, D. Hirata, I. Tanihata, O. Yamakawa, K. Omata, K. Sugimoto, D. Olson, W. Christie, and H. Wieman. Interaction cross sections and radii of the mass number A = 17 isobar (^{17}N, ^{17}F, and ^{17}Ne). *Phys. Lett. B*, 334(1):18 – 22, 1994.

[OMNP12] J. Okołowicz, N. Michel, W. Nazarewicz, and M. Płoszajczak. Asymptotic normalization coefficients and continuum coupling in mirror nuclei. *Phys. Rev. C*, 85:064320, Jun 2012.

[OST01] A. Ozawa, T. Suzuki, and I. Tanihata. Nuclear size and related topics. *Nucl. Phys. A*, 693(1):32 – 62, 2001.

[OT99] M. Oinonen and The Isolde Collaboration. Nuclear physics at ISOLDE. *Czech. J. Phys.*, 49(2):193–203, Feb 1999.

[Ots13] T. Otsuka. Exotic nuclei and nuclear forces. *Phys. Scr.*, T152:014007, Jan 2013.

[OZV99] Yu. Ts. Oganessian, V. I. Zagrebaev, and J. S. Vaagen. "Di-Neutron" Configuration of ^{6}He. *Phys. Rev. Lett.*, 82:4996–4999, Jun 1999.

[PB62] F. Perey and B. Buck. A non-local potential model for the scattering of neutrons by nuclei. *Nucl. Phys.*, 32:353 – 380, 1962.

[PCH+07] S. D. Pain, J. A. Cizewski, R. Hatarik, K. L. Jones, J. S. Thomas, D. W. Bardayan, J. C. Blackmon, C. D. Nesaraja, M. S. Smith, R. L. Kozub, and M. S. Johnson. Development of a high solid-angle silicon detector array for measurement of transfer reactions in inverse kinematics. *Nucl. Instrum. Methods Phys. Res. B*, 261(1):1122 – 1125, 2007.

[PKGR12] M. Pfützner, M. Karny, L. V. Grigorenko, and K. Riisager. Radioactive decays at limits of nuclear stability. *Rev. Mod. Phys.*, 84:567–619, Apr 2012.

[PNM07] D.-Y. Pang, F. M. Nunes, and A. M. Mukhamedzhanov. Are spectroscopic factors from transfer reactions consistent with asymptotic normalization coefficients? *Phys. Rev. C*, 75:024601, Feb 2007.

[PP74] C. M. Perey and F. G. Perey. Compilation of phenomenological optical-model parameters 1969–1972. *At. Data Nucl. Data Tables*, 13(4):293 – 337, 1974.

[PR18] M. Pfützner and K. Riisager. Examining the possibility to observe neutron dark decay in nuclei. *Phys. Rev. C*, 97:042501, Apr 2018.

[PRN+08] S. Pullanhiotan, M. Rejmund, A. Navin, W. Mittig, and S. Bhattacharyya. Performance of vamos for reactions near the coulomb barrier. *Nucl. Instrum. Methods Phys. Res. A*, 593(3):343 – 352, 2008.

[Raa09] R. Raabe. ACTAR: the New Generation of Active Targets. *AIP Conf. Proc.*, 1165(1):339, 2009.

[RAB+08] R. Raabe, A. Andreyev, M. J. G. Borge, L. Buchmann, P. Capel, H. O. U. Fynbo, M. Huyse, R. Kanungo, T. Kirchner, C. Mattoon, A. C. Morton, I. Mukha, J. Pearson, J. Ponsaers, J. J. Ressler, K. Riisager, C. Ruiz, G. Ruprecht, F. Sarazin, O. Tengblad, P. Van Duppen, and P. Walden. β-delayed deuteron emission from ^{11}Li: Decay of the halo. *Phys. Rev. Lett.*, 101:212501, Nov 2008.

[Ram71] P. Ramond. Dual theory for free fermions. *Phys. Rev. D*, 3:2415–2418, May 1971.

[Raw74] G. H. Rawitscher. Effect of deuteron breakup on elastic deuteron - nucleus scattering. *Phys. Rev. C*, 9:2210–2229, Jun 1974.

[RBD09] V. Rotival, K. Bennaceur, and T. Duguet. Halo phenomenon in finite many-fermion systems: Atom-positron complexes and large-scale study of atomic nuclei. *Phys. Rev. C*, 79:054309, May 2009.

[REF+02] P. Reiter, J. Eberth, H. Faust, S. Franchoo, J. Gerl, C. Gund, D. Habs, M. Huyse, A. Jungclaus, K. P. Lieb, H. Scheit, D. Schwalm, H. G. Thomas, P. van Duppen, and D. Weisshaar. The MINIBALL array. *Nucl. Phys. A*, 701(1):209 – 212, 2002. 5th International Conference on Radioactive Nuclear Beams.

[Ref16] J. Refsgaard. *Resonances, R-matrix - Rotations in* ^{12}C. PhD thesis, Aarhus University, 2016.

[Rei68] R. V. Reid. Local phenomenological nucleon-nucleon potentials. *Ann. Phys.*, 50(3):411 – 448, 1968.

[RFHP14] E. Ryberg, C. Forssén, H.-W. Hammer, and L. Platter. Constraining low-energy proton capture on beryllium-7 through charge radius measurements. *Eur. Phys. J. A*, 50(11):170, Nov 2014.

[Rii94] K. Riisager. Nuclear halo states. *Rev. Mod. Phys.*, 66:1105–1116, Jul 1994.

[Rii13] K. Riisager. Halos and related structures. *Phys. Scr.*, 2013(T152):014001, 2013.

[Rut11] E. Rutherford. The scattering of alpha and beta particles by matter and the structure of the atom. *Phil. Mag. Ser.6*, 21:669–688, 1911.

[SAB+02] P. Schmidt, F. Ames, G. Bollen, O. Forstner, G. Huber, M. Oinonen, and J. Zimmer. Bunching and cooling of radioactive ions with REXTRAP. *Nucl. Phys. A*, 701:550–556. 7 p, 2002.

[Sat64] G. R. Satchler. The distorted-waves theory of direct nuclear reactions with spin-orbit effects. *Nucl. Phys.*, 55:1 – 33, 1964.

[Sat83] G. R. Satchler. *Direct Nuclear Reactions*. International series of monographs on physics. Clarendon Press, 1983.

[Sat90] G. R. Satchler. *Introduction to Nuclear Reactions*, pages 21–88. Palgrave Macmillan UK, London, 1990.

[SB97] J.-M. Sparenberg and D. Baye. Supersymmetry between phase-equivalent coupled-channel potentials. *Phys. Rev. Lett.*, 79:3802–3805, Nov 1997.

[SCO+04] E. Sauvan, F. Carstoiu, N. A. Orr, J. S. Winfield, M. Freer, J. C. Angélique, W. N. Catford, N. M. Clarke, N. Curtis, S. Grévy, C. Le Brun, M. Lewitowicz, E. Liégard, F. M. Marqués, M. Mac Cormick, P. Roussel-Chomaz, M.-G. Saint Laurent, and M. Shawcross. One-neutron removal reactions on light neutron-rich nuclei. *Phys. Rev. C*, 69:044603, Apr 2004.

[Ser47] R. Serber. The production of high energy neutrons by stripping. *Phys. Rev.*, 72:1008–1016, Dec 1947.

[SFB+16] D. Sharp, S. Freeman, B. Back, P. Butler, W. Catford, A. Deacon, L. Gaffney, C. Hoffman, R. Janssens, B. Kay, T. Kröll, M. Labiche, G. Lotay, A. Matta, R. Page, R. Raabe, and D. Steppenbeck. Single-particle behaviour towards the "island of inversion" - ^{28,30}Mg$(d,p)^{29,31}$Mg in inverse kinematics. Technical Report CERN-INTC-2016-030. INTC-P-470, CERN, Geneva, Jun 2016.

[Sim19] simX. `https://git.kern.phys.au.dk/ausa/simX/wikis/home`, Accessed: Jul 2019.

[SJA+13] K. T. Schmitt, K. L. Jones, S. Ahn, D. W. Bardayan, A. Bey, J. C. Blackmon, S. M. Brown, K. Y. Chae, K. A. Chipps, J. A. Cizewski, K. I. Hahn, J. J. Kolata, R. L. Kozub, J. F. Liang, C. Matei, M. Matos, D. Matyas, B. Moazen, C. D. Nesaraja, F. M. Nunes, P. D. O'Malley, S. D. Pain, W. A. Peters, S. T. Pittman, A. Roberts, D. Shapira, J. F. Shriner, M. S. Smith, I. Spassova, D. W. Stracener, N. J. Upadhyay, A. N. Villano, and G. L. Wilson. Reactions of a ^{10}Be beam on proton and deuteron targets. *Phys. Rev. C*, 88:064612, Dec 2013.

[SJB+12] K. T. Schmitt, K. L. Jones, A. Bey, S. H. Ahn, D. W. Bardayan, J. C. Blackmon, S. M. Brown, K. Y. Chae, K. A. Chipps, J. A. Cizewski, K. I. Hahn, J. J. Kolata, R. L. Kozub, J. F. Liang, C. Matei, M. Matoš, D. Matyas, B. Moazen, C. Nesaraja, F. M. Nunes, P. D. O'Malley, S. D. Pain, W. A. Peters, S. T. Pittman, A. Roberts, D. Shapira, J. F. Shriner, M. S. Smith, I. Spassova, D. W. Stracener, A. N. Villano, and G. L. Wilson. Halo nucleus ^{11}Be: A spectroscopic study via neutron transfer. *Phys. Rev. Lett.*, 108:192701, May 2012.

[SKGa+03] P. Santi, J. J. Kolata, V. Guimãraes, D. Peterson, R. White-Stevens, E. Rischette, D. Bazin, B. M. Sherrill, A. Navin, P. A. DeYoung, P. L. Jolivette, G. F. Peaslee, and R. T. Guray. Structure of the ^{10}Li nucleus investigated via the ^{9}Li(d,p)^{10}Li reaction. *Phys. Rev. C*, 67:024606, Feb 2003.

[SN08] N. C. Summers and F. M. Nunes. Extracting (n, γ) direct capture cross sections from coulomb dissociation: Application to ^{14}C$(n, \gamma)^{15}$C. *Phys. Rev. C*, 78:011601, Jul 2008. Corrected in "Erratum", *Phys. Rev. C*, 78:069908, Dec 2008.

[SNE+06] R. Sánchez, W. Nörtershäuser, G. Ewald, D. Albers, J. Behr, P. Bricault, B. A. Bushaw, A. Dax, J. Dilling, M. Dombsky, G. W. F. Drake, S. Götte, R. Kirchner, H.-J. Kluge, Th. Kühl, J. Lassen, C. D. P. Levy, M. R. Pearson, E. J. Prime, V. Ryjkov, A. Wojtaszek, Z.-C. Yan, and C. Zimmermann. Nuclear charge radii of ^{9,11}Li: The influence of halo neutrons. *Phys. Rev. Lett.*, 96:033002, Jan 2006.

[SP13] O. Sorlin and M.-G. Porquet. Evolution of the N = 28 shell closure: a test bench for nuclear forces. *Phys. Scr.*, T152:014003, Jan 2013.

[TAB+08] I. Tanihata, M. Alcorta, D. Bandyopadhyay, R. Bieri, L. Buchmann, B. Davids, N. Galinski, D. Howell, W. Mills, S. Mythili, R. Openshaw, E. Padilla-Rodal, G. Ruprecht, G. Sheffer, A. C. Shotter, M. Trinczek, P. Walden, H. Savajols, T. Roger, M. Caamano, W. Mittig, P. Roussel-Chomaz, R. Kanungo, A. Gallant, M. Notani, G. Savard, and I. J. Thompson. Measurement of the Two-Halo Neutron Transfer Reaction ^{1}H(^{11}Li,^{9}Li)^{3}H at 3A MeV. *Phys. Rev. Lett.*, 100:192502, May 2008.

[TAC+02] L. Trache, A. Azhari, F. Carstoiu, C. A. Gagliardi, A. M. Mukhamedzhanov, X. D. Tang, R. E. Tribble, and S. Zhou. *Tex. A&M Cyclotron Prog. Rep.*, 1:16, 2002.

[Tan96] I. Tanihata. Neutron halo nuclei. *J. Phys. G*, 22(2):157, 1996.

[TB05] S. Typel and G. Baur. Electromagnetic strength of neutron and proton single-particle halo nuclei. *Nucl. Phys. A*, 759(3):247 – 308, 2005.

[TBC+14] R. E. Tribble, C. A. Bertulani, M. La Cognata, A. M. Mukhamedzhanov, and C. Spitaleri. Indirect techniques in

nuclear astrophysics: a review. *Rep. Prog. Phys.*, 77(10):106901, Oct 2014.

[TBD+06] N. K. Timofeyuk, D. Baye, P. Descouvemont, R. Kamouni, and I. J. Thompson. ^{15}C−^{15}F charge symmetry and the ^{14}C$(n,\gamma)^{15}$C reaction puzzle. *Phys. Rev. Lett.*, 96:162501, Apr 2006.

[THH+85] I. Tanihata, H. Hamagaki, O. Hashimoto, Y. Shida, N. Yoshikawa, K. Sugimoto, O. Yamakawa, T. Kobayashi, and N. Takahashi. Measurements of Interaction Cross Sections and Nuclear Radii in the Light *p*-Shell Region. *Phys. Rev. Lett.*, 55:2676–2679, Dec 1985.

[Tho88] I. J. Thompson. Coupled reaction channels calculations in nuclear physics. *Comput. Phys. Rep.*, 7(4):167 – 212, 1988.

[Tho02] I. J. Thompson. Halo physics. *Nucl. Phys. A*, 701(1):7 – 13, 2002. 5th International Conference on Radioactive Nuclear Beams.

[Tho06] I. J. Thompson. FRESCO, coupled reaction channels calculations. `http://www.fresco.org.uk`, 2006.

[TKY+88] I. Tanihata, T. Kobayashi, O. Yamakawa, S. Shimoura, K. Ekuni, K. Sugimoto, N. Takahashi, T. Shimoda, and H. Sato. Measurement of interaction cross sections using isotope beams of Be and B and isospin dependence of the nuclear radii. *Phys. Lett. B*, 206(4):592 – 596, 1988.

[TN09] I. J. Thompson and F. M. Nunes. *Nuclear Reactions for Astrophysics: Principles, Calculation and Applications of Low-Energy Reactions*. Cambridge University Press, 2009.

[TPM15] Y. Tian, D.-Y. Pang, and Z.-Y. Ma. Systematic nonlocal optical model potential for nucleons. *Int. J. Mod. Phys.*, E24(01):1550006, 2015.

[TTIK12] J. A. Tostevin, M. Toyama, M. Igarashi, and N. Kishida. University of Surrey version of the code TWOFNR. `http://www.nucleartheory.net/NPG/code.htm`, 2012.

[TU60] I. Talmi and I. Unna. Order of Levels in the Shell Model and Spin of ^{11}Be. *Phys. Rev. Lett.*, 4:469–470, May 1960.

[TYA+99] M. Thoennessen, S. Yokoyama, A. Azhari, T. Baumann, J. A. Brown, A. Galonsky, P. G. Hansen, J. H. Kelley, R. A. Kryger, E. Ramakrishnan, and P. Thirolf. Population of ^{10}Li by fragmentation. *Phys. Rev. C*, 59:111–117, Jan 1999.

[TZ94] I. J. Thompson and M. V. Zhukov. Effects of ^{10}Li virtual states on the structure of ^{11}Li. *Phys. Rev. C*, 49:1904–1907, Apr 1994.

[UDN12] N. J. Upadhyay, A. Deltuva, and F. M. Nunes. Testing the continuum-discretized coupled channels method for deuteron-induced reactions. *Phys. Rev. C*, 85:054621, May 2012.

[VD06] P. Van Duppen. *Isotope Separation On Line and Post Acceleration*, pages 37–77. Springer Berlin Heidelberg, Berlin, Heidelberg, 2006.

[vK14] U. van Kolck. *Effective Field Theories of Loosely Bound Nuclei*, pages 123–182. Springer Berlin Heidelberg, Berlin, Heidelberg, 2014.

[VTM+91] R. L. Varner, W. J. Thompson, T. L. McAbee, E. J. Ludwig, and T. B. Clegg. A global nucleon optical model potential. *Phys. Rep.*, 201(2):57 – 119, 1991.

[Wen10] F. Wenander. Charge breeding of radioactive ions with EBIS and EBIT. *J. Instrum*, 5(10):C10004–C10004, Oct 2010.

[WG86] P. R. Walter and P. P. Guss. Proc. int. conf. santa fe 1079. In *(1985), Rad. Effect*, volume 95, page 73, 1986.

[WH68] D. M. Wayte and E. B. Helwig. Halo nevi. *Cancer*, 22(1):69–90, 1968.

[Wit81] E. Witten. Dynamical breaking of supersymmetry. *Nucl. Phys. B*, 188(3):513 – 554, 1981.

[WMB+04] L.-B. Wang, P. Mueller, K. Bailey, G. W. F. Drake, J. P. Greene, D. Henderson, R. J. Holt, R. V. F. Janssens, C. L. Jiang, Z.-T. Lu, T. P. O'Connor, R. C. Pardo, K. E. Rehm, J. P. Schiffer, and X. D. Tang. Laser spectroscopic determination of the ^{6}He nuclear charge radius. *Phys. Rev. Lett.*, 93:142501, Sep 2004.

[WSB+07] A. H. Wuosmaa, J. P. Schiffer, B. B. Back, C. J. Lister, and K. E. Rehm. A solenoidal spectrometer for reactions in inverse kinematics. *Nucl. Instrum. Methods Phys. Res. A*, 580(3):1290 – 1300, 2007.

[WWW+75] K. H. Wilcox, R. B. Weisenmiller, G. J. Wozniak, N. A. Jelley, D. Ashery, and J. Cerny. The (^{9}Be,^{8}B) reaction and the unbound nuclide ^{10}Li. *Phys. Lett. B*, 59(2):142 – 144, 1975.

[XTG+13] Y. Xu, K. Takahashi, S. Goriely, M. Arnould, M. Ohta, and H. Utsunomiya. NACRE II: an update of the NACRE compilation of charged-particle-induced thermonuclear reaction rates for nuclei with mass number A < 16. *Nucl. Phys. A*, 918:61 – 169, 2013.

[YBF+93] B. M. Young, W. Benenson, M. Fauerbach, J. H. Kelley, R. Pfaff, B. M. Sherrill, M. Steiner, J. S. Winfield, T. Kubo, M. Hellström, N. A. Orr, J. Stetson, J. A. Winger, and S. J. Yennello. Mass of ^{11}Li from the ^{14}C(^{11}B,^{11}Li)^{14}O Reaction. *Phys. Rev. Lett.*, 71:4124–4126, Dec 1993.

[YBK+94] B. M. Young, W. Benenson, J. H. Kelley, N. A. Orr, R. Pfaff, B. M. Sherrill, M. Steiner, M. Thoennessen, J. S. Winfield, J. A. Winger, S. J. Yennello, and A. Zeller. Low-lying structure of ^{10}Li in the reaction ^{11}B(^{7}Li,^{8}B)^{10}Li. *Phys. Rev. C*, 49:279–283, Jan 1994.

[YC18] J. Yang and P. Capel. Systematic analysis of the peripherality of the ^{10}Be$(d,p)^{11}$Be transfer reaction and extraction of the asymptotic normalization coefficient of ^{11}Be bound states. *Phys. Rev. C*, 98:054602, Nov 2018.

[YMM+12] M. Yahiro, T. Matsumoto, K. Minomo, T. Sumi, and S. Watanabe. Recent Development of CDCC. *Prog. Theor. Phys. Supp.*, 196:87–101, Oct 2012.

[ZDF+93] M. V. Zhukov, B. V. Danilin, D. V. Fedorov, J. M. Bang, I. J. Thompson, and J. S. Vaagen. Bound state properties of borromean halo nuclei: ^{6}He and ^{11}Li. *Phys. Rep.*, 231(4):151 – 199, 1993.

[ZHN+95] M. Zinser, F. Humbert, T. Nilsson, W. Schwab, Th. Blaich, M. J. G. Borge, L. V. Chulkov, H. Eickhoff, Th. W. Elze, H. Emling, B. Franzke, H. Freiesleben, H. Geissel, K. Grimm, D. Guillemaud-Mueller, P. G. Hansen, R. Holzmann, H. Irnich, B. Jonson, J. G. Keller, O. Klepper, H. Klingler, J. V. Kratz, R. Kulessa, D. Lambrecht, Y. Leifels, A. Magel, M. Mohar, A. C. Mueller, G. Münzenberg, F. Nickel, G. Nyman, A. Richter, K. Riisager, C. Scheidenberger, G. Schrieder, B. M. Sherrill, H. Simon, K. Stelzer, J. Stroth, O. Tengblad, W. Trautmann, E. Wajda, and E. Zude. Study of the Unstable Nucleus ^{10}Li in Stripping Reactions of the Radioactive Projectiles ^{11}Be and ^{11}Li. *Phys. Rev. Lett.*, 75:1719–1722, Aug 1995.

[ZHN+97] M. Zinser, F. Humbert, T. Nilsson, W. Schwab, H. Simon, T. Aumann, M. J. G. Borge, L. V. Chulkov, J. Cub, Th. W. Elze, H. Emling, H. Geissel, D. Guillemaud-Mueller, P. G. Hansen, R. Holzmann, H. Irnich, B. Jonson, J. V. Kratz, R. Kulessa, Y. Leifels, H. Lenske, A. Magel, A. C. Mueller, G. Münzenberg, F. Nickel, G. Nyman, A. Richter, K. Riisager, C. Scheidenberger, G. Schrieder, K. Stelzer, J. Stroth, A. Surowiec, O. Tengblad, E. Wajda, and E. Zude. Invariant-mass spectroscopy of ^{10}Li and ^{11}Li. *Nucl. Phys. A*, 619(1):151 – 176, 1997.

[ZNP14] X. Zhang, K. M. Nollett, and D. R. Phillips. Marrying *ab initio* calculations and Halo-EFT: the case of $^{7}\mathrm{Li} + n \to {}^{8}\mathrm{Li} + \gamma$. *Phys. Rev. C*, 89(2):024613, 2014.

[ZZB10] J. F. Ziegler, M. D. Ziegler, and J. P. Biersack. SRIM – The stopping and range of ions in matter (2010). *Nucl. Instrum. Methods Phys. Res. B*, 268(11):1818 – 1823, 2010. 19th International Conference on Ion Beam Analysis.

[ZZK+14] V. I. Zagrebaev, S. G. Zemlyanoy, E. M. Kozulin, Yu. Kudryavtsev, V. Fedosseev, R. Bark, Z. Janas, and H. A. Othman. Multi-nucleon transfer reactions for production and study of heavy neutron rich nuclei. *J. Phys.: Conf. Ser.*, 533:012025, Sep 2014.

[a] ÉCOLE POLYTECHNIQUE DE BRUXELLES
PHYSIQUE NUCLÉAIRE ET PHYSIQUE QUANTIQUE (CP 229)
B-1050 Brussels
jiecyang@ulb.ac.be
http://pntpm4.ulb.ac.be/pntpm/

[b] FACULTY OF SCIENCE
DEPARTMENT OF PHYSICS AND ASTRONOMY
INSTITUTE FOR NUCLEAR AND RADIATION PHYSICS
Celestijnenlaan 200D box 2418
B-3001 Leuven
jiecheng.yang@kuleuven.be
https://fys.kuleuven.be/iks